

DISS. ETH Nr.: 26325

**EXPERIMENTAL INVESTIGATION AND MODELING  
OF DIAMOND WIRE SAWING OF  
SINGLE-CRYSTAL SILICON**

A thesis submitted to attain the degree of  
DOCTOR OF SCIENCES of ETH ZÜRICH  
(Dr. sc. ETH Zürich)

presented by

UYGAR PALA  
MSc. University of Nottingham

born on 22.08.1984

citizen of  
Turkey

accepted on the recommendation of

Prof. Dr.-Ing. Dr. h.c. Konrad Wegener  
Prof. Dipl.-Ing. Dr.techn. Friedrich Bleicher  
Prof. Dr.-Ing. Bahman Azarhoushang

2020



*I dedicate this dissertation to a brilliant and truly inspiring person,  
Kamâl Atatürk, the founder of the Republic of Turkey; and in his name,  
to all the revolutionists who would not accept the world as it is.*





# Acknowledgements

The work presented in this dissertation covers the research work I have conducted during my affiliation with the Institute of Machine Tools and Manufacturing (IWF) of ETH Zürich. During this time, I have learned and understood a great deal of aspects on science, research and myself. I would like to mention and thank the people who made this happen.

First of all, I would like to express my deepest gratitude to Prof. Konrad Wegener whom I would mention as an exceptional person to work for and with. His enthusiasm and the long discussions on the scientific aspects have given me the motivation and energy to complete this work. On the other hand, I also have to mention that his tolerance, generosity and work ethics have set a great example personally.

I am particularly grateful for the guidance by Dr. Fredy Kuster, who has contributed to this work significantly. His trust and support even through the hardest times made this dissertation possible. I feel privileged to work with him during my time at IWF.

I further would like to thank my co-examiners, Prof. Friedrich Bleicher and Prof. Bahman Azarhoushang for their time and inputs; Prof. Robert Smith for proof-reading my dissertation; and Innosuisse-Swiss Innovation Agency, Swiss National Science Foundation and Meyer Burger AG for their financial support.

I thank my long-time office mate and research partner Stefan Süssmaier for his valuable contributions and tolerating me on (almost) daily basis. I would like to thank Dr. Ricardo Knoblauch and Dr. Robert Transchel for their collaboration in the Meyer Burger project; and Christoph Baumgart, Dr. Felipe Barata, Bircan Bugdayci and Fabian Kneubühler for their inputs and for the interesting conversations on research and science. I thank our lab and workshop responsables Jens Boos for his support in experiments; Albert Weber and Sandro Wigger for their support in parts manufacturing. I also would like to thank our students Bruno Sbravati,

Philipp Schöni, Jan-Hendrik Bastek and Daniel Solano for their contributions. Finally, I would like to thank all my colleagues and friends at IWF and inspire for their friendship and making my PhD years enjoyable.

I am deeply blessed to have my family, Neriman Pala, Tuncay Pala and Gözde Pala by my side all this time and ever before; and Alyona Pukhova with her support and trust.

Uygar Pala

Zurich, February 2020

# Table of Contents

<b>Acknowledgements</b>	<b>ii</b>
<b>Nomenclature</b>	<b>vi</b>
<b>Abstract</b>	<b>xvi</b>
<b>Kurzfassung</b>	<b>xviii</b>
<b>1 Introduction</b>	<b>1</b>
1.1 Photovoltaics . . . . .	2
1.2 Process Technology . . . . .	5
1.2.1 Crystalline Silicon . . . . .	6
1.2.2 Multi-Wire Sawing . . . . .	7
1.2.3 Electroplated Diamond Wire . . . . .	9
1.3 Motivation . . . . .	10
<b>2 Literature Review</b>	<b>12</b>
2.1 Wire Sawing Technology . . . . .	13
2.2 Material Removal Mechanisms . . . . .	18
2.2.1 Brittle Material Removal Mechanism . . . . .	19
2.2.2 Ductile Material Removal Mechanism in Brittle Material Processing . . . . .	22

2.2.3	Ductile to Brittle Transition . . . . .	23
2.3	Grain Scratch Tests . . . . .	25
2.4	Modeling and Simulation of Abrasive Processes . . . . .	30
2.4.1	Overview of the Modeling Approaches . . . . .	31
2.4.2	Kinematic Modeling and Simulation . . . . .	34
2.4.3	Tool Wear and Approaches in Wear Modeling . . . . .	41
<b>3</b>	<b>Research Gap</b>	<b>48</b>
<b>4</b>	<b>Experiment Setups and Methods</b>	<b>51</b>
4.1	Experiment Setups . . . . .	51
4.1.1	Wire Wrapped Grinding Wheel Setup . . . . .	52
4.1.2	Scratch Test Setup . . . . .	61
4.2	Measurement Tools and Methods . . . . .	63
4.2.1	Alicona 3D Infinite Focus Microscope . . . . .	63
4.2.2	Force Measurement System . . . . .	65
4.2.3	Temperature Measurement System . . . . .	65
4.2.4	Imprinting Technique . . . . .	66
4.3	Software Analysis Tools and Methods . . . . .	66
4.3.1	Wire Analysis Software . . . . .	66
4.3.2	Surface Analysis Software . . . . .	74
<b>5</b>	<b>Evaluation of Diamond Wires and Si Surfaces</b>	<b>78</b>
5.1	Morphological Analysis . . . . .	78
5.2	Evaluation of the Process Force Behavior . . . . .	79
5.2.1	Influence of Diamond Size and Protrusion . . . . .	82

---

5.2.2	Influence of Diamond Density . . . . .	82
5.3	Evaluation of Si Workpiece Surfaces . . . . .	83
5.4	Evaluation of the Wear Mechanisms . . . . .	86
<b>6</b>	<b>Wire Sawing Process Model</b>	<b>91</b>
6.1	Tool Model . . . . .	92
6.1.1	Grain Geometry Model . . . . .	93
6.1.2	Stochastic Wire Model . . . . .	95
6.2	Kinematic Process Model . . . . .	100
6.2.1	Grain Position . . . . .	100
6.2.2	Grain Path and Grain Penetration . . . . .	103
6.2.3	Definition of the Workpiece Geometry . . . . .	106
6.3	Material Removal Model . . . . .	107
6.4	Force Model . . . . .	115
<b>7</b>	<b>Wear</b>	<b>121</b>
7.1	Evaluation of the Wear Mechanisms . . . . .	122
7.2	Wear Model . . . . .	124
7.3	Temperature Model . . . . .	134
<b>8</b>	<b>Process Simulation</b>	<b>142</b>
8.1	Details of the Simulation . . . . .	142
8.2	Results . . . . .	146
<b>9</b>	<b>Conclusion and Outlook</b>	<b>157</b>
	<b>Bibliography</b>	<b>159</b>

# Nomenclature

## Greek Letters

$\alpha$	Wire wrap angle	$[\circ]$
$\beta$	Angle of the wheel-workpiece contact	$[\circ]$
$\delta_z$	Vertical resolution of the sample analysed by the WAS	$[\mu m]$
$\epsilon_f$	Force ratio	$[-]$
$\gamma$	Position of grain tip on wire cross-section	$[\circ]$
$\kappa$	Thermal diffusivity	$[m^2/s]$
$\kappa_c$	Material dependent constant	$[-]$
$\kappa_g$	Thermal diffusivity of diamond	$[m^2/s]$
$\kappa_w$	Thermal diffusivity of silicon	$[m^2/s]$
$\mu$	Mean of the dataset	$[-]$
$\nu$	Possion's ratio	$[-]$
$\omega$	Angular velocity	$[1/s]$
$\psi$	Half-included angle of the indenter tip	$[\circ]$
$\rho$	Material density	$[kg/m^3]$
$\rho_c$	Cluster density	$[cluster/\mu m^2]$
$\rho_{gr}$	Grain density	$[grain/\mu m^2]$
$\rho_g$	Material density of diamond	$[kg/m^3]$
$\rho_w$	Material density of silicon	$[kg/m^3]$
$\sigma$	Standard deviation of the dataset	$[-]$
$\sigma_c$	Cutting stress	$[GPa]$

$\sigma_n$	Normal stress	[GPa]
$\sigma_r$	Principal stress	[GPa]
$\sigma_t$	Contact stress	[MPa]
$\tau_p$	Bonding strength	[MPa]
$\tau_s$	Shear stress	[GPa]
$\theta$	Angle of rotation	[°]
$\theta_s$	Step angle of wheel rotation	[°]
$\theta_z$	Rotation angle of the wheel around its center	[°]
$\varphi$	Active wire surface angle	[°]
$\zeta_0$	Dimensionless constant	[–]
$\zeta_L$	Dimensionless constant	[–]

## Capital Letters

$\underline{\underline{M}}_{TR}$	Transformation matrix	[–]
$\underline{R}_{CG}$	Position of the grain tip wrt. the wire cross-section center	[–]
$\underline{R}_{SC}$	Position of the wire cross-section center wrt. the wheel center	[–]
$A$	Dimensionless constant	[–]
$A_{\perp}$	Orthogonal grain area in the direction normal to the workpiece surface	[ $\mu m^2$ ]
$A_b$	Grain base area	[ $\mu m$ ]
$A_{cu}$	Penetrated grain area	[ $\mu m^2$ ]
$A_{diff}^l$	Difference between the superposed area and sum of individual bounding boxes at layer $l$	[ $\mu m^2$ ]
$A_f$	Fractured workpiece area	[ $\mu m^2$ ]
$A_i^l$	Area of an individual bounding box $i$ at layer $l$	[ $\mu m^2$ ]
$A_{simp}^l$	Sum of the areas of superposed bounding boxes at layer $l$	[ $\mu m^2$ ]
$B$	Temperature dependent constant	[K]
$C$	Distance between two adjacent scratches on the STS	[ $\mu m$ ]
$C_f$	Geometric aspect ratio of a grain	[–]

## Nomenclature

---

$C_i$	Center point of $i^{th}$ wire cross section	$[-]$
$C_p$	Specific heat	$[J/kgK]$
$C_p^g$	Specific heat of diamond	$[J/kgK]$
$C_p^w$	Specific heat of silicon	$[J/kgK]$
$C_v$	Volumetric aspect ratio of a grain	$[1/\mu m]$
$C_{wheel}$	Circumference of the WWGW	$[mm]$
$E$	Elastic modulus	$[GPa]$
$E_a$	Activation energy	$[kJ/mol]$
$F_0$	Apparent threshold load	$[MPa]$
$F_{c,n}^k$	Measured cutting and normal forces	$[N]$
$F_{c,n}^s$	Simulated cutting and normal forces	$[N]$
$F_c$	Cutting force	$[N]$
$F_n$	Normal force	$[N]$
$F_r$	Grain retention force	$[N]$
$F_r^{lim}$	Grain retention force limit	$[N]$
$G$	Grinding ratio	$[-]$
$G_{h,v}$	Horizontal/vertical correction values in the SAS	$[px]$
$H$	Hardness	$[GPa]$
$I_{wire}$	Intensity factor	$[mm^3/mm]$
$K$	Coefficient of wear	$[mm^3/Nm]$
$K_{h1,2/v1,2}^{u/l}$	Limit tolerances in the SAS	$[px]$
$K_{IC}$	Fracture toughness	$[MPa\sqrt{m}]$
$L$	Average distance between two kinematically active grains	$[\mu m]$
$L_{dw}$	Length of a wire wrap	$[mm]$
$L_i$	Distance between two subsequential kinematically active grains	$[\mu m]$
$L_{mt}$	Distance between two nodes along wire length	$[\mu m]$



---

$L_{mw}$	Distance between two nodes along workpiece length	$[\mu m]$
$L_{nt}$	Distance between two nodes on the wire peripheral	$[\mu m]$
$L_{nw}$	Distance between two nodes along workpiece width	$[\mu m]$
$L_s$	Sliding distance	$[mm]$
$L_t$	Wire length	$[mm]$
$L_w$	Length of workpiece model	$[\mu m]$
$L_{zw}$	Distance between two nodes along workpiece depth	$[\mu m]$
$M$	Coefficient of dulling	$[-]$
$m_h$	Horizontal distance from the central pixel in the SAS	$[px]$
$m_v$	Vertical distance from the central pixel in the SAS	$[px]$
$N_{act}$	Total number of active abrasive grain edges on the wire	$[-]$
$N_c$	Number of clusters	$[-]$
$N_g$	Total number of grains on wire	$[-]$
$N_g^s$	Number of single grains	$[-]$
$N_{nm}$	Number of wire nodes	$[-]$
$P$	Position on the wire surface	$[-]$
$P(h)$	Cumulative probability distribution function at height $h$	$[-]$
$P_c$	Probability of occurrence of a cluster	$[-]$
$P_g$	Probability of occurrence of a grain	$[-]$
$P_i$	Position of the $i^{th}$ grain on wire surface	$[-]$
$Q_{ch}$	Heat distributed to the chip	$[W]$
$Q_f$	Heat distributed to the cutting fluid	$[W]$
$Q_g$	Heat distributed to the grain	$[W]$
$Q_r$	Material removal rate	$[mm^3/s]$
$Q'_r$	Specific material removal rate	$[mm^3/mms]$
$Q_t$	Total heat generation	$[W]$
$Q_w$	Heat distributed to the workpiece	$[W]$
$R_a$	Arithmetic mean roughness	$[\mu m]$

$R_g$	Universal gas constant	$[J/molK]$
$R_q$	Root mean square roughness	$[\mu m]$
$R_z$	Maximum height of roughness profile	$[\mu m]$
$T$	Temperature	$[K]$
$T_b$	Temperature of the bonding material	$[K]$
$T_f$	Flash temperature at the grain tip	$[K]$
$T_h$	Horizontal tolerance in the SAS	$[-]$
$T_{ij}$	Position of a wire node	$[-]$
$T_v$	Vertical tolerance in the SAS	$[-]$
$V_g$	Grain volume	$[mm^3]$
$V_t$	Volumetric tool wear	$[mm^3]$
$V_w$	Volumetric workpiece wear	$[mm^3]$
$V'_w$	Material removal volume per unit wire length	$[mm^3/m]$
$W$	Grain wear	$[mm^3]$
$W_a$	Abrasive wear term	$[mm^3/s]$
$W_{i,j}^{norm}$	Normalized grayscale value of $i^{th}$ row and $j^{th}$ column	$[-]$
$W_{ij}$	Grayscale value of $i^{th}$ row and $j^{th}$ column	$[-]$
$W_t$	Peripheral of the wire model	$[\mu m]$
$W_w$	Width of workpiece model	$[\mu m]$

## Small Letters

$\dot{q}_g$	Heat flux to the grain	$[W/m^2]$
$\dot{q}_t$	Total heat flux	$[W/m^2]$
$\dot{q}_w$	Heat flux to the workpiece	$[W/m^2]$
$a$	Edge length of grain model base	$[\mu m]$
$b$	Edge length of grain model top	$[\mu m]$
$b_{cu}$	Width of chip or cut width	$[\mu m]$
$b_D$	Effective grinding width	$[mm]$

$b_d$	Length of perpendicular projection active width onto the axis of rotation of the wheel	[mm]
$b_f$	Removal width of a wire wrap	[mm]
$b_{wheel}$	Thickness of the WWGW	[mm]
$b_{wp}$	Workpiece thickness	[mm]
$c^L$	Limiting crack function	[-]
$c_g$	Half contact length between the indenter and surface	[ $\mu m$ ]
$c_l$	Lateral crack length	[ $\mu m$ ]
$c_p$	Radius of the plastic zone	[ $\mu m$ ]
$d_s$	Diameter of the WWGW	[mm]
$d_{wp}$	Workpiece diameter	[mm]
$h$	Mean plane separation	[ $\mu m$ ]
$h_0$	Initial grain penetration	[ $\mu m$ ]
$h_{b,\%}$	State of grain bonding	[%]
$h_b$	Embedded grain height	[ $\mu m$ ]
$h_{cu,crit}$	Critical depth of cut	[ $\mu m$ ]
$h_{cu,max,av}$	Average maximum undeformed chip thickness	[ $\mu m$ ]
$h_{cu}$	Undeformed chip thickness	[ $\mu m$ ]
$h_f$	Workpiece depth of removal	[mm]
$h_{g,r,\%}$	Percentage reduction in grain protrusion	[%]
$h_g$	Grain protrusion height	[ $\mu m$ ]
$h_g^{max}$	Maximum grain protrusion on the wire sample	[ $\mu m$ ]
$h_{i,cu,max}$	Maximum undeformed chip thickness of $i^{th}$ grain	[ $\mu m$ ]
$h_{i,cu}$	Undeformed chip thickness of $i^{th}$ grain	[ $\mu m$ ]
$h_{lim}$	Limit grain penetration	[ $\mu m$ ]
$h_p$	Depth of the plastic zone in brittle removal regime	[ $\mu m$ ]
$h_{sc}$	Depth of scratch	[ $\mu m$ ]
$h_s$	Step advance of grain onto the workpiece	[ $\mu m$ ]

## Nomenclature

---

$h_w$	Depth of wire in the wheel groove	$[mm]$
$k$	Thermal conductivity	$[W/mK]$
$k_c$	Specific cutting force	$[N/mm^2]$
$k_{gc}$	Average number of grains per cluster	$[-]$
$k_g$	Thermal conductivity of diamond	$[W/mK]$
$k_w$	Thermal conductivity of silicon	$[W/mK]$
$l_c$	Geometric contact length	$[mm]$
$l_g$	Grain length	$[\mu m]$
$l_{kin}$	Kinematic contact length	$[mm]$
$l_m$	Evaluated workpiece length	$[\mu m]$
$l_{wp}$	Si workpiece length	$[mm]$
$m_c$	Constant in force model	$[-]$
$p(h)$	Height probability distribution function at height $h$	$[-]$
$r_{eff}$	Effective radius of the indenter	$[\mu m]$
$r_g$	Grain diameter	$[\mu m]$
$r_s$	Radius of the WWGW	$[mm]$
$r_w$	Wire radius	$[\mu m]$
$s$	Feed per cutting edge	$[\mu m]$
$t$	Time	$[s]$
$t_{cut}$	Cutting time	$[s]$
$u$	Specific energy	$[J/\mu m^3]$
$v_c$	Cutting speed	$[m/s]$
$v_{fr}$	Feed rate in radial direction	$[mm/min]$
$v_{fz}$	Feed rate in vertical direction	$[mm/min]$
$v_f$	Feed rate	$[mm/min]$
$v_{rel}$	Relative sliding velocity	$[m/s]$
$w_g$	Grain width	$[\mu m]$
$z$	Perpendicular distance from the base plane	$[\mu m]$

## Abbreviations

$\mu$ c-Si	Micro-crystalline silicon
ANN	Artificial neural network
APAC	Asia-Pacific Countries
BA	Bearing area
c-Si	Crystalline silicon
CBN	Cubic boron nitride
CNC	Computer numeric control
Cz	Czochralski
EDM	Electrical discharge machining
FEM	Finite element model
FEPA	Federation of European Producers of Abrasives
FRF	Frequency response function
FZ	Float zone
IFM	Infinite focus microscope
mc-Si	Multi-crystalline silicon
MD	Molecular dynamic
MEA	Middle East and Africa
Ni	Nickel
ODE	Ordinary differential equation
pc-Si	Poly-crystalline silicon
PDF	Probability distribution function
Pe	Peclet number
PV	Photovoltaic
SAS	Surface Analysis Software
sc-Si	Single-crystal silicon
SEM	Scanning electron microscope
Si	Silicon

## Nomenclature

---

SiC	Silicon carbide
STS	Scratch Test Setup
TTV	Total thickness variation
WAS	Wire Analysis Software
WWGW	Wire Wrapped Grinding Wheel

# Abstract

The global interest in clean energy has resulted in an expansion of the photovoltaic industry and correspondingly, research on the production of large-scale silicon surfaces received further scientific and industrial interest. The interest resulted in an efficiency breakthrough in silicon wafer manufacturing as well as leading to the introduction of new production technologies. However, among other methods such as kerfless wafering technologies, wire sawing is still by far the most efficient and prominent method in wafer manufacturing; and the latest technology leap, diamond wire sawing, has dominated the single-crystal silicon processing and is increasing its share in the total silicon wafer production.

Diamond wire sawing of silicon accommodates multiple complexities resulting from the process kinematics, grain geometry and size, effects of grain wear and brittle nature of silicon. Beside the extensive experimental and theoretical research on abrasive processes and developed models in micro- and macro-scales, diamond wire sawing is still to be understood. This thesis presents the experimental investigation and theoretical study of diamond wire sawing of single-crystal silicon to establish a profound understanding of the process in terms of the silicon surface, diamond wire and abrasive grain wear.

For this purpose, two experimental setups are designed to evaluate the wire wear and to investigate the process at single grain level; two propriety software packages are developed to characterize diamond wires and the silicon workpiece surface; several models are constructed to work in a modular manner, as the kinematic process model, stochastic-geometric wire model, material removal model, force model, grain flash temperature model and grain wear model.

The Wire Wrapped Grinding Wheel (WWGW) test setup is constructed and it combines the kinematics of the grinding and wire sawing processes, to evaluate the process at high cutting speeds. The test setup enables quick-wear tests with low material consumption, as well as providing individual grain wear monitoring over

the wire lifetime. The second experimental setup is the Scratch Test Setup (STS), constructed to examine the process at single grain level, at high cutting speeds with the measurement of the surface, grain wear, process forces and temperature at the grain tip.

Initially, several diamond wires are characterized with the wire analysis software and experimentally investigated to determine the influence of wire properties on process forces and silicon surface quality. Further, the influence of wire speed and feed rate on surface quality is experimentally evaluated as silicon surfaces are characterized with the surface analysis software.

The kinematics of the WWGW setup are described in detail for the kinematic-geometric process model. The working principles of the setup and the microscopic interaction between the abrasive grains and workpiece are studied. The stochastic-geometric wire model is constructed and the wire analysis software is used to determine the wire properties and grain geometries as the model inputs. The material removal model is based on the single grain contact and considers both brittle and ductile removal regimes. The modified Kienzle force model is introduced as well as the temperature model for the estimation of the flash temperature at the grain tip. The material removal, force and temperature models are validated through single grain scratch tests at the cutting speeds between 5-20  $m/s$ . The abrasive grain wear model is presented and validated at 30 and 60  $m/s$  cutting speeds. Results of the kinematic-geometric and wear simulations are discussed.

Main results can be summarized as follows. Lower process forces are evident at high cutting speeds, but there is a cutting speed threshold, where the force behavior of diamond wires changes depending on their grain size and density. The abrasive grains wear through fracture, dulling and pullouts. The bonding wear changes its behavior at a point and wears rapidly, leading to grain pullouts. The results show that at higher wire speeds, better silicon surface quality and lower wire wear is possible.

The methods, tools and models developed in this research offers new ways and instruments for the process level understanding of the diamond wire sawing of silicon. Developed software packages provide standardized and fast tools for the characterization of diamond wires and silicon surfaces. At the lowest possible cost, diamond wires can be evaluated in terms of the diamond wear, process forces and resultant workpiece surface quality. The developed models and tools can be employed in other applications concerning the abrasive removal of brittle materials.



# Kurzfassung

Die globale Nachfrage nach sauberer Energie führt zu einem anhaltenden Wachstum der Photovoltaik-Industrie. Entsprechend steigt das Interesse von Wissenschaft und Industrie für die Erforschung von Technologien zur Produktion von Siliziumwafern. Die Effizienz in der Produktion wurde signifikant gesteigert und neue Technologien wurden zur Marktreife gebracht. Neben neuen Methoden wie Kerfless Wafering ist das Diamantdrahtsägen nach wie vor das am weitesten verbreitete Verfahren zur Herstellung von Wafern aus monokristallinem Silizium. Die letzte Entwicklung, das Sägen mit diamantbelegten Drähten, löst das Sägen mit Slurry sukzessive ab.

Das Diamantdrahtsägen von Silizium vereint verschiedene komplexe Aspekte, wie eine veränderliche Prozesskinematik, geometrisch unbestimmte Schneiden unterschiedlicher Grösse, Verschleiss und dem spröden Materialverhalten des Siliziums, in einem Prozess der noch nicht vollständig verstanden ist. Umfangreiche experimentelle Studien und theoretische Untersuchungen wurden durchgeführt und führten zur Entwicklung verschiedener Modellansätze auf makroskopischer und mikroskopischer Ebene. Die vorgestellte Dissertation erweitert das Prozessverständnis in den Bereichen Oberflächengeneration, Kornverschleiss, sowie Beschreibung der Drähte und ihres Einflusses auf das Prozessergebnis.

Zur Evaluierung des Drahtverschleisses und zur Untersuchung des Prozesses auf Einzelkornebene wurden je ein Versuchstand aufgebaut. Zwei Softwareanwendungen zur Charakterisierung der Drähte und der Werkstückoberfläche wurden programmiert. Ein modulares Prozessmodell bestehend aus einem kinematischen Prozessmodell, einem stochastisch-geometrischen Drahtmodell, einem Materialabtragmodell, einem Kraftmodell, einem Korn-Flash-Temperaturmodell und einem Kornverschleissmodell, wurde erarbeitet.

Mithilfe der beiden Versuchsstände kann der Prozess eingehend untersucht werden. Eine Drahtumwickelte Schleifscheibe (engl. Wire Wrapped Grinding Wheel, WWGW), eingesetzt auf einer Werkzeugschleifmaschine, kombiniert die Kinematik eines Schleifprozesses mit dem Werkzeug des Diamantdrahtsägens und ermöglicht die Analyse des Prozesses bei sehr hohen Schnittgeschwindigkeiten. Durch den Aufbau können Drähte schnell und gezielt verschlissen werden ohne grosse Mengen an Draht oder Werkstückmaterial zu verbrauchen. Darüber hinaus können einzelne Körner über ihre gesamte Standzeit hinweg beobachtet werden. Ein zweiter Aufbau für Einzelkornkratzversuche (Kratzversuchsaufbau, engl. Scratch Test Setup, STS) wurde realisiert um den Prozess hinsichtlich der an einem einzelnen Korn wirkenden Kräfte und Temperaturen, sowie die resultierende Oberfläche, ebenfalls bei hohen Schnittgeschwindigkeiten analysieren zu können.

Mehrere Diamantdrähte wurden mithilfe der entwickelten Software reproduzierbar charakterisiert und anschliessend als WWGW eingesetzt um den Einfluss der Drahteigenschaften auf Prozesskräfte und Oberflächenqualität des Siliziums zu bestimmen. Weiter wurde der Einfluss der Schnitt- und Vorschubgeschwindigkeit auf die Oberflächengüte des Werkstücks experimentell ermittelt und mit der Oberflächenanalysesoftware quantifiziert.

# Chapter 1

## Introduction

The ever increasing need for energy and pro-environmental policy pressure led to a new era of renewable energy. The global solar electric power generating capacity grew explosively by a factor of 40 in the last decade [124]. A year-to-year increase of 50% in installed solar capacity was achieved in 2016, the same year when for the first time solar energy has become cheaper than wind energy [191]. The annual renewable power capacity increase was led by solar since 2016 (Figure 1.1); and at 2018, the share of renewables in the global power generation capacity has increased to 33% [177,192]. By the year 2035, the share of renewables in the total electricity consumption is predicted to be around 50% and by 2050 to be 75%, with solar being the leading source [158]. The advances in renewable energy technologies are revolutionizing the energy production and consumption. Clean energy is not a topic of the future anymore, but a current opportunity to reduce dependency on fossil fuels, transform the energy and technology markets and build a sustainable society.

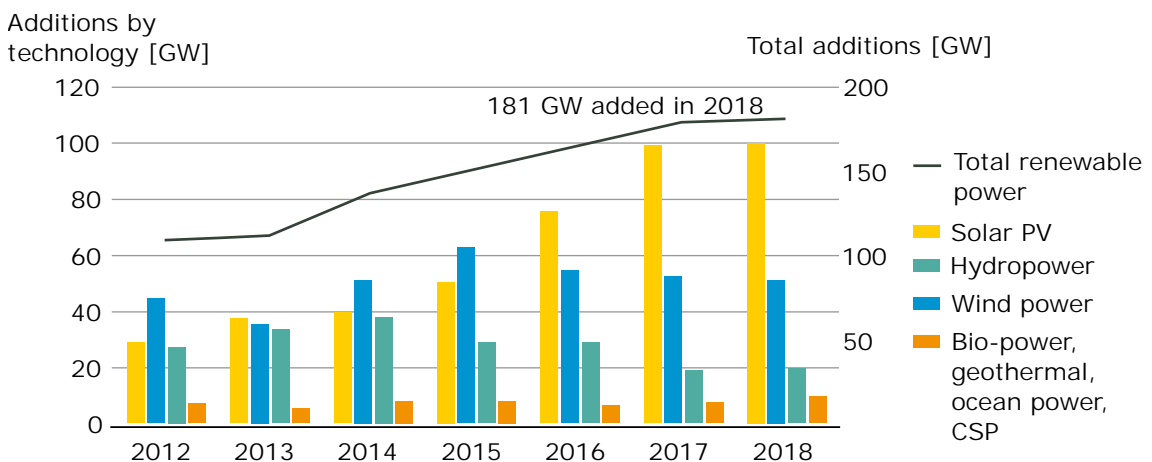


Figure 1.1: Annual increase in renewable power capacity between 2012-2018 [177].

This work focuses on the silicon (Si) based wafer production with a primary focus on diamond wire sawing of single-crystal silicon (sc-Si). Prior to the introduction of the scientific aspects, first, an introduction to the PV technology is presented including the history, market and technology to establish a wider understanding of the topic.

## 1.1 Photovoltaics

The physical/chemical phenomenon behind solar energy production is the photovoltaic effect that can be briefly described as the conversion of energy from light to electricity. It was first observed by the French physicist Alexandre E. Becquerel in 1839 and it took more than 40 years until the first solar module was built in 1883 by the American inventor Charles E. Fritts [68]. The science behind the photovoltaic effect was eventually explained by Albert Einstein in 1905 [64] which awarded him the Nobel Prize in physics in 1921. The commercialization of solar energy however did not start until the first practical and highly efficient Si-based PV cell was developed at the Bell Labs in 1953 by Gerald L. Pearson, Daryl M. Chapin and Calvin S. Fuller [147, 190, 197].

The PV industry started its expansion in the early 80's and experienced a rapid growth during the 90's [103]. The growth was mainly driven by the increasing fuel costs [48] and boosting attention to renewable energy and encouraging industry through the renewable energy policies and governmental subsidies [79]. During the 90's, the process technology has evolved from the inner/outer diameter saws to slurry-based multi-wire sawing that led to a rapid 66% increase in the number of wafers produced from the same amount of silicon [103]. A substantially increased wafer quality, lower wafer thickness variation and better sustainability in terms of coolant and kerf recycling were reached [48, 53, 103, 122, 234].

After 2005, diamond wire sawing technology, which is based on wires with fixed abrasive grains delivered high efficiency to the PV wafer production while increasing the wafer quality, cell efficiency and enabling high cost reductions. For the transition from slurry-based sawing, machines require very few modifications to operate with diamond wires [167] which resulted in a rapid technology shift at the lowest possible cost. Moreover, the standard cell lifetime was set over 30 years with increased product reliability that led to ecological as well as economical advantages [52]. On the material side, in Si-based PV manufacturing, sc-Si cell efficiency increased from 17% in 1970's to 28% by the year 2013 [208].

The competitiveness of solar power increased with the rapidly decreasing production costs through higher process efficiency and global competition. PV module manufacturing costs as high as 21 USD/W in 1980 have dropped to 6 USD/W by 1990 and to less than half of it by the year 2002 [103]. Accordingly, the price of a single PV module dropped 10 times during the same period [103, 200]. In the last decade, the share of solar power generation in global generation has increased 22 times and the cost of solar electricity generation has decreased more than 7 times, under 50 USD/MWh based on the levelized cost of energy analysis [133], summarized in Figure 1.2.

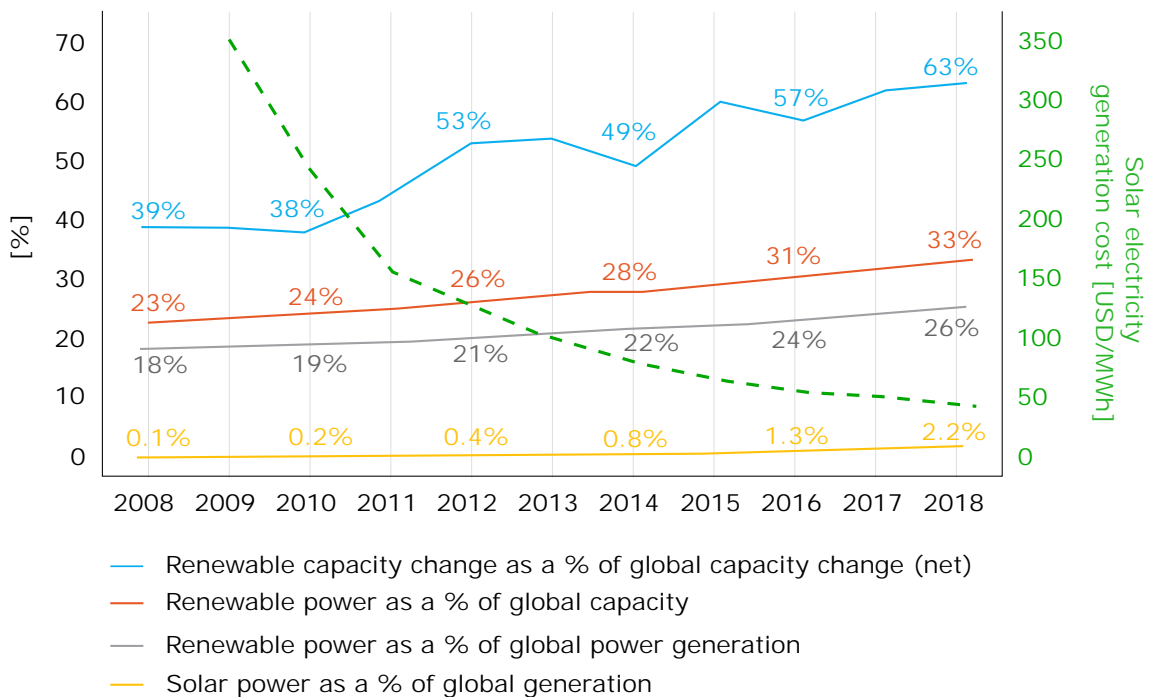
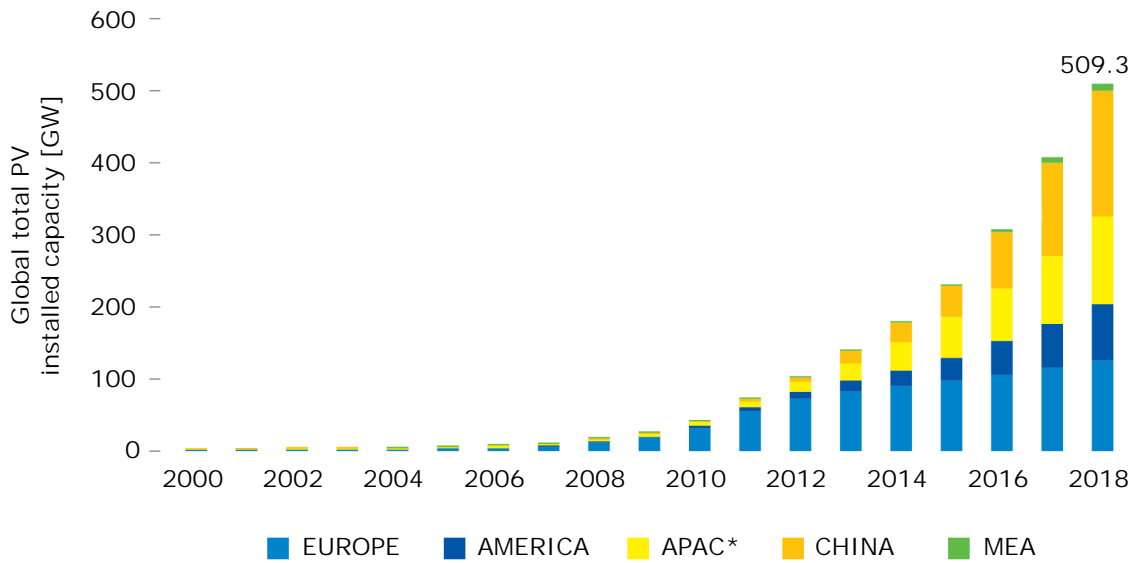


Figure 1.2: Share of renewable and solar power generation and capacity in global power and the change in solar electricity generation costs [192].

The increase in the global total PV installed capacity during the period of 2000-2018 is presented in Figure 1.3. The capacity has grown 320 times since the beginning of the millennium and increased over 3,200% in the last decade, while in 2018, a year-to-year increase of 25% was achieved [192]. China became the leader of the global solar PV market in 2015 and has kept its place since then [191] and increased its solar capacity in 2018 more than the rest of the top 10 countries combined [192]. By the year 2018, China owns 34.4% (295.7 GW) of the total solar PV installed capacity, followed by the United States with 12.2% (62.1 GW) and Japan with 11.0% (55.9 GW) [192]. Germany, the longtime solar market leader, is ranked fourth and currently holds 9.0% (45.9 GW) of the total installed capacity [192]; leaving no European country in the top 3 of the global solar market.



\*APAC excl. China

Figure 1.3: Global total PV installed capacity with the contribution of Europe, America (including North, Central and South America), China, Asia Pacific Countries (APAC) and Middle East and Africa (MEA) between 2000-2018 [192].

PV Module prices are expected to continue dropping with the technological progress and increasing installed capacity. A forecast to the year 2023 is shown in Figure 1.4 with low, high and medium scenarios [192]. An increase of more than twice of currently installed PV capacity is expected for the low scenario and more than three times is expected for the high scenario.

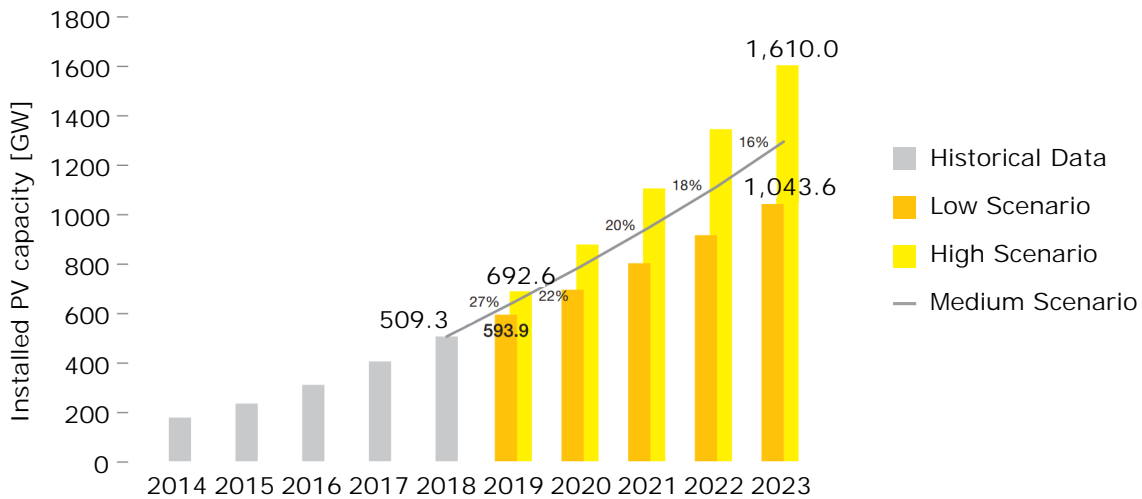


Figure 1.4: A forecast of installed PV capacity until 2023 with low, high and medium scenarios [192].

## 1.2 Process Technology

The manufacturing process of Si-based PV modules can be separated into four major steps as the ingot production, wafering, cell processing and module assembly [103]. The process sequence is illustrated in Figure 1.5 where four main processing steps and the subprocesses of the wafering step are presented. In ingot production, sc-Si is mostly grown by the famous Czochralski process to form cylindrical ingots with high purity (solar-grade Si), by dipping a seed crystal into the molten silicon. Multi-crystalline Si (mc-Si) on the other hand, is mainly produced from metallurgical grade Si by chemical purification [147, 249].

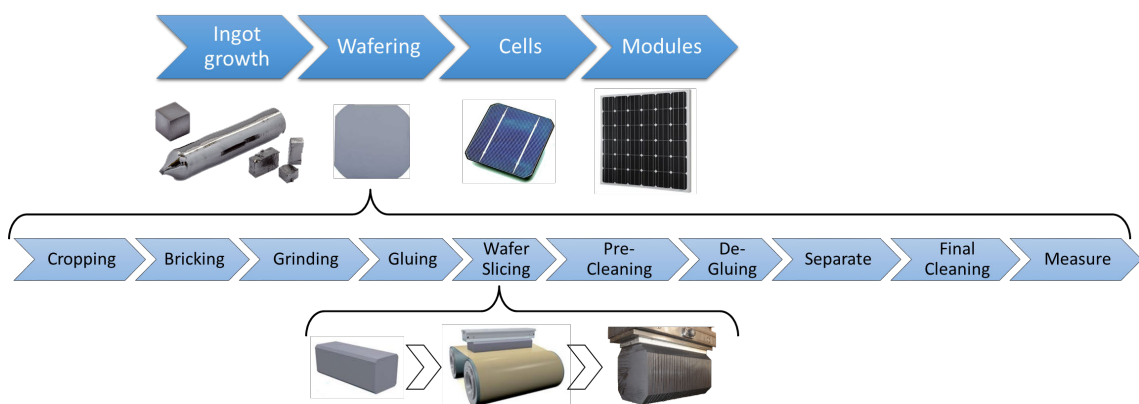


Figure 1.5: Primary steps in crystalline silicon module value chain and details of the wafering step based on the process by Meyer Burger AG, Switzerland [161].

The wafering process consists of cropping of the ingot and bricking into its square shape for sawing, wafer slicing and subprocesses i.e. gluing, de-gluing, separation of wafers, cleaning and wafer quality measurements. Wafering is followed by the cell production process including the post-processing of the wafer surfaces by etching (to reduce the saw damages on wafer surface), coating and evaluation of the cell efficiency. Finally, the circuit installation and final PV module assembly are performed.

Breakdown of the PV module fabrication costs are presented in Figure 1.6 where the production of silicon wafer (includes material costs, ingot growth and wafering) covers 65% of the total costs including the raw material costs and ingot growth. Raw material accounts for 36%, ingot growth accounts for 35% and sawing (wafering) covers the remaining 29% of the silicon wafer production costs. Despite the material related costs, wafering is economically of high importance and improvements in efficiency would have high impacts on the final product.

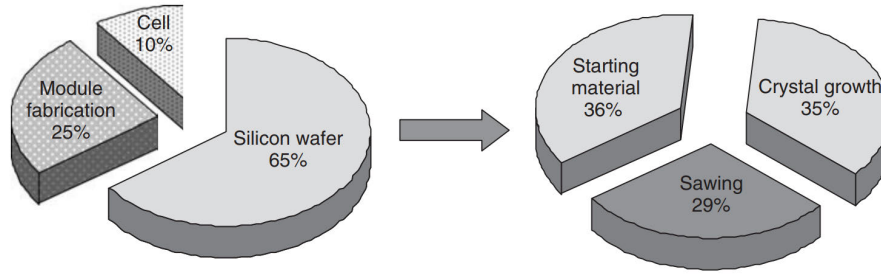


Figure 1.6: Share of the production costs of module and silicon wafers in wire sawing [147].

### 1.2.1 Crystalline Silicon

Despite some attempts in kerfless technologies, around 90% of the wafer production for PV industry is still dependent on wafering of crystalline silicon (c-Si) [97, 98, 165, 173]. Crystalline silicon dominates the industry for its advantages such as high purity, availability of large single crystals, effective conductivity, non-toxicity and natural abundance, at a level where Si is the second most abundant material composing 26% of the Earth's crust in weight [48, 79, 147, 173]. Moreover, studies predict crystalline cells will sustain their market share in the medium term for their established processing technology [48, 200]. A widely accepted terminology for c-Si proposed by Basore [24] is given in Table 1.1, where the names of c-Si technologies, symbols, grain sizes and common growth techniques of various types are tabulated.

Table 1.1: Terminology for various types of crystalline silicon (c-Si) [24].

Descriptor	Symbol	Grain size	Common growth techniques
Single-crystal	sc-Si	$> 10\text{ cm}$	Czochralski (Cz) float zone (FZ)
Multi-crystalline	mc-Si	$1\text{ mm} - 10\text{ cm}$	Cast, spherul, sheet, ribbon
Poly-crystalline	pc-Si	$1\ \mu\text{m} - 1\text{ mm}$	Chemical-vapor deposition
Micro-crystalline	$\mu\text{c-Si}$	$< 1\ \mu\text{m}$	Plasma deposition

Figure 1.7a summarizes the efficiency and prices of different PV module technologies such as c-Si based PV modules, organic solar cells, thin films and concentrating PV technologies. Crystalline silicon have established the optimum performance in terms of module price per square meter, per watt and efficiency among several PV module technologies. In Figure 1.7b, types of c-Si based wafers and their market shares are given, where the market is dominated by sc-Si and mc-Si.



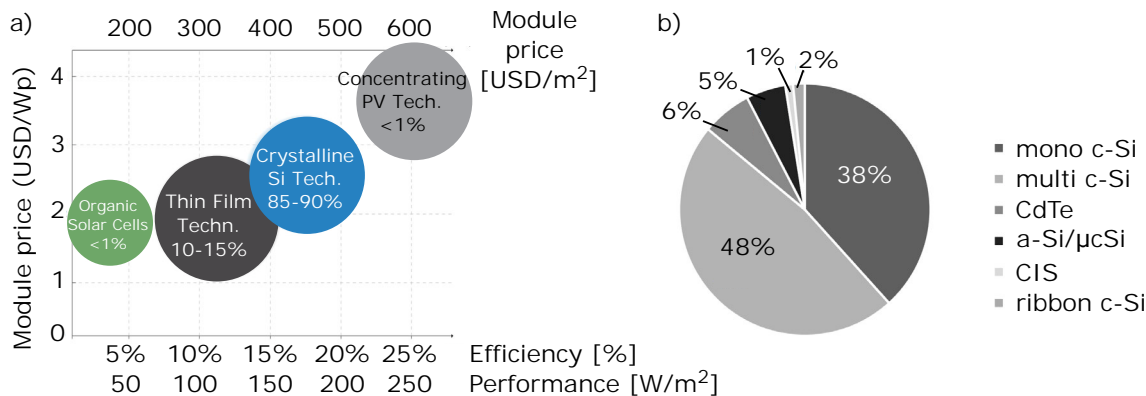


Figure 1.7: (a) Efficiency and module price of different PV module technologies in USD per Watt peak as of 2008 [97]. (b) Breakdown of several process technologies in PV market [147].

Crystalline silicon wafering is the most prominent technology in PV module production. Around 38% of the c-Si based wafer manufacturing depends on sc-Si [147] which provides the highest power conversion efficiency among commercial PV modules [73]. Due to their low defect density, sc-Si possess 5-6% higher efficiencies when compared to mc-Si cells or thin films [77]. On the cost side, silicon accounts around 46% of the total module production costs, making the material a primary concern.

## 1.2.2 Multi-Wire Sawing

Chandra [48] broadly defines the solar cell production as the manufacturing of surfaces and interfaces in a very large scale where no technological product quality is dependent on these features as the PV panel. Multi-wire sawing (or wire sawing) is the primary processing technology to produce such large scale surfaces for PV and microelectronic industries [29, 166]. Wire sawing can be broadly defined as an abrasive removal process with geometrically undefined cutting edges. As in other abrasive removal processes such as grinding or lapping, the process is stochastic in nature due to the characteristics of the tool and the tool-workpiece interaction.

Multi-wire sawing is usually employed to machine hard and difficult-to-cut materials such as Si, SiC and sapphire. Moreover, wire saws are used for cutting oxide semiconductors and magnetic materials [79, 89]. Although the manufacturing and processing costs have largely been cut over the years, wafering costs are still high and make up around 29-30% of the total wafer production costs and 20% of total module costs [147, 165].

Schematics of the multi-wire sawing is illustrated in Figure 1.8a. The multi-wire saw describes both slurry-based and diamond wire sawing processes. The ingot is fed onto the wire web that is created by winding the wire around guiding rollers with 600-800 parallel grooves. The wire movement is provided by two spools for releasing and collecting the wire and guiding rollers ensure the positioning distance between consecutive wires on the web. Wire tension is controlled and typically set to 15-25  $N$ . The rollers are able to travel in both directions with typical wire speeds of 25-35  $m/s$ . The wire accelerates in one direction, decelerates and moves backwards with a shorter distance than the initial direction, hence new wire sections are introduced in each cycle [167]. Such wire movement is called as the reciprocating or pilgrim mode. The interaction between the workpiece and abrasive grains on wire is determined by wire bow, wire speed and feed rate among other process parameters.

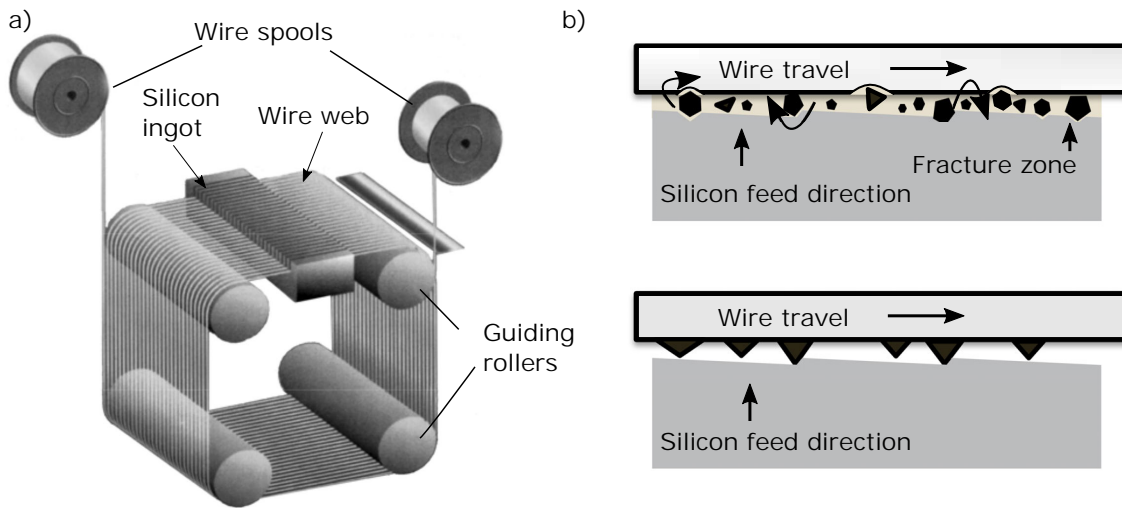


Figure 1.8: (a) Schematic of multi-wire sawing process [166]. (b) Material removal in slurry sawing. (c) Material removal in diamond wire sawing [122].

In slurry-based sawing, a steel wire is traveling between the two wire spools and a slurry with SiC grains is deployed to the cutting zone. A three-body abrasion is present in material removal as described in Figure 1.8b, where the material is removed as a result of the workpiece feed rate and wire traveling speed. The material removal mechanism can be defined with the rolling-indenting model [165]. In diamond wire sawing, abrasive grains are fixed on the wire body with electroplating or resin bonding that results in a two-body abrasion described in Figure 1.8c. The abrasives that are attached on the wire surface follow a path denoted by the wire trajectory with wire speed, feed rate and tension. Water-based coolant is mainly applied to remove the debris and decrease the temperatures in the cutting zone. Mainly mc-Si wafers are fabricated with slurry-based sawing and diamond wire sawing is mostly used for the manufacturing of sc-Si wafers; as diamond wire sawing of mc-Si has reported to be less efficient than slurry-based sawing [41, 167].

In the last decade, diamond wire saws have emerged as the main technology to cut hard and brittle materials and are widely used in manufacturing sc-Si wafers in PV industry. Diamond wire sawn sc-Si wafers have proven to provide high cell efficiency and mechanical strength which enables the production of thinner wafers thus increasing efficiency [243].

### 1.2.3 Electroplated Diamond Wire

The interest in electroplated diamond wire technology is enhanced as diamond wire sawing becomes the most common processing technology in wafering. Electroplated diamond wires are composed of a steel wire core and diamond grains that are secured on the surface by depositing the filler metal (nickel or nickel-cobalt alloys) by electroplating (Figure 1.9a). Typical wire core diameters are in the range of 80-140  $\mu\text{m}$  with typical abrasive grain sizes in the range of 8-25  $\mu\text{m}$ . Today down to 60  $\mu\text{m}$  core diameter wires are used in production. A scanning electron microscope (SEM) image of an electroplated diamond wire is presented in Figure 1.9b. The surface of the unworn wire and the diamond grains are completely or partly covered with the Ni-filler material that wears off as the wire wear propagates; leading to exposure of cutting edges of diamond grains.

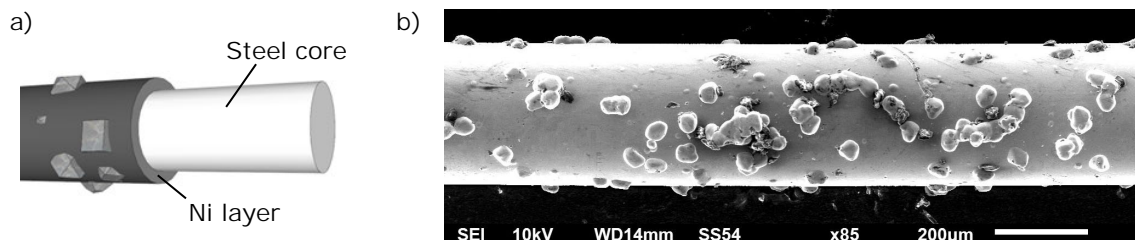


Figure 1.9: (a) Steel core and Ni-filler layer of an electroplated diamond wire. (b) SEM image of an unworn electroplated diamond wire.

Figure 1.10a presents the cost distributions of slurry-based and diamond wire sawing of c-Si. The cost of diamond wire, by 80%, has the highest share in diamond wire sawing; where the wire cost is 30% in slurry-based saving.

In diamond wire sawing, the wire length involved per cut is typically between 50-100  $\text{km}$  [194] and the wire cost is more than hundred times higher per  $\text{km}$  compared to the steel wire employed in the slurry-based sawing. The cost of the extensive wire lengths are up to 20% of the total production costs [147]. Hence a wire break during diamond wire sawing process is highly critical and may compromise economical output of the whole slicing operation [57].

Diamond wires have proven themselves with higher efficiency and improved surface quality [57]. Moreover, electroplated diamond wires obtained 90% of the sc-Si based PV market by 2017 for mainly due to the drastically increased production speed; and lower wire wear rate, high bonding strength and increased wafer quality. Market share projections on the other hand show that the domination of diamond wire will be continuing over the next decade, as shown in Figure 1.10 [98].

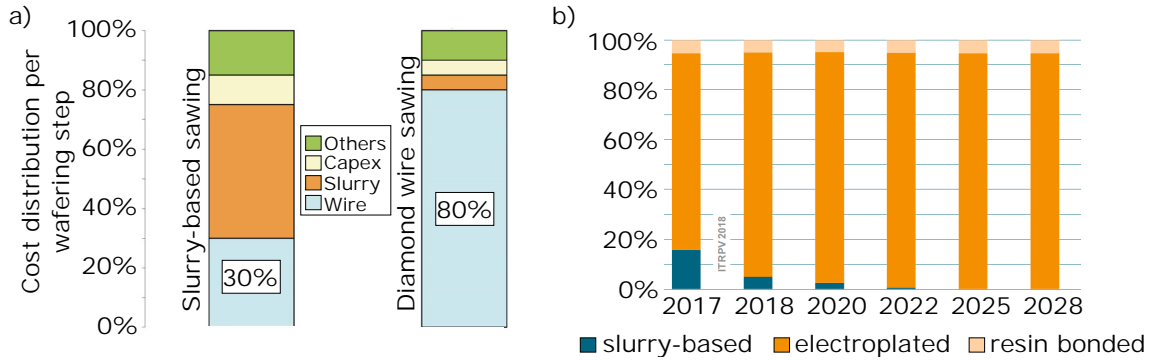


Figure 1.10: (a) Distribution of costs in slurry-based and diamond wire sawing of c-Si [57]. (b) Market shares of sc-Si wafering technologies with a forecast to 2028 [98].

### 1.3 Motivation

Several kerfless wafering technologies such as laser, plasma, ion implantation, electrochemical etching or heat pulses have been applied in wafer manufacturing [167]. But none of the stated fabrication methods could yet reach the production level due to their high cost and low efficiency. Electroplated diamond wire sawing of sc-Si currently provides the optimum processing solution in terms of efficiency, wafer quality and sustainability in wafer production. It is unlikely that the process will be overtaken in the midterm, considering the production capacity increase as a result of the improvements in the machine and processing technology.

The efficiency of the wire sawing process is determined by the output rate that can be defined as the number of wafers produced per Si block. However almost half of the work material is wasted with kerf loss and post-conditioning of the sawn surfaces [48,184] and reduction of kerf loss has been of interest to reduce the material consumption [166]. As the wire diameter decreases, the material loss is reduced and output rate increases with increasing number of wafers per Si block. Today, wire diameters used in production (60-140  $\mu m$ ) are the half of industry standards a decade ago and the wire diameters are predicted to be continuously reducing over the following years [98].

On the other hand, with decreasing wafer thickness, higher number of wafers can be produced from the same ingot size, leading to higher process efficiency and reduction of manufacturing costs [57, 69, 73, 167]. However, there is a lower limit for the wafer thickness due to its brittle characteristics [48] and stated by Powell [172] that there is a generally held boundary that the lower limit of wafer thickness is  $80 \mu m$ , where [171] reports the c-Si wafer thickness as  $170 \mu m$  in 2017.

Both developments make the sawing process more complex as thinner wafers and wires are more prone to failure. Improvement in the process results is possible with a through understanding of the wire, diamond grains and the conditions of grain-workpiece interaction. The complexity of the process requires scientific investigation in a wide process parameter range and different interaction setups.

# Chapter 2

## Literature Review

*“It is not the result of scientific research that ennobles humans and enriches their nature, but the struggle to understand while performing creative and open-minded intellectual work.”*

— Albert Einstein,  
*The World As I See It, 1934*

Experimental investigation and modeling of diamond wire processing of silicon necessitates the review of several fields covering the wire sawing process, diamond wire technology, material removal mechanisms in brittle materials and modeling and simulation of abrasive processes concerning the process, material removal and wear modeling. Additionally, the experimental methods employed in this thesis compel to study the literature on grain scratch tests and some aspects of abrasive removal processes.

In this chapter, a literature review on the diamond wire sawing process will be presented regarding its aspects on the process, surface, wear, modeling and simulation. To be able to develop a fundamental understanding of the subject, significant studies on material removal mechanisms in brittle materials and transition of material removal regimes and modeling and simulation of abrasive processes will be detailed. The relevant work concerning the diamond wire sawing process will be discussed in each section separately.

## 2.1 Wire Sawing Technology

In Chapter 1 of this work, multi-wire sawing technology is briefly introduced. In the current chapter, literature on wire sawing technology will be discussed with a primary focus on diamond wire sawing of brittle materials.

A schematic representation of input and output parameters of the diamond wire sawing process is presented in Figure 2.1. The primary process inputs for the diamond wire are abrasive grain and wire properties. For the work material, they are hardness, fracture toughness and elasticity. For the process parameters they are wire speed, feed rate, wire acceleration, wire tension and sawing mode (wire motion in one or both directions). For the machine parameters, the inputs are axis distance (distance between two rollers) and pitch distance (distance between two consecutive wires on the wire web). Finally, there are inputs for the coolant (type, rate, etc.).

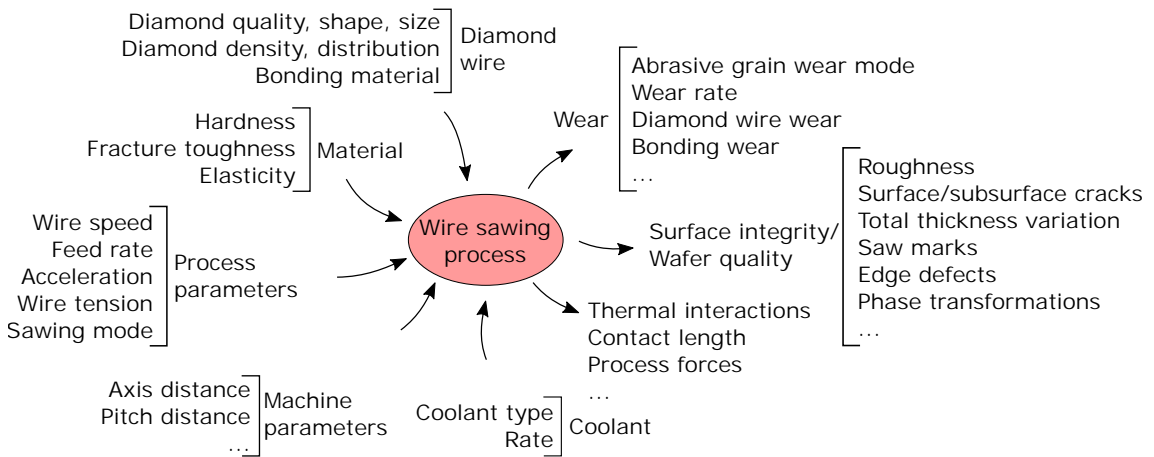


Figure 2.1: Primary input and output parameters in wire sawing process.

The output parameters can be stated as the tool wear, wafer surface integrity and quality (roughness, surface and subsurface cracks, total thickness variation (TTV), saw marks), process forces, temperatures and contact length. Among several wafer characterization measures, Möller [167] points out that TTV is the commonly used parameter in industry and is defined as the difference of wafer thickness measured on four corners and the middle of the wafer which is independent of the wafer thickness and directly influenced by the mechanism of material removal.

Research on the wire sawing process has gained significant advance in the last two decades [48]. A considerably higher share of the research work was conducted on slurry-based sawing and the research on diamond wire sawing had mainly progressed in the last five years. In diamond wire sawing, researchers predominantly focused on the influence of parameters such as wire speed, feed rate, wire tension on process

kinematics and wafer surface quality and accuracy by evaluating the average roughness, surface and subsurface cracks, brittle and ductile material removal regimes and wafer thickness variation and strength. A few number of research studies were conducted to evaluate the wire lifetime and wear.

Researchers worked to determine the process capabilities in the prior studies on diamond wire sawing, mainly by evaluating the quality of sawn surfaces and investigating the process kinematics in terms of wire bow and trajectory. Clark [55, 56] conducted experiments on ceramics, wood and foam materials on a single wire saw, Hardin [82] studied sawing of SiC with diamond wires of 0.22 *mm* nominal diameter. Liu [142] theoretically analyzed the wire trajectory in diamond wire sawing and conducted single wire sawing experiments on marble and granite to verify the results. Meng [160] studied the material removal mechanisms in wire sawing of granite via indentation fracture model on an endless wire saw. The transition of material removal regime from brittle to ductile with lower grain depths of cut was observed. Zhang [245] established a mathematical model for counterweight and saw trajectory to investigate the process efficiency in wire saws. However the diamond wires used in the experiments and analysis are not comparable with today's diamond wire technology for its aspects such as diamond quality, geometry or bonding technology.

Gao [71] conducted single wire sawing experiments with sc-Si to investigate the wafer quality. At wire speeds of 1-2 *m/s*, it is shown that wafer surface roughness, TTV and warp improve with increasing wire speeds. A single wire saw was employed by Ozturk [168] to conduct multiple regression analysis of the process parameters for predicting the influence of feed rate and wire speed on  $R_a$ . However, it was stated that the optimization is only valid for the experimental setup used and require validation for multi-wire sawing. Würzner [229] experimentally investigated the influence of wire speed on mc-Si wafer quality. The wafer surface damage was characterized at the wire speeds of 5, 10 and 15 *m/s*. It was reported that with an increase in wire velocity, higher fluctuations on surface roughness, lower values of maximum crack depth, lower forces and more inhomogeneous stress distribution with compressive and local tensile stress areas are observed. Sopori [193] stated that the magnitude and distribution of surface damage can be defined as a function of the resultant wire velocity. Later Sopori [194] studied the mechanisms affecting surface roughness and causing subsurface damage and showed that the resultant surface is strongly correlated with the sawing kinematics and wire motion. Huang [90] investigated the material removal in diamond wire sawing of SiC and stated that although the material removal is dominated by brittle fracture, more plowing strives are identified at higher wire speeds up to 10 *m/s*.



Through numerical simulation, Chung [54] investigated the distribution of abrasives on diamond wire and stated that the larger abrasive interval results in higher material removal rate. It was concluded that for higher material removal, the abrasive interval should be larger than a critical value. Kim [114] studied the cutting ability of electroplated diamond wires and also concluded that lower diamond concentration leads to higher material removal rates.

Chung [52] modeled the wire geometry as a function of diamond size. Abrasive grains were modeled as conical geometries with  $90^\circ$  tips and the material removal model only includes mapping of the abrasive grain profiles onto the workpiece surface, brittle fracture was not considered. The influence of wire speed, feed rate, size and distribution of the diamond grains on the sawn wafer surface quality were investigated at the wire speed of  $8\text{ m/s}$ . Results show that increasing wire speed and feed rate increases process productivity and also maintains the quality of the wafer surface.

Chung [51] investigated the effects of depth of cut per abrasive grain in diamond wire sawing and stated that there is no proportional relation between the number of active diamond grains and wire speed and feed rate. However, it was mentioned that a proportional increase of feed rate and wire speed would lead to higher wafer surface quality. It is also pointed out that the number of active grains is only a small portion of total number of abrasive grains on the wire; and more active grains are present at the bottom of the groove, in the direction of the feed rate. Sopori [193] found out that the damage depth is strongly influenced by the grain size as well as wire diameter with a smaller degree. Suzuki [198] conducted sawing experiments at wire speeds of around  $30\text{ m/s}$  and analyzed the Si surface, wire topography and chip morphology. It is concluded that smaller diamonds result in lower saw marks and as the number of sawing cycles increase, number of micro dents and saw marks are reduced. Finer diamonds would result in flow-type chips and lead to higher share of ductile material removal.

Wang [221] introduced an analytical force model for diamond wire sawing of SiC. The brittle and ductile material removal modes are considered and it was concluded that the process forces increase with increasing feed rate, wire diameter, diamond density and decreasing wire speed. A depth of cut and force model for sawing sc-Si with resin bonded diamond wires was developed by Liu [145], based on the indentation fracture mechanics and the grain distribution and elasticity of the resin bonding were taken into account. Li [137] developed an analytical force model for wire sawing, based on investigations on forces generated with a single diamond, from the viewpoint of chip formation and friction between the diamond and workpiece.

The analytical model considers the influence of feed rate, wire speed and contact length.

The studies on process kinematics of diamond wire sawing mainly concern the wire bow, tension and trajectory. Wire tension is critical in the sawing process to reach better surface quality i.e. lower vibrations, less sawing marks and prevention of wire breakage [167]. A tension control system with higher precision was proposed by Feng [66]. Li [136] developed an adaptive feedback controller to regulate the normal force in wire sawing of SiC. A static force model is developed and experimentally validated where results show that lower surface roughness can be achieved through controlling the normal force.

The effects of initial wire deflection on wire wear and wafer thickness variation was investigated by Kim [111] on sapphire material. Experiments were conducted at the wire speed of 400 *m/min* with diamond wires of 180  $\mu\text{m}$  core diameter and 30-40  $\mu\text{m}$  grain size. Results showed that with an increase in initial wire bow, forces increase, leading to higher wear rates. However, by adjusting the initial wire bow the parameters can be controlled. Further, it was stated that wafer thickness variation is strongly affected by the cutting speed and an increase in feed rate and wire speed results in higher sawing forces.

Lee [134] considered the break-in characteristics of diamond wire, a phenomenon defined as the reason for the instabilities introduced due to the initial progress of wire wear. The results were variation in wafer thickness, increased kerf loss and lower form accuracy of the wafers. Experiments were conducted with sapphire at the wire speed of 15 *m/s*. It was concluded that the wear behavior of diamond wire strongly influences the break-in characteristics. Kim [113] investigated multi-wire sawing of sapphire and concluded that the break-in effect, when feeding the new wire in reciprocating motion, influences the cutting force, wafer shape and roughness. The break-in effect and initial wear of the diamond wire significantly influence the thickness variation of wafers. It was suggested that through controlled wire consumption, the influence of break-in effect and excessive initial wear can be regulated.

Studies on diamond wire technology on the other hand is limited to the research in industry and very few scientific reports had been published. A modified electroplating method was developed by Ge [72] and tested on an endless wire saw. Yao [237] studied the characteristics and manufacturing methods of the diamond wires and concluded that metallic bonding (electroplated, deposition EDM) and resin-bonding (heat-curing, ultraviolet-curing) introduce different application aspects to the saw-

ing process. Anspach [9] developed a structured steel wire for slurry-based sawing to replace the straight wire which resulted in 100% increase in throughput and around 10% lower specific energy consumption. The effects of Ni layer thickness on cutting performance was studied by Yeh [239]. A sapphire ingot was sawn using 100  $\mu m$  diamond wires with diamond grain size of 8-12  $\mu m$  and Ni layer thickness of 12, 13 and 14  $\mu m$ . The influence of Ni layer thickness, wire tension, wire speed and feed rate on average surface roughness, material removal rate, wire wear rate and TTV of the wafers were investigated. Taguchi method was employed to determine the most significant sawing parameters and it was found that layer thickness is the most significant by 31.7% and wire speed is the second most significant parameter by 29.9%. The suggestion is, with an optimized layer thickness, 33% less roughness, 20% lower diamond wear, 12% lower TTV and 20% higher material removal rate are possible.

One of the few studies on abrasive wear was conducted by Yang [235]. The phase transformations and stress evolution of diamonds in wire sawing of Si using 100  $\mu m$  core diameter wires with diamond concentration at the wire speed of 15  $m/s$  and a feed rate of 1  $mm/min$  were investigated. 21 diamonds samples were analyzed over a wire length of 2  $km$ . Graphitic phases were observed in three of the diamond grains and it was concluded that graphitization of diamonds occurs due to the high compressive stresses measured on the Si surface. It was reported as a possible reason for cutting efficiency loss in wire sawing.

Single wire sawing experiments were conducted by Gao [71] using diamond wires with 0.28  $mm$  core diameter and diamonds of 30-40  $\mu m$  in size with defined geometric shapes. The wire shows an unconventional wear of coating exfoliation. Even though the wire characteristics and manufacturing method vary significantly from the current industry standards, it shall be noted that diamond pullouts were reported as the main wear form. Jaeggi [102] studied the influence of wire wear on the wafer roughness and mechanical strength and stated that even with evident wire wear, no significant impact on wafer morphology and strength were measured.

More on the topic of macro-wear, Schwinde [184] focused on the reduction of kerf loss in slurry-based wire sawing. Worn wire samples from a multi-wire saw were analyzed to find that the abrasion occurs mainly on one side of wire, which provided the reasoning for the development of wires with non-circular cross-section. The observation holds for slurry-sawing and are not confirmed for diamond wire sawing.

Although diamond wire sawing technology has been available for almost twenty years, scientific research on the topic has not yet been sufficiently developed. Studies show that there is a strong relation between the wire speed, feed rate and wafer surface and subsurface quality. It is theoretically and experimentally shown that at higher wire speeds, better surface quality is possible. However, the process limits have not been reached and no research have been done for wire speeds higher than 30  $m/s$ . Moreover, even in the current process limits, systematic measurements of forces and temperatures are still lacking [167]. Until this day there is no significant research on the optimization of wire lifetime or a definitive understanding of the influence of wire wear on process outputs.

For a better understanding of the wafer quality and surface characteristics, it is essential to investigate the material removal mechanisms and resultant surface morphology. Hence, the literature on the material removal characteristics of brittle materials and material removal mechanism in wire sawing should be discussed.

## 2.2 Material Removal Mechanisms

In diamond wire sawing, material removal is achieved through the simultaneous contact between the randomly distributed diamond grains on the wire surface and the workpiece; similar to abrasive machining processes such as grinding, lapping or polishing. The primary quality measures are efficiency, wafer strength, TTV, surface roughness and morphology or surface/subsurface damage are dependent on the material removal characteristic, hence investigation of the mechanisms behind is crucial for a profound understanding of the diamond wire sawing process. Möller [167] points out that currently the mechanisms of material removal are well defined for ductile materials but the knowledge lacks in the understanding of silicon processing.

Material removal is defined as the irreversible energy dissipation when the resolved shear stress exceeds the elastic yield stress at any point of the material. Three main forms of groove wear were listed by Gahr [70] as microplowing, microcutting and microcracking and are presented in Figure 2.2.

Microplowing and microcutting are predominant in ductile materials. In microplowing, material is plastically deformed and pushed towards the edges of the groove and ideally no material is removed from the surface. However, continuous engagement of multiple cutting edges leads to fatigue and results in abrasive removal of the work material. In the case of microcutting, the material is removed in the form of

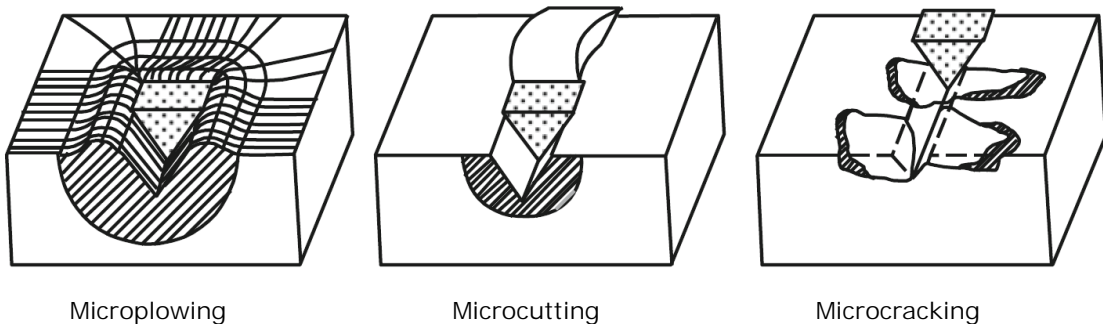


Figure 2.2: Three forms of material removal by abrasive parts as microplowing, microcutting and microcracking [70, 117].

chips and the removed volume is assumed equal to the groove volume that can be approximated as the cross-sectional area of the penetrated cutting edge multiplied by the groove length. Microcracking occurs in machining of materials with higher brittleness, where the material is removed in the form of small scale fractures that may further propagate through highly localized stress areas. The removed volume is higher than the groove volume and it results in a reduced surface quality in terms of roughness and fracture measure [70, 117].

### 2.2.1 Brittle Material Removal Mechanism

The dominant material removal mechanism in brittle materials depends on the scale of indentation and shape of the abrasive particle [129] and can be investigated in two modes namely the brittle material removal mode, where brittle fracture and propagation of cracks take place on the characteristic cleavage plane; and ductile material removal mode, where plastic deformation observed on the characteristic slip plane, in the form of sheared chips [30, 31, 74, 188].

Indentation fracture mechanics is used to define the process of brittle material removal for explaining the crack generation and propagation. Lawn [131] investigated the mechanics of point indentation fracture and defined the crack formation under point indentation where two main types of cracks were observed. Median cracks which propagate downward below the contact point during loading and lateral cracks that propagate sideways of the contact point during unloading of the indenter.

The median crack initiation in elastic/plastic indentation field was investigated by Lawn [127]. Further, Lawn [128] defined the evolution of the median/radial crack system for sharp indenter contacts in brittle materials and proposed a model where the elastic/plastic field under the indenter tip is defined by its elastic and residual

components. The model is able to predict the median and radial growth characteristics in several ceramics through calibrated equations. The net indentation force is divided into well-defined components; and the properties of stress intensity factors according to the definition by Lawn [126] are applied, which consider the superposition of the residual stresses and elastic contact fields after unloading [128]. Microfracture from scratching sapphire and glass are investigated by Swain [199] using a Vickers indenter. Three distinct states in crack formation were observed as low loads where no visible cracks are seen; medium loads where well-defined median and lateral cracks occur; and high loads where the plastically deformed groove shatters and size of lateral and median cracks get smaller compared to the ones in medium-high loads.

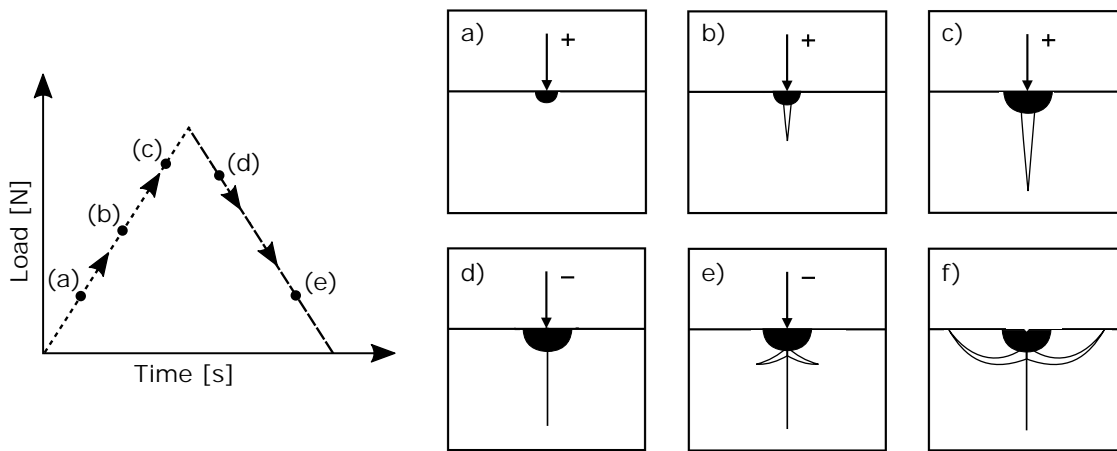


Figure 2.3: Chip generation process in brittle materials machining [131, 132].

Lawn's [131] definition of formation of a crack under a sharp indentation edge is schematically represented in Figure 2.3. The crack formation and brittle material removal is explained in the sequence:

1. Initial loading forms a plastic deformation zone under the point indenter.
2. At a critical load, the median crack is initiated where the maximum stress concentration is present.
3. As the load increases, median crack propagates and extends further.
4. With the initial unloading, median crack begins to close.
5. As the unloading continues, prior to the removal of the indenter, residual tensile stresses are superimposed with the relief of the deformed material. These intense residual stresses lead to lateral crack propagation [154, 196].
6. With the completion of the unloading, propagation of the lateral cracks may lead to chipping. On the other hand it should be realized that the crack

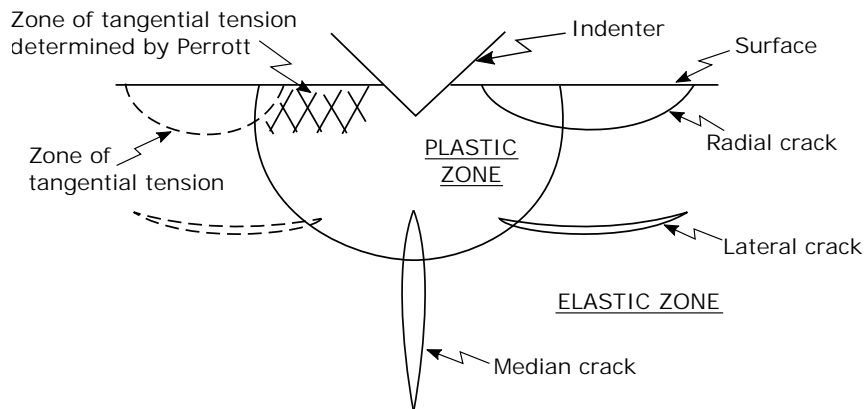


Figure 2.4: The elastic-plastic contact zone under the indenter, generating radial, median and lateral cracks [50].

initiation may have strong relation with the fracture geometry, however here, elaboration phase of the crack is in focus [128, 132].

Later, Marshall [155] defined the mechanics of lateral crack propagation in brittle solids and proposed an experimentally validated model for the phenomenon. The main influence for lateral cracking was also explained with the residual stresses. The elastic/plastic zones and the three crack mechanisms are summarized in Figure 2.4. In an elastic-plastic contact condition, the median cracks originate at the bottom of the elastic-plastic zone, normal to the indentation direction whereas the lateral cracks are originated in the lower part of the elastic-plastic zone and travel in lateral direction. Under sufficient loading and also unloading conditions, the lateral cracks propagate to surface and contribute to the material removal. Radial cracks on the other hand, originate on the surface near the elastic-plastic zone and contribute to the material removal as well.

The index of brittleness was introduced by Lawn [130] as the ratio of hardness (resistance to deformation) to fracture toughness (resistance to fracture) ( $H/K_{IC}$ ). Later, Moore [164] studied the indentation properties of several brittle solids and stated that the fracture mechanism is dominant with higher indentation depth, sharp abrasives and low fracture toughness to hardness ratio ( $H/K_{IC}$ ).

Moore [164] stated that material is removed by a fracture mechanism if lateral cracks adjacent to the grooves intersect those from other grooves or propagate to the surface. The volume of material removed can be much greater than the groove volume since the lateral cracks extend well beyond the boundaries of the grooves. He proposed a model which considers material removal both by plastic deformation and indentation fracture. However, the developed model for material removal mechanisms

in brittle materials was not validated for Si due to reported phase transformations during machining of Si.

### 2.2.2 Ductile Material Removal Mechanism in Brittle Material Processing

In ductile regime machining, the chips experience a plastic deformation, leaving a crack-free surface where a better surface finish is observed [31]. From the energy balance point of view, for brittle materials, ductile material removal takes place when plastic flow is more energetically favorable, especially at smaller depths of cut.

Ductile material removal regime in brittle materials was first observed by King [115], stating that in case of frictional wear of rock-salts, plastic deformation is present along with surface cracks and fragmentations. Furthermore, Bridgman [36] showed that glass material experience ductile material removal under high hydrostatic pressures and Lawn [132] identified the transition from brittle to ductile material removal regime during nano-indentation tests on glass. Moore [164] investigated the indentation properties for engineering ceramics and brittle solids to understand the plastic deformation and fracture characteristics. When the load on abrasive is low, plastic deformation is favored, while with high loads (e.g. blunt abrasives), plastic deformation and fracture were observed in combination. Liu [143] stated that the large compressive and shear stresses lead to ductile chip formation and by suppression of the stress intensity factor  $K_{IC}$ , the progression of preexisting flaws in the material were prevented. Furthermore, it is commonly accepted that high contact pressures lead to ductile behavior of Si due to the transformation of diamond cubic phase of Si to a metallic phase [14, 30, 45, 143, 187, 220, 232].

Inasaki [95] discussed the fundamental principles of material removal in hard and brittle materials. His work referred to Hill's [85] elastic/plastic internal cavity analysis to define the plastic deformation zone for indentation. The definition suggests a positive linear correlation between the relative plastic zone radius  $c_p/r_{eff}$ , where  $c_p$  is the radius of the plastic zone and  $r_{eff}$  is the effective radius of the indenter; and  $E/H$ , where  $E$  is the elastic modulus and  $H$  is the material hardness.



### 2.2.3 Ductile to Brittle Transition

The available research on ductile to brittle machining modes consider several properties of the process and tool that have influence on the active material removal modes.

Lawn [127] suggested a model to predict the threshold load for fracture initiation for a diamond indenter. Blake [33] studied the influence of tool nose radius in brittle-ductile transition and experimentally investigated the effect of critical depth of cut in brittle-ductile transition in single-point turning of Si and Germanium. Also considered the influence of rake and clearance angles, cutting speed and crystal orientation and material properties on critical depth of cut. Later, an experimental critical depth of cut model was proposed by Bifano [31] that only considers the material properties  $E$ ,  $H$  and  $K_{IC}$ .

$$h_{cu,crit} = \kappa_c \left( \frac{E}{H} \right) \left( \frac{K_{IC}}{H} \right)^2 \quad (2.1)$$

where  $h_{cu,crit}$  is the critical depth of cut for transition from ductile to brittle material removal regime and  $\kappa_c$  is the material constant.

Arefin [14] found out an upper limit of the tool cutting edge radius above where the chip formation mechanism transforms from ductile to brittle, even though the undeformed chip thickness remains smaller than the tool edge radius, in single point turning of Si. Wu [226] studied the influence of abrasive shape (spherical and conical indenters) in ductile to brittle transition in single grit scribing of diamond with a finite element based model. Simulation results showed that an increase in the tip radius for spherical or included angle for conical indenters result in an increase in critical depth of cut by delaying the onset of crack initiation in Si. It was suggested that with sharp tips, large tensile stresses are generated on the material, that may initiate median and lateral cracks on subsurface. The effect of size and shape of abrasive grain on ductile machining of sc-Si was also investigated by Kumar [121] through low-speed scratching with spherical and crushed tungsten carbide grains. It was concluded that spherical grain geometries result in more ductile material removal with less micro-cracks than crushed grains and as the depth of scribe increases, brittle fracture and larger cracks on the Si surface are present.

The brittle-ductile transition mechanism in high speed grinding of SiC was studied by Li [135] through experiments and it was concluded that high speeds change the contact behavior of diamond and SiC, so that the material removal can be increased without fracture crack occurrence. Wang [219] studied the subsurface damage in high speed grinding of brittle materials and concluded that when the maximum undeformed chip thickness is higher than the critical chip thickness, the removal is mainly brittle. Lateral crack system was studied as the main material removal mechanism in brittle mode. Chung [53] stated that there is a critical loading condition on abrasive grains where the material removal regime changes from ductile to brittle, leading to an increase in material removal rate.

According to Wu [225], at very low cutting depths, applied pressures can be high enough, where it leads the transformation of the material to plastic state, hence making ductile mode of cutting possible in diamond scribing of Si. Through single point diamond scribing tests, it was observed that in some directions, ductile material removal is more visible on sc-Si in three crystallographic planes. It was concluded that ductile material removal of silicon is accompanied by phase transformations where diamond cubic and amorphous silicon (a-Si) phases were observed in the areas where plastic deformation and brittle fracture were present and only diamond cubic phase was present in the areas with brittle material removal mode.

Further Wu [227] developed a mathematical model to calculate the average depth of cut of a diamond grit, based on Si material removal by lateral crack propagation. A theoretical study was conducted and the ductile mode in diamond wire sawing was analyzed with the extended finite element method. The work is based on the indentation fracture mechanics approach. It was concluded that the shape of the grit influences the cutting mode and sharp grit edges lead to brittle fracture. The critical depth for Si was found to be between 41 and 143 *nm* based on process parameters. Later, through theoretical calculations and finite element modeling, Wu [224] analyzed the grain-Si interaction for ductile regime. It is noted that the ductile mode cutting is sensitive to grit shape and sharp edges easily result in brittle fracture. Simulation results showed that an increase in the tip radius for spherical or included angle for conical indenters result in an increase and sharp edges easily result in brittle fracture. Through simulations, Chung [51] studied the effects of depth of cut and abrasive distribution on material removal to conclude that the removal is mainly in brittle regime, due to the frequent involvement of large depth of cuts as a result of varying diamond grain protrusions.

Theoretical and experimental research that consider material removal in brittle materials are reviewed and the transition characteristics of material removal regimes depending on the material, tool and process parameters are discussed. In brittle material removal regime, the onset and propagation of median/radial and lateral cracks in brittle materials are well defined, mainly under a sharp indenter and also for spherical contacts for a range of brittle materials. Developed models explain the dimensions of the elastic/plastic zones as a function of the material and indentation characteristics. However, the research work explains the phenomenon for static and quasi-static events and a vast amount of assumptions for the dynamic cases. Further, the material, tool and process properties for ductile mode material removal in brittle materials are investigated. It can be concluded that lower penetration depths, high hydrostatic stresses/contact pressures that may be also the results of blunt cutting edges result in ductile material removal mode.

Established models on the transition of brittle-ductile material removal regimes consider the critical penetration depth and focus on the material properties. Although experimental work suggests that the transition may further be dependent on conditions such as tool geometry, cutting speed or crystallographic orientation. Work on the topic is mainly in experimental research and recent studies focus on finite element models. A profound understanding of the material removal characteristics necessitate the observation of the interaction in the single grain level, where the contact is isolated from conditions of a higher complexity.

## 2.3 Grain Scratch Tests

Due to the physical limitations for the observation and measurement of the grain-workpiece contact during abrasive machining and the stochastic nature of the process, single grain scratching experiments are widely employed to emulate the contact conditions and to examine the process at single grain level. Beside quasi-static and dynamic indentation methods, single grain scratching experiments provide valuable insights for the grain-material interaction. In this section, single grain scratching methods are reviewed with a focus on the scratching of brittle materials. Significant studies of single grain scratching for the investigation of material removal modes in brittle materials, anisotropy of and alterations on the Si material are discussed. Further, measurement and analysis of process forces in single grain level are studied. Finally, several scratching experimental methods and setups are reviewed.

Scratching of brittle materials is a frequently visited topic in literature, where critical depth of cut at the onset of ductile to brittle transition, material removal mechanisms, stress fields, process forces, temperature and influence of cutting grain geometry such as grain shape and tip radius on process outputs are widely studied. Sasaki and Okamura [183] performed single grain scratch tests to investigate the influence of cutting depth and cutting edge angle on the cutting mechanism of grain. Liu [143, 144] analyzed the resultant stresses in Si material and suggested that in ductile material removal mode, large compressive stresses in front of the cutting tool prevents the crack propagation of existing material flaws. Zhao [247] conducted diamond scratching tests on SiC and investigated the material removal and grain wear mechanisms with diamond shapes of prism, pyramid and inclined prism. It was concluded that the brittle fracture and plastic deformation are present at the same time and the diamond wear occurs at the stress concentration region. Moreover, the ratio of the vertical and tangential scratching forces were stated to be critical for the determination of the active material removal regime.

Through experiments, Li [138] showed that it is possible to machine sc-Si material in ductile mode by changing the tool tip radius and the undeformed chip thickness. The material removal mode transforming from completely ductile to a combination of ductile and brittle to completely brittle fracture with increasing depths of cut was observed by Wu [225]. Gu [78] investigated the chipping behavior and material removal mechanisms in optical BK7 glass through scratch tests with a nanoindenter at the tangential speed of  $10 \mu\text{m}/\text{s}$  and at several normal loads. Plowing is determined to be predominant in ductile mode material removal. Resultant surface morphology, removed volume and depth ratio were reported to be strongly correlated with normal load and separation distance in brittle material removal regime. Wu [226] performed scratching experiments with conical ( $60^\circ$  included angle) and truncated conical ( $10^\circ$  included angle and  $3 \mu\text{m}$  tip radius) shaped scribes and developed an XFEM model considering the influence of abrasive grain geometry, friction coefficient and external hydrostatic stressed on brittle-ductile transition of sc-Si. The experiments were conducted at the speed of  $1 \text{ mm}/\text{min}$  and for  $0\text{-}2 \mu\text{m}$  depths of cut. Recently, Kumar [123] performed scratching experiments using an electroplated diamond wire with a core diameter of  $120 \mu\text{m}$  on sc- and mc- silicon. The influence of grit shape on surface and subsurface characteristics and critical depth of cut were investigated at the scratching speed of  $100 \text{ mm}/\text{min}$  and with a scratch length of  $5 \text{ mm}$ . The effect of speed and grain wear by repeated scratches were omitted. The dependency of the surface cracks on grain geometry was investigated to conclude that the abrasive grain shape has a higher influence on the resulting surface morphology than the crystallographic orientation.

Si anisotropy has also been studied through scratch tests and single point turning [49, 92, 187, 233]. Shibata [187] experimentally investigated the influence of crystallographic orientation in turning of sc-Si and concluded that the dependence of surface features on crystallographic orientation is related with the ease of the occurring slip deformation. Chao [49] conducted single point turning experiments and proved that the critical depth of cut is strongly related to the crystallographic direction where lower values are present in easily fractured directions. The crystallographic direction was found to have a strong influence on the crack initiation and propagation.

Si has cubic structure at atmospheric pressure and experiences phase transformations to crystalline and amorphous states at higher pressures. Using single point diamond scribing, Wu [225] reported Si phase transformations as diamond cubic and a-Si phases. Trachet [206] conducted quasi-static and dynamic indentation tests with a Vicker's indenter to evaluate the phase changes in mc-Si. The phase distributions under the indenter were measured to determine the phase transformations in terms of the strain rate. The results show that Si hardness is inversely related to its strain rate. Through diamond indentation experiments at room temperature, Callahan [46] observed phase transformations at very low loads.

Measurement of process forces on single grain is of high importance in modeling and simulation of the abrasive processes. Matsuo [157] conducted single grain scratching experiments on steel and alumina, using diamond and CBN grains; and investigated the material pile up and process forces to find that the grinding forces are highly dependent on the grain geometry. A positive linear relationship was determined between the cutting force and the cross-sectional groove area, independent of the work material and the grain type (CBN or diamond). Malkin [149] proposed that the grinding force is composed of cutting and plowing forces by investigating the relationship between the grinding force and the removal area through grinding experiments. Further, Malkin [150] showed that grinding power is proportional to the components of grinding force. Azizi [21] developed an analytical grinding force model based on single grain interaction and investigated the influence of the process parameters, number of active grains and grain sharpness on process forces through experiments. The abrasive grains on the grinding wheel were modeled as pyramids. An exponential relationship was determined between the cutting force and increasing number of active grains and abrasive grain slope.

Specific cutting energy (grooving/scratching energy) was widely used to characterize the process at the single grain. Vingsbo [216] measured the energy consumed during the cut and calculated the specific grooving energy which is defined as the grooving energy consumed for unit mass loss, as a measure of abrasion resistance. A modified Charpy pendulum impact tester was employed for the experiments.

Feng [65] conducted high-speed scratch tests with steel workpiece and studied the groove and chip morphologies, area removal ratio, grinding force ratio and specific grinding force. It was concluded that plowing decreases with increasing groove cross-section area and grinding speed and surface integrity is improving with increasing cutting speed. It was shown that the grinding force ratio  $\epsilon_f$  increases with the groove cross-section area on the cutting plane. The grinding force ratio was reported to be larger for blunt grains and was expressed as:

$$\epsilon_f = \frac{F_c}{F_n} \quad (2.2)$$

where  $F_c$  is the cutting force and  $F_n$  is the normal force acting on the single grain.

Several scratch tests setups are proposed in the literature. A pin attached to a rotating disc was employed by Transchel [207], Bredell [35], Graham [75], Brinksmeler [39] and Aurich [20]; a pendulum by Vingsbo [216] and Liang [140]. Further the grain can be linearly guided as was done by Vargas [214], Buhl [42] or Perfilyev [170]. Setups of the mentioned experiments are presented in Figure 2.5.

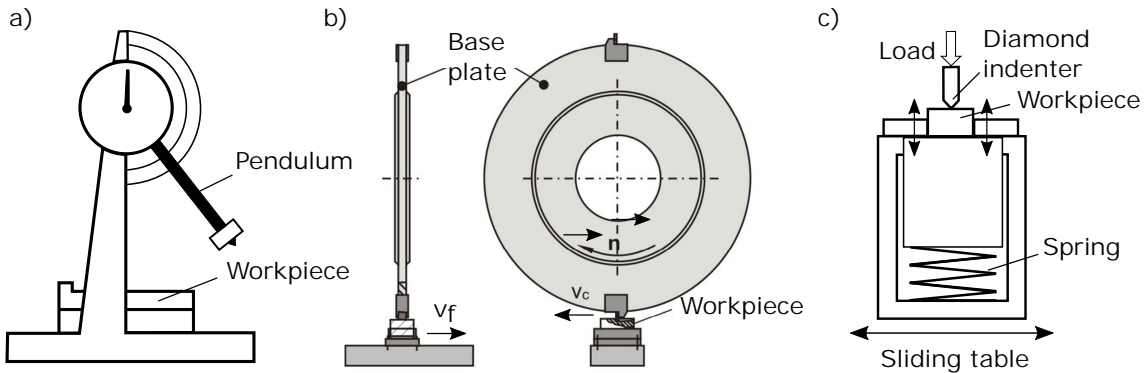


Figure 2.5: (a) Pendulum type scratching setup [140]. (b) Pin-wheel scratching setup [20]. (c) Linear scratching setup [170].

However, the measurement of process forces are limited at high cutting speeds at rotating pin and pendulum setups because of the presence of high excitation frequencies. Short contact time between the cutting edge and the workpiece material

lead to such high frequencies [189]. Due to this, experiments were commonly conducted at low cutting speeds such as  $100 \mu\text{m}/\text{s}$  by Perfilyev [170],  $1 \text{ mm}/\text{min}$  by Wu [226] or  $10 \text{ mm}/\text{s}$  Wang [220] to be able to measure process forces.

In linear scratching, high acceleration distances are required to reach higher speeds, hence cutting speeds are limited with the physical capabilities of the setups. Gu [78] performed linear scratch tests with a nanoindenter at a tangential speed of  $10 \mu\text{m}/\text{s}$ . For a reliable measurement of the process forces on single grain, dynamometers with high natural frequencies are essential [58, 75]. Such dynamometers are available in literature that enable force measurements at the cutting speed of  $5 \text{ m}/\text{s}$  [169, 207].

Another approach to overcome the high frequency phenomenon is to increase the tool-workpiece contact time by increasing the scratching distance. As previously mentioned, investigation of the wire sawing process at single grain requires introduction of longer contact lengths and chipping distances in comparison to grinding. To measure the process forces at high cutting speeds and with long contact lengths, relative rotational motion of workpiece and cutting edge are usually employed. Rotational scratching of an Si wafer with a three-faceted pyramidal diamond tip on an ultra-precision grinder to investigate the changes on Si surface were conducted by Zhang [246]. Influence of tip radius and included angle on the mechanisms of Si wafering were investigated, forces and stresses at the onset of chip and crack formations were calculated for scratching speeds between  $8.4$  and  $15 \text{ m}/\text{s}$ . Tamaki [202] performed diamond scratch tests with glass to investigate the influence of rake angle, edge angle, wedge angle and cutting edge radius on critical depth of cut at cutting speed of  $550 \text{ m}/\text{min}$ . The workpiece was installed on a CNC face turning machine and the circular workpiece is tilted, hence the grit comes into contact with the workpiece in a circular arc groove in each revolution of the plate. Huo [93] developed a single grain setup to investigate the brittle-ductile transition in grinding of mc-Si with grain sizes of  $50 \mu\text{m}$  at the grinding speed of  $45 \text{ m}/\text{s}$ , rotational speed of  $120 \text{ s}^{-1}$  and an infeed rate of  $6 \mu\text{m}/\text{min}$ . The critical depth of cut was reported as  $40 \text{ nm}$ . Examples from the mentioned settings are presented in Figure 2.6.

Scratching tests with single grains and single point tools provide useful information on the tool and material behavior. Moreover, such tests are the primary methods to understand the forces and temperatures at the single grain level and to develop an understanding of the cutting conditions in abrasive processes. This kind of understanding is essential for process modeling.

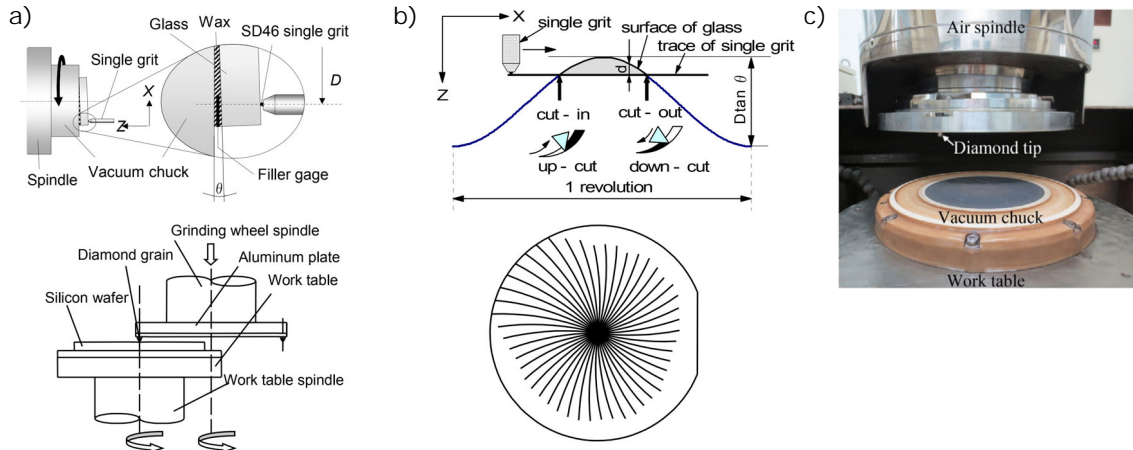


Figure 2.6: (a)-top: Inclined scratching setup [202]. (a)-bottom: Trace of the grain tip on workpiece. (b)-top: Rotating tool-workpiece scratch test setup [93]. (b)-bottom: Grooves on workpiece surface. (c) Rotational scratching of silicon wafer [246].

On the topic of wire sawing, the presence of long contact lengths, small grain sizes, dependency of the wire trajectory on process parameters or properties of Si material necessitates the investigations through scratch tests. Even though pioneering studies on the subject had been published, the literature lacks the investigation of contact temperature and systematic measurement of forces at the single grain and their interrelation with the grain and surface.

In this aspect, an experimental setup for single grain scratching is required to be able to measure the process on the abrasive grains of size comparable to the ones on an electroplated diamond wire. Moreover, to overcome the stated limitations on force measurements at higher cutting speeds over  $5\text{ m/s}$ , long grain-workpiece contact lengths shall be possible. Additionally, the setup shall be designed and operate to make the temperature measurements possible at a location as close as possible to the contact location.

## 2.4 Modeling and Simulation of Abrasive Processes

In the following section, the modeling and simulation of abrasive processes are reviewed. Initially, an overview of the literature in modeling techniques is presented. Following, the details of the kinematic-geometric modeling and simulation are given including the tool topography generation and process force modeling approaches. In the last part, the wear phenomenon and approaches on the modeling of abrasive wear are discussed. The review shall go beyond the models developed for wire sawing since the research work on the topic is currently limited.



It is often unpractical, costly and time consuming to determine ideal parameters for a process. Engineering models are developed to define the instantaneous state of the system with a finite number of parameters, by defining their interaction mathematically, based on physical laws [23]. They are crucial for the understanding of the process behavior and moreover, create a basis for the simulation of the process in certain boundary conditions and for a limited field of application. Tönshoff [210] defined the term model from the viewpoint of manufacturing as “a model is the abstract representation of a process which serves to link causes and effects”. However, an accurate modeling is extremely difficult and is not possible for abrasive processes [107], mainly due to the dependency on high number of parameters, complexity of the removal process and transient nature of the interaction [209]. Moreover, as suggested by Brinksmeier [37] developing a model that predicts the abrasive removal process behavior, the dynamic behavior of the process, such as the tool wear, shall be taken into account.

The term simulation is explained from the engineering point of view as “the imitation of discrete values of time of a dynamic process on the basis of a model” [210] and by Brinksmeier [37], it is further stated as the established tools for the assessment and optimization of machining processes.

### 2.4.1 Overview of the Modeling Approaches

A review of modeling approaches was given by Brinksmeier [37] where, based on their development method, models were investigated as physical, empirical and heuristic process models, summarized in Figure 2.7. Physical process models were split into fundamental analytical, finite element (FEM), kinematic, molecular dynamic (MD) and regression models; empirical process models as regression, artificial neural network (ANN) models and heuristic approaches were mentioned as rule based models. On the modeling of abrasive processes, a further classification can be stated as the microscopic process models where a detailed 3D description of the abrasive grains, their random distribution and orientation on the tool are provided through topography analysis; and macroscopic process models where tool-workpiece contact was defined by the macro-geometry of the tool, overlooking the individual grain contact [17]. The outcomes can be implemented in different approaches such as molecular dynamics, finite element or kinematic models.

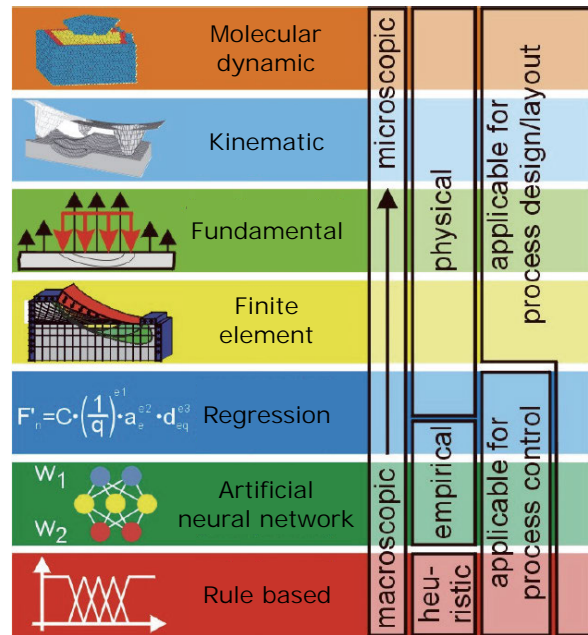


Figure 2.7: Modeling techniques and the application areas for process simulation [37].

In the physical modeling approach, quantitative models are derived from the physical principles defined with mathematical formulation and can be transferred to other machining conditions. Empirical models are constructed on the parameters that are determined with regression analysis and able to accurately define one machining application only. A purely physical model of an abrasive process is rarely used since the physical relationships in abrasive processes cannot be accurately defined [209].

MD simulation provides a deeper understanding of the microscopic material behavior through modeling in atomic level. The studies on the topic have started at the end of 50's in the field of statistical mechanics, but its application to machining have started by the late 80's [118]. The simulation method had been applied to many fields i.e. tribology, diamond synthesis and laser interactions [81, 118]. In MD simulations, a few nanometers of contact length in picosecond time frames are considered. A better understanding of the influence of lattice structure and orientation or micro-defects are possible through MD simulations [37].

Kinematic modeling is based on the description of kinematics of the tool-workpiece interaction. In kinematic models, definition of the penetration of a single grain determines the material removal and is of high importance. The workpiece is usually considered as ideal and do not posses any thermo-elastoplastic properties, the interaction between the tool and the workpiece are only geometrical. A detailed description of kinematic models with a focus on kinematic-geometric models is presented in Section 2.4.2.

Fundamental analytical approaches define the process with the physical interrelations of its elements through mathematical formulations. Hence, a broad knowledge of the grain-workpiece interaction to determine the contact conditions and material removal is essential. The abrasive tool topography and chip thickness models are used to define the process kinematics and from these, force models are developed to estimate abrasive grain wear and forces, further, surface roughness is predicted [37, 209].

FEMs are widely used to simulate the deformations, forces and temperature fields in machining processes with geometrically defined or non-defined cutting edges. The area of interest is divided into a finite number of elements that are connected by element nodes. Typical FEMs include the material properties and geometry of the workpiece to determine its stiffness, mechanical and thermal loads, process parameters, heat transfer coefficients between lubricant and workpiece, cooling and boundary conditions. FEMs can be applied in macroscopic or microscopic level. Macroscopic models are used to determine the temperature distribution and form deviation of the workpiece; the plastic material behavior and chip formation are not included. In microscopic models, a small area of contact is considered [37, 151].

Regression models aim to define functional interrelations between the data points (dependent variables) and independent random variables through statistical methods. The models usually describe static cases with no time dependency to increase the applicability i.e. tool wear is not considered to reduce complexities [7, 37, 209].

Artificial neural networks (ANN) are used for modeling of non-stationary processes with high complexity that are dependent on a number of input variables and mainly applied for pattern recognition, data compression and function approximating. ANNs determine the weights of successful and unsuccessful outcomes of the training sessions, such that the actions of the human brain are simulated [209]. No physical description of the process is required and the models are constructed through training based procedures on the measured data [37, 244]. An application of the approach by Sakakura [182] was done through establishing a process model with neural network approach for cylindrical grinding. The decision making process of the operator was investigated and found out the importance of operator's associative memories on information processing. A model was suggested based on the findings and two types of neural networks as Feedforward and Brain-State-in-a-Box were employed.

The idea behind rule-based models is to utilize the computers for low-level, high-volume decision making through the use of knowledge-based and fuzzy-logic systems; and leaving the high-level, low-volume decision making processes to human beings

[179]. The basis behind the approach is to correctly formulating the rules for the model.

It was stated by Brinksmeier [37] that among the reviewed methods, kinematic, finite element and molecular dynamics modeling approaches are the most prominent ones.

## 2.4.2 Kinematic Modeling and Simulation

The kinematics of abrasive material removal processes can be explained with individual engagements of stochastically distributed cutting edges on the abrasive tool. Kinematic modeling and simulation provide valuable insights in abrasive processes where monitoring of the grain-workpiece contact conditions are limited.

First kinematic models in abrasive machining have started with two dimensional models in the early 70's and higher degree models have been developed since 80's with the availability of faster computers [37]. In the work on the advances in modeling and simulation of grinding processes by Brinksmeier [37], kinematic modeling and simulation works were divided into basic kinematic approaches, kinematic-geometric models and kinematic-empirical models. Basic kinematic approaches include ideal kinematics of the tool and workpiece and two dimensional grain models. Primary interest lies on modeling of the surface profile. More recent work consider grain chipping space, chip geometry, number of dynamic cutting edges and grain wear. Kinematic-geometric models on the other hand, consider the three-dimensional contact and penetration of the grain-workpiece at a higher level of discretization. Kinematic-empirical models differ from the kinematic-geometric models in the way that in kinematic-empirical models, empirical and analytical equations are used to calculate the process characteristics and results.

Kinematic-geometric modeling enables the calculation of process outputs such as forces on single grain, stress distribution on workpiece surface, chip thickness or share of kinetic and static grains. Ideal cutting conditions are considered i.e. plastic deformations in the contact zone are omitted. However, some models include further descriptions like material pile-up, compliance of the tool or thermo-mechanical aspects of the interaction. The advances provided further insights on the grain and tool wear.

The kinematic simulation defines the geometry of the removed area in discrete time steps and superposition of the calculations determine the final geometry of the workpiece [209]. An overview of the kinematic-geometric simulation for grinding by Au-

rich [19] is given in Figure 2.8. Simulation inputs are stated as the ideal process kinematics, ideal workpiece geometry and generated tool topography; simulation of the process covers calculation of the grain penetration in single grain level; and output parameters are grinding forces and resultant workpiece surface.

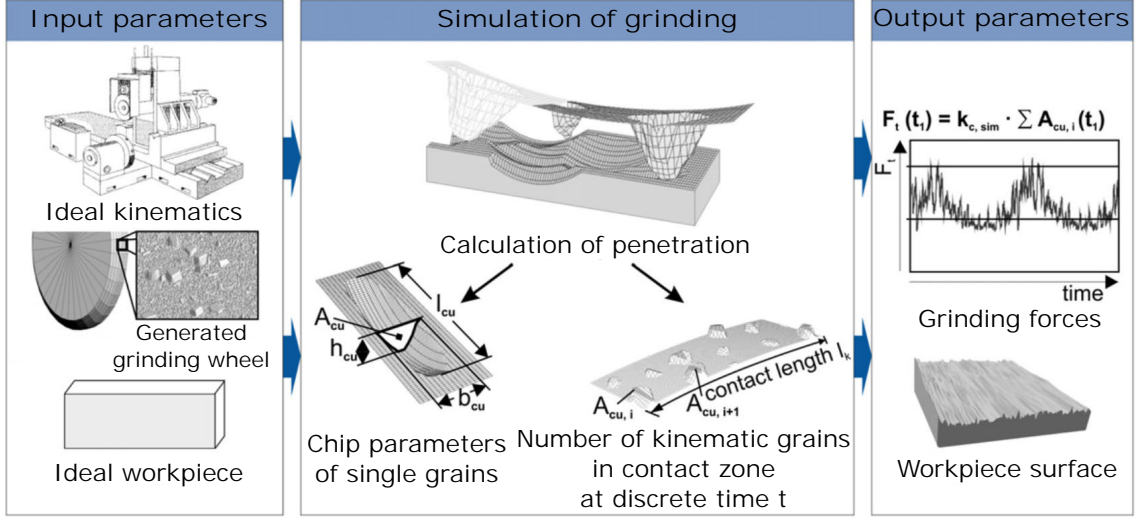


Figure 2.8: Inputs and outputs of the kinematic simulation [19].

Three elements are essential in kinematic-geometric modeling and simulation of the process:

1. **Tool Geometry:** The description of micro- and macro- geometry of the abrasive tool is the primary and highly critical part in kinematic modeling. The macro-geometry of the tool is defined by its eccentricity and micro-geometry is defined by the grain size, geometry, strength and abrasive layer characteristics [37, 209]. The geometric and material properties of the abrasive layer has critical influence on the process as well, especially from the viewpoint of abrasive grain wear which is interrelated to material removal, process forces and temperatures in the cutting zone.
2. **Process Kinematics:** The definition of process kinematics through mathematical formulation is required to calculate the relative motion between the tool and workpiece. Using a detailed description of the micro- and macro-properties of the tool i.e. diameter, abrasive grain positions, size and protrusion, it is possible to estimate the individual grain penetration. Additionally, elasto-mechanical and thermo-mechanical properties of the contact or damping behavior of the machine structure can be introduced for more realistic engagement conditions.
3. **Process Forces:** The simulation outputs of undeformed chip thickness, chip length, chip width and chip cross-section area can be used to estimate the

process forces [19]. Through the calculated or measured forces and/or grain removal depths, wear behavior of the abrasive tool can also be estimated. In the case of brittle material machining, when a detailed understanding of micromechanical removal process is reached, determination of the active material removal mechanism for individual grain penetration is possible.

### a Measurement and Modeling of the Tool Topography

Determination of the tool geometry is possible by direct and indirect measurements on the surface or statistical evaluation of the grain and tool properties. Several reviews are available in the literature on the measurement of abrasive tool topographies and generation of topography models [63,146,210,215]. In the case of diamond wires, very few measurement methods are proposed, hence this work concerns also the measurement of grinding wheel topographies.

Several classifications of the topography measurement methods are proposed such as grain counting, profilometry and taper print methods by Verkerk [215]; contact and non-contact methods by Lonardo [146], where non-contact methods can further be investigated in optical and non-optical; static, dynamic and kinematic methods by Marinescu [153]. Dynamic methods depend on machining conditions and actual abrasive grains effective in cutting are measured; kinematic methods combine the process kinematics and distribution of statically determined abrasive positions [40,153]. In the kinematic approach, trajectories of single grains are reproduced through geometric contact conditions and process parameters. Figure 2.9 shows the distributions and definitions of static and dynamic edges on an abrasive tool.

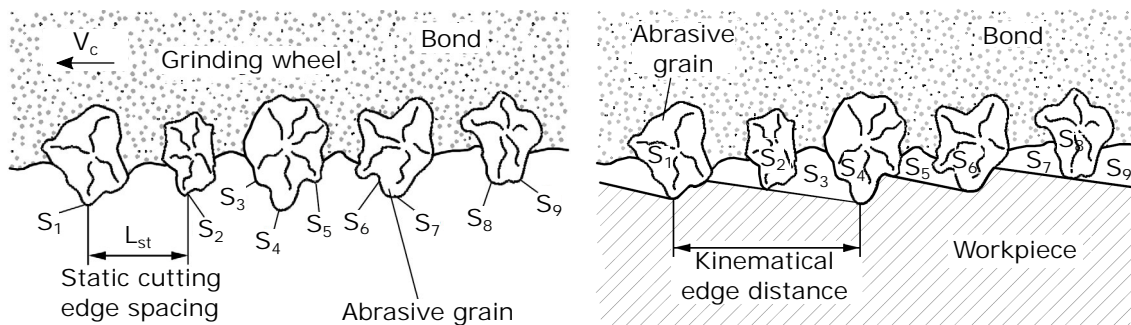


Figure 2.9: (left) Static and (right) kinematic cutting edges [153].

Figure 2.10 summarizes details of the classification proposed by Marinescu [153]. Several techniques were mentioned such as roughness measurement of the wheel topography, qualitative analysis through optical images, quantitative characterization of topography by counting the grains directly on the wheel or on surface prints, piezoelectric and thermoelectric measurements to determine the number of active cutting edges, photoelectric measurements based on reflection of the light from the cutting area, mirror workpiece method where number of scratch marks are counted on a mirror-like surface to determine the overall number of grains on the tool; and workpiece penetration method where a thin steel plate or stationary workpiece is penetrated and the surface roughness is measured for the comparative assessment of different tool topographies.

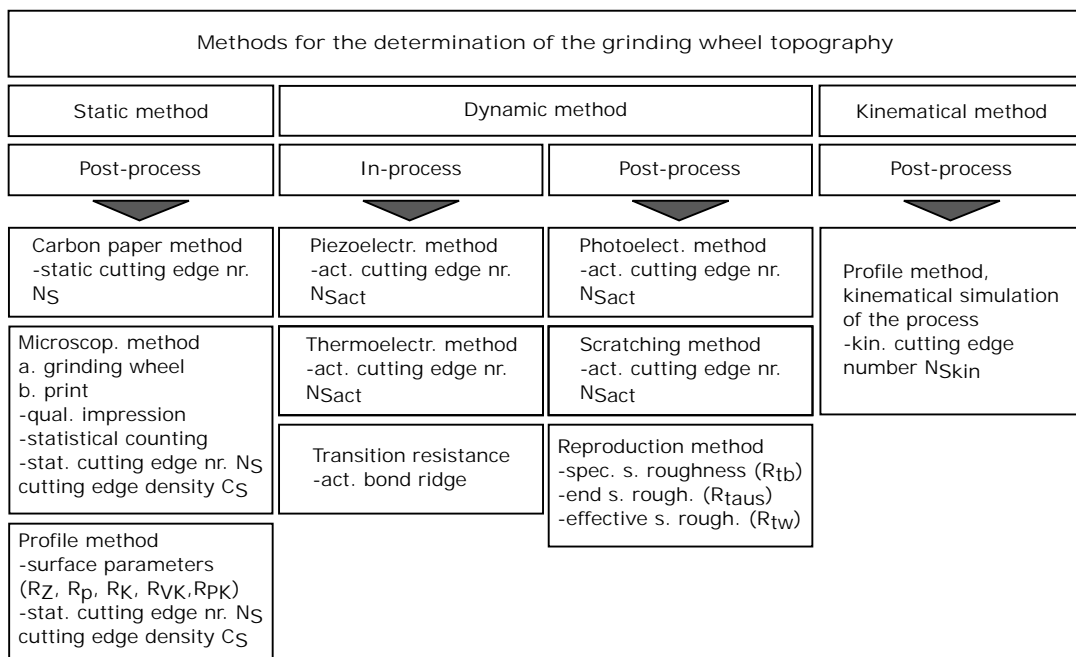


Figure 2.10: Grinding wheel topography characterization methods [40, 153].

A three-dimensional contacting profilometry was used by [34], an automated non-contact 3D wheel scanning system was used by [60], a 3D laser microscopy was employed by [230], 3D grain positions were derived from contact measurements by [231], optical profilometry was employed by [96], SEM measurements of the grinding wheels were used by [94], imprints of the wheel on a polished lead sample were used by [83] and photoelectric measurements were used by Brinksmeier [38].

The bearing area fraction, a useful parameter for the characterization of engineering surfaces was introduced by Abbott and Firestone in 1933 [6]. The area is visualized by the Abbott-Firestone curve (or material ratio curve) to determine the material ratios of the surfaces at a given height which can also be used to characterize abrasive tool topographies.

The curve is derived from the profile of the surface where the intersect length of the material along a line is measured and summed together and plotted as the proportion of the total length. This procedure is repeated through a number of slices of infinitesimal thickness for the complete profile height. The calculation represents the proportion of the true area to the nominal area [195, 204].

From the viewpoint of statistics, the curve is derived from the height probability distribution function  $p(z)$  and for a Gaussian distribution, it is the cumulative probability distribution function  $P(z)$  described in Figure 2.11, where  $z$  is the perpendicular distance from the base plane,  $\Delta z$  interval between two consecutive layer heights and  $h$  is the mean plane separation.

The bearing area at height  $h$  is the complement of the cumulative probability distribution function and can be defined as:

$$BA = \int_h^{\infty} p(z) dz = 1 - P(h) \quad (2.3)$$

where  $BA$  is the bearing area and  $P(h)$  is the cumulative probability function at height  $h$  [204].

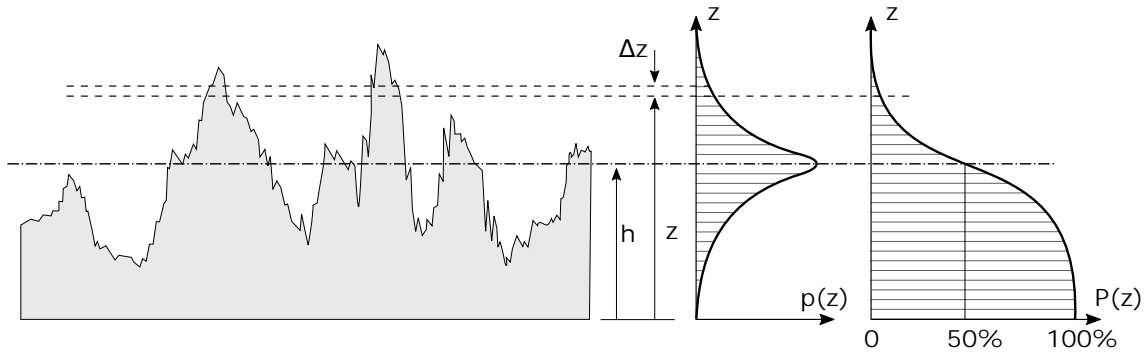


Figure 2.11: Profile of a surface shown as the profile height distribution  $p(z)$  and cumulative height distribution  $P(z)$  [204].

Bearing ratio parameters for surface roughness are described in Figure 2.12. The blue line crosses the vertical lines at 0% and 100%. Core roughness depth ( $Rk$ ), peak ( $Rmr1$ ) and bottom ( $Rmr2$ ) material ratios are determined from the crossing points and reduced peak height ( $Rpk$ ), reduced valley height ( $Rvk$ ) are defined accordingly. The same descriptions are applied to primary and waviness profiles of surfaces [8].



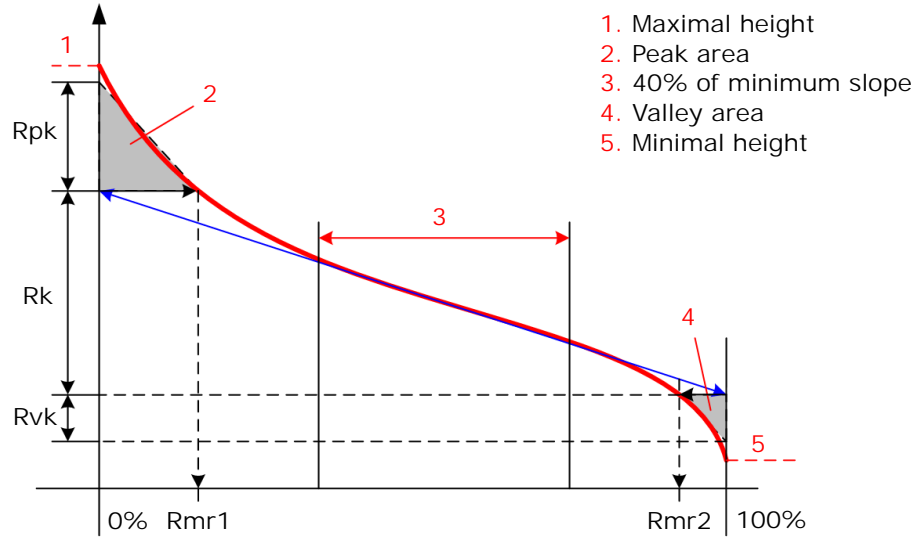


Figure 2.12: Description of bearing area parameters [8].

On the topic of topography measurements, four types of dimensional definitions are important to mention. Based on 2D projections and 3D grain shapes, aspect ratio, projection area, convexity and sharpness are highly useful to define the geometric measurements [61,99]. Aspect ratio is the ratio of the major to minor grain diameter for the description of the grain elongation. Grain convexity is used to determine the grain strength, abrasive potential and shape irregularity. Convexity is defined as the ratio of the idealized grain dimensions stretched across the projection area to the projected grain area. The fourth definition is the sharpness, which is a measure used to characterize the degree of penetration of an abrasive grain and was defined by De Pellegrin [62]. It was denoted as the ratio of the groove and projected penetration areas and related to particle orientation.

On the topic of modeling of diamond wires, available studies include only the grain protrusion heights and assume conical grain shapes [52, 145, 221, 224] with identical tip angles. Chung [54] developed a 2D numerical abrasive distribution model to determine the influence of abrasive interval. Further, a geometric wire model was developed by [52] where the randomly distributed diamond grains were modeled as conic shape of normally distributed sizes. Effects of diamond grain distribution on material removal was investigated by [53] through numerical simulations. Using the same wire model, at different wire speeds and feed rates, grit depth of cut was investigated by [51]. A cutting model based on FEM was presented by Wu [224]. The stress on the single diamond was analyzed and stress deformation of single diamond particles in the cutting area was calculated. Through theoretical calculations and FEM, Wu [227] compared the cutting forces generated by a spherical and a Vickers indenter in sc-Si scratching. For the measurement of diamond wire topogra-

phies, Lee [134] introduced a quick measurement system of diamond wire protrusion measurements where image processing methods were applied and diamond height distribution was measured.

## b Modeling of Process Forces

Pioneer research on the measurement of process forces and specific cutting energies date back to 50's in machining of metals [22] in the same era when a force model was introduced by Kienzle [109] for turning, based on the cross-sectional area of the undeformed chip thickness. A modified version of the approach was proposed where the forces are calculated through the experimentally determined specific cutting force  $k_c$  and width and depth of the undeformed chip [19]. A typical form of Kienzle equation is given as:

$$F_c = k_{c1.1} \cdot b_{cu} \cdot h_{cu}^{1-m_c} \quad (2.4)$$

where  $F_c$  is the tangential cutting force,  $k_{c1.1}$  is the specific cutting force required to remove a chip of width  $b_{cu} = 1 \text{ mm}$  and depth of  $h_{cu} = 1 \text{ mm}$ ,  $b_{cu}$  and  $h_{cu}$  are the cut width and undeformed chipping thickness or grain penetration depth respectively and  $m_c$  is a constant depending on the process and material pair.

However, experimental validation of the process forces and chip parameters is limited due to the nature of tool-workpiece contact in abrasive removal processes. For this reason, single grain scratch tests are widely applied to construct force models to correlate the grain geometry and the resultant process forces [22, 157], reviewed in Section 2.3.

On the topic of force modeling in diamond wire sawing process, an analytical static normal force model considering feed rate, wire saw velocity, rotation speed and wire tension as the input parameters was proposed by Li [137] and a numerical sawing force predicting method was introduced by Wang [221] for diamond wire sawing of SiC. An analytical cutting force and a depth of cut model was developed by Liu [145] for resin bonded wire sawing. The diamonds on the wire were modeled as conical grains of sizes with Gaussian distribution. Elasticity of the resin bonding was taken into account.

### 2.4.3 Tool Wear and Approaches in Wear Modeling

Wear is defined as “the progressive loss of material from the surface of a solid body due to mechanical interaction i.e. the contact and relative motion against a solid, liquid or gaseous counterbody” in DIN 50320 [1]. However, this broad definition considers the phenomenon in the spectrum of abrasive wear to sliding wear. A more solid definition of wear was given by Bhushan [27] as “the amount of volume loss and state of the wear surface”. In this part, the wear phenomenon is covered by focusing on the abrasive tool wear. Modeling and investigation of wear is handled in the context of wear of the diamond and also includes the research work on abrasive grains and single- and multiple- point cutting tools.

The understanding of wear progress and its mechanisms is crucial for the prediction of process outputs. Tool wear may lead to dimensional changes or secondary problems such as vibrations; moreover the created wear debris may lead additional damages in the system if not removed properly [70]. It is generally accepted that wear depends on load, speed, temperature, time, contact geometry, surface roughness, lubricant characteristics and material surface compositions [27]. Uetz [211] remarked that the wear resistance is not a characteristics of a single material but a combined effect resultant from the velocity and thermal condition on the three media as the base body, counter body and intermediate matter.

Tool wear, either in single-point or abrasive removal processes, occurs in combination [16] and several wear mechanisms may be present in wear of sliding surfaces: mechanical wear such as adhesive, abrasive, fatigue and impact which are induced by deformation and fracture; chemical or corrosive wear due to chemical reactions in the contact zone; and thermal wear due to thermal stresses, where high temperature and frictional heating are present [27, 28, 105, 141, 201]. It is also important to realize that the wear modes may be the product of more than one wear type [105] and dominant wear mechanisms can differentiate in different operating regions [27]. Tool wear may also be related to the material removal mode [238].

Yoshikowa [241] classified grinding wheel wear as attritious and fracture wear. Attritious wear is the result of the physical and chemical interaction between the abrasive grain and work material, leading to wear flats and increased forces and high levels of fracture at the end. Fracture wear results in micro- and macro- breakouts from the abrasive grain surface. A further wear mechanism is the grain pullout, the result of a mismatch between the toughness of the grain and bonding strength. When the bonding strength is low, the abrasive grain is pulled out before reaching the end

of its lifetime, resulting in a total break-out and efficiency loss in the process [99]. Types of abrasive grain wear are presented in Figure 2.13.

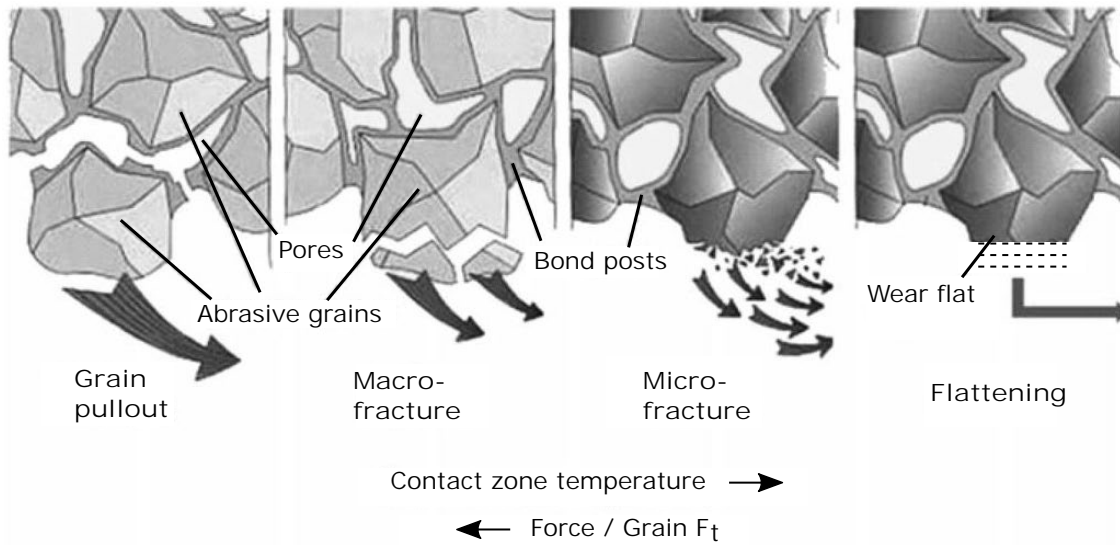


Figure 2.13: Wear modes in abrasive tools based on force and temperature. Temperature is increasing towards right and force on single grain is increasing towards left [99].

Takeyama [201] investigated the mechanisms of flank wear in turning and classified it in two types as mechanical abrasion which is proportional to the cutting distance and independent of the temperature and physico-chemical wear which is associated with the temperature in the cutting zone. When cutting temperatures are low or cutting conditions are mild, mechanical abrasion is dominant. Kramer [119] also stated that mechanical wear is predominant in lower temperature and chemical stability of the tool determines the wear resistance at higher temperature values.

In abrasive grain wear, mechanical abrasion is highly correlated with the geometry, hardness and distribution of the abrasive grains and directly correlated with the cutting length; while diffusion wear is a physico-chemical effect and interrelated with the temperatures in the cutting region [16,185,201]. De Pellegrin [62] suggested that the degree of wear is correlated with the shape of the abrasive grain. Matsuo [156] stated that the wear of superhard abrasive grains against various hard materials vary linearly with increasing distance and the wear volume is proportional to load. Gahr [70] concluded that the wear of a single abrasive is proportional to the sliding distance and applied force and Kramer [119] determined the abrasive wear volume is dependent on the sliding distance and hence proportional to the cutting speed. Malkin [149] found that the wear flat area is directly related to the grinding forces.

The wear of diamond was investigated by Crompton [59] when it is rubbed against a softer material; and stated that the rate of wear is mainly dependent on the hardness of the second member. It was told that the rules of wear are obeyed when the workpiece material hardness is over a critical value; and below this value there is an induction period where the diamond shows no apparent wear. With a sufficient hardness value, the diamond reaches the fracture stress and the wear becomes visible. Shaw [185] also pointed out that the hardness of the contacting parts are of prime importance in abrasive wear.

Tönshoff [210] concluded that the separate engagement of the kinematic cutting edges results in wear of the grinding wheel. Yu [242] explained that grains with higher protrusion will take the initial overload and lead to failure. After the high protrusion grains are worn down, local stresses are redistributed to the grains in the zone, resulting in a steady wear behavior. He studied the wear in nickel electroplated CBN grinding wheels. Two wear types were identified as grain pullout and attritious-fracture. Through the topographic study of wheel wear it was found that the grain protrusion height distribution transforms from a normal distribution to a bi-modal distribution. Electroplated layer strength was evaluated by applying quasi-static load on a grain to determine the residual strength of the grain-wheel interface. Aurich [18] explained that in electroplated grinding wheels, with the progressing grain wear, number of kinematically active grains increase, which causes a decrease in chipping space. Higher number of grains are distributed more evenly and irregular engagements limit prediction of the process behavior.

During mechanical removal, the biggest share of the energy input is transformed into thermal energy and distributed on the tool, workpiece, chip, coolant and surroundings [210]. Experimental research proves that 95% of the energy dissipation happens in the top 5  $\mu m$  of the bodies in contact [108] and it is mainly agreed that almost all of the energy dissipation through friction is transformed into heat [211] even though there are disagreements on the mechanism of energy transformation [27]. Highest temperature occurs at the contact between the peaks and asperities of the surface and local peak of the abrasive grain are of short duration and called the flash temperatures [12]. The temperatures can be as high as 1000°  $C$  and may last as long as the contact is present that could be less than 10  $\mu s$  [27]. Measurements of temperatures are based on heat conduction or heat radiation [209].

Due to the high complexity of wear, it is difficult to develop precise models to predict the wear behavior. The phenomenon is usually neglected or simplified to macroscopic tool wear such as volumetric and geometric loss [27, 120]; and studies mainly focus on the dominant wear mechanisms only. An important parameter

used for quantitative description of wear in grinding tools is the grinding ratio  $G$  is defined as:

$$G = \frac{V_w}{V_t} \quad (2.5)$$

where  $V_w$  is volumetric workpiece wear and  $V_t$  is the volumetric tool wear [222].

It has been more than a century since the famous empirical wear equation was introduced by Taylor [203]. Since then, enormous number of scientific and industry origin work had been reported from the viewpoint of mechanical, chemical and/or physical effects, but wear models still contain uncertainties and broad assumptions; or are based on empirical data [141]. On the other hand, lack of empirical wear laws makes it impossible to define a universal wear coefficient in the sense of defining a coefficient of friction or Young's modulus [44].

A primary issue is the quantification of wear in modeling. It is usually parameterized with the wear rate, which is the wear volume per unit distance and the specific wear rate which is defined as the wear rate per unit load [27]. Several other variables were used in models for wear quantification i.e. wear volume, wear coefficient, normalized wear rate and mass loss. Some of these parameters are seldom used, however it shows how the research on wear modeling is varying in the way it is quantified [176], similar to the high scatter in wear rate data obtained in the experiments [217]. Here, it is useful to comment on the wear coefficient, a term frequently used in modeling. There are several interpretations of the true meaning of the wear coefficient. Meng [159] suggest the definition as the probability that a loosened particle will leave the system. Rabinowicz [174] explains it as the probability of a wear particle occurring in a number of particular events or average number of events required for the occurrence of a wear particle. It can also be explained as the measure of the efficiency of material removal [248]. Another definition by Hirst [86] suggests that it is related to the number of small encounters necessary to develop a strain pattern beneath the surface.

Several wear models based on different approaches were suggested i.e. finite element models, statistical models where no physical parameters are considered and differential models where time dependent wear is modeled [120]. Attanasio [16] developed an analytical 3D finite element model that takes the diffusive wear mechanism into account, using a modified wear model from Takeyama [201] for the prediction of tool wear in metal cutting. Li [139] studied the bonding force in electroplated

CBN grains through FEM and analyzed for different grain orientations and bond thickness. Jacobson [100] studied the abrasive wear through a numerical simulation model. Abrasives grains were defined as a function of the tip radius and cone angle and grain-workpiece contact was simulated by successive grooving. Distribution of the grain protrusion heights and deviation of an individual grain protrusion from the average value were applied as the model variables and a statistical-based dimensionless wear equation was derived. Hagiwara [80] pointed out that the grain edge fracture characteristics has direct influence on edge formations and grain cutting ability. Proposing ten edge models, the grain edge fracture and grain shape transition were studied by employing the Markov process, simply meaning that the time-homogeneous probability of the edge shape fitting to a specific model after  $(n + 1)^{th}$  event or fracture depends only on the edge shape after  $n^{th}$  event.

Reviews of and surveys on wear models are available in the literature [105, 159]. In his work, Meng [159] reviewed over 300 models and pointed out the discontinuity and slow progress in wear modeling. Moreover, the lack of a common language and the mismatch in definitions in wear research were mentioned; and the wear models are categorized as empirical, contact-based and material-failure mechanism based.

One of the first contact-based constitutive wear equations was established by Holm [87]. He considered the wear as an atomic process and suggested that the wear volume is directly proportional to the sliding distance, number of atoms removed per atomic encounter (or probability of removing an atom) and normal pressure; and inversely proportional to the flow pressure of material. Holm assumed the removal as individual atoms, however Burwell [44] stated that a large part of it is removed by large aggregates of atoms. Further, Archard [11] replaced the concept of removal of atoms by removal of wear particles and formulated the equation for abrasive wear, where the wear volume is formulated as directly proportional to the sliding distance, pressure and inversely proportional to the hardness of the worn material.

$$V_t = K \cdot \frac{\sigma_t \cdot L_s}{H} \quad (2.6)$$

where  $V_t$  is the wear volume,  $K$  is the wear coefficient,  $\sigma_t$  is the load normal to the wear surface,  $L_s$  is the sliding distance and  $H$  is the hardness of the softer material. Archard [13] later stated the laws of wear:

1. The rate of wear is reproducible and total wear is proportional to the sliding distance.

2. The rate of wear is independent of the apparent area of contact and related to the true area of contact.
3. The wear rate is proportional to the load if the surface conditions are identical.

The influence of the cutting temperatures were considered by Takeyama [201] assuming the average temperature affects the wear mechanism. The total wear rate was suggested to be a combination of the abrasive wear as the effect of cutting distance and physico-chemical wear which is dependent on the activation energy and absolute temperature, an approach governed by the Arrhenius law of diffusion. The equation was expressed in the form:

$$\frac{dW}{dt} = K \cdot e^{\left(\frac{-E_a}{R_g \cdot T}\right)} + W_a \quad (2.7)$$

where  $dW/dt$  is time dependent wear,  $K$  is the wear coefficient,  $E_a$  is the activation energy,  $R_g$  is the universal gas constant,  $T$  is the temperature and  $W_a$  is the abrasive wear term dependent on the feed rate and cutting speed.

Based on the adhesive wear model by Shaw [186], Usui [212] delivered a wear model for crater wear of carbide tools, considering the normal contact stress, chip temperature and cutting speed, based on orthogonal cutting conditions. The time-dependent wear was expressed as:

$$\frac{dW}{dt} = K \cdot \sigma_t \cdot v_c \cdot e^{\left(\frac{-B}{T}\right)} \quad (2.8)$$

where  $K$  is the wear coefficient,  $\sigma_t$  is the contact stress,  $v_c$  is the cutting speed,  $T$  is temperature of the chip and  $B$  is a constant which is functionally the same as  $E_a/R_g$  in Eq. (2.7), considering the thermal softening, diffusion of wear asperities into the workpiece and probability of occurrence of a wear particle [125]. Kitagawa [116] applied the crater wear equation to flank wear of tungsten carbide tools in turning plain carbon steels and reported that the wear equation holds for the flank wear as well. Later, Maekawa [148] successfully simulated the flank wear using the developed model. A chemical dissolution wear model was integrated by Kramer [119] into the abrasive wear model defined by Rabinowicz [175].



In his study on the influence of the sliding speed on wear of diamond-like carbon coatings, Jiang [104] later interpreted the Archard wear coefficient and through regression analysis, suggested that the sliding speed is negatively correlated with the volumetric wear rate:

$$W = K \cdot \frac{L_s \cdot F_c}{v_c} \cdot e^{\left(\frac{-E_a}{R_g \cdot T}\right)} \quad (2.9)$$

Despite the differences in diamond wires and grinding wheels, the performance of both depend on the abrasive grains from which they were manufactured. On the topic of bonding, the bonding strength and volumetric proportion are critical as well as type of the bond, where in electroplated abrasive tools, a single layer of abrasives are attached on the tool surface unlike bonding types i.e. metal or vitrified in which it is possible to have multiple layers of abrasive grains on the tool. This results in a varying cutting performance during the wire lifetime [114].

A few number of studies were reported on diamond wire wear observations and modeling. Through diamond wire sawing experiments, Kumar [121] presented some instances of grit fracture and pullout, while mentioning blunting of diamonds. Lee [134] stated that for the abrasive grains to reach a higher cutting performance, it is important how rapidly the filler material is worn out and the grains are exposed. Kim [112] modeled the diamond wire wear using spherical abrasive geometries. It was stated that the diamond wire wear can be defined in two regimes as the rapid diamond wear and drop in the contact pressure as a result of increased contact between the wire and workpiece.

Up to now, no process models of diamond wire sawing process have been developed that handles the process as a whole considering the wire and abrasive geometry, process kinematics, process forces, temperatures in the cutting zone and tool wear. Available research lacks the realistic grain modeling which is a key element in process kinematics and do not consider the change in grain geometry through the wire lifetime. Moreover, no wear model had been suggested where the effect of temperatures are considered. It is clear, a all-around process model for the diamond wire sawing is required for the prediction of process outputs such as the surface quality, process forces and tool wear.

# Chapter 3

## Research Gap

The review of available research on the scientific aspects of the diamond wire sawing process the literature review shows that the understanding of the geometric identities of the diamond wire is limited due to the lack of information on abrasive grain properties and only preliminary work is available on the determination of the wire and abrasive grain characteristics. Abrasive grain wear in the wire sawing process is yet to be investigated and no experimentally verified model is reported on the phenomenon. Moreover, the diamond wire wear progress and the limits of abrasive lifetime are to be defined. Available studies lack the investigation of the resultant Si surface appearance generated with wire speeds higher than 30 *m/s* and there is no quantitative understanding of the sawn Si workpiece quality in terms of brittle and ductile removal. Measurements of process forces also have not yet been carried out for such a speed range. The process modeling was handled rather by simple grain geometries and not considering the influence of different wire properties. Understanding of the diamond wire sawing process on the single grain level is limited. The influence of temperature and forces on the single grain are lacking.

The objective of the thesis is to develop a profound understanding of sawing sc-Si with electroplated diamond wire through analysis, experimentation and modeling of the wire, workpiece and process. The primary objectives of the presented work are:

1. To develop quantitative parameters for the evaluation of electroplated diamond wires.
2. Investigate the sawing process in terms of material removal, wire wear, surface quality and process forces, beyond current process limits i.e. wire speeds over 30 *m/s*, where better surfaces and lower tool wear are possible.

- 
3. Determine the influence of primary process parameters and their influence on the process outputs.
  4. Develop relevant models of the wire and abrasive grains, grain flash temperature, material removal, process forces and abrasive grain wear so that prediction of the process behavior becomes possible.

Investigations on diamond wire sawing of silicon can be divided into the fields concerning the diamond wire as the wire characteristics (micro- and macro- features) and their influence on the process including the wear behavior; material removal mechanisms and the resultant workpiece surface quality; process force behavior; modeling of the process and its elements; and the grain-workpiece interaction on single grain level. A modular process model shall be developed that includes the tool, material removal, process forces and wear models.

For this purpose, analytical tools are developed to characterize the wire and abrasive grain properties and the resultant workpiece surface. Two novel experimental setups are developed to investigate the material removal, tool wear and the process at single grain level. The Wire Wrapped Grinding Wheel setup aims to investigate the process up to the wire speed of  $75\text{ m/s}$  with the analysis of the Si surface, process forces and wire wear while providing the possibility of monitoring identical diamond grains throughout their lifetime. The Scratch Test Setup is developed which aims to investigate the grain-workpiece interaction at single grain level concerning the material removal, forces and temperatures in the cutting zone. Two proprietary software tools are developed for a detailed understanding of the wire topography and diamond grain properties; and resultant workpiece surfaces from the viewpoint of brittle-ductile material removal. The kinematic-geometric process model, stochastic-geometric wire model, material removal model, force model, grain flash temperature model and grain wear model are developed and validated.

The dissertation is structured in nine chapters. In the introduction, a review of the photovoltaic industry including the history and commercial aspects are presented. An overview of the technological and aspects of the wire sawing, silicon and diamond wire are given. Chapter 2 covers the available work on wire sawing technology and diamond wire sawing process including the tool and material, literature on material removal in brittle materials and ductile to brittle transition, a review on grain scratch tests and studies on modeling and simulation of abrasive processes concerning the process characteristics, material removal and abrasive grain wear. Following the literature review, in this chapter, the research gap is identified to guide the rest of the work. Chapter 4 is divided into two main sections as experimental setups

and analytical tools. Primarily, two novel setups are detailed and further software tools that are developed for the characterization of diamond wires and Si workpiece surfaces are introduced in detail. Information on measurement tools and systems are also given in this chapter. Chapter 5 covers the evaluation of diamond wire and abrasive grain properties and process behavior of several wire types. The influence of process parameters on the Si workpiece surface are discussed via additional experiments. The chapter doesn't include simulation experiments and is limited to the experiments for the evaluation of wire and process behavior characteristics. In Chapter 6, the kinematic-geometric process model covering the process kinematics, stochastic-geometric tool model, workpiece model, material removal model and force model and their validation. Chapter 7 includes the description and validation of the wear and temperature models. In Chapter 8, the general simulation scheme is defined and the simulation results of surface removal and diamond wear based on single grain interaction are presented and discussed. Chapter 9 covers the conclusion and outlook.

# Chapter 4

## Experiment Setups and Methods

*“Life can be much broader once you discover one simple fact and that is everything around you call life was made up by people that were no smarter than you.”*

— Steve Jobs,  
*Secrets of Life, 1994*

In this chapter, the experimental setups, developed software tools and only the measurement and sampling methods used in the study are introduced. Initially, the experiment setups are discussed and following, proprietary software that are developed for the analysis of diamond wires and Si surfaces are detailed. Finally, the sampling methods and measurement tools are defined.

### 4.1 Experiment Setups

The investigation of the grain-workpiece interaction requires measurement of the resultant workpiece surface, abrasive grain wear, process forces and thermal interactions in the contact zone. To realize this, it is essential to developed experiment setups, where the process elements can be isolated, monitored and the outputs can be measured.

The two experimental setups named “Wire Wrapped Grinding Wheel (WWGW) Setup” and “Scratch Test Setup” (STS) are designed to investigate the wire sawing process through isolating specific interaction characteristics. In this section, the setups are studied in terms of their working principles and details of the process kinematics.

### 4.1.1 Wire Wrapped Grinding Wheel Setup

The wire sawing process shall be measured beyond the process capabilities of today's commercially available wire saws. Above the available wire speeds of 25-30  $m/s$  better surfaces with higher ductility and lower abrasive grain wear is possible. However, dynamic limitations of the wire web and the machine as well as the requirement of long wire lengths for wire acceleration restrain the realization of high wire speeds. Moreover, performing wire wear experiments require high workpiece and wire consumption. Quick-wear tests are commonly used in such cases to reduce the material, time and labor consumption [212]. Further, in the case of wire sawing, identification of the identical grains is not possible due to the involvement of long wire lengths. These points can be realized with the combination of wire sawing with other process technologies such as grinding.

The WWGW setup is a novel-design experimental setup for the quick-wear test of diamond wires, where monitoring of the identical grains through their lifetime is possible with the investigation of diamond and wire wear, resultant workpiece surface and process forces at high cutting speeds. Overview of the setup is given in Figure 4.1 and dimensions of the elements are given in Figure 4.2.

The setup is prepared on a Rollomatic Grind Smart 628 XS 5-axis grinding machine and composed of an aluminum wheel with the wire wrapped around its helically grooved cylinder mantle surface and a concave silicon workpiece with a diameter equal to that of the wheel. The diamond wire is fixed at both ends to minimize relative movement between the wire and the wheel. The force measurement system is composed of a Kistler MiniDyn Type 9256C1 3-component force sensor, Kistler Type 5080A charge amplifier, National Instruments NI 9222 analog-to-digital converter and a measurement laptop with Labview software. Tap water is applied as cooling agent with a fixed flow rate of 4.3 *liter/min* in all experiments.

The similarities and differences of the WWGW process to that of wire sawing can be stated as follows:

1. The WWGW setup can emulate long grain-workpiece contact lengths in wire sawing process, with a contact length of 65 *mm*.
2. Wire speeds up to 75  $m/s$  (10'000 *RPM*) are possible, whereas wire saws have typical wire speeds of 15 to 25  $m/s$ .

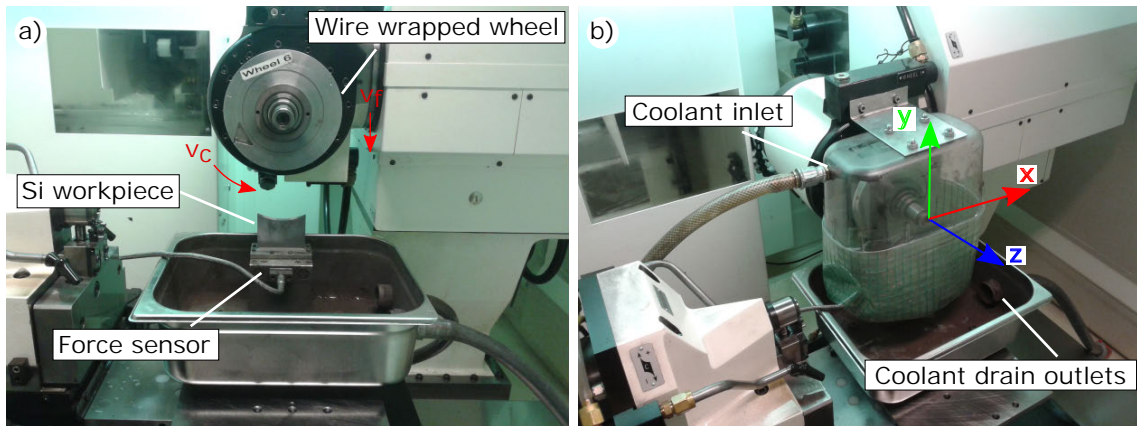


Figure 4.1: Overview of the Wire Wrapped Grinding Wheel experimental setup: (a) open mode and (b) operation mode.

3. In the WWGW setup, an aluminum wheel supports the wire, resulting in a stiff contact between the two elements, while a wire bow prevails in sawing.
4. In the wire sawing process, the wire has three degrees of freedom (two translational and one torsional); whereas in the WWGW process, the wire is fixed on the wheel groove and its motion is limited to the cutting direction.
5. The resultant surface in the WWGW setup is the workpiece surface below the wire, which corresponds to the kerf front in wire sawing. A study of material removal characteristics and resultant silicon surface properties is required.

Geometries of the wheel and the Si workpiece are presented in Figure 4.2, where wheel dimensions and a close-up view of the wheel grooves and the dimensions of the Si workpiece are given.

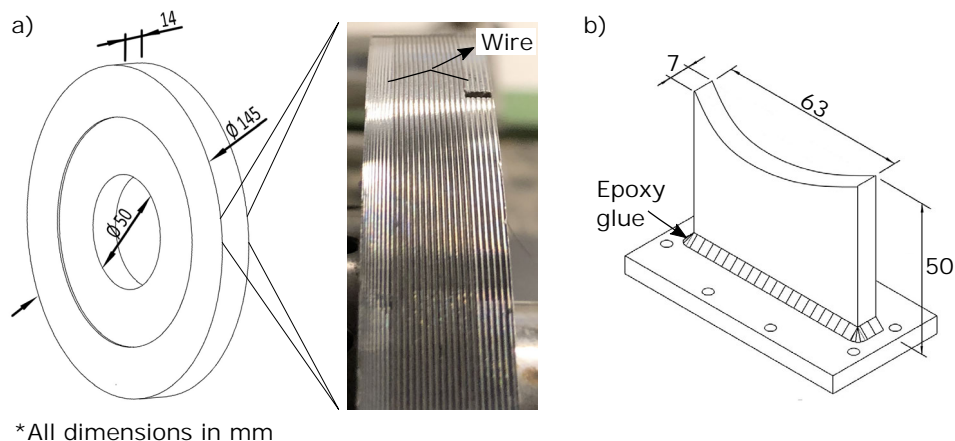


Figure 4.2: (a) Wheel dimensions and close-up view of the wheel grooves and the wrapped diamond wire. (b) Dimensions of the Si workpiece.

The parameters necessary to describe the kinematics of the WWGW setup are introduced in Figure 4.3. The schematic of the workpiece is given in Figure 4.3a. The wheel travels in the feed direction  $-y$ , towards the pre-shaped workpiece with a diameter  $d_{wp}$ , which is equal to the wheel diameter  $d_s$ . The removal width of one wire wrap is indicated by  $b_f$  in red color. Figure 4.3b shows the view on the mantle surface of the aluminum wheel where the diamond wire is wrapped along the helical grooves on its side surface. In Figure 4.3c, the unwrapped, opened wire with a length of  $L_{dw}$  is represented in blue color and wheel circumference  $C_{wheel} = \pi d_s$  is shown. The position of an arbitrary point  $P$  on the wire surface and its corresponding path on the workpiece surface are indicated. Both elements are visualized on 2D plane and the dimensions are highly distorted for easier visualization.

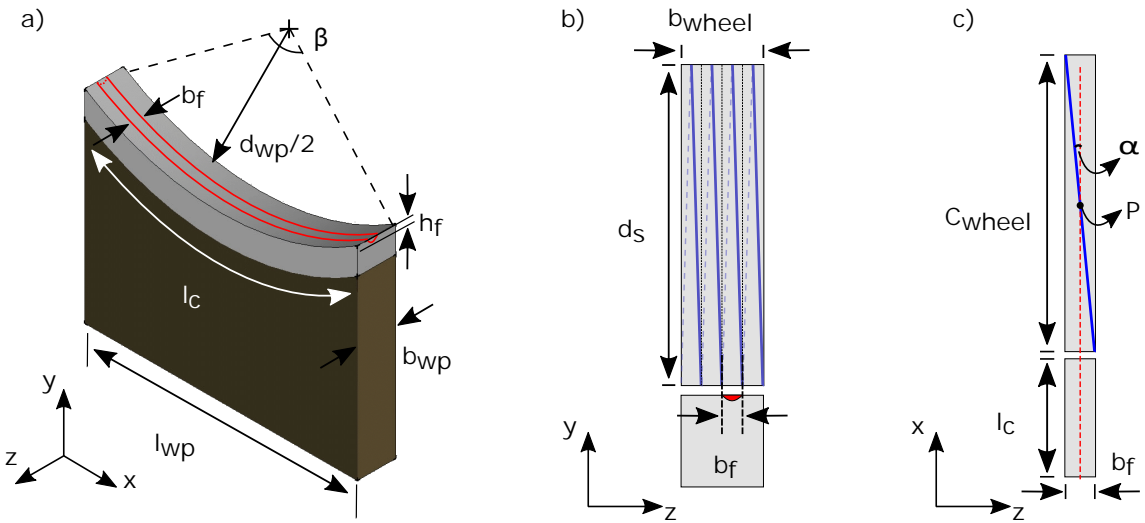


Figure 4.3: (a) Details of the wire-workpiece contact. Path of wire wrap on the workpiece contact length. (b) The view on the mantle surface of wheel workpiece contact. (c) View of the open-unwrapped wire and contact path of wire section on the workpiece.

### a Wire-Workpiece Contact Geometry

Contact geometry of the wire and the workpiece surface are given in Figure 4.4. In Figure 4.4a, the wheel is rotating around the  $z$  axis with wire speed  $v_c$  and removes material from the concave surface of the workpiece with a rate equal to the feed rate  $v_f$ . Line  $A - A'$  is passing through the middle of the workpiece surface which is the lowest position on surface on the  $y$  axis. In Figure 4.4b an open wire with the length  $L_{dw} = \pi d_s$  is represented with blue color and the cut (removed) and uncut (new) workpiece surfaces are colored with light and dark gray. The figure is plotted from the viewpoint of an observer looking at the surface from a location in between the wheel and the wire, and the projection of the wire on the workpiece surface is visualized. The wire wrap angle  $\alpha$  measures the angle between the wire centerline



and the cutting direction in  $x$  axis. In the ideal case of both wheel rotation and feed cease at the same moment of time, a surface is obtained as shown in Figure 4.4b.

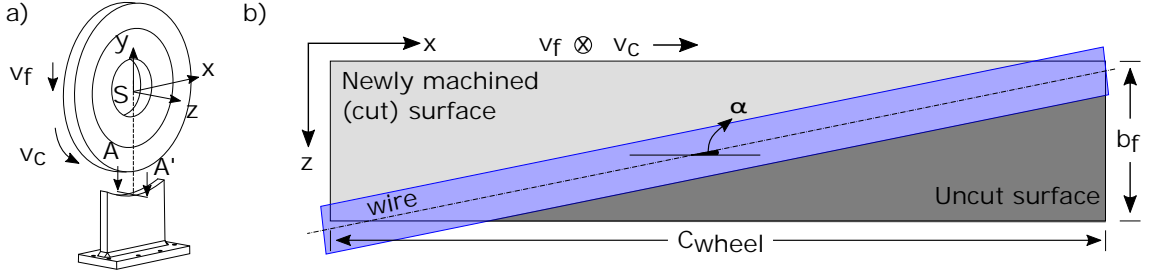


Figure 4.4: (a) Position of the wheel and silicon workpiece and line  $A - A'$ . (b) Position of wrapped wires and cut-uncut surfaces.

Cutting paths of diamond grains are shown in Figure 4.5a where the top view of the workpiece surface is presented. Each of the cutting paths in the cutting direction can be attributed to a diamond grain that is on the active surface of the wire. The roughness profile of the workpiece section  $B - B'$  is shown in red color in Figure 4.5b. Surface waviness profile, given in blue color shows that each wire wrap is machining a groove-shaped geometry on the workpiece surface which corresponds to the width  $b_f$  and has a depth of  $h_f$ . The geometry of the groove can be defined as a function of the wire geometry, wire wrap angle and wheel diameter.

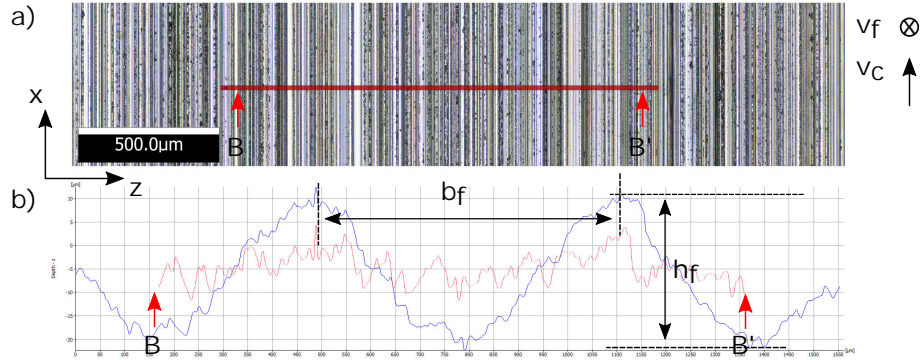


Figure 4.5: (a) Top view of the workpiece surface. (b) Cross-section of line  $B - B'$  with primary and waviness removed surface profiles.

Top view of two adjacent wheel grooves is given in Figure 4.6a where  $C_i$  and  $C_{i+1}$  indicate the center of the wire section. Position of two adjacent wires at  $A - A'$  are shown in Figure 4.6b. The removal width  $b_f$  is measuring  $600 \pm 10 \mu m$  and can be expressed as:

$$b_f = L_{dw} \sin \alpha \quad (4.1)$$

where  $\alpha$  is the wire wrap angle resultant of the helical wheel grooves and  $L_{dw}$  is the length of one wire wrap.

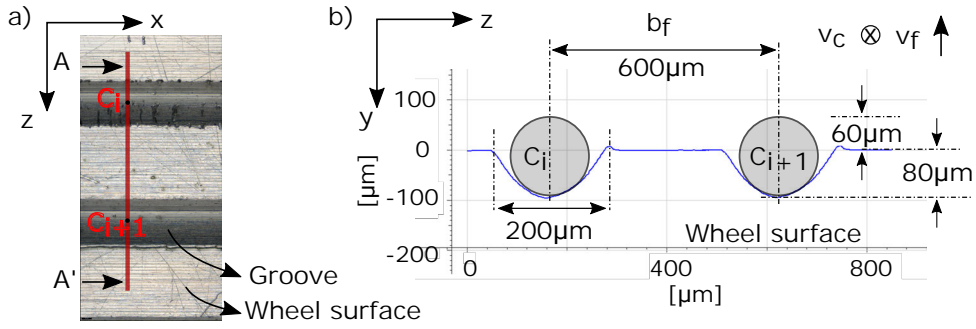


Figure 4.6: (a) Top view of wire grooves. (b) View of cross-section  $A - A'$ .

The cross-section of the wire on the  $y - z$  plane is orthogonal to the direction of cutting speed and is shown in Figure 4.7. The active wire angle  $\varphi$  indicates the kinematically active wire surface effective in material removal. The wire cross-section is not symmetrical with respect to the vertical line passing through the center, since the wire is rotated by angle  $\alpha$ . The value of  $C'_i - C_i$  denotes the distance between two consecutive wire cross-sections.

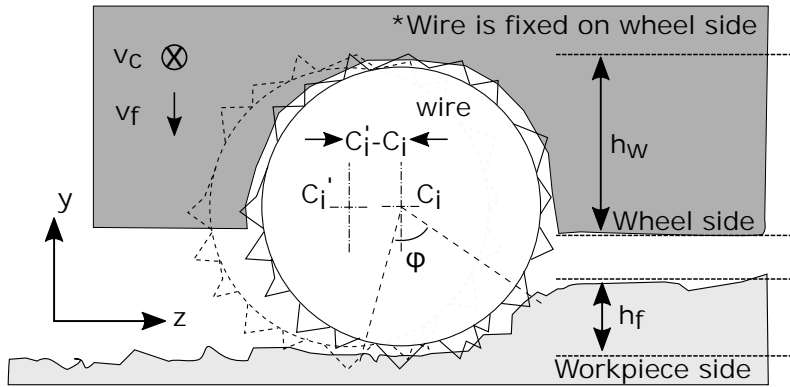


Figure 4.7: Projection of the wire section on the cutting plane  $y - z$ .

## b Contact Length

The kinematic contact length  $l_{kin}$  is equal to the geometric contact length  $l_c$  given in Figure 4.3a and can be expressed as:

$$l_{kin} = \frac{d_{wp}}{2} \beta \quad (4.2)$$

where  $d_{wp}$  is the diameter of the concave workpiece surface and  $\beta$  is the angle of contact between the wheel and workpiece.

### c Grain Penetration Depth

Figure 4.8 shows the discrete motion of the point  $P_i$ . The point rotates by an angle step of  $\theta_s$  and advances towards the workpiece by feed per cutting edge  $s$ . Maximum depth of cut is observed when  $\theta_z = 3\pi/2$  or  $\beta = 0$  and shown as  $h_{i,cu,max}$ . The feed per cutting edge  $s$  is the product of the feed rate  $v_f$  and the time between successive cuts  $L/v_c$ , where  $L$  is the average distance between two kinematically active grains.

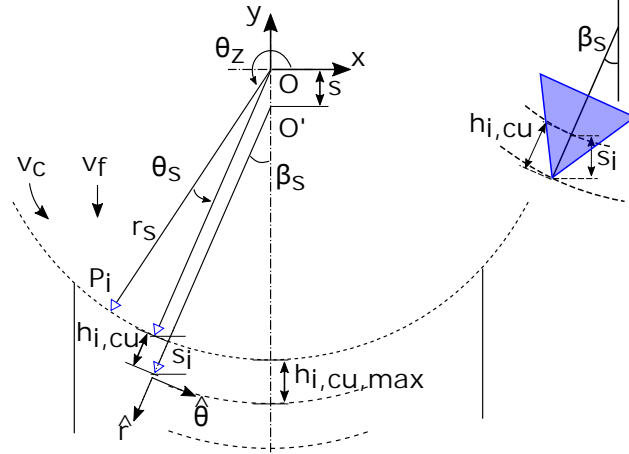


Figure 4.8: Feed per cutting edge and maximum chipping thickness.

For an individual grain  $i$ , it can be written that:

$$s_i = \left( \frac{L_i}{v_c} \right) v_f \quad (4.3)$$

where  $L_i$  is the distance between two subsequential kinematically active cutting edges  $P_i$  and  $P_{i+1}$ . The chipping thickness  $h_{cu,i}$  is always normal to the workpiece surface and is expressed as:

$$h_{cu,i}(\beta_s) = \frac{s_i}{\cos \beta_s} \quad (4.4)$$

The maximum chipping thickness for the  $i^{th}$  grain at  $\beta_s = 0$  can be expressed as:

$$h_{cu,i,max} = \left( \frac{L_i}{v_c} \right) v_f \quad (4.5)$$

Hence, the average maximum chipping thickness  $h_{cu,av,max}$  is defined as the average of the maximum chipping thicknesses of all kinematically active cutting edges.

$$h_{cu,av,max} = \frac{1}{N_{act}} \sum_{i=1}^{N_{act}} h_{cu,i,max} \quad (4.6)$$

where  $N_{act}$  is the total number of active abrasive grain edges on the wire.

#### d Specific Material Removal Rate

The specific material removal rate  $Q'_r$  is defined as the rate of material removal  $Q_r$  per effective grinding width  $b_D$ , which is the length of perpendicular projection of the active grinding wheel profile onto the axis of rotation of the grinding wheel in ISO 3002-5 [3].

$$Q'_r = \frac{Q_r}{b_D} \quad (4.7)$$

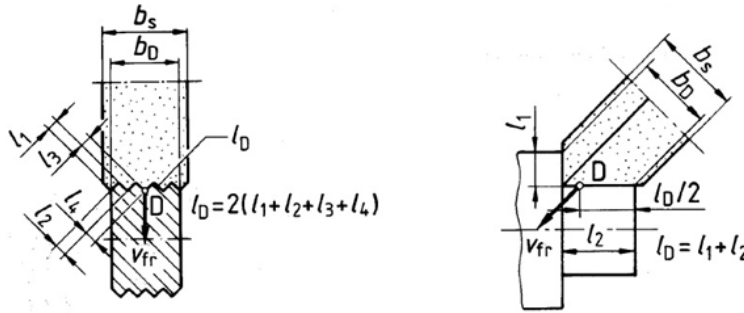


Figure 4.9: Active grinding width  $b_D$  according to ISO 3002-5 [3].

The material removal rate  $Q_r$  is the volume  $V_w$  of material removed per unit time  $\Delta t$ .

$$Q_r = \frac{V_w}{\Delta t} \quad (4.8)$$

and

$$V_w = \frac{d_{wp}}{2} \cdot \beta \cdot h_f \cdot b_{wp} \quad (4.9)$$

where  $d_{wp}$  is the diameter of the concave workpiece surface,  $\beta$  is the angle of contact

between the wheel and the workpiece,  $h_f$  is the depth of removed material from the workpiece surface and  $b_{wp}$  is the width of the workpiece. Hence, the specific material removal rate  $Q'_r$  in the WWGW process then can be expressed as:

$$Q'_r = \frac{d_{wp}}{2} \cdot \beta \cdot v_f \cdot \frac{b_{wp}}{b_D} \quad (4.10)$$

where  $b_{wp} = b_D$  and  $v_f = h_f/\Delta t$ .

The correlation of the specific material removal of the WWGW process and wire sawing process requires further interpretations on the role of the active grinding width  $b_D$ . In the case of material removal with diamond wires, the active grinding width  $b_D$  can be correlated with the active wire section, which is indicated as  $\varphi$  in Figure 4.7. 330° images are constructed with Alicona IFM and is presented in Figure 4.10a. Two positions of the same wire are shown, where the differences in grain protrusion heights can be determined. Superposed wire cross-sections that are orthogonal to the wire centerline is given in Figure 4.10b. It is clear that the abrasive wear is present only on a section of the wire peripheral, resulting in a decrease in grain protrusion on that section. The active wire angle  $\varphi$  shown on Figure 4.7 and Figure 4.10b is measured as  $\pi/4$  for the WWGW process.

In the case of wire sawing process, higher degrees of freedom is present where the wire is free to move in torsional direction, resulting in a wear around the complete wire circumference. Due to this phenomenon, the active grinding width  $b_D$  is assumed to be equal to the diamond wire peripheral.

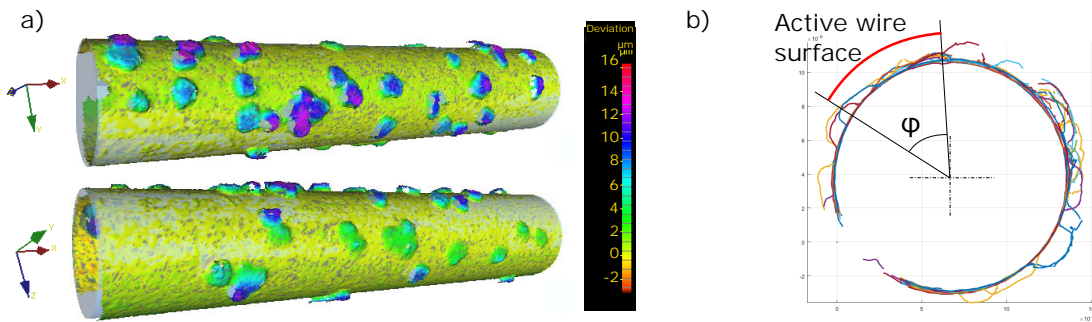


Figure 4.10: (a) 3D images of a wire used in WWGW process. (b) Superposition of the cross-sections orthogonal to the wire centerline of the measured profile.

A further correlation factor for the volume of material removal per unit length of diamond wire should be introduced for the comparison of the WWGW and wire sawing processes. Hence, the specific material removal volume per unit wire length  $V'_w$  can be written as:

$$V'_w = \frac{V_w}{L_t} \quad (4.11)$$

where  $V_w$  is the workpiece removal volume and  $L_t$  is the wire length. Additionally, an intensity factor  $I_{wire}$  is defined to compare the amount of wire employed to remove a volume of workpiece material and can be expressed as:

$$I_{wire} = V'_w \frac{2\pi}{\varphi} \quad (4.12)$$

where  $\varphi$  is the active wire surface angle equal to  $\pi/4$  for the WWGW process and equal to  $2\pi$  for the wire sawing process. Resulting from Eq. (4.12), the intensity factor  $I_{wire}$  increases with increasing material removal volume per unit wire length and decreases with increasing active wire surface.

### e Spindle Eigenfrequencies

The WWGW setup operates on a wide range of rotational speeds up to 10,000 *RPM* which makes it critical to determine the dominant spindle eigenfrequency, so that the cutting speeds exciting this frequency and multiplies of it can be avoided.

A measurement system composed of a LDS FocusII real-time signal analyzer, 3D accelerometers with a measurement limit of 100  $m/s^2$  and a measurement laptop with Vibrat software and a Kistler Type9722 impact hammer is used for excitation. The sensor locations and impact direction  $-y$  are described in Figure 4.11. The dominant rotational eigenfrequency is determined at 93 *Hz*, corresponding to a rotational velocity of 42.3  $m/s$  for the wheel radius of 72.4 *mm*.

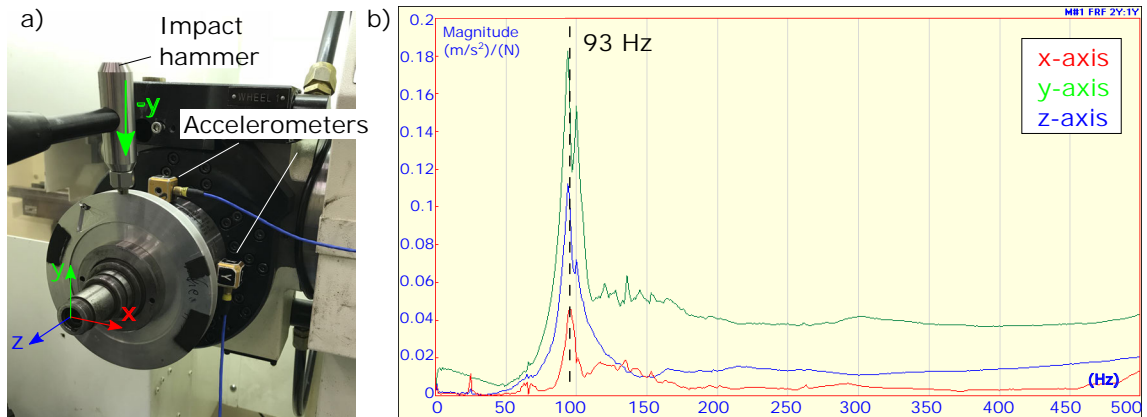


Figure 4.11: (a) Measurement locations and direction of the excitation. (b) Plot of the FRF of the excited frequencies.

### 4.1.2 Scratch Test Setup

The Scratch Test Setup (STS) is designed to conduct high speed grain scratching experiments with long contact lengths and measurement of process forces and flash temperatures in the cutting region. The overview of the experimental setup is presented in Figure 4.12a and details of the pin is shown in Figure 4.12b where the machine axes and position of the two-color fiber pyrometer are identified. The workpiece is rotating with an angular velocity  $\omega$  and the pin is stationary on the fixed diamond wire. The diamond wire is positioned and guided in a groove at the top of the aluminum pin and fixed at both ends. A single grain on the diamond wire is isolated at the top of the pin which has a tip radius of  $0.5\text{ mm}$ . In Figure 4.12c, a microscope image of the wire and pyrometer fiber are shown.

The setup is mounted on a Fehlmann Versa 825 5-axis milling machine and the force measurement system is composed of a Kistler MiniDyn Type 9256C1 3-component force sensor, Kistler Type 5080A charge amplifier, National Instruments NI 9222 analog-to-digital converter and a measurement laptop with Labview software. Temperature measurement system is composed of Fire-3 two-color fiber optic pyrometer. No coolant is applied.

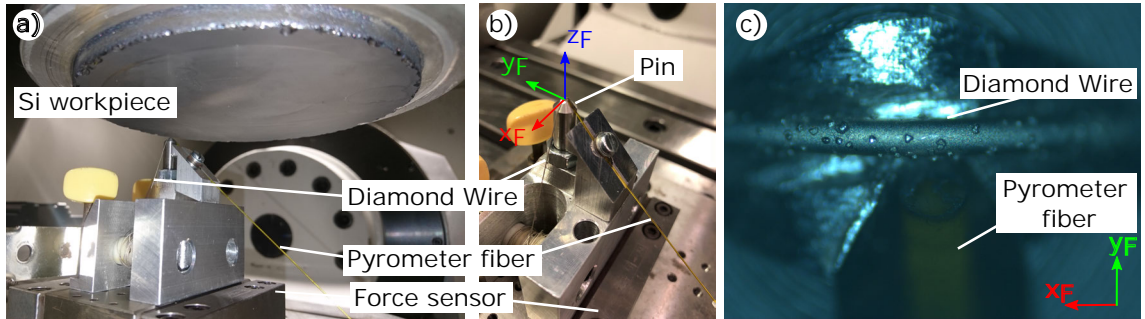


Figure 4.12: (a) Positions of the workpiece and single grain on the STS b) Details of the pin and the position of the wire. (c) Alicona IFM image of the isolated grain on pin tip and fiber of the pyrometer.

Cutting kinematics and axes are defined in Figure 4.13. The contact is described from the viewpoint of point  $P$  on the grain tip which is assumed to be moving over the cutting path instead of workpiece rotation. Both approaches represent the identical kinematic conditions, while the earlier serves simplicity of the explanation. The grain starts its motion with zero penetration at  $K$  and moves with an angular velocity  $\omega$  in counterclockwise direction. Grain is advanced onto the surface with the vertical feed rate  $v_{fz}$ ; and the radial feed rate  $v_{fr}$  denotes the distance  $C$  between two consequent scratches.



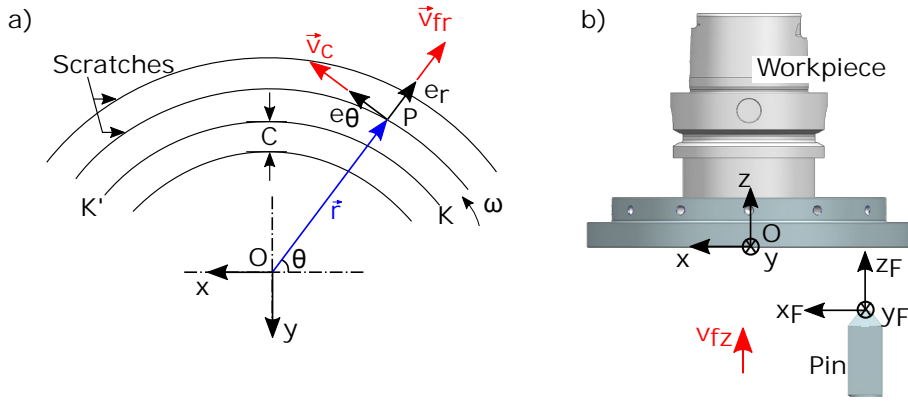


Figure 4.13: (a) Scratch paths on the workpiece surface viewed from the bottom of the workpiece. (b) Motion of the grain cutting edge.

Figure 4.14a shows the lapped and polished, mirror-like Si workpiece surface with a surface roughness value of  $R_z = 0.49 - 0.52 \mu m$ . In Figure 4.14b, an Alicona imaging of multiple scratches on the workpiece surface are presented. Each identified section shows passes by the same grain and consists of several consequent scratches. A continuous contact between the grain and Si workpiece is not possible, instead, a section of the surface is scratched where the contact length of one grain pass is  $4 cm$  and an average total contact distance of the grain is  $0.8 m$ . The cutting time is determined from the measured force signal.

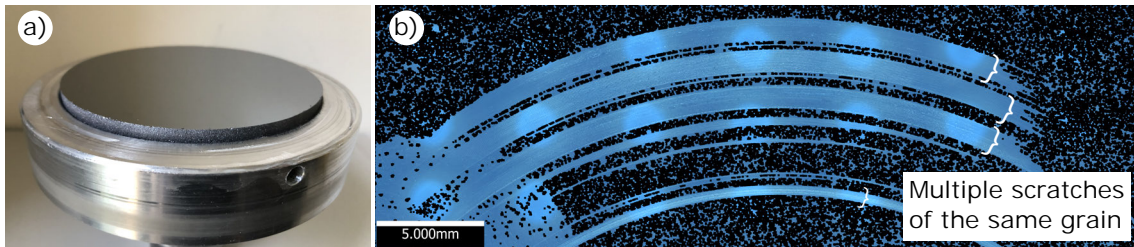


Figure 4.14: (a) Mirror-like surface of the SGT workpiece obtained through several lapping and polishing steps. (b) Scratched surface sections from several cuts.

Figure 4.15a shows top view of the Alicona IFM image of an isolated abrasive grain on the pin tip and Figure 4.15b shows the grain cross-sections normal and orthogonal to the cutting direction. The grain protrusion  $h_g$  is measured from the surface of the wire. The grain penetration depth of  $h_{cu}$  and cutting area  $A_{cu}$  are shown.

A section of multiple scratches by the same grain is given in Figure 4.16. The grain-workpiece contact starts from the lowest scratch. The transition from brittle to ductile material removal due to break-out from the abrasive grain structure can be clearly seen.



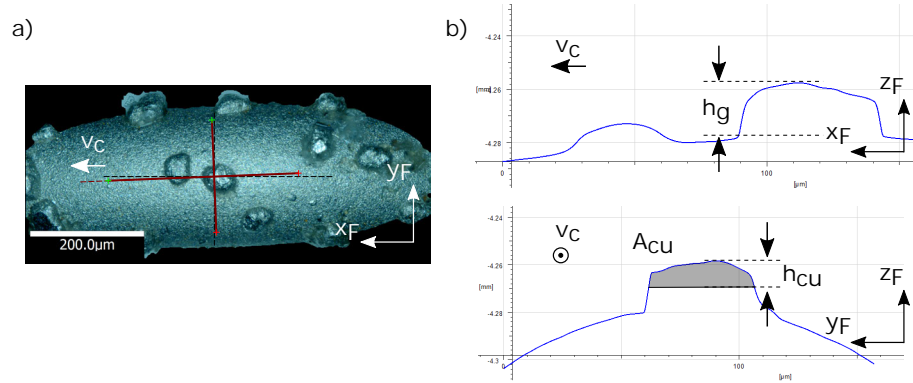


Figure 4.15: (a) Alicona IFM image of an abrasive grain on pin tip. (b) Grain cross-sections orthogonal and normal to the cutting direction.

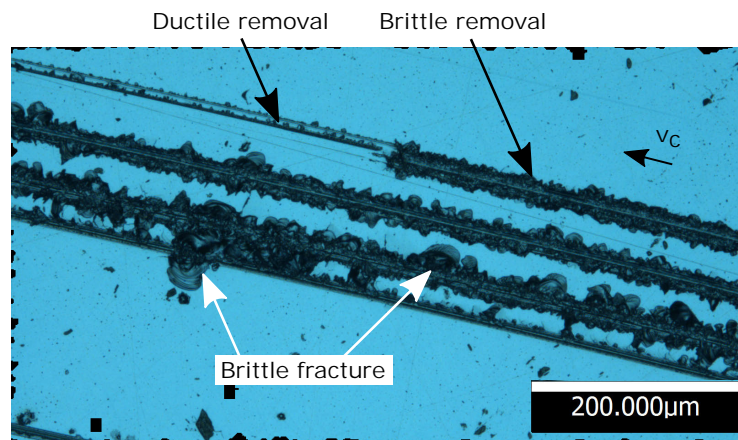


Figure 4.16: Several passes of the same grain over the workpiece. Brittle fractured zones and the transition from brittle to ductile removal are shown.

Multiple scratches by the same grain and their corresponding cross-section profiles, cutting and normal force measurements are given in Figure 4.17. As the material removal mode changes from brittle to ductile from left to right, the profile depth increases. On the other hand, cutting and normal forces drop as the material removal mode transforms from ductile to brittle.

## 4.2 Measurement Tools and Methods

### 4.2.1 Alicona 3D Infinite Focus Microscope

An Alicona IFM is employed for wire topography, grain geometry, surface texture measurements and schematically described in Figure 4.18. The microscope provides 3D surface data measurements through vertical scanning of the complete object height by the focus variation technique. Each layer of the target object is focused at

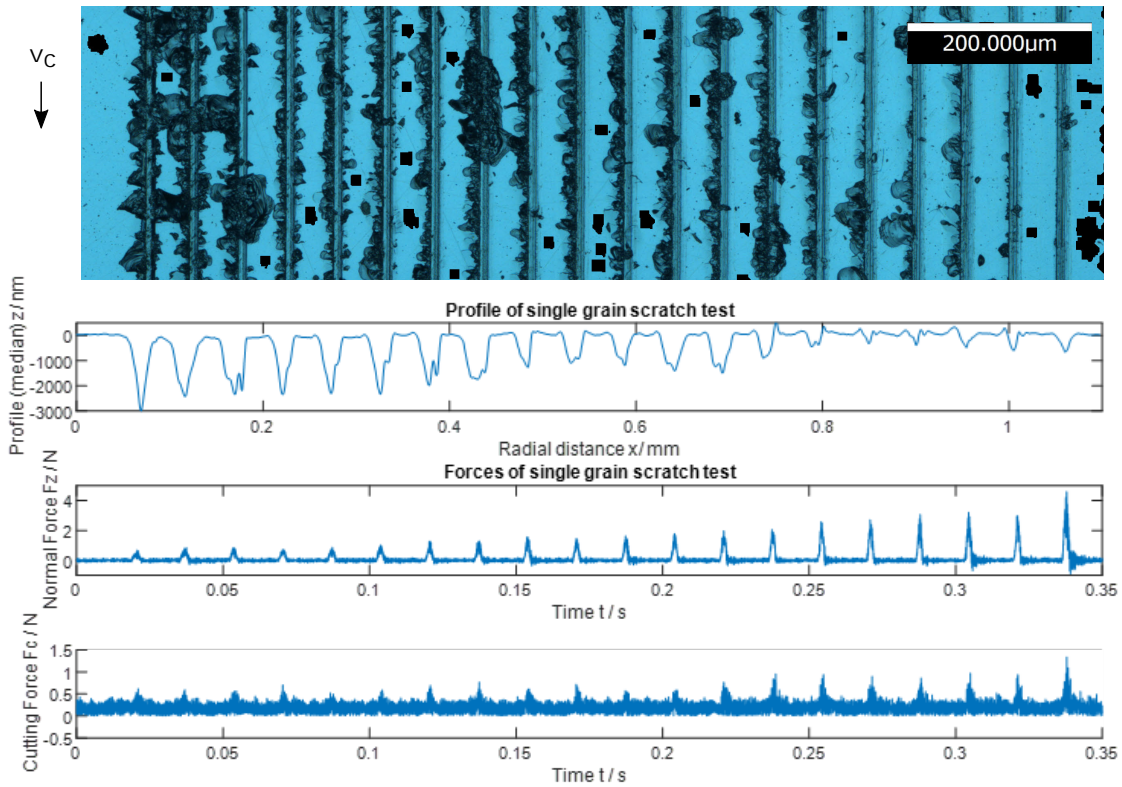


Figure 4.17: Multiple scratches by the same grain and their corresponding profile cross-sections and process forces.

the vertical position and the data is converted to 3D information using embedded algorithms while providing real color information of the sample.

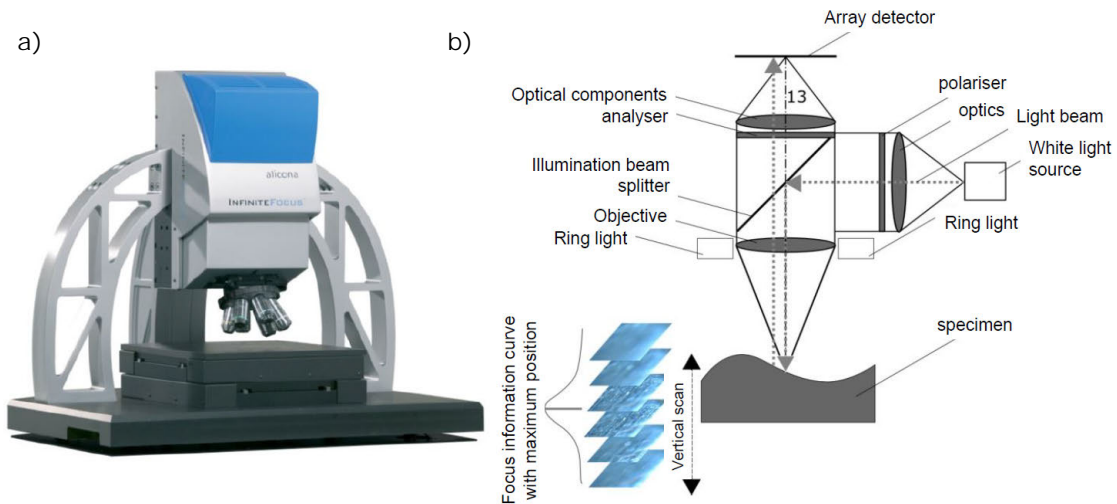


Figure 4.18: (a) Alicona IF microscope [8]. (b) Working principle of the focus variation technique [5, 152].

### 4.2.2 Force Measurement System

The force measurement system used for both the STS and WWGW setup is composed of a Kistler MiniDyn Type 9256C1 3-component dynamometer, Kistler Type 5080A charge amplifier, National Instruments NI 9222 analog-to-digital converter and a measurement laptop with Labview software. The setup is presented in Figure 4.19. The operating temperature range of the dynamometer is  $0-70^{\circ}C$  and the force measurement range is set as  $0-100\text{ N}$ . A low pass filter of  $1000\text{ Hz}$  is applied at the charge amplifier. The dynamometer sensitivity values set on the charge amplifier for this force measurement range is given in Table 4.1.

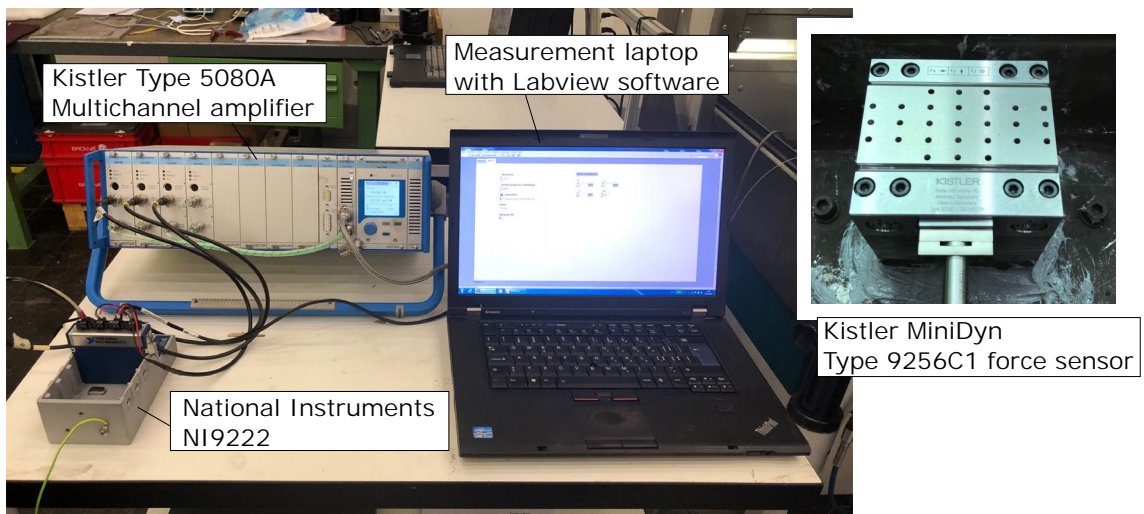


Figure 4.19: Components of the force measurement system.

Table 4.1: Sensitivity values set on the amplifier based on the dynamometer calibration range  $0-100\text{ N}$ .

Direction	$F_x$	$F_y$	$F_z$
Sensitivity	$-24.34\text{ pC/N}$	$-12.73\text{ pC/N}$	$-25.10\text{ pC/N}$

### 4.2.3 Temperature Measurement System

For the measurement of process temperatures at the single grain, a Fire-3 two-color fiber optic pyrometer is used. The device and measurement setup values are shown in Figure 4.20. The system conducts non-contact temperature measurements on metallic or non-metallic surfaces with unknown emissivities. The pyrometer uses a quartz fiber and detects the thermal radiation of the target at two different wavelengths so that a measurement on a broader range is possible. Fire-3 employs a bandpass

filter of 100 nm and operates at central wavelengths of  $\sim 1.65$  and  $\sim 1.95 \mu\text{m}$ . The acquired data is amplified and recorded with a data acquisition card which is embedded in the PC box. For the measurements, the gain value is set to  $10^9$  for both wavelengths and a scan rate of 50 Hz is used which corresponds to 250k data points over the measurement time of 5 seconds. The emissivity of the silicon surface is assumed to be 1.

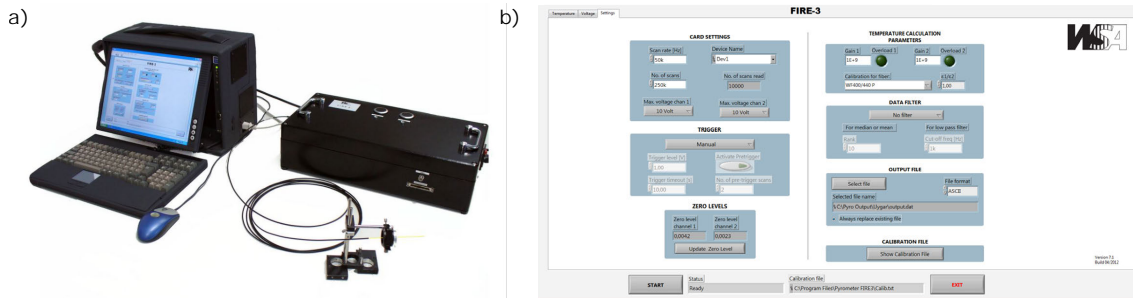


Figure 4.20: (a) Fire-3 two-color pyrometer. (b) Measurement setting used for the grain scratch tests.

## 4.2.4 Imprinting Technique

IWF-Wunder method is an in-situ, positive replication technique developed by Wunder [228]. The method enables the reproductive sampling of engineering surfaces and tool topographies without disrupting the experimental setup and reduces the setup-up times.

The application is shown in Figure 4.21. On the WWGW setup, negative copies are generated using vinyl terminated polysiloxane, directly on the wheel surface at two positions. Following, positive replicas are developed by casting the negative form with an epoxy-hardener solution. The method was evaluated for wear evolution of grinding wheels [228] and later for surface roughness [84].

## 4.3 Software Analysis Tools and Methods

### 4.3.1 Wire Analysis Software

A systematic investigation of the abrasive and wire properties is essential to develop a comparative understanding of the wire behavior as well as their influence on process outputs. Feed per cutting edge, undeformed chip thickness, abrasive wear volume and material removal regime heavily depend on the abrasive geometry and



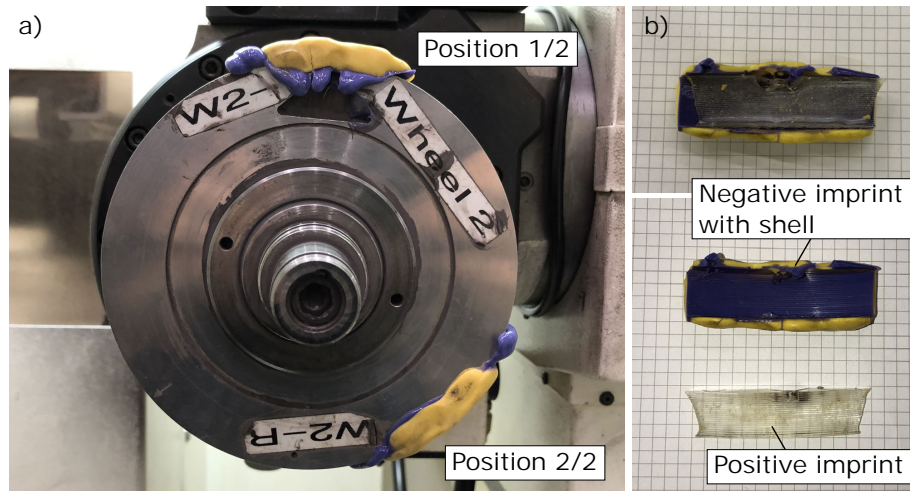


Figure 4.21: (a) Two sampling positions on the WWGW. (b) Positive and negative imprints of the diamond wire surfaces.

wire properties. On the other hand, diamond wire manufacturers are reluctant to provide data on wires and briefly offer information on the abrasive grain size range, relative grain density and core wire diameter. A reference characterization method is required to compare wire properties among each manufacturer as well as wires from different suppliers.

The Wire Analysis Software (WAS) is developed to provide a software tool to analyze electroplated diamond wires in terms of grain geometries, cutting edge distribution and density and other related wire and abrasive grain properties i.e. chipping space, grain protrusion, volume, material ratio or tip angles. Development of such method requires use of microscopy imaging tools as well as image processing algorithms. Additionally, the analysis results are the main inputs to model the stochastic nature of the wire, reproduce it, and use to simulate the grain-workpiece interaction for the process in focus i.e. the WWGW process or wire sawing.

The software is able to measure and analyze several wire samples from different sections of the wire to determine the wire and abrasive grain properties. It includes a number of algorithms that are developed for the determination of the wire reference level which defines the outer wire surface. Grain protrusion height and protruded grain volume are measured from this reference surface.

#### a Measurement and Preprocessing of Wire Samples

The software employs optical images taken with an Alicona IFM and the cylindrical wire surface form is removed as shown in Figure 4.22. The form removal software

of Alicona Microscope is used, confirming ISO Standards [2, 4] and has a maximum standard deviation less than  $0.2 \mu m$  and a mean standard deviation of less than  $0.03 \mu m$  in 95% confidence interval.

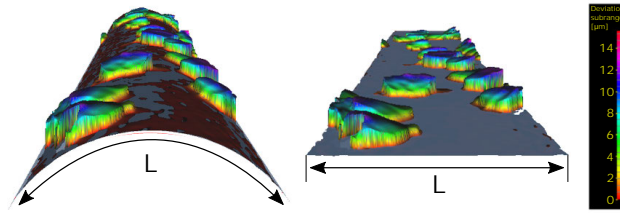


Figure 4.22: Comparison of cylindrical and derived stretched out surface surfaces.

The image is then transformed into a threshold image of 256 grayscales defined by the grain protrusion height, where 0 is the zero level (black) and 255 is the top level (white). The resolution depends on on the maximum value of grain height of the sample, where  $20 \mu m$  is typical for the diamond wires investigated in this work. The vertical resolution of the WAS is then defined as:

$$\delta_z = h_g^{max} / 256 \quad (4.13)$$

where  $h_g^{max}$  is the maximum grain protrusion on the wire samples that are analyzed,  $\delta_z$  is the vertical resolution of the analysis which is equal to  $0.0781 \mu m$  and the number of grayscale values is 256. Figure 4.23 shows the real color Alicona IFM image of the wire surface (top) and the grayscale image (bottom) which are stretched out, thus flat.

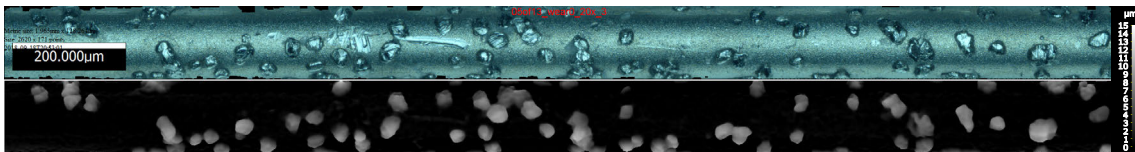


Figure 4.23: Stretched out real color Alicona IFM and 256 layer grayscale images as analysis input.

## b Details of the Analysis

The WAS process flowchart is presented in Figure 4.24. Several wire sections of the same wire types are used as individual inputs to determine the wire and abrasive grain characteristics. Processing of a sample starts with thresholding the input image to 256 layers. For the first layers, a size filter is applied using the MATLAB function `bwareaopen()` to filter out the surface elements with a size smaller than

$A_{lim}$  from the layer topography data. For each layer, the function  $bwconncomp()$  is used to determine the surface elements with 8-point connectivity and the function  $regionprops()$  is used to extract the areas, center positions of the topographic elements.

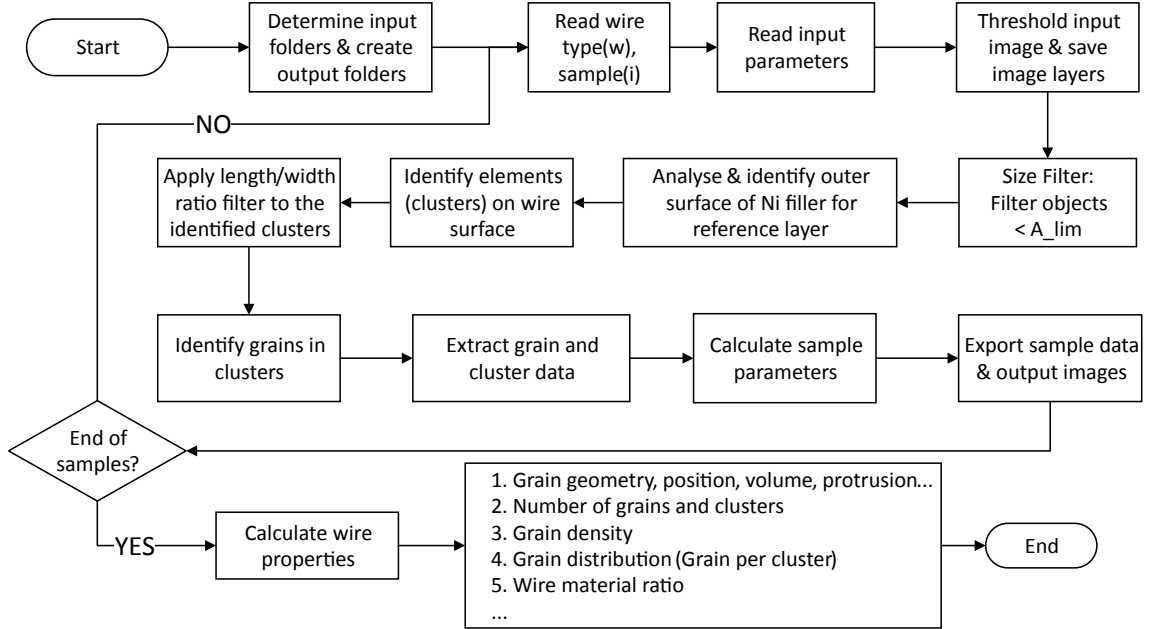


Figure 4.24: Algorithm process flow of the Wire Analysis Software.

Figure 4.25 introduces the parameters of abrasive grain characterization by WAS. The base frame area is measured at the outer surface, corresponding to the outer layer of the Ni-filler material which is denoted as the zero level. The grain length  $l_g$  is along the wire length and grain width  $w_g$  orthogonal to the wire length. The grain base area  $A_b$  is measured at the same level. Grain protrusion  $h_g$  is measured from the zero level to the maximum protrusion height and the grain volume  $V_g$  is the volume enveloped by the same dimensions.

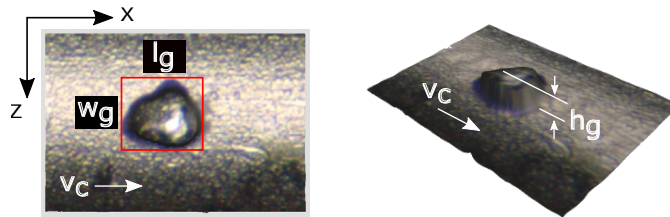


Figure 4.25: Some of the geometric parameters measured by the Wire Analysis Software.

Individual grains are required be distinguished from the other surface elements that are the result of Ni-filler material deposition (See layer 1 in Figure 4.27). This is possible at a height, where grains are the only visible elements on the layer surface and this layer is dependent on the wire type or can also be at different layers for samples of the same wire type. Hence, determination of individual reference layers

for each sample is required. After the grains are identified at the reference layer, the grain positions and cross-sections are saved and grains are evaluated through the layers above and below the reference layer.

For the calculation of reference layer, bounding boxes are plotted around each and every surface element on each layer, at their maximum points along and orthogonal to the wire length as shown in Figure 4.26a. The bounding boxes are separately shown in Figure 4.26b. The box areas are analyzed for their 8-point connectivity and the total area covered are saved for each layer, which is called the superposed layer surface as shown in Figure 4.26c.



Figure 4.26: (a, b) Bounding boxes plotted around surface elements at their maximum points along and orthogonal to the wire length. Frames around the elements (c) Superposed bounding box areas.

The difference between the sum of individual bounding boxes and the superposed area is calculated for each layer as:

$$A_{diff}^l = A_{simp}^l - \sum_{i=1}^n A_i^l \quad (4.14)$$

where for layer  $l$ ,  $A_{diff}^l$  is the difference between the superposed area  $A_{simp}^l$  and the sum of individual bounding boxes  $A_i^l$ ,  $i$  is the individual surface element and  $n$  is total number of the surface elements.

It is suggested that layer  $l$  is the reference layer if and only if:

$$A_{diff}^{l-1} < 0 \wedge A_{diff}^l > 0 \quad (4.15)$$

$A_{diff}^l$  for the first 64 layers of the analyzed sample are plotted in Figure 4.27. According to Eq. (4.15), layer 7 which corresponds to the vertical height of  $0.5469 \mu m$  (Eq. (4.13)), measured from the reference layer of this wire sample.



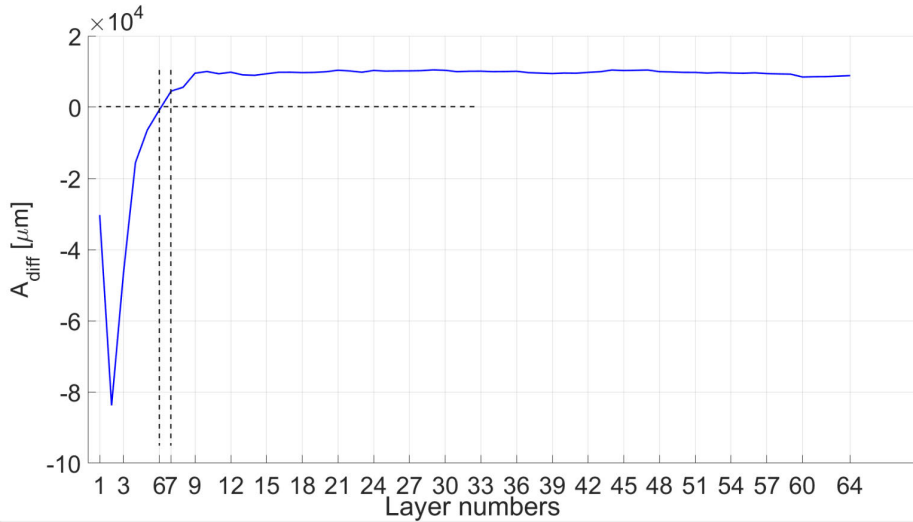


Figure 4.27: Difference between the bounding boxes and actual areas of grains in layers 0 to 64.

Figure 4.28 shows layers 1, 6 and 7 of the same wire sample of Figure 4.27, where the surface topography of the layer is given on top and plotted bounding boxes on the same layer is given below for each layer.

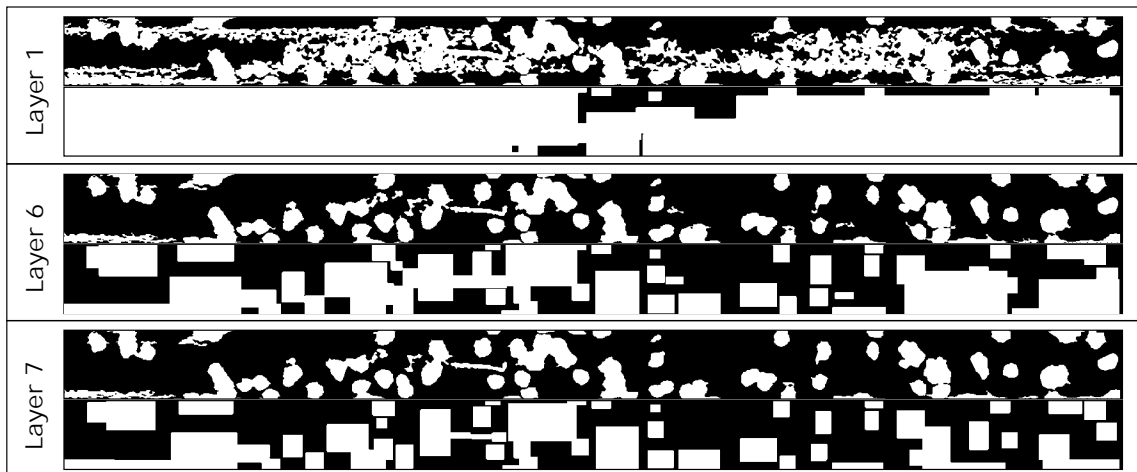


Figure 4.28: Layers 1, 6 and 7 from Asahi 12-25 high concentration diamond wire. Actual wire layer is given on top and same layer with bounding rectangles is given below for each layer.

The grains on the reference layer are identified and numbered. A size ratio filter is applied, so the software can evaluate the length/width ( $l_g/w_g$ ) ratios of the elements of wire topography, determine the outliers and delete them from the database of identified grains. One standard deviation is used as described in Figure 4.29.

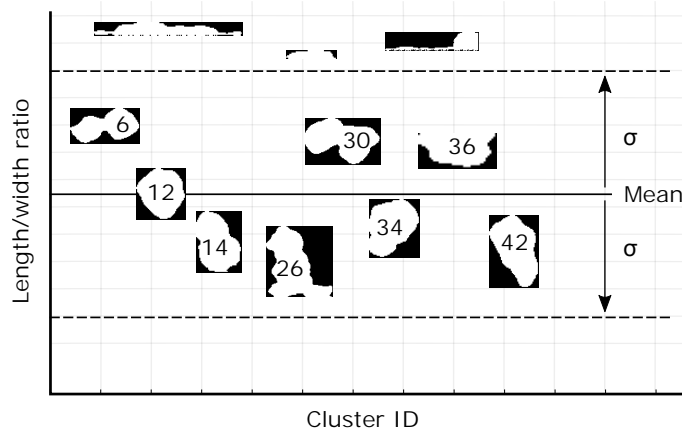


Figure 4.29: A representation of the length/width ratio filter of one standard deviation. Base areas that are measured at the reference layer are shown and topographic elements that are outside the upper and lower control limits are not included in the analysis.

Identified grain base areas measured at the reference layer of the wire sample are given in Figure 4.30. It can be seen that the surface elements can be divided into two categories as individual grains and two or more grains that are a part of the same surface structure that are called clusters.

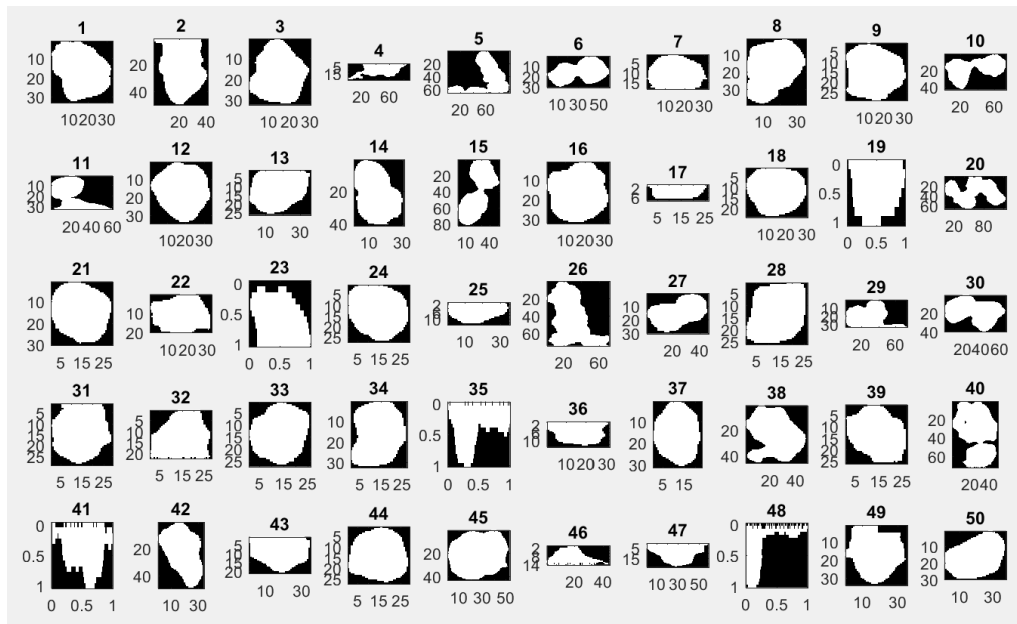


Figure 4.30: Identified cluster base areas at the reference layer.

A cluster can be defined as the aggregation of several grains. They are the result of a non-homogeneous distribution of diamonds on the wire surface where the distances between the diamonds are close enough and usually filled with the Ni-filler material. Cluster occurrence influence the available chip space on the wire surface and clusters are sources of loading risk and premature failure of the abrasive layer. Formation of clusters may affect the cutting ability since grains with highest protrusion in

the cluster is kinematically active, hence leaving the other grains in the proximity inactive. A visualization of the cluster formations are shown in Figure 4.31.

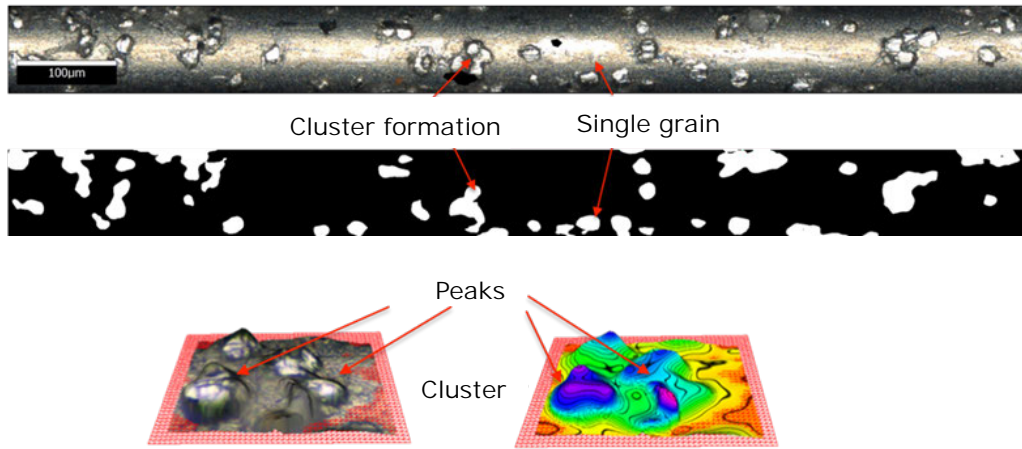


Figure 4.31: Comparison of single grains and clusters on the diamond wire surface.

Figure 4.32 explains how the cutting edges or grains can be determine in a cluster structure. As the area of the bounding box for each topographic structure followed through the layers, grains can be counted on each topographic element on the wire surface and their protrusion height can be determined.



Figure 4.32: Horizontal cross-sections of the same cluster structure at different heights from Layer 30 to Layer 140. Grain peaks points in the cluster structure can be identified.

### c Validation of the WAS Results

Validation of the WAS outputs is done for Asahi 12-25, 120  $\mu\text{m}$  core diameter standard concentration wire. WAS outputs of the Abbott-Firestone curve [6] which is a useful representation of the material ratios along the protrusion height of abrasive grains and the distribution of grain protrusion heights are compared with measurements conducted with the Alicona IFM Software.

Figure 4.33 presents the comparison of the WAS analysis results and the results of measurement conducted with Alicona IFM software. It can be concluded that the WAS is able to determine the distribution characteristics and maximum grain protrusion heights of the analyzed wires.

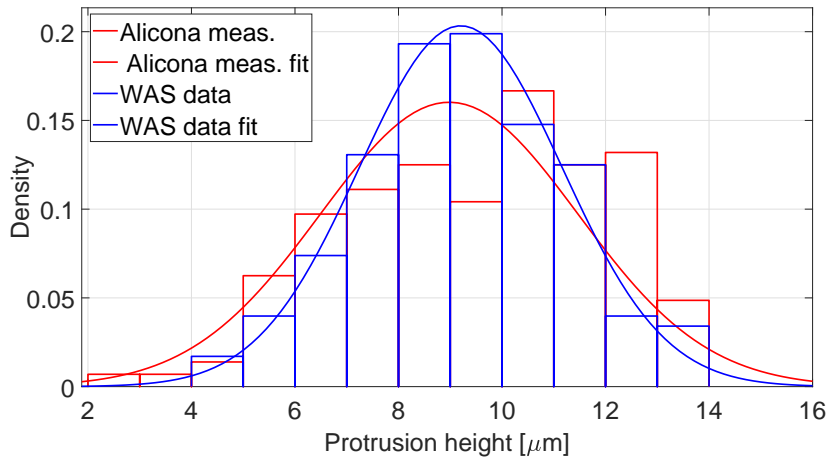


Figure 4.33: Distribution data and curve fits of grain protrusion heights of 4 samples of Asahi 12-25 120  $\mu\text{m}$  core standard concentration wire measured with the WAS and the Alicona IFM software.

### 4.3.2 Surface Analysis Software

The Surface Analysis Software (SAS) can process output images of an SEM or Alicona IFM and provides a method for fast and accurate characterization of the share of brittle-ductile removal regimes in Si workpiece surfaces.

#### a Details of the Analysis

The software computes a global threshold of the target image which is then transformed into a matrix, where each pixel in its position represents a value between 0 (black, brittle) and 255 (white, ductile) and gradient values in between.

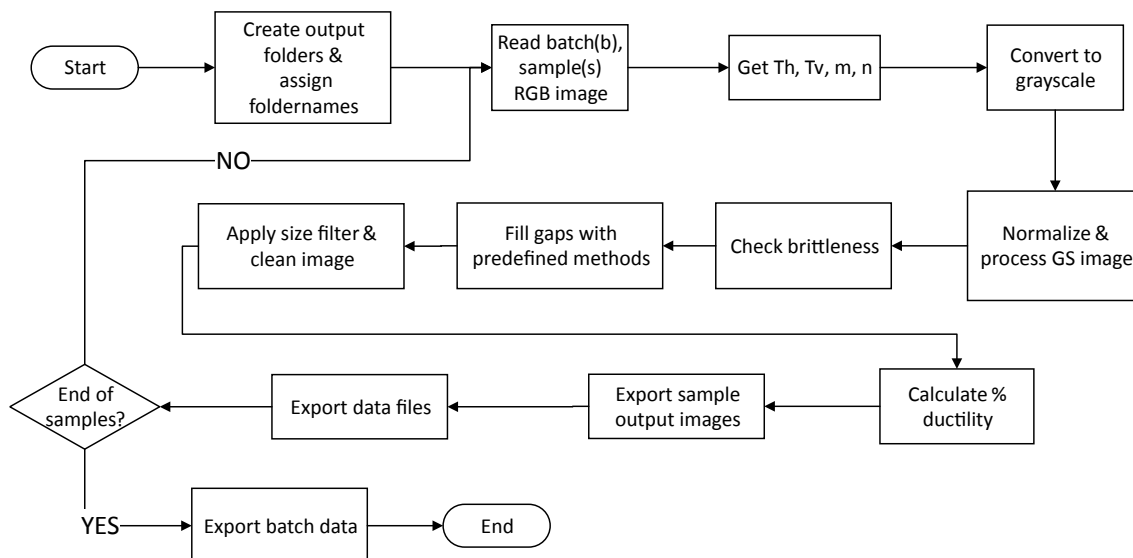


Figure 4.34: Algorithm process flow of the Surface Analysis Software.

The average gray value of each column and the whole image are calculated to determine a correction for shifting the column average to the total average:

$$\mu_j = \frac{1}{m} \sum_{i=1}^m W_{i,j} \quad (4.16)$$

$$\mu_{ij} = \frac{1}{mn} \sum_{i=1}^m \sum_{j=1}^n W_{i,j} \quad (4.17)$$

where  $W_{i,j}$  is the grayscale value of  $i^{th}$  row and  $j^{th}$  column,  $\mu_{ij}$  is the total average grayscale value of the image,  $\mu_j$  is the average value of  $j^{th}$  column and  $m$  and  $n$  are the number of rows and columns of the image matrix. The image is normalized by applying the correction to each cell, called normalization of the grayscale image, shown in Figure 4.35. The normalized image  $W_{i,j}^{norm}$  is expressed as:

$$W_{i,j}^{norm} = W_{i,j} - \mu^{corr} \quad (4.18)$$

where  $\mu^{corr} = \mu_j - \mu_{ij}$ .

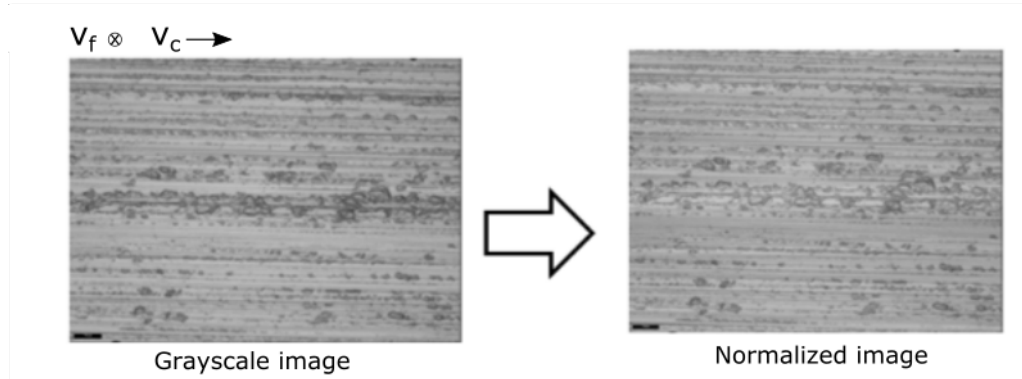


Figure 4.35: Normalization of a grayscale image.

The share of brittleness is determined by evaluating the vertical and horizontal gradient of gray, according to a certain tolerance  $T_v$  and  $T_h$ , in pixels  $m_v$  and  $n_h$  far from the center pixel  $W_{i,j}$  shown in Figure 4.36. The absolute difference between the cell and an adjacent cell is stored which is then compared to the preset tolerance. If the stored value exceeds the preset tolerance, final brittle area is identified. The binary image  $W_{i,j}^{comp}$  is calculated as:

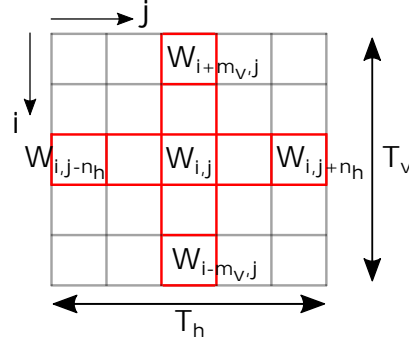


Figure 4.36: Vertical and horizontal tolerances and neighboring of pixels.

$$W_{i,j}^{comp} = \begin{cases} 0, & [(K_{v_1}^u > W_{i,j}^{norm} \vee W_{i,j}^{norm} > K_{v_2}^u) \wedge \\ & (K_{v_1}^l > W_{i,j}^{norm} \vee W_{i,j}^{norm} > K_{v_2}^l)] \vee \\ & [(K_{h_1}^u > W_{i,j}^{norm} \vee W_{i,j}^{norm} > K_{h_2}^u) \wedge \\ & (K_{h_1}^l > W_{i,j}^{norm} \vee W_{i,j}^{norm} > K_{h_2}^l)] \\ 1, & \text{otherwise} \end{cases} \quad (4.19)$$

where

$$\begin{aligned} K_{v_1}^u &= W_{i+m_v,j}^{norm} - T_v \\ K_{v_2}^u &= W_{i+m_v,j}^{norm} + T_v \\ K_{v_1}^l &= W_{i-m_v,j}^{norm} - T_v \\ K_{v_2}^l &= W_{i-m_v,j}^{norm} + T_v \end{aligned} \quad (4.20)$$

and

$$\begin{aligned} K_{h_1}^u &= W_{i,j+n_h}^{norm} - T_h \\ K_{h_2}^u &= W_{i,j+n_h}^{norm} + T_h \\ K_{h_1}^l &= W_{i,j-n_h}^{norm} - T_h \\ K_{h_2}^l &= W_{i,j-n_h}^{norm} + T_h \end{aligned} \quad (4.21)$$

The unconditioned pixels in between are filled as brittle regions with the predefined methods given in Eq. (4.22) for several values of  $G_v$  and  $G_h$ .

$$W_{i,j}^{comp} = \begin{cases} 0, & W_{i \pm G_v, j}^{comp} = 0 \\ 0, & W_{i, j \pm G_h}^{comp} = 0 \\ \text{same,} & \text{otherwise} \end{cases} \quad (4.22)$$

## b Validation of the SAS Results

Inputs and analysis results of the software are shown in Figure 4.37 where the Si surfaces machined at cutting speeds in the range of 15-75  $m/s$  and feed rates in the range of 0.01-2  $mm/min$  are given on top and the output images are given below. The ductility percentages are indicated for each image. Ductile surface appearance is increasing from left to right and shows that outputs of the analysis algorithm can successfully discriminate the brittle and ductile removal regimes.

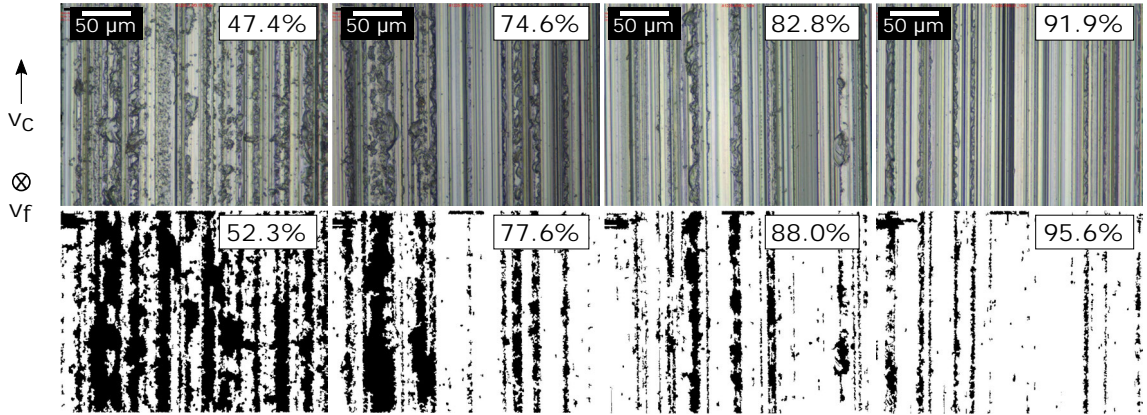


Figure 4.37: Sample Si surface images, outputs of surface analysis algorithm and measured percentages of ductility.

# Chapter 5

## Evaluation of Diamond Wires and Si Surfaces

In the following chapter, the evaluation of diamond wires and Si surfaces is presented. Initially, a morphological study of the electroplated diamond wires on wire cross-sections and detached diamond grains will be conducted. Following, several diamond wires are analyzed using the WAS and experimentally assessed for their process force behavior. Later, an experimental evaluation of the diamond wire wear mechanism is presented and the wear behavior of individual diamonds is analyzed. Finally, an experimental investigation of Si workpiece surfaces is provided.

### 5.1 Morphological Analysis

A morphological analysis of the wire cross-sections is expected to contribute to the understanding of the positioning of diamond grains on new wires and the Ni-filler material. Additionally, detached diamonds shall provide information on grain geometries which is later required for the geometric modeling of grains to be employed in the kinematic-geometric process model. It shall be noted that the diamond wires used throughout this work are from the same manufacturer and of the same production technology.

For the analysis of wire cross-sections, 30 wire sections are submerged into the epoxy material which is casted in cylindrical molds. After curing, the casts are polished in several steps so that the cross-sections are visible for evaluation. The epoxy workpieces each containing six wire samples are shown in Figure 5.1.





Figure 5.1: Epoxy probes each containing six wire cross-section samples.

The resultant wire cross-sections are presented in Figure 5.2 showing the abrasive grain positions on the wire. In a-f grains that are protruded over the filler material and in images f-h grains that are partly or fully covered with the Ni-filler material are shown. The surface of the new wire and the diamond grains are completely or partly covered with the Ni-filler material which wears off as the wire wear propagates and diamond grains are exposed.

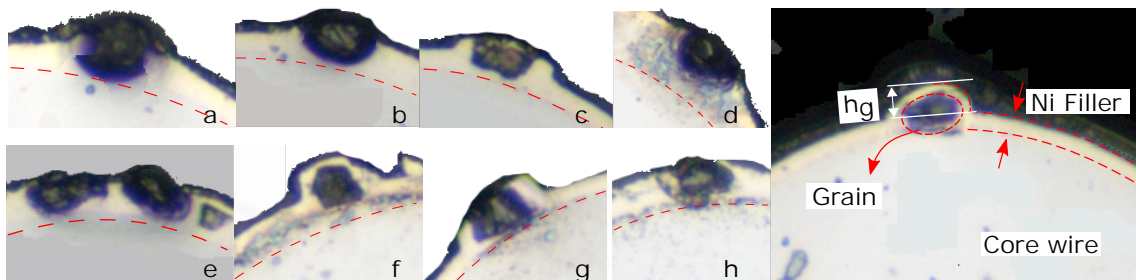


Figure 5.2: Left: Cross-section samples of diamond wire. Right: Indicated layers and grain position.

For the identification of the abrasive grain geometries, diamonds are removed from the wire surface by etching and detached diamonds are shown in Figure 5.3. For the diamond wire grain size range of  $12\text{-}25\ \mu\text{m}$ , grains fall in the mesh size range of 1000-1500 and FEPA designation of D23-D26. It is comprehended that diamond grains on the wire do not possess any specific geometric shape and measurement results indicate that it is reasonable to assume the grain volume is quarter of the grain volume measured by the WAS.

## 5.2 Evaluation of the Process Force Behavior

Four electroplated diamond wires from the same manufacturer are analyzed and tested at wire speeds between 15 and 75  $m/s$  and feed rates of 0.3  $mm/min$  and 0.6  $mm/min$ . The diamond wire properties and results of the wire analysis algorithm are tabulated in Table 5.1. Wires are selected to determine the influence of

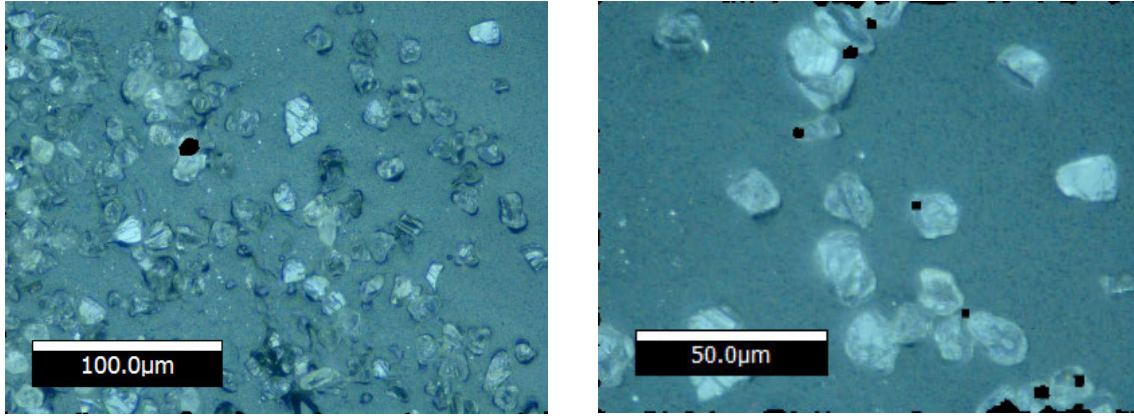


Figure 5.3: Abrasive grains removed from the electroplated diamond wire surface.

diamond size, protrusion and density on cutting and normal forces. Sample images of the wire topographies are given in Figure 5.4, where the variations in diamond sizes and formations can be clearly identified.

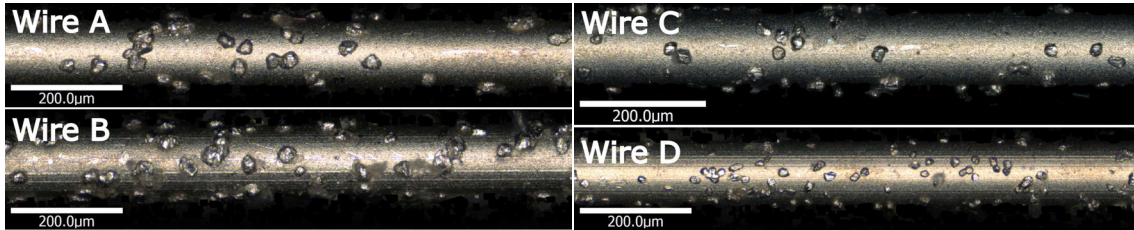


Figure 5.4: Sample images of tested wires taken with Alicona IFM.

Table 5.1: Properties of diamond wires used in experiments, determined by the wire analysis software.

	Wire A	Wire B	Wire C	Wire D
<b>Core wire diameter</b> [ $\mu m$ ]	120	120	120	120
<b>Diamond size</b> [ $\mu m$ ]	12-25	12-25	10-20	8-16
<b>Av. protrusion</b> [ $\mu m$ ]	$9.0 \pm 2.0$	$11.0 \pm 2.0$	$4.5 \pm 1.5$	$5.5 \pm 2.0$
<b>Grain density</b> [ $grain/mm^2$ ]	$133.0 \pm 15.6$	$211.4 \pm 42.7$	$139.4 \pm 9.7$	$512.3 \pm 38.4$
<b>Number of analyzed grains</b>	1293	1351	1192	997

Four measurements are performed for each data point and 13 steps of force measurements are conducted for wire speeds from 15  $m/s$  to 75  $m/s$ . The experiments are conducted in a procedure presented in Figure 5.5: (a) After installing the new (unused) diamond wire on the wheel, an initial cut of 0.1  $mm$  of material depth with 75  $m/s$  wire speed and 0.3  $mm/min$  feed rate is carried out to remove the Ni-filler on abrasive grains. (b) Without changing the wire, a second measurement set is conducted from 75  $m/s$  to 15  $m/s$ . (c) Following that, a new wire of the same

type is installed and the filler material removal procedure is repeated for the newly installed wire. (d) Afterwards, the same methodology is applied for two additional measurement sets of the same process parameters.

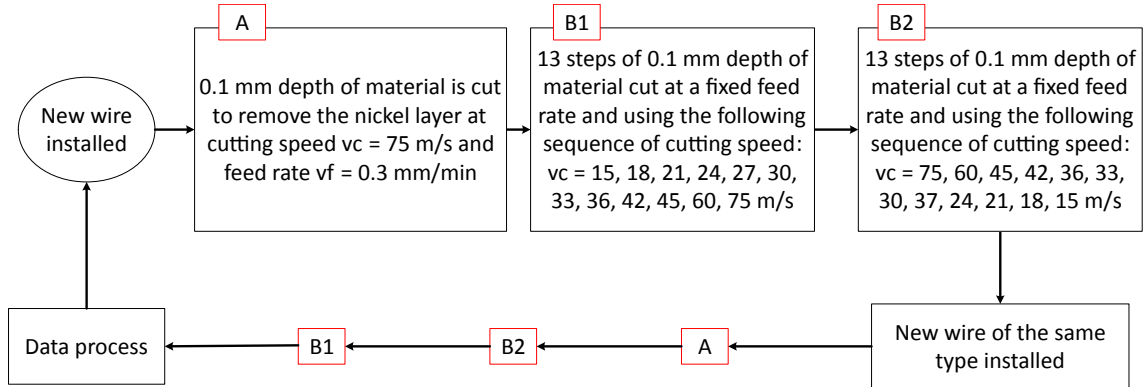


Figure 5.5: Sequence for conducted force measurement experiments.

The comparison of cutting and normal forces for four diamond wires A, B, C and D are presented in Figure 5.6 and Figure 5.7. A comparative study is conducted to discuss the influence of diamond size, protrusion and density on the process forces.

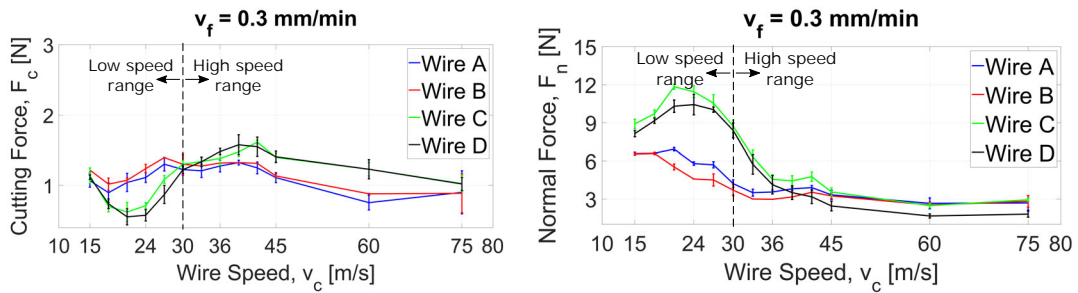


Figure 5.6: Cutting and normal forces at  $v_f = 0.3$  mm/min feed rate.

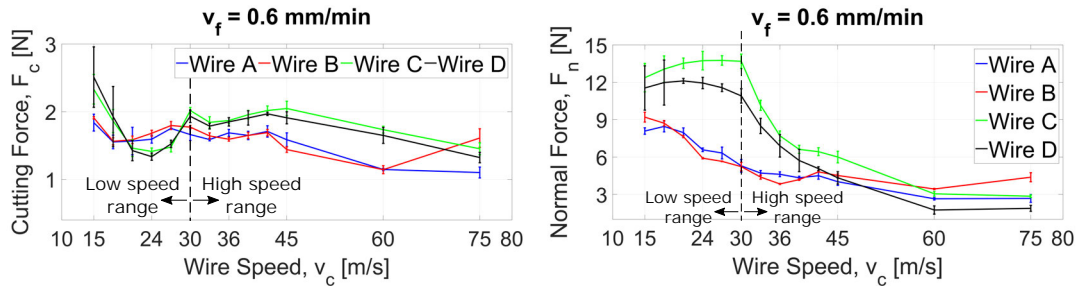


Figure 5.7: Cutting and normal forces at  $v_f = 0.6$  mm/min feed rate.

### 5.2.1 Influence of Diamond Size and Protrusion

Based on wire properties and their process force behavior, wires can be investigated in two groups as bigger grain size/higher protrusion (A-B) and smaller grain size/lower protrusion (C-D). From the viewpoint of process forces, wires A and B experience higher cutting forces below the wire speed threshold of around 30  $m/s$ . Above this threshold, wires C and D show higher cutting force values. On the other hand, A and B experience lower normal forces below the wire speed threshold of around 45  $m/s$ , compared to that of wires C and D. Above this threshold, difference between the normal force values reduce as the wire speed approaches to 75  $m/s$ . In the high wire speed range of 30 to 75  $m/s$ , cutting and normal forces gradually decrease for all wire types. Both statements are valid for the feed rates tested, while higher cutting and normal forces are measured at the higher feed rate.

### 5.2.2 Influence of Diamond Density

To reveal the influence of the diamond density, wires C and D with similar diamond size, protrusion and diamond distribution value but different diamond densities are compared. Wire D has higher diamond density and experiences lower cutting and normal forces in the wire speed range tested. The wires have the minimum cutting force values at wire speeds between 20 to 25  $m/s$  in the lower speed range. In the wire speed range of 30 to 75  $m/s$ , cutting forces gradually decrease with increasing wire speeds. The observation holds for both feed rates, however, the difference between the normal forces are more distinct for the higher feed rate of 0.6  $mm/min$ . In the case of normal forces, lowest values are observed between 60 to 75  $m/s$  for both wires and both feed rates.

As the wire speed increases, feed per cutting edge decreases, hence resulting in a decrease in the instantaneous undeformed chip thickness which is further expected to lead to a decrease in the cutting force. In that sense, wires A and B behave as expected, having lower cutting forces with increasing wire speed, however this observation doesn't hold for wires C and D below the wire speed of 30  $m/s$ . This effect is clearly not a result of the diamond density since wires C and D highly differ in diamond densities, but is likely to be an outcome of smaller diamond sizes.

The results show that the diamond wire and abrasive grain properties of size, protrusion and density have significant influence on the process force behavior. Below the wire speed threshold of around 30  $m/s$ , wires with smaller average diamond size,

lower average diamond protrusion experience lower cutting forces and higher normal forces. The behavior reverses over this threshold and also cutting and normal forces are less affected by the change in diamond size and protrusion. Above the wire speed threshold of around  $30\text{ m/s}$ , cutting and normal forces of all wires gradually decrease with a similar trend as wire speeds increase. Diamond size and protrusion have stronger influence on process forces than diamond density.

### 5.3 Evaluation of Si Workpiece Surfaces

Si workpiece surfaces are experimentally evaluated for the active material removal regimes and process roughness at wire speeds of  $15\text{-}25\text{-}50\text{-}75\text{ m/s}$  and feed rates of  $0.01\text{-}0.1\text{-}0.3\text{-}0.6\text{-}1.2\text{ mm/min}$ . The resultant workpiece surfaces and process forces are discussed. Wire A is employed and three experiments are conducted for each data point. Workpiece surfaces are measured with Alicona IFM and the SAS is employed.

Figure 5.8 presents two workpiece surfaces with the marginal values of the parameter range, lowest wire speed and highest feed rate (biggest chipping depth) and highest wire speed and lowest feed rate (smallest chipping depth). It is seen that the ductile and brittle material removal regimes are present all the time due to the involvement of different diamond protrusions. It is also observed that the removal regime may change several times along a cutting path that clearly can be attributed to one and the same grain. This means that depending on the chipping depth, which is responsible with the protrusion between brittle cut and ductile cut, a range exists where the behavior of the material removal depends on stochastic properties in the material like grain orientation and size, internal stresses etc.

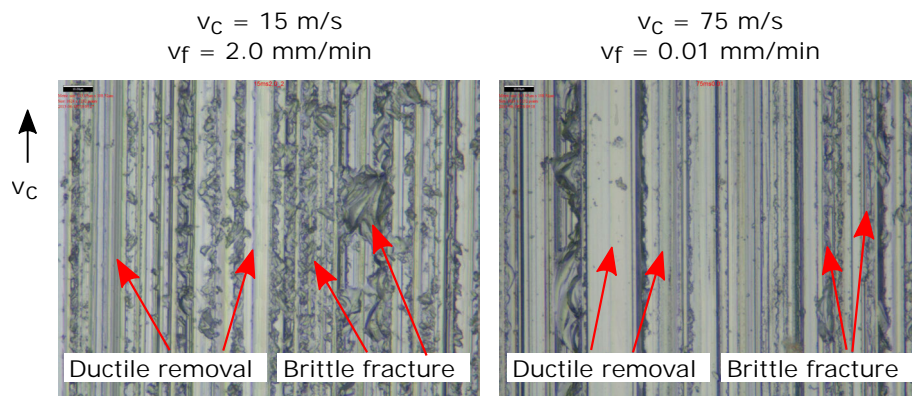


Figure 5.8: Comparison of two workpiece surfaces at the process parameters' upper and lower limits.



Results of the brittle-ductile characterization of workpiece surfaces are summarized in Table 5.2 and visualized in Figure 5.9 where ductility percentage indicates the percentage of the workpiece surface with ductile removal characteristics. A positive correlation between ductility and wire speed is observed where for the feed rates tested, higher ductility is measured as the wire speed increases.

Table 5.2: Percentage ductility of the workpiece surfaces at  $v_c = 15 - 75$  m/s and  $v_f = 0.01 - 1.2$  mm/min.

$v_f \setminus v_c$	15 m/s	25 m/s	50 m/s	75 m/s
<b>0.01 mm/min</b>	40.0±4.8	54.0±4.5	56.0±4.8	83.5±3.1
<b>0.3 mm/min</b>	51.2±9.4	47.5±5.7	62.6±3.0	61.0±8.8
<b>0.6 mm/min</b>	46.5±5.7	36.8±2.5	59.8±2.2	72.7±2.7
<b>1.2 mm/min</b>	36.6±6.2	58.1±5.8	79.0±1.2	62.2±2.9

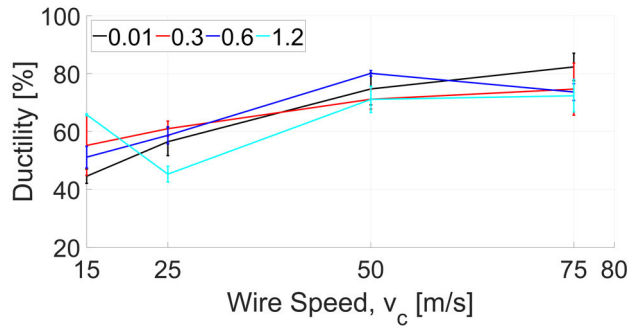


Figure 5.9: Percentage surface ductility vs. wire cutting speed at  $v_c = 15 - 75$  m/s and  $v_f = 0.01, 0.3, 0.6$  and  $1.2$  mm/min.

The comparison of workpiece surface roughnesses ( $R_a$ ,  $R_z$ ) and workpiece ductility at several wire speeds is given in Figure 5.10. The roughness measurements are conducted along the cutting direction since only the process roughness and not the kinematic roughness, due to the grain distribution shall be investigated. At the feed rates of 0.3 and 0.6 mm/min with the increasing cutting speed,  $R_a$  and  $R_z$  decrease and share of ductile removed surfaces increases. At high wire speeds, ductile removal dominates through the decrease in chipping depth.

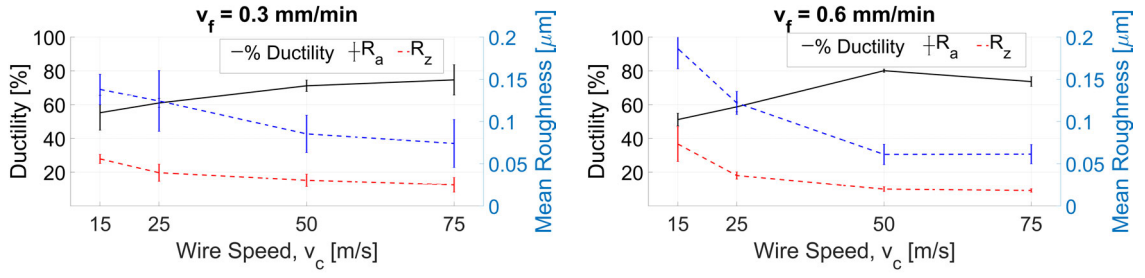


Figure 5.10: Percentage surface ductility vs. workpiece surface roughness measurements along cutting direction at  $v_c = 15 - 75$  m/s and  $v_f = 0.3$  and  $0.6$  mm/min.

The relationship between the cutting and normal forces and workpiece surface quality at feed rates of  $0.3$  and  $0.6$  mm/min are presented in Figure 5.11. As the wire speed increases, cutting and normal forces decrease and percentage ductility increases. In machining of brittle materials such as Si, high loads exerted by the abrasive grain lead to brittle fracture which results in a lower surface quality. Hence it can be stated that at high cutting speeds, normal and cutting forces decrease, resulting in domination of ductile material removal mechanism in diamond wire sawing of sc-Si.

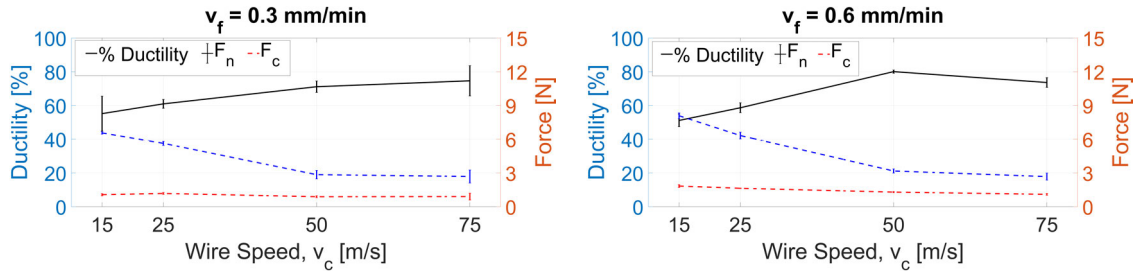


Figure 5.11: Percentage surface ductility vs. cutting and normal forces at  $v_c = 15$  and  $75$  m/s and  $v_f = 0.3$  and  $0.6$  mm/min.

Analysis on the Si workpiece surfaces clearly show that ductile and brittle material removal regimes are present at the time and each abrasive grain can cause brittle or ductile material removal regime and the material removal regime may change along a cutting path of an abrasive grain due to dynamic effects. Moreover, ductile finish property of Si is positively correlated with the wire speed. High wire speeds and low feed rates result in surfaces with mainly ductile removal. With increasing wire speed, normal and cutting forces decrease, resulting in domination of ductile material removal mechanism and lower surface roughness in diamond wire sawing of sc-Si

## 5.4 Evaluation of the Wear Mechanisms

An Asahi 12-25 standard concentration wire with  $140 \mu\text{m}$  is employed in the wear evaluation experiments. Figure 5.12 presents the wire topography in intermediate wear stages with color coded images. Cumulative material removal volume is increasing from top to bottom image and the dashed red line identifies the same wire position. It can be seen that the protrusion heights of abrasive structures as well as the base areas, which are measured from the wire reference level, are decreasing with wear propagation. In addition to single grains, cluster formations that are a result of a non-homogeneous diamond distribution on the wire surface are apparent. In a cluster of grains, the wear occurs as a combination of Ni-filler and diamond wear. Wear monitoring of clusters shows that in a cluster, initially the grain with the highest protrusion wears out until the next grain becomes kinematically active. From that point on, the wear rate of the two diamonds are comparable.

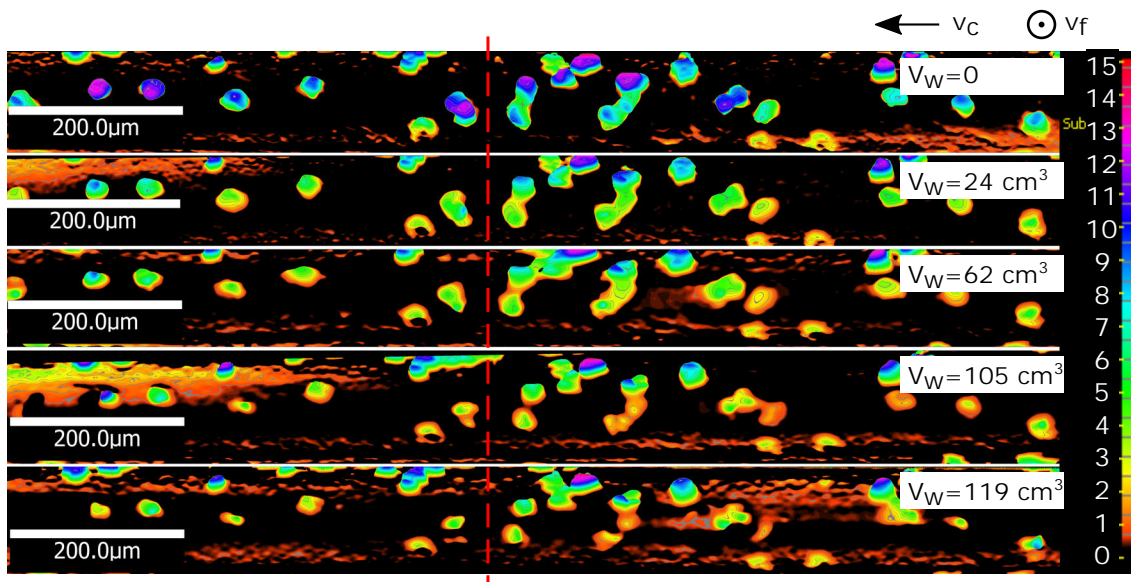


Figure 5.12: Color coded images of identical diamond wire sections and diamonds with wear progress at  $v_c = 50 \text{ m/s}$  and  $v_f = 0.9 \text{ mm/min}$ . The cumulative material removal volume  $V_w$  is increasing from the top to bottom image.

Figure 5.13 shows the results of the wear analysis performed using the WAS. (a) shows the change in average grain protrusion, (b) the change in the average grain base area and (c) the change in the average volume of clusters and isolated grains with respect to cumulative material volume. Whereas the reduction of the protrusion and volume can be approximated with an exponential function throughout the whole process, the development of the base areas shows two distinctive ranges: In the beginning, the grain base areas experience no deviation from their initial state. As the protrusion decreases, the filler material accumulated around the base of the grain



is eventually exposed to the process and starts to wear rapidly, thereby reducing the base area (See Figure 5.14). As the filler is being removed around the abrasive grain/cluster base, the risk of the occurrence of pullouts increases and the software is able to identify individual grains in clusters. Furthermore, rapid decrease of grain volume at the initial cutting phase can be accounted to the removal of Ni-filler which typically covers the grains on a new wire.

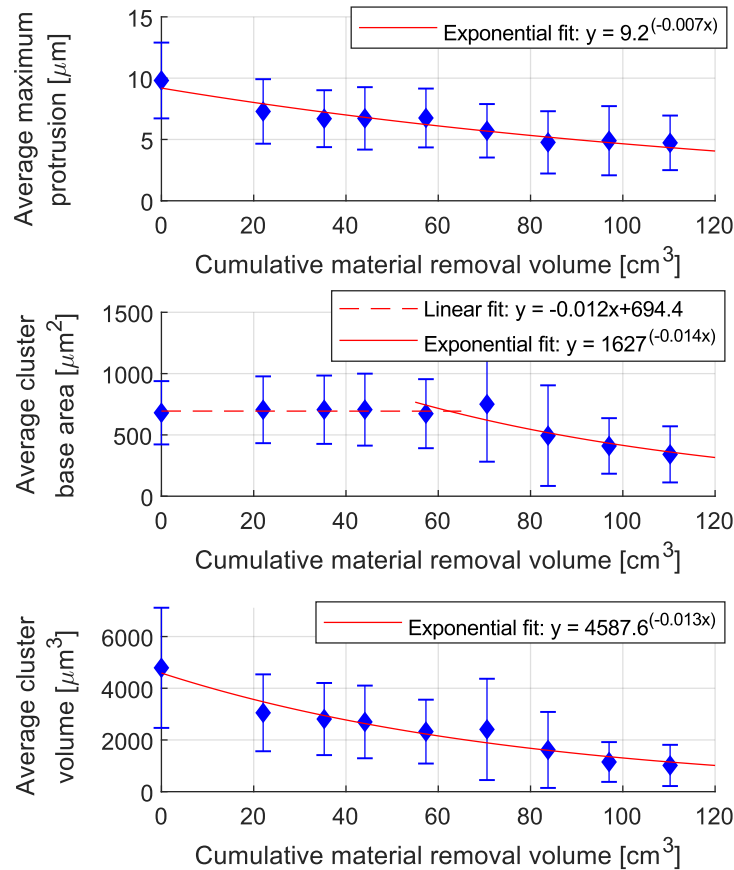


Figure 5.13: Evolution of the average protrusion, base area and volume of abrasive grains with increasing wire wear at  $v_c = 50$  m/s and  $v_f = 0.9$  mm/min, measured with the WAS.

The wear stages of individual diamond grains and clusters show that the dominant wear modes are micro- or macro-fractures and comparably few grain pullouts are observed. A typical wear sequence of a grain is presented in Figure 5.14. The initial and final states are shown on top and maximum cross-sections are compared in the bottom image. In the first stages, the grain loses a considerable share of its volume, and the wear rate reduces as the grain wear propagates while breaking-off grain edges. In some cases it is also observed that the Ni-filler can be deposited at the back of the grain as indicated in the figure in shaded area.

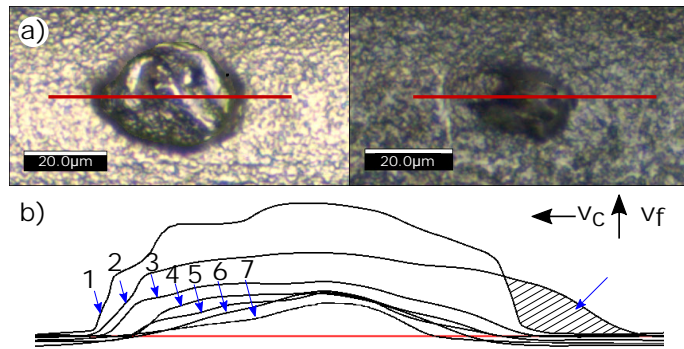


Figure 5.14: (a) Initial and final wear states of a diamond. (b) Maximum cross-sections of the diamond through its lifetime.

Three of the identified wear modes are presented in Figure 5.15, where top images show the new grains and their maximum cross-sections and lower images show the final states and their maximum cross-sections. A grain wear of gradual grain fracture/dulling is shown in (a), a premature pullout in (b) and pullout at the end of grain lifetime in (c).

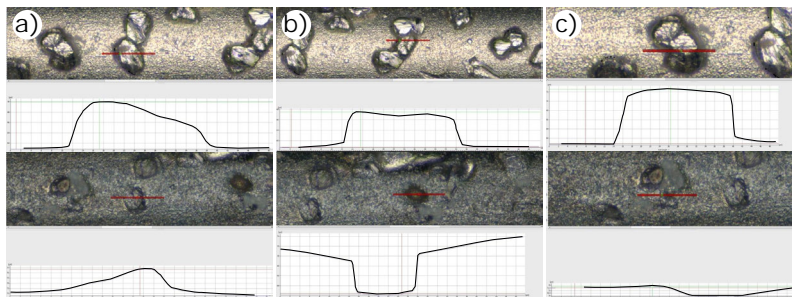


Figure 5.15: Three diamond wear modes observed on wire: (a) Fracture/dulling (b) Premature pullout (c) Pullout at the end of wear lifetime.

Measurement of process forces with progressing wear is presented in Figure 5.16. It can be interpreted that with progressing wear, dulling of grain edges leads to an increase in the normal and cutting forces, while a higher rate of increase is observed in normal forces.

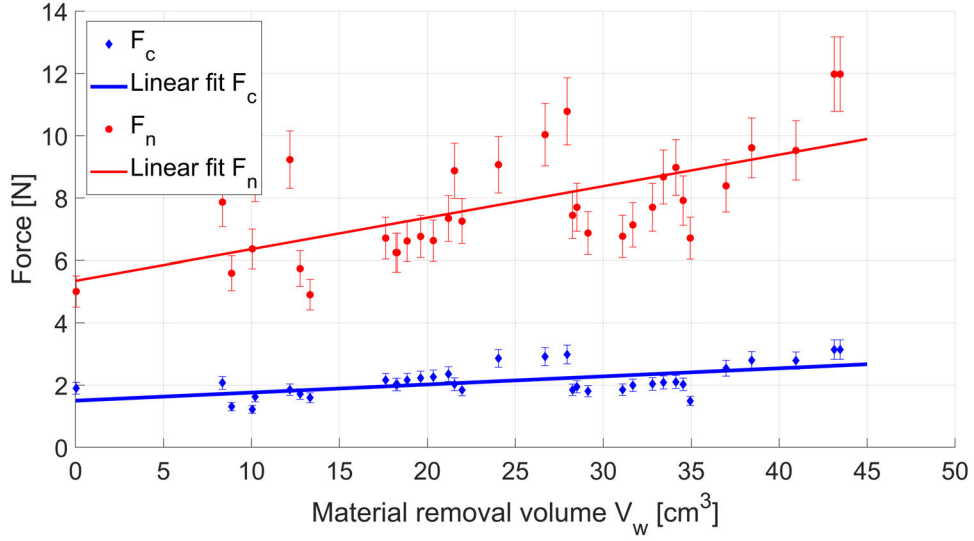


Figure 5.16: Evolution of the cutting and normal forces with progressing wire wear at  $v_c = 50$  m/s and  $v_f = 0.9$  mm/min.

Further, an Asahi 10-20 standard concentration  $120 \mu\text{m}$  core diameter diamond wire is employed in sawing of sc-Si on a Meyer Burger DW288 multi-wire saw at the wire speed of  $25$  m/s and the feed rate of  $1.5$  mm/min. Three stages of wire wear are measured with WAS, as the new wire,  $6.54$  cm<sup>3</sup>/m and  $8.10$  cm<sup>3</sup>/m of specific material removal rates which is defined as the total material removal volume per unit length of wire. The average values are tabulated in Table 5.3 and sample wire sections are given in Figure 5.17.

Table 5.3: Evaluation of the diamond wire wear of Asahi 10-20 standard concentration  $120 \mu\text{m}$  core diameter diamond wires.

	New Wire	6.54 cm <sup>3</sup> /m	8.10 cm <sup>3</sup> /m
<b>Grain protrusion</b> [ $\mu\text{m}$ ]	8.50±4.53	4.05±2.30	3.00±2.41
<b>Cluster protrusion</b> [ $\mu\text{m}$ ]	9.17±4.32	4.12±2.33	2.83±2.52
<b>Grain per cluster</b>	1.68±0.77	1.60±0.87	1.42±0.71
<b>Grain density</b> [grains/ $\mu\text{m}^2$ ]	413±150	462±190	521±288
<b>Cluster vol.</b> [ $\text{mm}^3$ ]	2.58e-6±0.28e-6	1.3e-6±0.14e-6	0.9e-6±0.087e-6
<b>Number of analyzed grains</b>	1421	1458	1481

The results show that the average grain and cluster protrusions reduce with progressing wear. Moreover, the number of grains per cluster is reducing and the grain density is increasing with progressing wear, which is due to the wear of bonding material that fills the voids in cluster structures. This results in a decrease of the

number of grains per cluster and an increase in the grain density. Additionally, measurements show that the average cluster volume is decreasing which also points out the clusters are breaking out with wear progress.

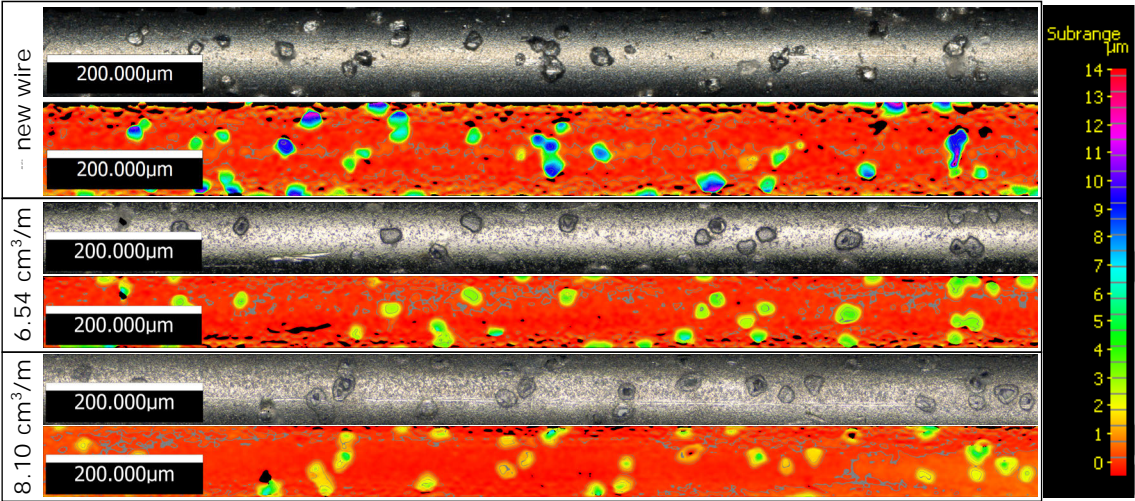


Figure 5.17: Three wear stages of Asahi 10-20 standard concentration 120 μm core wires at  $v_c = 25$  m/s and  $v_f = 1.5$  mm/min on a multi-wire saw. Real color Alicona images are on top and color coded images are below each sample.

# Chapter 6

## Wire Sawing Process Model

*“Essentially, all models are wrong, but some models are useful.”*

— George E. P. Box,  
*Science and Statistics, 1976*

The physics of abrasive wire cutting is fairly complex and consists of different aspects that are cast into a modular model, where each individual aspect can be modeled separately by sets of equations in a suitable degree of detail. The kinematic-geometric model of the wire sawing process is therefore composed of the tool model that includes the geometric grain and stochastic wire models, the workpiece model, the kinematic process model, the material removal model and the cutting force model.

Figure 6.1 presents the main elements of the wire sawing process model. Primarily, outputs of the Wire Analysis Software are employed to model the micro- and macro-features of the diamond wire. The geometry and material properties of the Si workpiece are defined in the workpiece model. Next, outputs of these two are fed into the kinematic model, together with the process parameters. The path of a single grain and grain penetration provides the geometric definition of the grain-workpiece interaction as well as the undeformed chip thickness and kinematically active grains. Further, they are introduced into the material removal model considering brittle and ductile removal modes to generate the workpiece surface. Here, the experimental results of single grain scratch tests are employed to determine the specific cutting force on the single grain to estimate wire sawing forces.

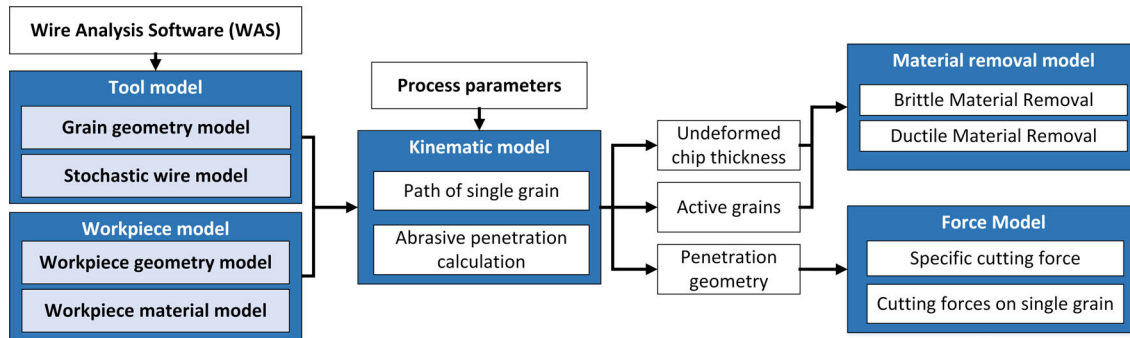


Figure 6.1: Overview of the modular modeling methodology.

## 6.1 Tool Model

A detailed tool model is one of the three essential elements of kinematic-geometric modeling (Section 2.4.2). A successful model of an abrasive tool shall be composed of a micro-geometry model that is based on realistic grain geometries and a macro-geometry model that considers the distribution, density and orientation of the cutting edges. The results of WAS which are introduced in Section 4.3.1 and the evaluation of the diamond wires presented in Section 5.1 of this work lays the fundamental framework for modeling of the abrasive grain geometries and wire properties of the diamond wire in focus. The tool model presented is based on these results and analysis. Here, it is necessary to discuss the challenges and details of abrasive grain geometric modeling of diamond wires:

1. The abrasive grains on the diamond wire possess no defined geometry but rather they are crushed diamond grains.
2. The clustering of grains result in a wire surface topology that is different than the case where only single grains are present. The Ni-filler material occupies the space in between the clustered grains. Hence, measurements of the grain volume by WAS result in higher values than the sum of the individual grain volumes in a cluster.
3. To be able to simulate the wire wear behavior that is discussed in Section 5.4, it is essential to consider the Ni-filler material volume covering the grain surface, and not only the detached grain dimensions.

In addition to the stated points, the high deviations in the topography over the length of the diamond wires challenge the definition of an average wire model. Figure 6.2 presents the Abbott-Firestone curves of 13 samples that have a total length of 15 cm, taken from different sections of an Asahi 12-25 high concentration

wire which is used to develop the model presented in this section and thus employed in the experiments and the process simulation. The dashed lines show material ratios over the protruded height of individual wire samples and the average curve is denoted with red color. The horizontal lines define a standard deviation of  $2\sigma$ , showing the scattering of the ratio of the topographic material at each height step. The average curve is considered as the Abbott-Firestone curve of the wire type.



Figure 6.2: Material ratios of the protruded height of individual wire samples of Asahi 12-25 high concentration wire and the average curve of the measurements.

### 6.1.1 Grain Geometry Model

Developing a realistic grain model for diamond wires is possible through the evaluation of detached grains as presented in Section 5.1 and measurements of protruded grains over the wire surface as done with the Wire Analysis Software. The grain models shall represent the initial state of the wire topography, hence are required to include the volume of the Ni-filler material over and around them. Three dimensional entities of the grains are measured by WAS that are the grain volume  $V_g$ , base area  $A_b$ , protrusion height  $h_g$ .

Figure 6.3 presents the four ideal grain geometry models: equilateral triangular pyramid, truncated equilateral triangular pyramid, rectangular pyramid and truncated rectangular pyramid that are symmetrical around their base surfaces.



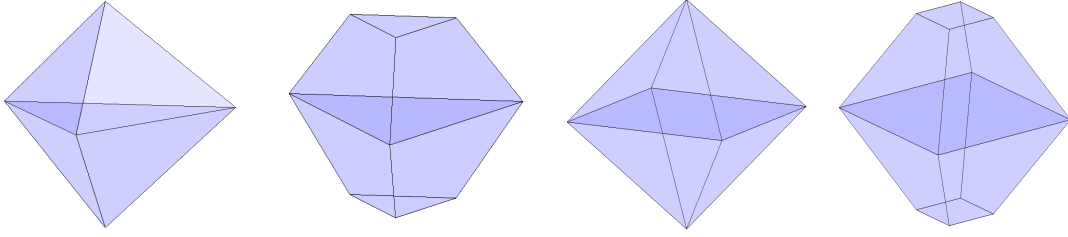


Figure 6.3: Four ideal grain geometry models developed: equilateral triangular pyramid, truncated equilateral triangular pyramid, rectangular pyramid and truncated rectangular pyramid.

The geometric features are introduced in Figure 6.4, showing the protruded part of the grain models. The grain models are parameterized with the grain protrusion height  $h_g$  measured from the grain base level, grain base area  $A_b$ , edge length  $a$  of the grain base area and edge length  $b$  of the grain top area.

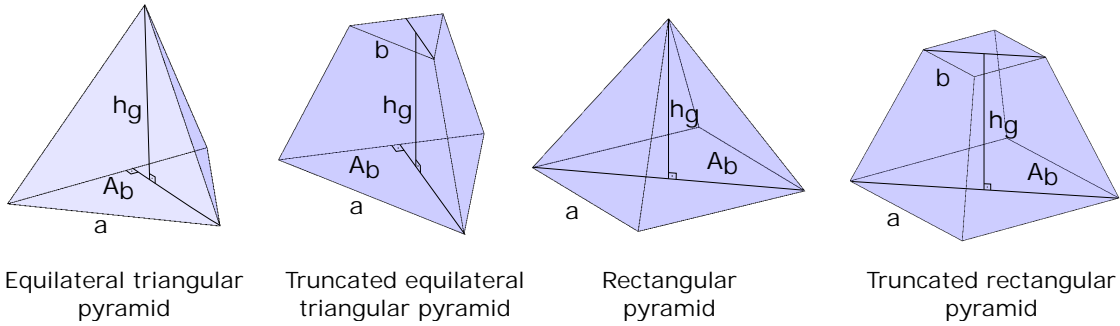


Figure 6.4: Descriptions of dimensional features of grain models with rectangular and equilateral triangle base areas.

The grain volumetric aspect ratio  $C_v$  defined as:

$$C_v = \frac{h_g}{A_b} \quad (6.1)$$

The grain geometric aspect ratio  $C_f$  defined as:

$$C_f = \frac{b}{a} \quad (6.2)$$

where  $0 < C_f < 1$ . Grain models with  $C_f = 1$  denote blunt/blocky grains,  $C_f = 0$  denote pointy/sharp grains and the rest in between.



The steps involved in the construction of the grain models are explained in Figure 6.5. The WAS measurements show that the grain protrusion height  $h_g$  and volumetric aspect ratio  $C_v$  are normally distributed. Through employing the mean and standard deviation of the measurements, probability density functions (PDF) of  $h_g$  and  $C_v$  of the form given in Eq. (6.3) are constructed:

$$f(x|\mu, \sigma) = \frac{1}{\sigma\sqrt{2\pi}} \exp\left(-\frac{(x - \mu)^2}{2\sigma^2}\right) \quad (6.3)$$

where  $\mu$  is the mean and  $\sigma$  is the standard deviation of the dataset  $x$ .

Next, based on the measured average material ratio (Section 4.3.1) of the diamond wire to be modeled, two values are determined: the share of each model geometry in the bundle and the geometric aspect ratio ( $C_f$ ) for truncated grain models. Through the random assignment of the geometries, grain protrusion volume  $V_g$ , base area  $A_b$ , edge length  $a$  of the grain base area and edge length  $b$  of the grain top area are determined

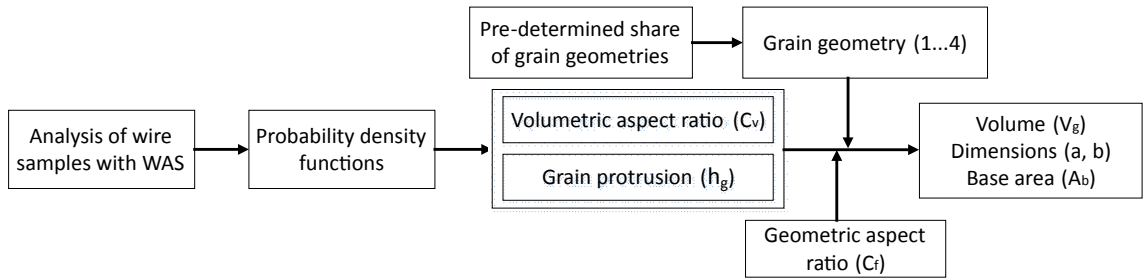


Figure 6.5: Flowchart for grain geometry modeling.

### 6.1.2 Stochastic Wire Model

The stochastic wire model is constructed by employing the WAS measurements of individual samples of the wire type to be modeled. The average of the grain and cluster densities of the samples is calculated; and number of grains and clusters of the wire to be modeled are determined. The wire geometry is constructed through discretization of the wire surface with equally spaced nodes along the cutting direction and in its periphery. Dimensions of the meshed wire surface are described in Figure 6.6a and the model of the meshed surface is shown in Figure 6.6b, where  $T_{ij}$  denotes the position of the wire node,  $L_{mt}$  is the distance between two nodes along the wire length and  $L_{nt}$  is the distance between two nodes on the wire peripheral;  $L_t$  is the length and  $W_t$  is the peripheral of the wire model. The wire radius is then  $r_w = W_t/2\pi$ .

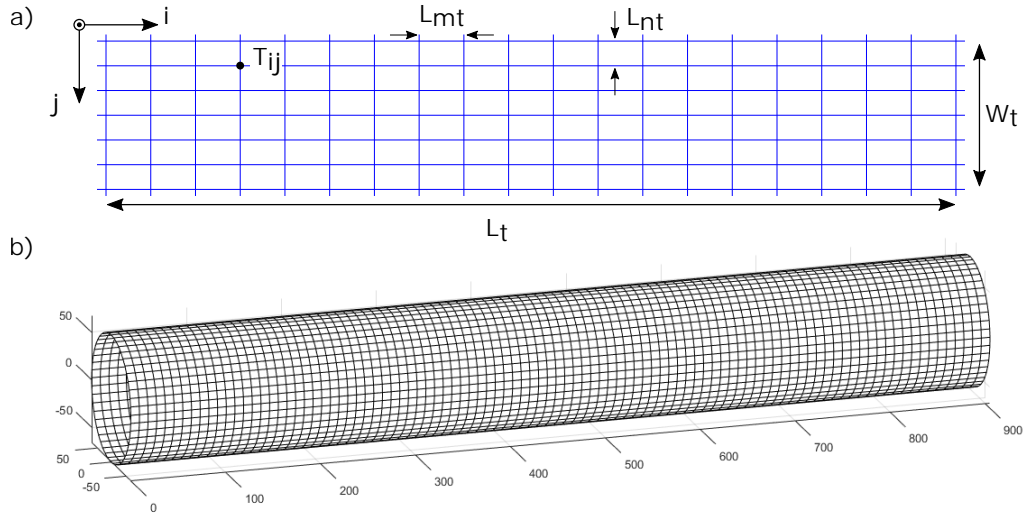


Figure 6.6: (a) Dimensions of wire surface mesh. (b) Meshed wire model.

The abrasive grain density is defined as the number of abrasive grains per unit area of the wire surface. Besides the single grains on the wire surface, clusters are modeled as measured with the WAS. The abrasive grain distribution denotes how the grains are evenly distributed on the wire and is described in Figure 4.31. The abrasive distribution value is defined as:

$$k_{gc} = \frac{N_g^s + N_c}{N_g} \quad (6.4)$$

where  $k_{gc}$  is the average number of grains in each location,  $N_g^s$  is the number of single grains,  $N_c$  is the number of clusters and  $N_g$  is the total number of grains on the wire surface. A wire with no cluster formation would have a distribution value of 1; and the value decreases for grain distributions with lower homogeneity.

The probability of occurrence of an abrasive grain  $P_g$  on a wire node  $T_{ij}$  is:

$$P_g = \frac{W_t \cdot L_t \cdot \rho_{gr}}{N_{nm}} \quad (6.5)$$

where  $\rho_{gr}$  is the grain density and  $N_{nm}$  is the number of nodes on the wire model in the area  $W_t \cdot L_t$ . The probability of occurrence of a cluster  $P_c$  on a wire node  $T_{ij}$  is:

$$P_c = \frac{W_t \cdot L_t \cdot \rho_c}{N_{nm}} \quad (6.6)$$

where  $\rho_c$  is the cluster density.

The flowchart explaining the primary steps in the development of the wire model is given in Figure 6.7. WAS outputs of cluster density and grain density are employed to determine the number from each, based on the wire model dimensions. Following, clusters are randomly placed to wire nodes and based on the probability distribution of the number of grains in each cluster, grains are distributed to 8-point proximity (considering 8 nodes around the center node) of the cluster positions.

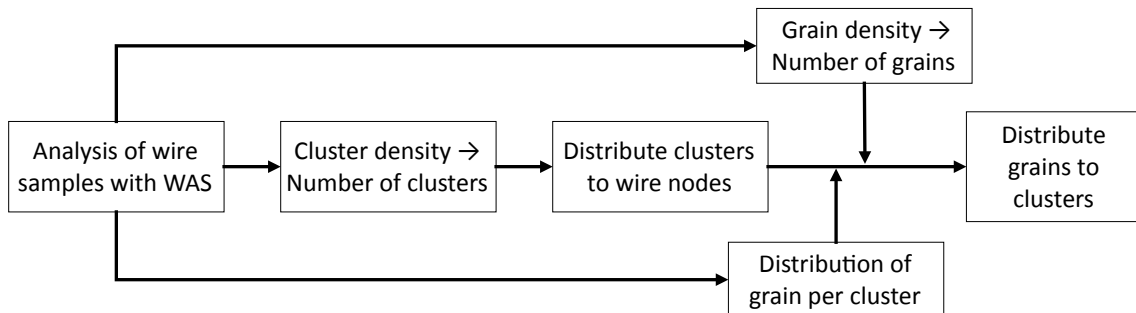


Figure 6.7: Flowchart for diamond wire modeling.

The orientations of the grain edges are randomly distributed. Each diamond grain is randomly rotated in the range of  $\pm 5^\circ$ , around an axis orthogonal to the wire centerline and further rotated  $\pm 180^\circ$  around the vertical axis passing through its center of mass.

Figure 6.8 shows the results of random rotation of 3D grain models and the red outline shows the convex hull of the grains on the plane orthogonal to the cutting direction which are also the outlines of the reduced 2D grain models.

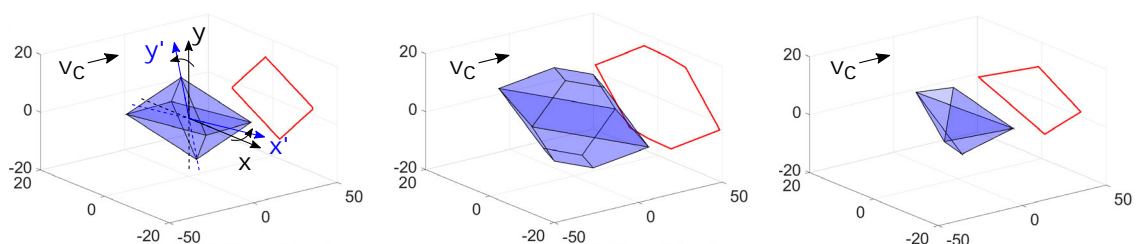


Figure 6.8: Examples of random grain rotations in two directions and convex hull of the grains on the plane orthogonal to the cutting direction.

Applying the described methodology, a diamond wire with a length of 452.76 mm, which corresponds to a single wire wrap on the WWGW is modeled with 58,966 different grain models. Further, the grain models are reduced to 2D geometries to save computation time. For this specific wire  $C_f = 0.4$  and the share of the shapes are 0.35 for each of the triangular and rectangular pyramids and 0.15 for each of the truncated grain geometries (Figure 6.4). A section of the simulated wire with

3D grains is presented in Figure 6.9a and the reduced model with 2D grains in Figure 6.9b.

The validation of the developed tool model shall be conducted on two levels. Primarily, it is required to compare the distribution properties of the single grain models to the grains on the actual wire surface. Further, the material ratios of the modeled and measured wire topographies shall be compared for 3D and 2D cases to validate the resemblance of the material ratio over the protruding height.

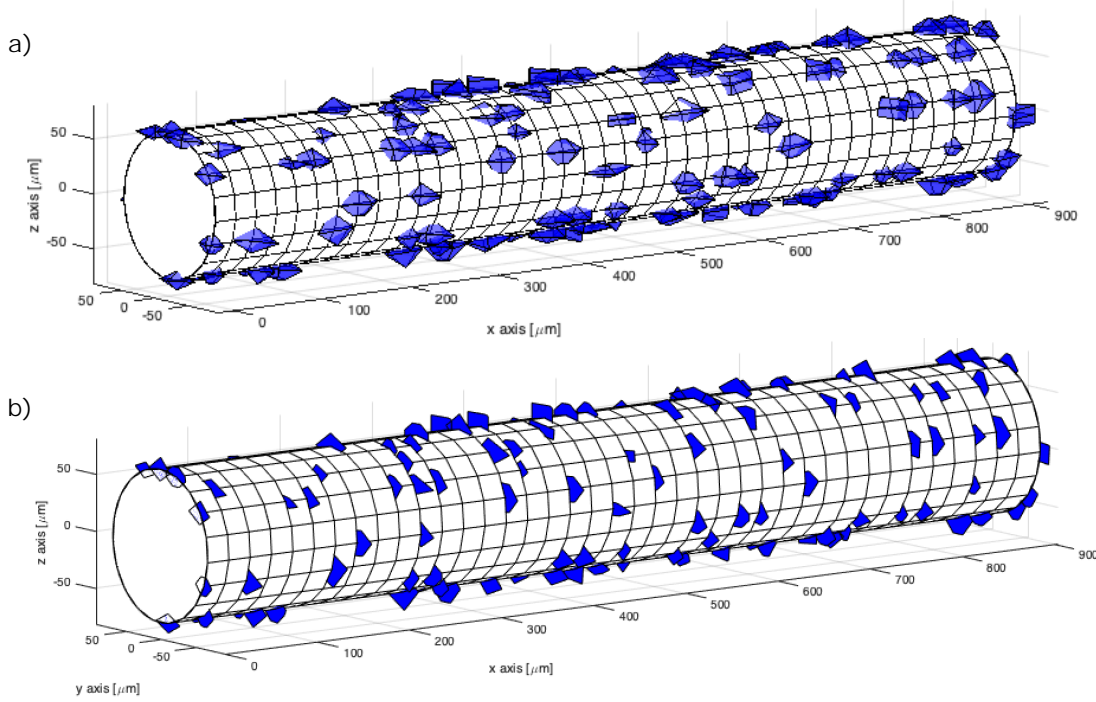


Figure 6.9: (a) Wire model with 3D grains. (b) Simplified wire model with 2D grains.

Figure 6.10a presents the grain protrusion heights  $h_g$  and volumetric aspect ratios  $C_v$ , where the blue color shows the WAS measurements and red color shows the model constructed using Eq. (6.3) with a standard deviation of  $\pm 2\sigma$ . Employing  $h_g$ ,  $C_v$ ,  $C_f$  and the share of grain shapes, as described in Figure 6.5, the grain base areas  $A_b$  and grain volumes  $V_g$  of the modeled grains are determined. Comparison of the grain base areas  $A_b$  and grain volumes  $V_g$  of WAS measurements and modeled grains is given in Figure 6.10b. The single grain property distributions are fitting well with the measured grain property distributions.

Abbott-Firestone curves of the modeled wire for 3D and 2D cases are presented in Figure 6.11 together with the comparison of the material ratio of the wire measured by the WAS. The deviation of the material ratios of 3D and 2D grain cases is clearly visible. For the process simulation 2D grain case will be employed, therefore the fit of 2D grain case is more significant.

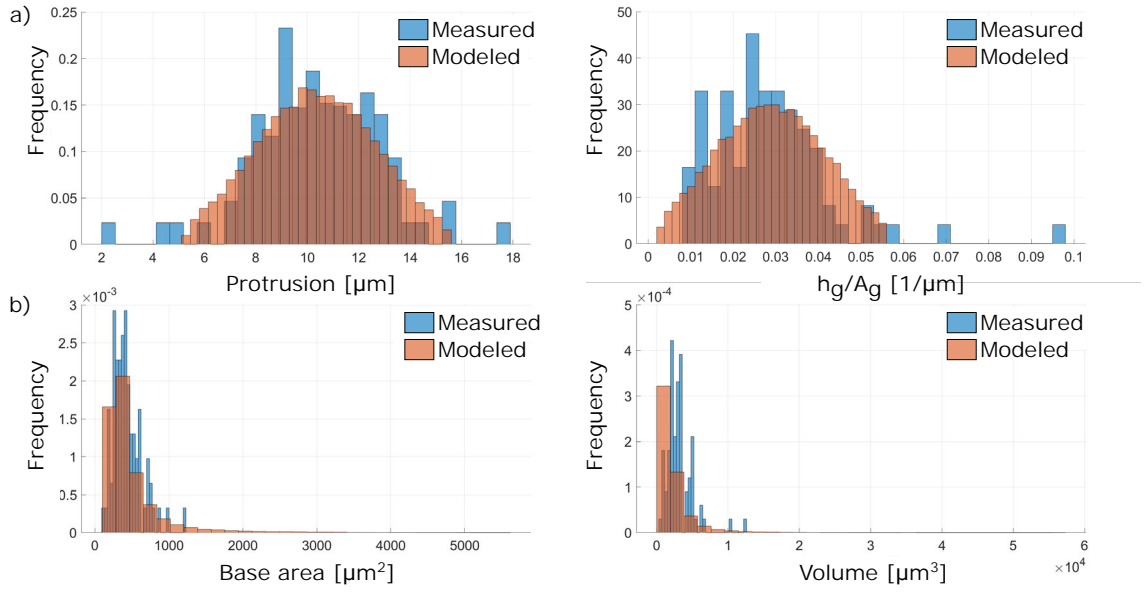


Figure 6.10: Comparisons of the distributions of grain protrusion  $h_g$ , volumetric aspect ratio  $C_v$ , base area  $A_b$  and volume  $V_g$  of measured and modeled single grains.

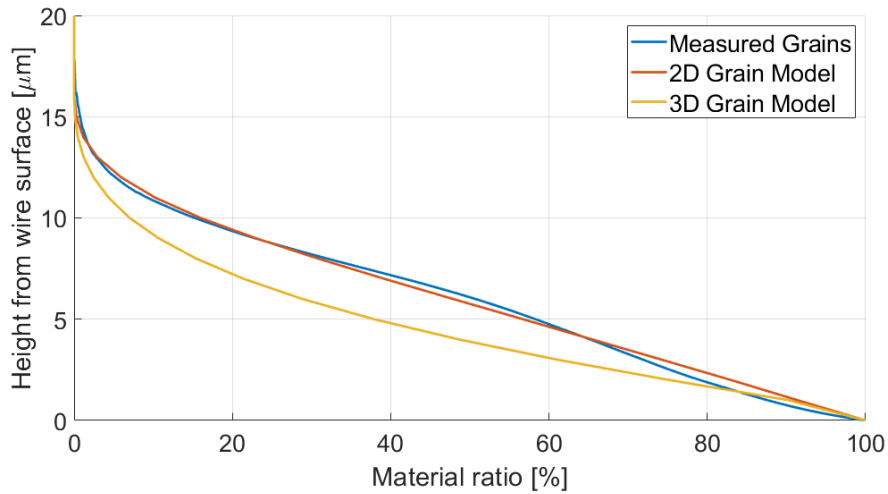


Figure 6.11: The comparison of the material ratio curves of the modeled wire with 2D and 3D grain geometry models and the measured wire.

In the 2D grain model case, the material ratio is measured on the length and in the 3D case it is measured on area, leading to a deviation between the two cases. The deviation is expected to increase when the grains are sharper (i.e. only pyramid geometries are used) and decrease when the grains are cuboid (i.e. only truncated grain geometries are used with a base/top ratio of 1). The two extreme cases are presented in Figure 6.12, where the highest possible deviation is shown with sharp grains and two curves fit perfectly when only cuboid grain models are considered.

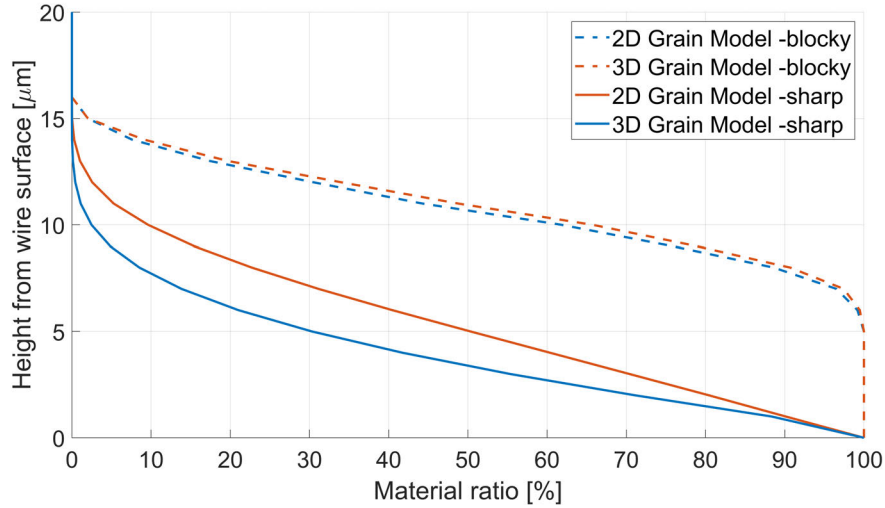


Figure 6.12: Comparison of the two extreme cases of wire material ratios. The term ‘blocky’ denotes the truncated equilateral triangular pyramid and truncated rectangular pyramid grains with  $C_f = 1$ ; and ‘sharp’ denotes equilateral triangular pyramid and rectangular pyramid grains.

## 6.2 Kinematic Process Model

The details of wire-workpiece contact geometry and working principles of the WWGW setup are presented Section 4.1.1. In the following section, the kinematic process model of the WWGW setup will be studied including the grain position, motion and penetration.

### 6.2.1 Grain Position

A sketch of an open wire along the wheel circumference  $C_{wheel}$  that is removing material from the surface of the workpiece with the width  $b_f$  is given in Figure 6.13. The wire centerline is passing through the center point  $C_i$  of the  $i^{th}$  wire section in  $x'_{C_i}$  direction and has a rotation of wire wrap angle  $\alpha$  (Figure 4.3) from the cutting direction in  $x_{C_i}$  direction.

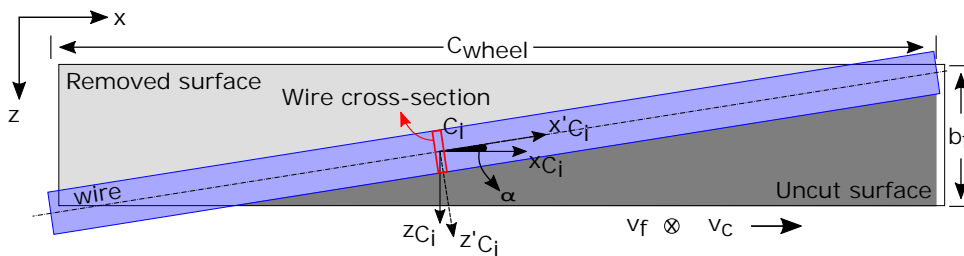


Figure 6.13: Schematics of the wire-workpiece contact shown with an open-unwrapped wire position on the workpiece surface.

Figure 6.14a introduces the vector  $\underline{R}_{SC_i}$  indicating the position of an arbitrary wire cross-section center  $C_i$  with respect to the origin of the wheel attached coordinate system  $S$  at the center of the wheel on  $x_S - y_S$  plane. The first subscript indicates the start and the following subscript indicates the end point of the vector. The center of the wheel attached coordinate system  $S$  is moving with the feed rate  $v_f$  in  $-y_S$  direction. The two ends of the single wire wrap are indicated  $K$  as the start and  $K'$  as the end points. The components of  $\underline{R}_{SC_i}$  with respect to the wheel attached coordinate system as shown in Figure 6.13 are:

$$\underline{R}_{SC_i} = \underline{R}_{SS_i} + \underline{R}_{S_iC_i} \quad (6.7)$$

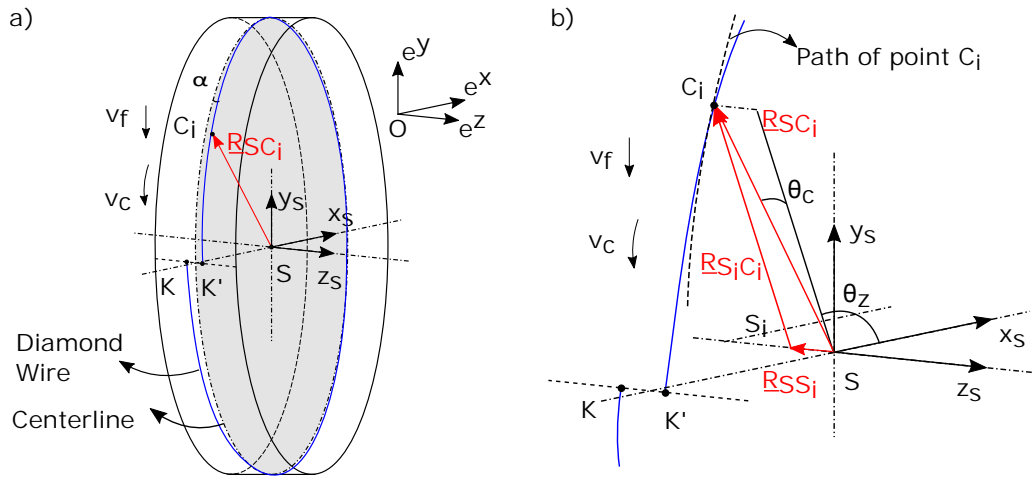


Figure 6.14: Position of an arbitrary wire cross-section with respect to the wheel center  $S$ .

Point  $S_i$  is in the center of the plane parallel to  $x_S - y_S$  plane and includes the center point of an arbitrary wire cross-section  $C_i$ .  $\underline{R}_{SC_i}$  is position vector of the wire center  $C_i$  with respect to  $S$ .  $\underline{R}_{SS_i}$  is the component of the position vector  $\underline{R}_{SC_i}$  in  $z_S$  axis and  $\underline{R}_{S_iC_i}$  is the component in  $x_S - y_S$  plane from  $S_i$  to  $C_i$ . Angle  $\theta_z$  denotes the angular position of  $C_i$  around  $z_S$  and  $\theta_c$  is the angle between  $\underline{R}_{SC_i}$  and  $x_S - y_S$  plane. The diamond wire follows the helical wheel groove and is indicated in blue color.

Figure 6.15a shows the position of an arbitrary wire cross-section at  $\theta_z = 3\pi/2$ . The position vector  $\underline{R}_{C_iG_{ij}}$  represents the position of an arbitrary grain tip  $G_{ij}$ , where  $i$  denotes the respective wire cross-section and  $j$  denotes the grain tip on that cross-section. The wire wrap angle  $\alpha$  determines the angle between the orientation vector of the wire and the direction of cut. The components of the  $\underline{R}_{C_iG_{ij}}$  are given in Figure 6.15b for better visualization, where it is decomposed into its components. The position vector of an arbitrary grain tip  $G_{ij}$  with respect to the wheel center  $S$  can be expressed as:

$$\underline{R}_{SG_{ij}} = \underline{R}_{SS_i} + \underline{R}_{S_iC_i} + \underline{R}_{C_iG_{ij}} \quad (6.8)$$

or similarly

$$\underline{R}_{SG_{ij}} = \underline{R}_{SC_i} + \underline{R}_{C_iG_{ij}} \quad (6.9)$$

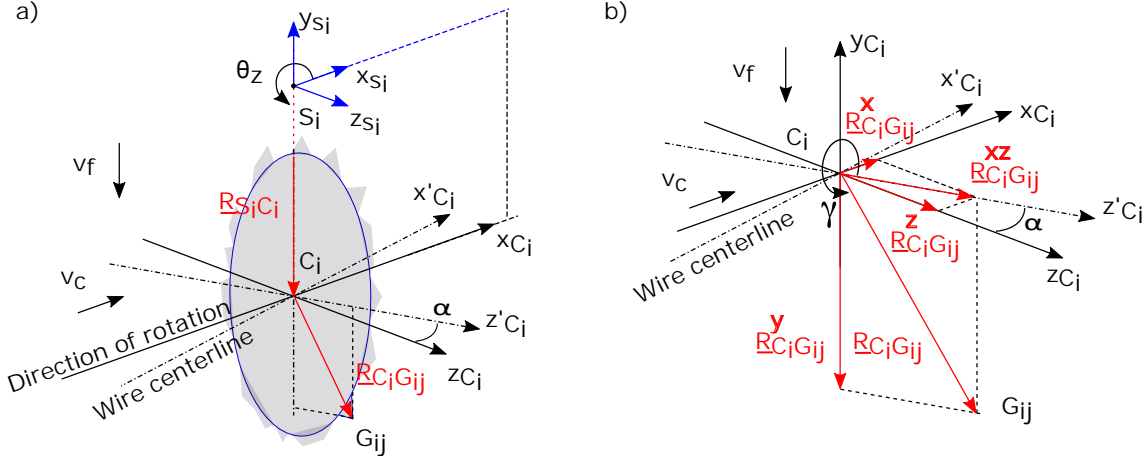


Figure 6.15: Position and direction of the grain tip  $G_{ij}$  on wire cross-section  $C_i$ .

The 3D position vector of an arbitrary grain tip  $G_{ij}$  with respect to the wheel attached coordinate system with its origin at  $S$  can be expressed in array form:

$$\underline{R}_{SG_{ij}} = \begin{bmatrix} |\underline{R}_{SC_i}| \cos\theta_c \cos\theta_z + |\underline{R}_{C_iG_{ij}}| \cos\gamma \sin\alpha \\ |\underline{R}_{SC_i}| \cos\theta_c \sin\theta_z + |\underline{R}_{C_iG_{ij}}| \sin\gamma \\ |\underline{R}_{SC_i}| \cos\theta_c + |\underline{R}_{C_iG_{ij}}| \cos\gamma \cos\alpha \end{bmatrix} \quad (6.10)$$

The position of a wire cross-section on the workpiece surface is visualized in Figure 6.16 in  $y-z$  plane, where the wire cross-section is asymmetrical around  $y$  axis due to the wire wrap angle  $\alpha$ . The chipping thickness  $h_{cu}$  is orthogonal to the cutting direction and perpendicular to  $\underline{R}_{C_iG_{ij}}$ .

The positions of cross-sections of a single wire wrap on the WWGW surface is visualized in Figure 6.17.



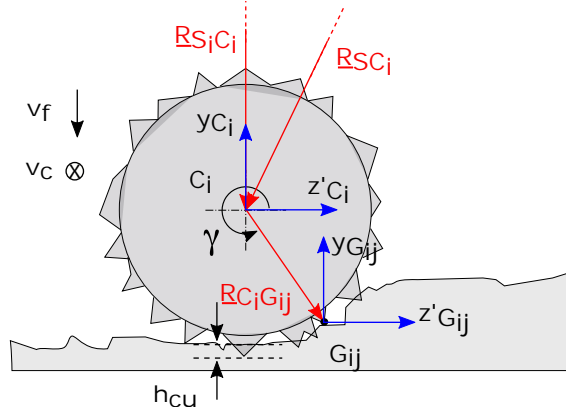


Figure 6.16: Position of the wire cross-section  $C_i$  and the grain  $G_{ij}$  in the plane orthogonal to the cutting direction.

### 6.2.2 Grain Path and Grain Penetration

In the WWGW process, the path of an arbitrary grain on the wire surface can be represented as a combination of a rotation and a translation as described in Subsection 4.1.1. The discrete motion of an arbitrary wire cross-section center  $C$  is shown in 2D space in Figure 6.18. The point rotates around the coordinate system with its origin at  $S$ , by the step angle  $\theta_s$  in the counterclockwise direction and advances towards the workpiece by the feed per motion step  $s$ , that is the product of the feed rate  $v_f$  and the time between two consecutive positions  $L/v_c$  of point  $C$ .

The feed per motion step  $s$  can be expressed as:

$$s = (L/v_c) v_f \quad (6.11)$$

where  $L$  is the distance between two consecutive positions of the grain and is defined as  $L = | \underline{R}_{SC}^{xy} | \theta_s$ , where  $| \underline{R}_{SC}^{xy} |$  is the magnitude of the position vector of the wire cross-section  $C$  on the  $x - y$  plane and defined from the center  $S$  of the wheel attached coordinate system. The feed per motion step  $s$  can further be written as:

$$s = \frac{| \underline{R}_{SC}^{xy} | \theta_s}{v_c} v_f \quad (6.12)$$

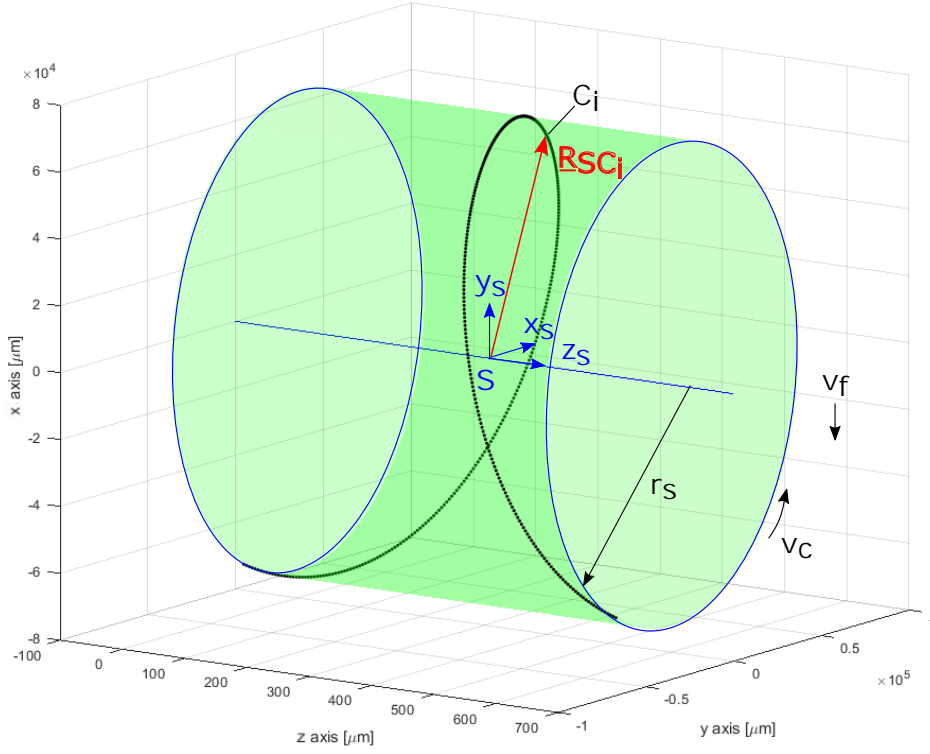


Figure 6.17: The cross-section positions of the simulation wire wrapped around the WWGW.

Hence, the transformation matrix for the motion of a point on the wire surface is:

$$\underline{\underline{M}}_{TR} = \begin{bmatrix} \cos\theta_s & -\sin\theta_s & 0 & 0 \\ \sin\theta_s & \cos\theta_s & 0 & -s \\ 0 & 0 & 1 & 0 \\ 0 & 0 & 0 & 1 \end{bmatrix} \quad (6.13)$$

The position of an individual grain tip can be expressed as dot product of the transformation matrix  $\underline{\underline{M}}_{TR}$  and the grain position vector  $\underline{R}_{SG_{ij}}$ :



### 6.2.3 Definition of the Workpiece Geometry

For the sake of simplicity, the concave workpiece geometry in the WWGW process is reduced to a flat model as described in Figure 6.19 where the dimensional parameters that are required for the definition of the surfaces are given. The workpiece is constructed of nodes in three directions with the node distances  $L_{mw}$  along its length,  $L_{nw}$  along its width and  $L_{zw}$  along its depth. The node distances can be individually defined for the desired resolution. For the simulation, the node spacing is set to  $L_{mw} = 0.17 \mu m$  and  $L_{nw} = L_{zw} = 0.1 \mu m$ .

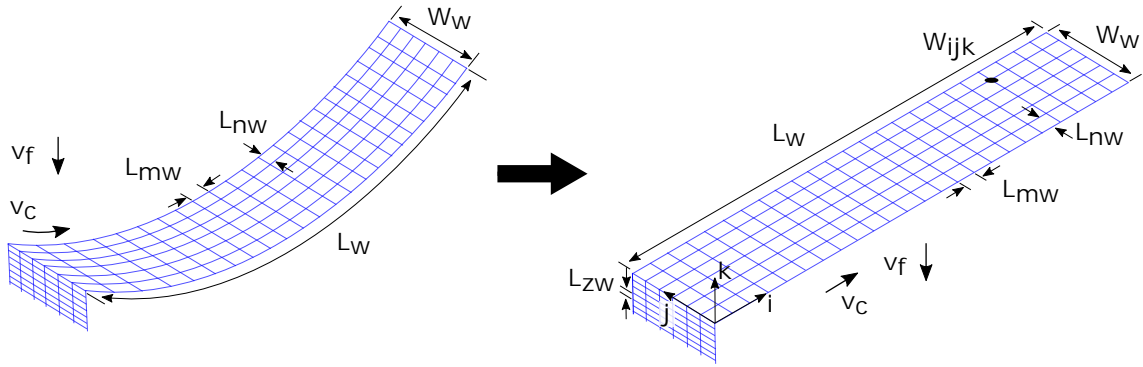


Figure 6.19: Concave and flat workpiece geometries and their respective node and dimensional parameters.

The original concave workpiece geometry is necessary to determine the position and penetration of each grain and acting forces on each angle position. The flat model geometry is used to simulate contact between the grain and workpiece, hence the material removal and grain wear.

Evaluation of the simulated workpiece surface can be done by evaluating the arithmetic mean roughness parameter  $R_a$  and the root mean square roughness parameter  $R_q$ :

$$R_a = \frac{1}{l_m} \int_0^{l_m} |Z(x)| dx \quad (6.17)$$

$$R_q = \sqrt{\frac{1}{l_m} \int_0^{l_m} Z^2(x) dx} \quad (6.18)$$

where  $l_m$  is the evaluated distance and  $Z(x)$  is the point deviation from the reference line.

## 6.3 Material Removal Model

For a complete description of the material removal model considering the ductile and brittle removal mechanisms, three primary definitions are required: the intersection area of the grain and workpiece, a criterion for the transition from ductile to brittle material removal modes and the definition of the workpiece removal area geometry, based on the active material removal mode.

The intersection area of the grain-workpiece contact depends on the wire topography, grain geometry, grain path and the topography of the workpiece surface at the respective contact position. The calculation of the contact area is based on the kinematic model presented in Section 6.2, the details of the removal simulation are presented in Chapter 8.

Following, a criterion defining the active material removal regime, namely the critical chipping thickness  $h_{cu,crit}$  is required. The critical chipping thickness model proposed by Bifano [31] is reviewed in Subsection 2.2.3 and given in Eq. (2.1). The model is developed based on the quasi-static indentation cases and based on the material properties  $E$ ,  $H$ ,  $K_{IC}$  and experimentally determined coefficient  $\kappa_c$ .

An experimental critical chipping thickness model is developed by employing several single grain scratch tests conducted on the Scratch Test Setup, presented in Subsection 4.1.2. For the determination of a critical chipping thickness threshold, scratch geometries are investigated for the present material removal modes. For each grain, 20 back to back scratches are done as shown in Figure 4.14b at the cutting speed of 10  $m/s$ .

Sample analysis from two scratches with ductile material removal (Figure 6.20) and brittle material removal (Figure 6.21) are given. For each, three arbitrary locations along the cut, at the lowest points of the scratches and their respective cross-section positions are indicated. In Figure 6.20, the scratch is considered ductile due to the size and number of shelling along its length. Higher brittleness is observed from right to the left side of the scratch (from point 3 with 0.266  $\mu m$  removal depth to point 1 with 0.545  $\mu m$  removal depth). This observation can be validated through the increasing cutting depths shown on the profile section plot below the image.

Figure 6.21 shows three highly brittle scratches with overlapping chipping areas. Similarly, three random positions are measured to show the interrelation of cutting depths and brittleness states of the scratches. In comparison to the ductile material

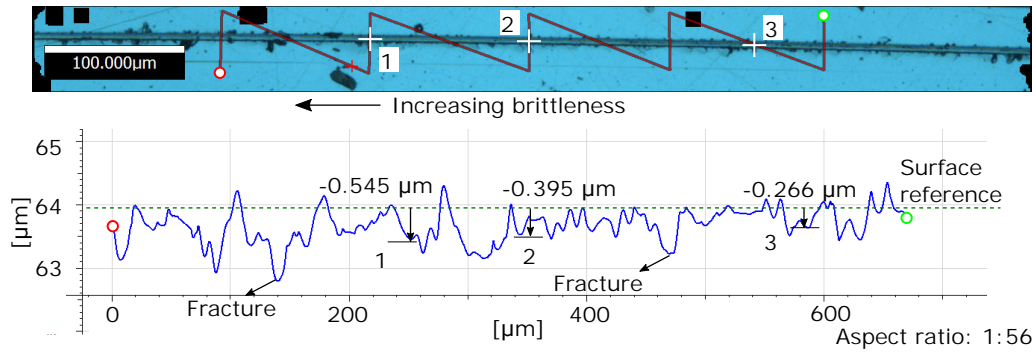


Figure 6.20: Top: A sample scratch with ductile material removal with the onset of brittle material removal mode. Bottom: Cross-section of the scratch with the indicated depths of three positions on its length.

removal, higher cutting depths in the vicinity of  $3 \mu m$  are measured, leading to extended chipping.

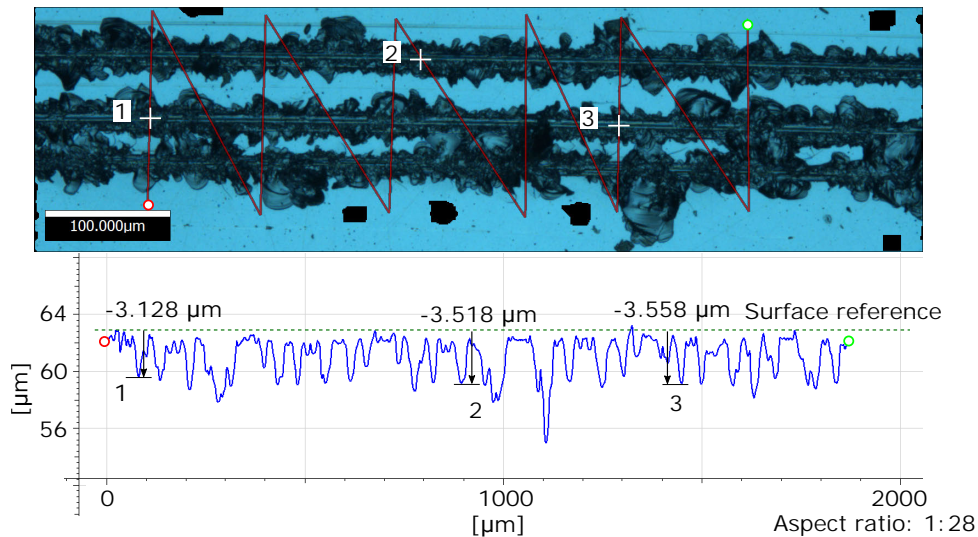


Figure 6.21: Top: Three scratches with brittle removal mode showing the overlapped fracture areas along their length. Bottom: Cross-section of the scratch with the indicated depths of three positions on its length.

A complete range of scratches showing the transition from ductile to brittle material removal is presented in Figure 6.22, where the color coded and real color Alicona IFM images are given on top and the median depths of the scratches given in the lower part. As brittle material removal is increasing from left to right of the figure, depth of the scratches, amount and size of chipping along the scratch lengths are increasing. The stochastic distribution of the material break-outs clearly show that in addition to the grain penetration and geometry, further effects such as dimensional inaccuracies, vibrations and/or material inhomogenities are present and influence the size and extent of fracture.

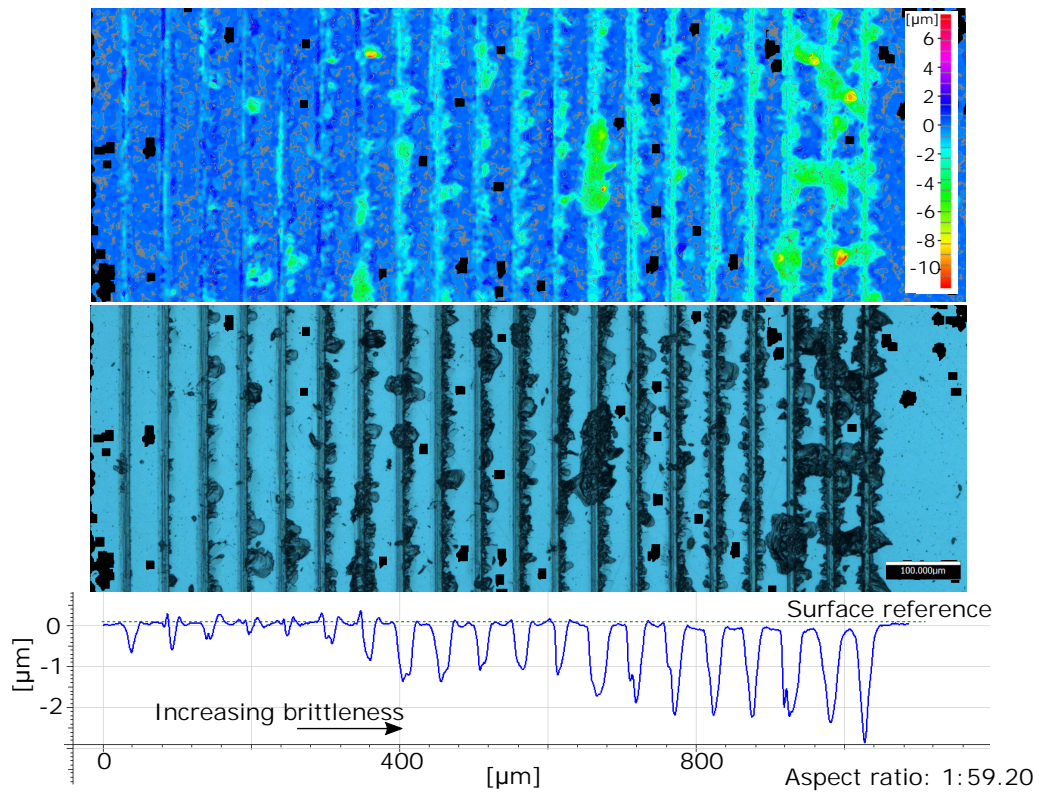


Figure 6.22: A full range of scratches showing the transition from ductile to brittle material removal and the median scratch depths increasing as the brittle removal mode is more evident.

Five categories are defined in the range of ductile to completely brittle material removal based on the median scratch depths. Figure 6.23 presents sample scratches from experiments and analysis result of 86 scratches of 6 grains with varying geometries. The size and extend of the scratches are considered for the determination of the removal mode. It can be stated that ductile to brittle transition starts in the vicinity of  $1.15 \mu\text{m}$  cutting depth.

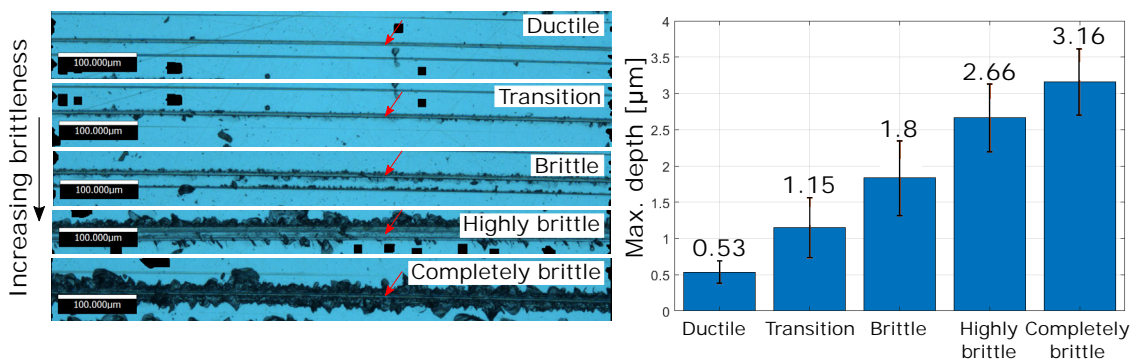


Figure 6.23: Left: A range of scratches for the definition of ductile, transition, brittle, highly brittle and completely brittle removal of Si workpiece. Right: The range of max. scratch depths for each removal mode.

Finally, definition of the workpiece groove dimensions based on the active material removal mode shall be introduced. In the case of ductile material removal regime, a widely used assumption is that the removed workpiece cross-section area in the direction orthogonal to the cutting direction is equal to the projection area of a grain in the same direction. Hence, the penetrated grain geometry is mapped onto the workpiece surface. However, in the brittle material removal case, a higher amount of material is removed due to lateral cracks propagating to the workpiece surface.

Determination of the crack sizes and the cross-section of the scratch in brittle machining mode is a highly complex problem. Developed models on this topic are focused on quasi-static cases of indentation with ideally sharp grain geometries. The static and quasi-static indentation hardness tests became the benchmark method for the determination of fracture characteristics of brittle materials [10]. The theoretical basis is discussed in Subsection 2.2.1. However, in the case of abrasive removal, variety of grain geometries, change in grain geometry due to wear, dynamic effects and influence of the workpiece crystallographic orientation results in further complexities. Meyer [162] states that the high strain rate in dynamic cases which is several orders of magnitude higher than the static indentation events, result in the change of material behavior significantly, also resulting in a considerable rise in temperature. Moreover, it should be noted that during scratching, the motion is in the direction parallel to the surface; and in the case of indentation, it is in the direction of the surface normal. In any case, the indentation method provides a widely applied and useful tool to estimate the fracture sizes in scratching of brittle materials as demonstrated by [15,218,219,227]. The presented brittle material removal model aims to transfer the reported crack system to abrasive scratching.

The cross-section of the workpiece showing the median/radial and lateral crack systems for brittle solids is shown in Figure 6.24a and illustrated for the case of grain scratching in Figure 6.24b. A peak point load  $F_n$  is applied onto the indenter with an included angle  $2\psi$  in the direction normal to the surface. The load  $F_n$  and dimension  $c_g$  define the extend of the force and resultant contact between the indenter and surface.

The lateral cracks denoted in Figure 6.24 are responsible with the material removal in the brittle regime and the length  $c_l$  of the lateral crack shows the location where it meets the workpiece surface. A compliance relation for the central deformation zone is developed by Marshall [155]. It is suggested that the thickness of material  $h_p$  above the crack plane can be approximated by the depth of the plastic zone, where lateral cracks are originated from. The boundary of the half-circle shaped plastic zone is then approximated by [155]:



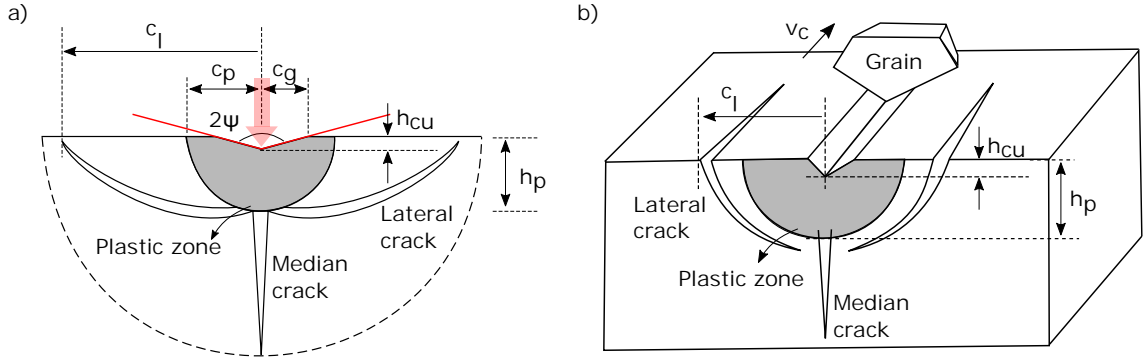


Figure 6.24: (a) Plastic zone, lateral and median cracks resultant of Vickers indentation [155]. (b) Schematics of an abrasive grain removing material from the workpiece surface [32].

$$h_p \approx c_p \approx [(E/H)^{1/2}(\cot\psi)^{1/3}(F_n/H)^{1/2}] \quad (6.19)$$

The case of Vicker's indentation of brittle materials is transferred to grinding by Bifano [32] to establish a relationship between the specific grinding energy and depth of cut. It is suggested that there is a power-law relationship between the lateral crack length  $c_l$  and the grain penetration depth  $h_{cu}$  and the diameter of the plastic zone is approximately equal to  $c_l$ . The relationship between the depth  $h_p$  of the plastic zone and grain penetration depth  $h_{cu}$  is proposed by [32]:

$$h_p \approx h_{cu}^{4/3} \quad (6.20)$$

The equilibrium crack size  $c_l$  is calculated as a function of the applied load, defined in [155]:

$$c_l = c^L [1 - (F_0/F_n)^{1/4}]^{1/2} \quad (6.21)$$

where  $c^L$  is called the limiting crack function and  $F_0$  is the apparent threshold load which is defined in [155]:

$$F_0 = (\zeta_0/A^{1/2})(\cot\psi^{-2/3})(K_{IC}^4/H^3)(E/H) \quad (6.22)$$

where  $\zeta_0$  and  $A$  are dimensionless constants independent of the material pair. The value of  $A$  and  $\zeta_0$  have been estimated by [155]. For the relative sizes of the lateral and radial cracks,  $A = 3(1-\nu^2)/4\pi$  for a full-plate approximation (lateral  $\gg$  radial),

$A = 0.75$  for a quarter-plate approximation (lateral < radial); and  $\zeta_0 = 1200$  for all cases.

The limiting crack function is derived by [155]:

$$c^L = \left\{ \left( \frac{\zeta_L}{A^{1/2}} \right) (\cot\psi)^{5/6} \left[ \left( \frac{E}{H} \right)^{3/4} / K_{IC} H^{1/4} \right] \right\}^{1/2} F_n^{5/8} \quad (6.23)$$

where  $\zeta_L$  is another dimensionless constant independent of the material pair and is given as  $\zeta_L = 0.025$ .

It is now essential to evaluate the presented model in dynamic conditions. To determine the conditions on the Si surface and identify crack sizes in brittle mode machining, several scratch tests are conducted with grains of varying geometries. The scratching experiments are conducted with six diamond grains performing 86 consecutive scratches using the methodology described in Subsection 4.1.2. Four of the grains are presented in Figure 6.25, where 3D geometries are shown together with their cross-sections orthogonal to the cutting direction. The grain geometries vary in dimension and shape.

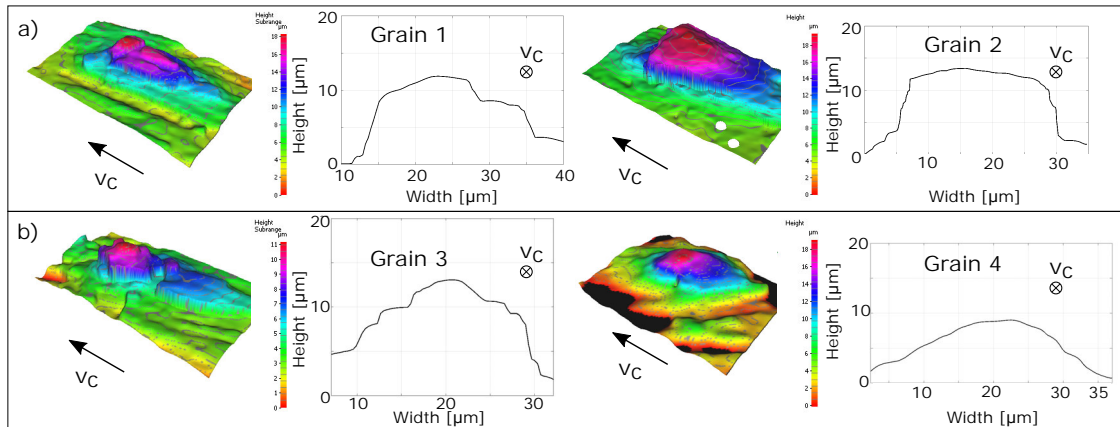


Figure 6.25: Four grains that are used to determine the relationship between the grain geometries and material removal volume: (a) dull grains (b) sharp grains.

The median profile of a scratch averaged over a distance of  $700 \mu m$  is presented in Figure 6.26a. The scratch depth  $h_{sc}$  is assumed to be equal to the depth of plastic zone  $h_p$  in Figure 6.24. The lateral crack size  $c_l$  is indicated. The groove cross-section area is the area confined with the groove boundary and the surface reference passing at  $y = 0$ . The dimensions of a representative grain is given in Figure 6.26b. The grain penetration depth  $h_{cu}$ , its width at the penetrated distance  $c_g$  and the penetrated area  $A_{cu}$  are indicated.

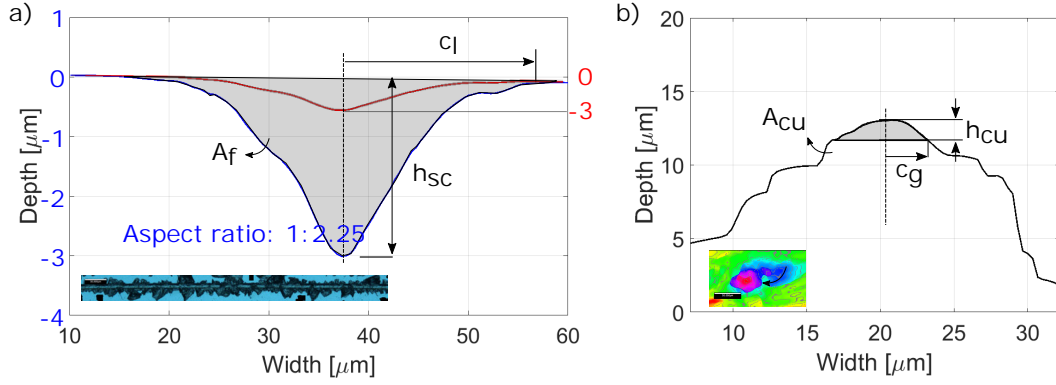


Figure 6.26: (a) Median profile of a brittle scratch. The red outline denotes the original scratch geometry and the blue plot has the indicated aspect ratio. (b) Dimensions of the cross-section of the grain responsible.

The fractured workpiece cross-section area  $A_f$  in the direction of cut can be best approximated with an ellipse with the radii  $c_l$  and  $h_{sc}$ :

$$A_f = \frac{c_l \cdot h_{sc} \cdot \pi}{2} \quad (6.24)$$

Mechanical properties of sc-Si and single-crystal diamond are presented in Table 6.1.

Table 6.1: Mechanical properties of sc-Si and Type IIa single-crystal diamond at 300 K.

	sc-Si	Diamond
<b>Elastic modulus <math>E</math> [GPa]</b>	162 [181]	910-1250 [163]
<b>Hardness <math>H</math> [GPa]</b>	10	60-100 [163]
<b>Fracture toughness <math>K_{IC}</math> [MPa<math>\sqrt{m}</math>]</b>	0.6	3.4-5 [67]
<b>Poisson's ratio <math>\nu</math> [-]</b>	0.278 [25]	0.10-0.29 [163]

Figure 6.27 shows the measurements of the lateral crack lengths  $c_l$  of the scratches conducted with 6 individual diamonds, plotted as a function of the grain penetration depth  $h_{cu}$ , and the outputs of the proposed brittle material removal model. The model employs the initial penetrated grain cross-sections measured with the MATLAB code and half-included tip angles that are assumed to be  $60^\circ$  at all times. The normal force in Eqs. (6.21) and (6.23) are calculated using the modified Kienzle force model (Eq. (6.30)), to be introduced in Section 6.4. The influence of grain wear from the consecutive scratches is ignored.

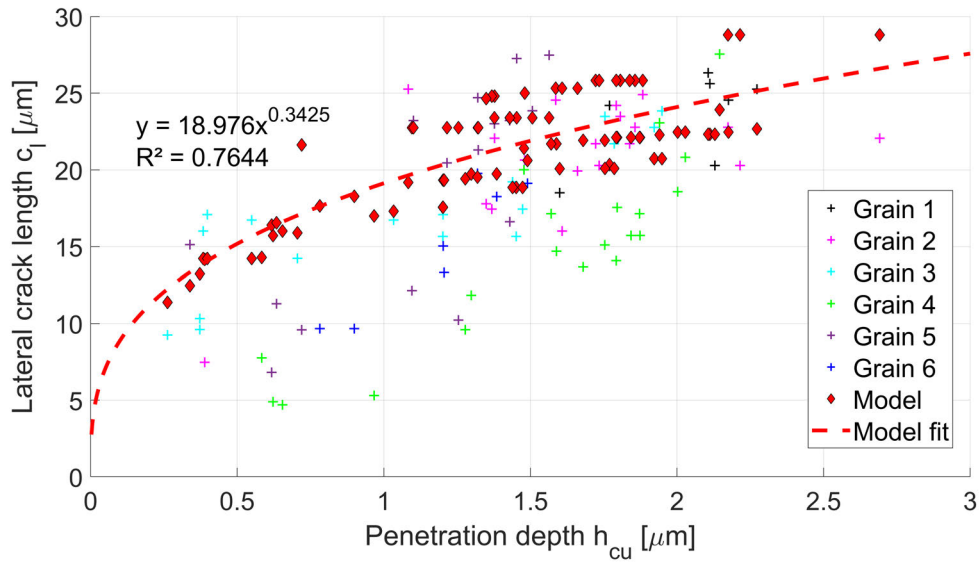


Figure 6.27: The lengths of lateral cracks from scratching experiments estimated with the developed model and the model fit.

Figure 6.28 shows the model fit and simulated crack dimensions for individual grains. The correlation between penetration depths and the corresponding lateral crack lengths show the same trend with the model fit. However, as the result of variations in grain and contact dimensions i.e. the ratio of grain penetration depth to the width of penetration, grain sharpness or grain wear, the removal area varies at the same penetration depths. For example grain 4 results in shorter lateral cracks in comparison to grain 3 at the same penetration depths.

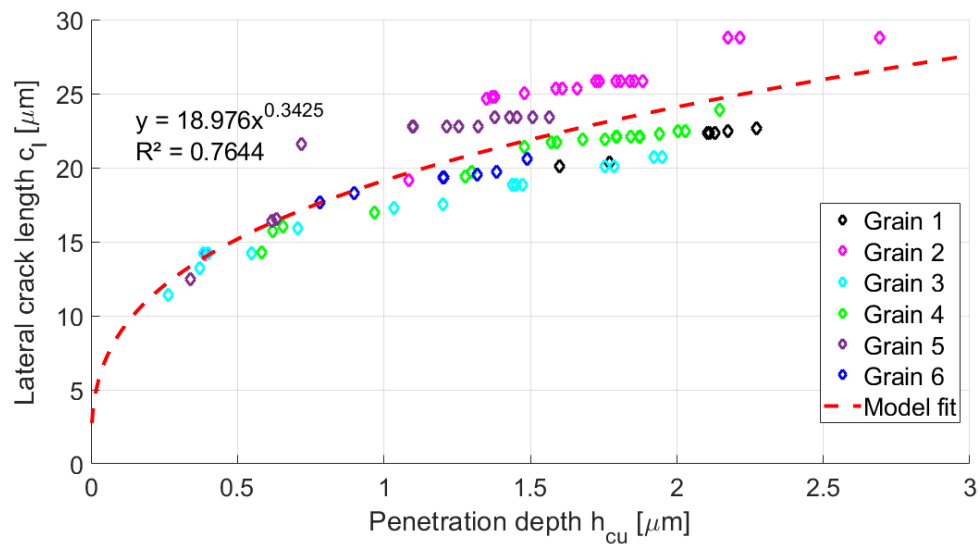


Figure 6.28: Simulated lateral crack lengths for individual grains and the model fit.

The lateral crack length as a function of the grain penetration depth can be estimated as:

$$c_l = 18.976 \cdot h_{cu}^{0.3425} \quad (6.25)$$

## 6.4 Force Model

Forces in metal cutting can be determined by modifying the empirical relationship that was established by Kienzle [109]:

$$F_c = k_{c1.1} \cdot b_{cu} \cdot h_{cu}^{1-m_c} \quad (6.26)$$

where  $b_{cu}$  and  $h_{cu}$  are the cut width and undeformed chip thickness respectively,  $k_{c1.1}$  is the specific cutting force required to remove a chip of width  $b_{cu} = 1 \text{ mm}$  and depth of  $h_{cu} = 1 \text{ mm}$ , and  $m_c$  is a parameter depending on the workpiece material and must be determined experimentally. The equation is originally developed for single-point cutting processes and the complexity associated with the interaction geometries between the abrasive grains and workpiece makes determination of the cut width and depth impossible. Thus, a modification of the Kienzle equation is proposed. The specific cutting force is defined as the ratio of the cutting force and removed chip cross-section area:

$$k_c = \frac{F_c}{A_{cu}} \quad (6.27)$$

Kienzle [110] determined the main value of the  $k_c$  in the model where  $b_{cu} = h_{cu} = 1 \text{ mm}$  and  $A_{cu} = 1 \text{ mm}^2$ . Considering the specific cutting force is strongly dependent on the cutting area, it can be written that:

$$k_c = \frac{k_{c1}}{A_{cu}^{m_c}} \quad (6.28)$$

where  $k_{c1}$  is the specific cutting force corresponding to the removal area of  $1 \text{ } \mu\text{m}^2$ . The relationship between  $k_c$  and  $A_{cu}$  can be determined empirically. Figure 6.29 shows the force measurement results of 82 scratches conducted with 6 grains with varying geometries, plotted in a double logarithmic scale. The corresponding linear

equation can be written as:

$$\log(k_c) = -m_c \cdot \log(A_{cu}) + \log(k_{c1}) \quad (6.29)$$

where  $k_c$  is in  $[N/\mu m^2]$ ,  $A_{cu}$  is in  $[\mu m^2]$  and  $m_c$  is non-dimensional.

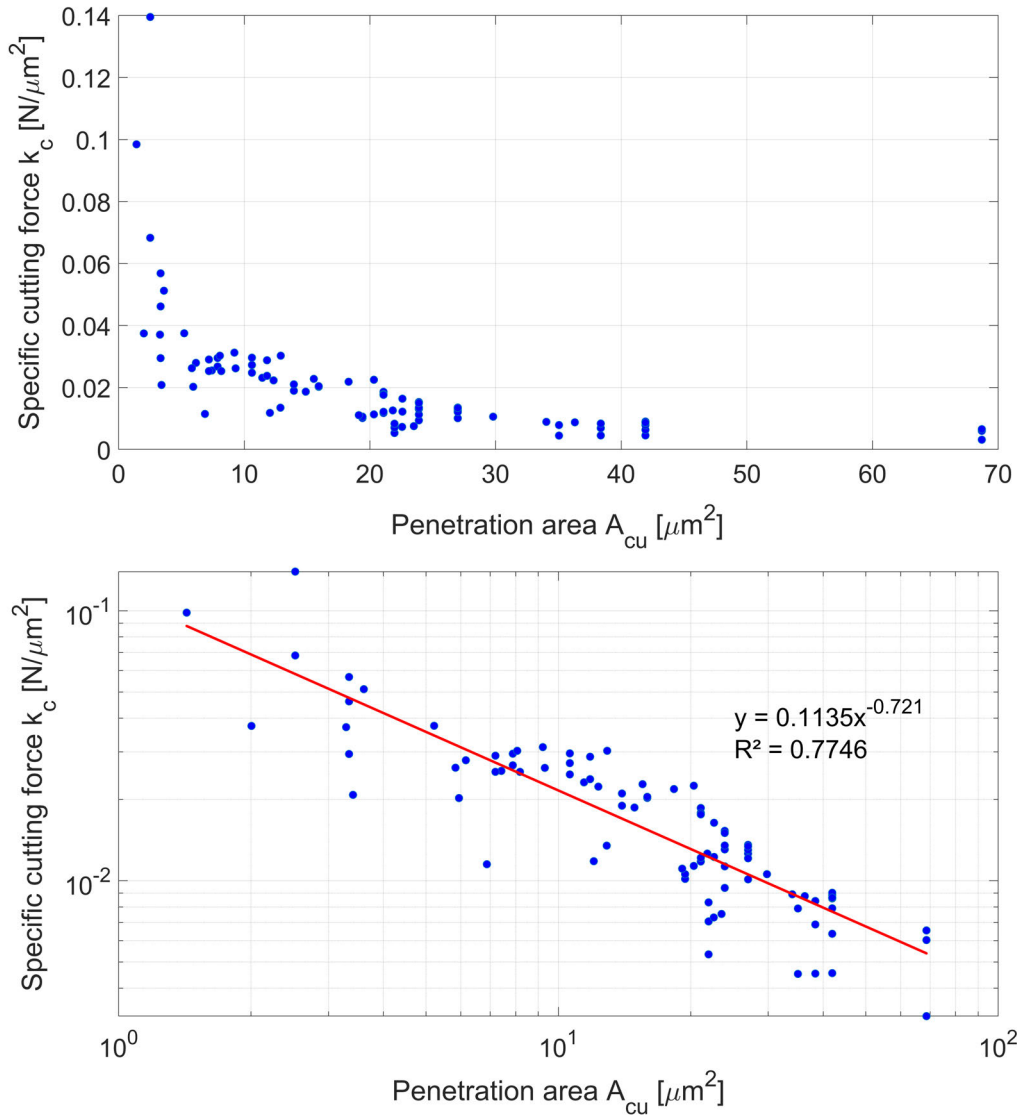


Figure 6.29: Top: Correlation between the specific cutting force  $k_c$  and cutting area  $A_{cu}$ . Bottom: Correlation between the specific cutting force  $k_c$  and cutting area  $A_{cu}$  in double logarithmic scale.

The comparison of the specific cutting force  $k_{c1}$  and material constant  $m_c$  at the cutting speeds of 10 and 20  $m/s$  is presented in Figure 6.30. The regression results show that at the cutting speed of 10  $m/s$ ,  $k_{c1} = 0.1135 N/\mu m^2$  and  $m_c = 0.721$ ; and at the cutting speed of 20  $m/s$ ,  $k_{c1} = 0.0647 N/\mu m^2$  and  $m_c = 0.558$  are determined as the model coefficients. It is evident that, at a lower cutting speed, the cutting

force will be higher at the same depth of cut, which can be mainly explained with the fracturing properties of silicon. The brittle removal mode is dominant at the higher cutting speed, which means that for the timely average, which the force measurement platform does, the force relief after crack initiation brings the averaged force down.

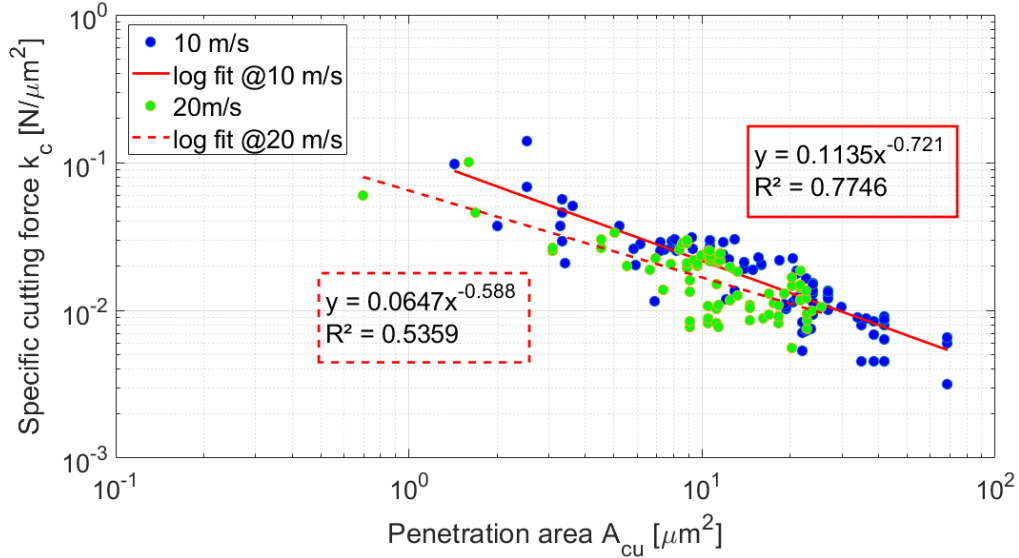


Figure 6.30: Comparison of the specific cutting force  $k_c$  and cutting area  $A_{cu}$  at  $v_c = 10$  and  $20$  m/s.

Combining Eqs. (6.27) and (6.28), the cutting force  $F_{c,i}$  of grain  $i$  at time  $t$  then can be written as:

$$F_{c,i}(t) = k_{c1} \cdot A_{cu,i}^{1-m_c}(t) \quad (6.30)$$

where  $A_{cu,i} [\mu m^2]$  is the cutting area of grain  $i$ . The total cutting forces acting at time  $t$  is the sum of the forces acting on individual grains and can be expressed as:

$$F_c(t) = \sum_{i=1}^n F_{c,i}(t) \quad (6.31)$$

where  $n$  is the number of active grains at time  $t$ . The normal force acting on the grain  $i$  can be approximated by:

$$F_{n,i} = \frac{F_{c,i}}{\epsilon_f} \quad (6.32)$$

where  $\epsilon_f$  is the grinding force ratio between  $F_n$  and  $F_c$  and determined empirically.

A further description is required to compare the modeled forces to the forces measured with the force sensor due to the differences in directions as schematically described in Figure 6.31. Initially a conversion is required for the simulated normal forces of the grains on wire cross-section peripheral:

$$F_n^s = F_n^{s0} \cdot \cos(\gamma_s) \quad (6.33)$$

where  $F_n^s$  and  $F_n^{s0}$  are the normal forces acting on the grain and  $\gamma_s$  is expressed as:

$$\gamma_s = | 3\pi/2 - \gamma | \quad (6.34)$$

To convert the simulated force to measured ones, it can be shown that:

$$F_c^k \begin{cases} F_c^s \cdot \cos(\beta_s) - F_n^s \cdot \sin(\beta_s), & \beta_s < 3\pi/2 \\ F_c^s \cdot \cos(\beta_s) + F_n^s \cdot \sin(\beta_s), & \beta_s > 3\pi/2 \end{cases} \quad (6.35)$$

$$F_n^k \begin{cases} F_c^s \cdot \sin(\beta_s) + F_n^s \cdot \cos(\beta_s), & \beta_s < 3\pi/2 \\ F_n^s \cdot \cos(\beta_s) - F_c^s \cdot \sin(\beta_s), & \beta_s > 3\pi/2 \end{cases} \quad (6.36)$$

where  $F_c^{s0}$  and  $F_n^{s0}$  are the force components of individual grains in the coordinate system of the cutting contact, while  $F_c^k$  and  $F_n^k$  are the components transformed to the coordinate system of the dynamometer platform and  $\beta_s = 3\pi/2 - \theta_z$ .

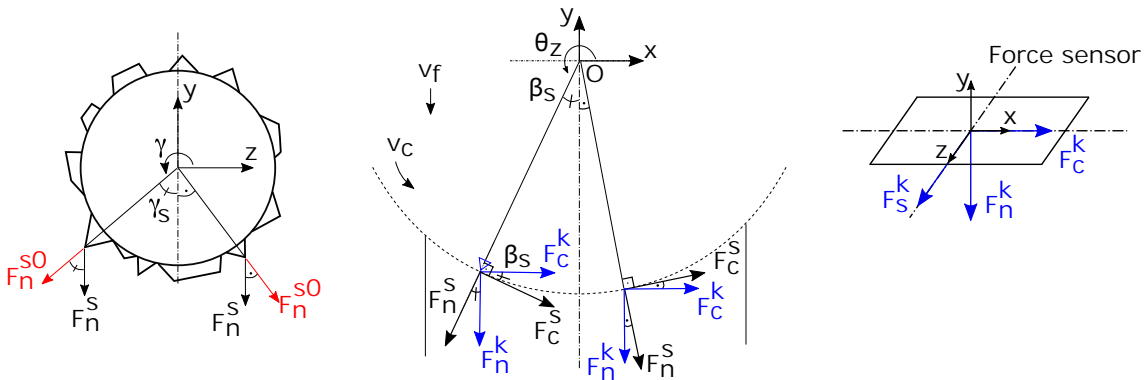


Figure 6.31: Transformation of force components from the local cutting contact coordinate system to the coordinate system of the force measuring platform.



The specific energy of chip formation can be determined through employing the force model to evaluate the influence of various cutting speeds on the specific energy of chip formation in identical chip thicknesses. The specific energy can be expressed as:

$$u = \frac{F_c \cdot v_c}{h_{cu} \cdot b_{cu} \cdot v_f} \quad (6.37)$$

where  $u$  is the specific energy,  $v_c$  is the cutting speed,  $h_{cu}$  is the undeformed chip thickness,  $b_{cu}$  is the cut width and  $v_f$  is the feed rate. The numerator in Eq. (6.37) is the power and the denominator is the volumetric material removal rate for a single grain. Assuming a rectangular grain edge, Eq. (6.30) takes the form:

$$F_c = k_{c1} \cdot (h_{cu} \cdot b_{cu})^{1-m_c} \quad (6.38)$$

Combining Eqs. (6.30) and 6.37, the specific energy  $u$  can be written as:

$$u = \frac{k_{c1} \cdot (h_{cu} \cdot b_{cu})^{-m_c} \cdot v_c}{v_f} \quad (6.39)$$

Through employing the specific cutting forces and exponents determined for the cutting speeds of 10  $m/s$  ( $k_{c1} = 0.1135 \text{ N}/\mu\text{m}^2$ ,  $m_c = 0.721$ ) and 20  $m/s$  ( $k_{c1} = 0.0647 \text{ N}/\mu\text{m}^2$ ,  $m_c = 0.558$ ), and setting  $b_{cu} = 2 \mu\text{m}$  and  $v_f = 1.8 \text{ mm}/\text{min}$ , Figure 6.32 presents the influence of varying cutting speeds on the specific energy of chip formation.

It can be seen that as the undeformed chip thickness increases, lower amount of energy is required to remove the same volume of Si material due to the size effect at both cutting speeds. The model suggests that with increasing cutting speeds, power increases. On the other hand, the single grain scratch tests show that process forces decrease with increasing cutting speeds for Si material. Hence it can be stated that an increase in the cutting speed has a greater influence on power than it has on the process forces, which results in an increase in the specific energy of chip formation when the undeformed chip thickness is higher than a certain value. In addition, below a certain value, where ductile material removal is more evident, the behavior reverses which may be the result of the change in material removal mechanism. It should be noted that the model doesn't distinguish the process forces for ductile and brittle material removal regimes, but rather suggests an average force.

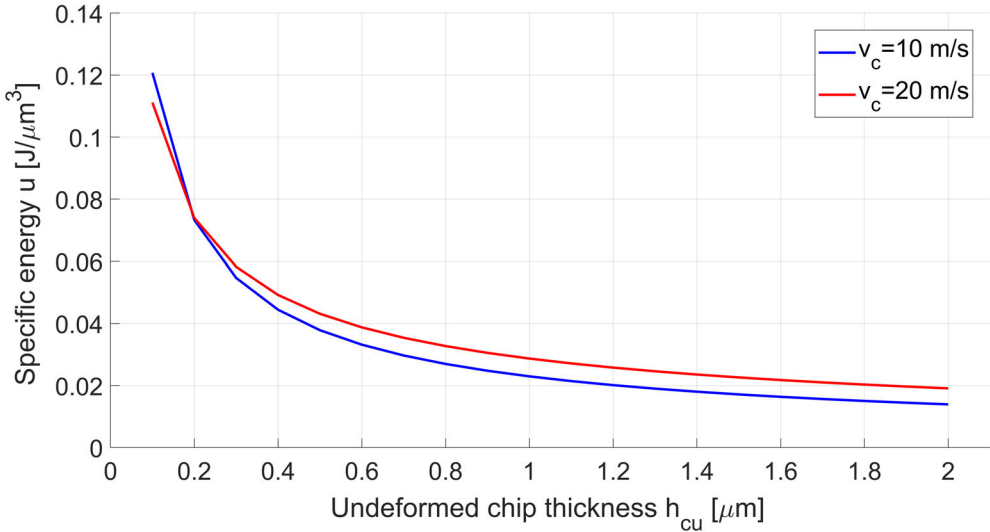


Figure 6.32: Comparison of the specific energy of chip formation in identical undeformed chip thicknesses at  $v_c = 10$  and  $20$  m/s.

# Chapter 7

## Wear

*“Wear is not a material property. It is a system response.”*

— Raymond G. Bayer,  
*Mechanical Wear Prediction and Prevention, 1994*

The following chapter considers the wear phenomenon in diamond wire sawing of silicon based on the WWGW process, through experimental analysis and theoretical description of the wear mechanisms, influencing parameters and developed models. A detailed review of the abrasive grain wear and wear modeling approaches in abrasive machining processes are introduced in Subsection 2.4.3 of the Literature Review Chapter. The most influential wear parameters can be stated as:

- Properties of the abrasive grain
- Properties of the work material
- Characteristics of the bond and size of the grain-bond interface
- Sliding distance, time of contact
- Cutting speed
- Contact stress
- Temperature in the cutting zone
- Amount, efficiency and type of coolant

The influence of these parameters makes the abrasive grain wear a highly complex issue, as well as the complexities resulted from the kinematics of the abrasive process itself. In this direction, the wear shall be studied as a system, considering its parameters and their dependencies as simple as possible.

It is the primary concern to determine the dominant wear mechanisms and their influencing elements for the modeling of abrasive grain wear. A reasonable approach is to identify the wear mechanisms and when possible, to isolate the influencing parameters for a definitive understanding of their effects. A relevant model that explains the wear behavior shall be defined, based on the approaches discussed previously in the Literature Review Chapter 2. In addition, definition of the wear criteria are required for the identified wear modes in order to simulate the wear.

## 7.1 Evaluation of the Wear Mechanisms

For the determination of the wear mechanisms and the wear progress, an initial set of experiments is conducted at the wire speed of 50  $m/s$  and the feed rate of 0.9  $mm/min$  with Asahi 12-25 standard concentration wire with 140  $\mu m$  core diameter. The results are discussed in Section 5.4 where the wear of individual grains are evaluated by investigating the grain geometry, protrusion, base area and volume. Identified wear modes are addressed and deviation of the process forces throughout the wire lifetime are shown. The evaluation of wear is conducted with the Wire Analysis Software which is introduced in Subsection 4.3.1 on the samples taken with the imprinting method described in Subsection 4.2.4. The initial experiments show that the reduction of the grain protrusion and volume can be explained with the power-law behavior (Figure 5.13). The primary wear modes identified in diamond wire sawing of silicon are the grain dulling/rounding off edges, fracture of diamonds and grain pullouts mainly at the end of the wire lifetime.

For the validation of the wear model that is presented in Section 7.2, experiments are conducted on the WWGW setup at the wire speeds of 30 and 60  $m/s$  and the feed rate of 1.8  $mm/min$ . Asahi 12-25 standard concentration wire with 120  $\mu m$  core diameter is used for the experiments and the same sampling and analysis methods are used for the experiments as for the initial wear tests. Figure 7.1 shows the increments on the workpiece positions where wire topography samples are taken and workpiece surfaces are measured.

It is evident that the wear behavior differs throughout the abrasive tool lifetime and wear occurs in different forms and also in combination. In the initial phase, the grains with higher protrusion will take the initial load and lead to failure as stated by [242]. Further, grain fracture which can be explained as the result of high stresses acting on the grains due to mechanical or thermal effects and/or presence of cracks in the abrasive grain takes place. Fracture occurs when the induced stresses

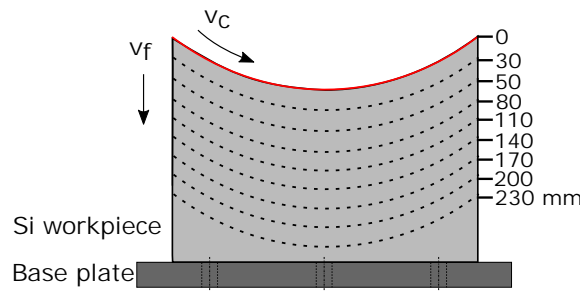


Figure 7.1: Sampling points along the wheel depth over the silicon workpiece.

exceed the grains' rupture strength and results in micro- and macro-breakouts from the abrasive grain surface; and it is considered comparable to the undeformed chip thickness [76].

A continuous wear of the diamond grain is possible through micro-breakouts from its surface with fracturing and rounding/dulling of the grain edges. The distinction between micro- and macro-fractures lays on the size of the separation from the grain's surface and depends on the contact conditions between the grain and the workpiece as well as the characteristics of the diamond. However, determination of the diamond breaking strength is not an elementary issue and depends on several parameters such as the form, homogeneity, crystallographic orientation, inclusions etc. Figure 7.2 shows two grains which experienced micro-fractures together with their color coded images. The locations of the separation are indicated with red arrows. It is evident that the grain micro-fracture occurs at the grain peaks, where the initial contact happens.

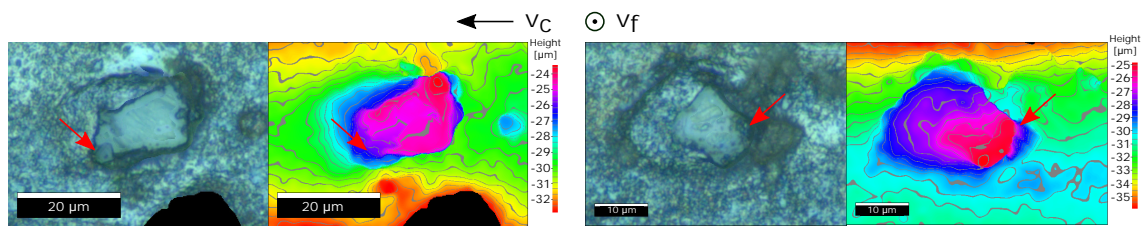


Figure 7.2: Two grains with micro-fracture wear. Real color Alicona IFM images shown on left, color coded images shown on the right.

Examples of two grains with macro-fracture wear are presented in Figure 7.2. The real Alicona IFM and color coded images are shown on top and the maximum of the grain cross-sections orthogonal to the cutting direction, effective in material removal are given below each grain image and the fractured grain parts are shown. The breakouts occur at the highest grain cross-sections leading to a reduction of grain protrusion. As well as micro-breakouts, it is not an elementary task to predict the direction or size of macro-breakouts.

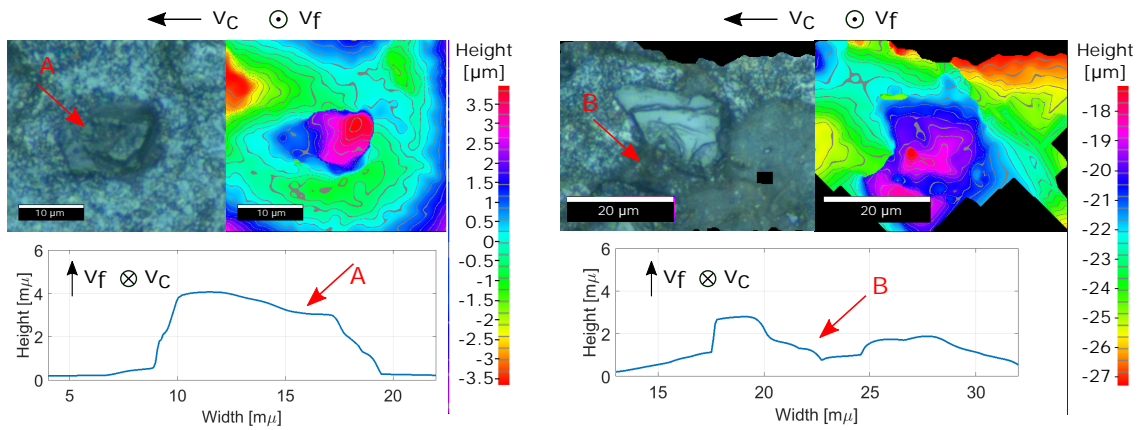


Figure 7.3: Two grains with macro-fracture wear are shown. Real color Alicona IFM images shown on left, color coded images shown on right; the maximum of the cross-sections orthogonal to the cutting direction are shown below.

The grain pullout depends on the embedded grain area, bonding strength and the stresses acting on the grain. It is evident that a pullout may occur at the initial stages of the wear as well as towards the end of the wire lifetime. Grain pullout happens when the acting force is larger than the grain retention force and the grain breakout is prevented due to its high grain strength. When the grain retention force is low, the abrasive grain is pulled out before reaching the end of its lifetime, resulting in efficiency loss [99]. On the other hand, always some grains are not sufficiently attached to the wire and those break out prematurely. However, grain dulling, is a continuous wear type. As a result of dulling the stresses acting on grains will increase and eventually lead to grain pullouts or macro-fracture.

An incident of grain pullout from the scratching experiments is shown in Figure 7.4, where the initial and final states of the grain are shown on the left with real color Alicona IFM and color coded images; and the grain cross sections of the two states orthogonal to the cutting direction are shown on the right. Through investigating the pre-scratch grain and void geometries, it is possible to establish a criterion for the grain pullout.

## 7.2 Wear Model

The initial phase of the diamond wire wear can be defined in two parts: wear of the bond over the abrasive grain (bonding material caps), which is rapid compared to the diamond wire wear; and the initial phase of diamond wear, where the load is borne by grain asperities. However, the wear of bonding material caps should be distinguished from the bonding wear, where the latter is responsible for grain retention. In the

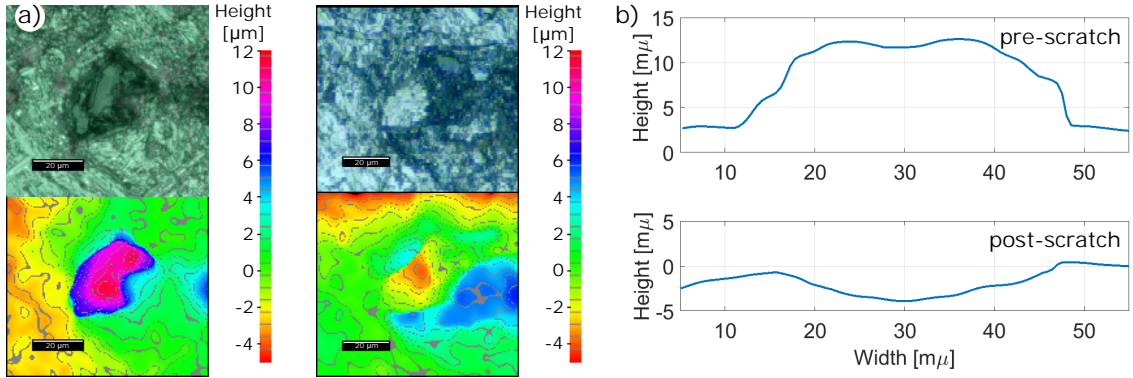


Figure 7.4: (a) Real color Alicona IFM and color coded images of initial and pulled out grain from a grain scratching experiment. (b)-top: Initial grain profile orthogonal to the cutting direction. (b)-bottom: Pulled out grain profile orthogonal to the cutting direction.

second phase, the wire topography reaches a more even grain protrusion height distribution and the load is distributed among the abrasive grains, leading to a more stable wear behavior. The abrasive grain wear progress can be expressed in the direction of the model developed by Takeyama [201], stating the relation of the wear rate and temperature, based on the reaction rates with an Arrhenius-type equation (Eq. (2.7)), the contact-based wear model developed by Usui [212], which considers the stresses acting on the grain, sliding distance and contact temperature (Eq. (2.8)) and by Jiang [104], who considers the sliding distance, cutting force, cutting speed and temperature effects in Eq. (2.9), in a similar manner to Takeyama [201]:

$$\frac{dW}{dt} = K \cdot F_c(t) \cdot v_c \cdot e^{\left(-\frac{E_a}{R_g \cdot T_f}\right)} \quad (7.1)$$

where  $dW/dt$  [ $mm^3/s$ ] is the time dependent wear,  $K$  [ $mm^3/Nm$ ] is the wear coefficient,  $F_c(t)$  [ $N$ ] is the cutting force acting on the grain at time  $t$ ,  $v_c$  [ $m/s$ ] is the cutting speed,  $T_f$  [ $K$ ] is the flash temperature at the grain tip,  $E_a$  is the activation energy and  $R_g$  is the universal gas constant.

The exponential term ( $E_a/R_g \cdot T_f$ ) comes from the Arrhenius equation that describes the effect of temperature on reaction rates. The term  $E_a/R_g$  depends on the contact characteristics of the two materials and can be assumed to be constant with limited variations in the contact conditions [213]. The term  $E_a/R_g$  can be replaced by a constant  $B$  that represents the temperature dependent effects and the probability of occurrence of a wear event [125]. In the case of diamond wire wear, in the initial wear phase, the wear of bonding material caps is rather rapid compared to the diamond wear. The assumption of constant contact conditions is reasonable, if the long duration of the wear progress is considered.

The alteration of the grain geometry with progressing wear and some parameters for the description of wear are presented in Figure 7.5. The initial grain penetration depth  $h_0$  is changing with the time dependent wear  $W(t)$ , leading to a decrease in grain protrusion height.

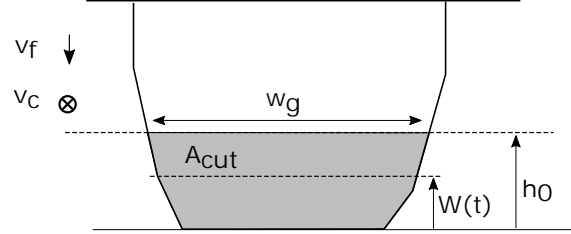


Figure 7.5: Grain wear parameters required for the wear calculation and the change of the orthogonal grain area.

The cutting force in Eq. (7.1) is changing with time and requires modification with progressing wear. The increase of load on grain is the result of grain dulling. With increasing time of contact, the grain gets duller, leading to an increase in the stress acting on the grain. The increasing load with progressing wear can be expressed with the increasing specific cutting force  $k_{c1}$ , an approach implemented by Wegener [223] and Kuffa [120]. Using the modified Kienzle force model given in Eq. (6.30), the evolution of the cutting force can be expressed as:

$$F_c(t) = \underbrace{k_{c1} \cdot \left(1 + M \cdot \frac{W(t)}{h_{lim}}\right)}_{k'_{c1}} \cdot A_{cut}(t)^{(1-m_c)} \quad (7.2)$$

where  $k'_{c1}$  is the modified specific cutting force,  $M$  is a coefficient considering the dulling characteristics of the edge and  $h_{lim}$  is the grain wear limit. The value of  $h_{lim}$  denotes the average maximum grain protrusion height loss reached at the end of the wire lifetime, where the wire lifetime is defined by the user based on the process requirements. Considering the grain width  $w_g$  as constant over the wear progress, the change in the development of the orthogonal grain area can be written as:

$$A_{cut}(t)^{(1-m_c)} = [(h_0 - W(t)) \cdot w_g]^{(1-m_c)} \quad (7.3)$$

Hence, the time dependent cutting force  $F_c(t)$  is defined through:

$$F_c(t) = k_{c1} \cdot \left(1 + M \cdot \frac{W(t)}{h_{lim}}\right) \cdot [(h_0 - W(t)) \cdot w_g]^{(1-m_c)} \quad (7.4)$$



The wear model in Eq. (7.1) therefore takes the form:

$$\frac{dW}{dt} = K \cdot v_c \cdot e^{\left(-\frac{B}{T_f}\right)} \cdot k_{c1} \cdot \left(1 + M \cdot \frac{W(t)}{h_{lim}}\right) \cdot [(h_0 - W(t)) \cdot w_g]^{(1-m_c)} \quad (7.5)$$

As  $0 < m_c < 1$ , using binomial expansion, the term  $(h_0 - W(t))^{(1-m_c)}$  is:

$$(h_0 - W(t))^{(1-m_c)} = h_0^{(1-m_c)} \sum_{n=0}^{\infty} \binom{1-m_c}{n} \left(\frac{-W(t)}{h_0}\right)^n \quad (7.6)$$

The differential equation in Eq. (7.5) doesn't have an analytical solution and can be solved numerically using MATLAB's ODE solver.

The wear coefficient  $K$  is originated from Archard's famous work on wear [11] and is defined in various ways in the literature depending on the derivation of the respective wear equation. Several interpretations of the wear coefficient are discussed in Subsection 2.4.3. Here, it is also useful to note that the published values differ by 1000% because they are measured under different conditions and as it is a strongly simplified equation, where a lot of influences are buried in  $K$ , the conditions must be exactly comparable. There are no established standard methods for testing and the coefficients from different research varies significantly [174, 236].

Nevertheless, the wear coefficient aims to define the wear phenomenon of the elements in contact under the same process conditions. The physical interpretation of the coefficient as "efficiency of the material removal for the amount of work done" is adequate in this case. Based on the interpretation by Archard, the wear coefficient can be defined as:

$$K = \frac{V_w}{F_c \cdot L_s} \quad (7.7)$$

where  $K$  [ $mm^3/Nm$ ] is the wear coefficient,  $V_w$  [ $mm^3$ ] is the volumetric wear of the softer material,  $F_c$  [ $N$ ] is the measured cutting force acting on the grain and  $L_s$  [ $m$ ] is the sliding distance. This interpretation is based on the macro wear analysis and considers the influence of the cutting speed and feed rate on  $L_s$  (i.e. with

increasing wire speed and decreasing feed rate the distance traveled by the wire grain increases); and the influence of wire properties (i.e. number of kinematically active grains, grain penetration area) on the cutting force  $F_c$ . The material removal volume in the WWGW process can be calculated with Eq. (4.9). Through this definition, the wear coefficient is useful to distinguish the abrasive wear affected by the process parameters within the same tribological system.

The empirical wear coefficient  $K$  is identified through WWGW experiments conducted at the wire speeds of 30 and 60  $m/s$  and the feed rate of 1.8  $mm/min$  with Asahi 12-25 standard concentration wire with 120  $\mu m$  core diameter. Figure 7.6 shows the material removal volume as a function of the work done. The slopes of linear curve fits indicate the wear coefficients at two wire speeds under the same experimental conditions. It should be noted that the linear curve fits don't necessarily explain the physical phenomenon behind the wear coefficient, but rather distinguish its effects at different wire speeds; and only valid at the range it is measured.

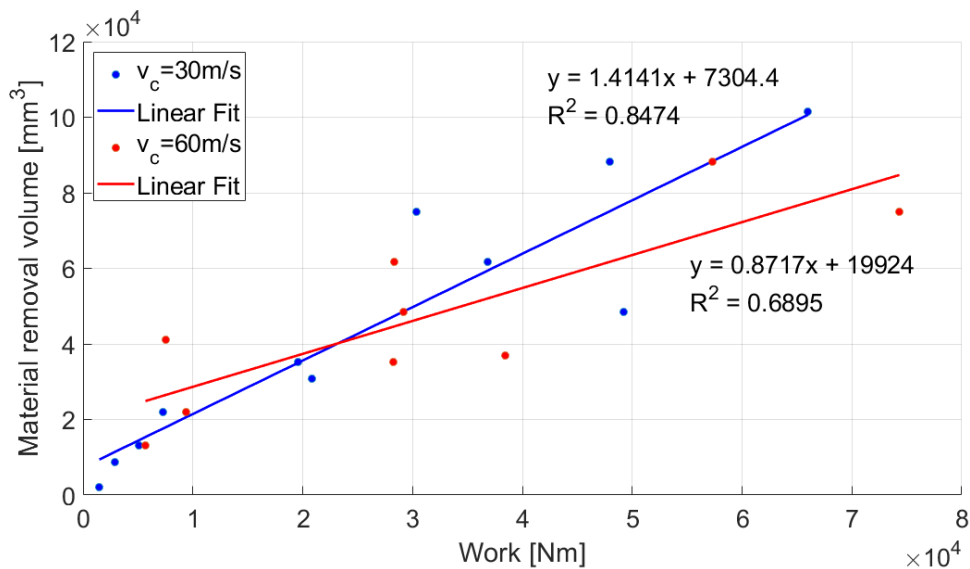


Figure 7.6: Material removal volume as a function of the work done.

The wear coefficients for each wire speed are then calculated as  $K_{30} = 1.41 \text{ mm}^3/Nm$  and  $K_{60} = 0.87 \text{ mm}^3/Nm$ . It should be noted that the values are based on volumetric removal and should be modified with workpiece dimensions when the grain edge wear is considered.

An additional description is required to define the wear of bonding that is responsible for the grain retention forces. The measurement of the grain-bond interface area and the cutting force acting on the grain allow an approximation of a kind of bonding strength. The criterion for bonding strength is also almost independent of the grain size when only grain pullout is considered [43]. The bonding strength can be

approximated as:

$$\tau_p = \frac{F_c}{A_b} \quad (7.8)$$

where  $F_c$  is the cutting force and  $A_b$  is the interface area between the embedded grain section and the bond. Describing the grain as an embedded cylinder, the interface area can be expressed as:

$$A_b = 2\pi \cdot r_g \cdot h_b \quad (7.9)$$

where  $h_b$  is the height of the grain below the surface of the bonding material.

Three grain pullouts are observed in the single grain scratch tests that are conducted on the Scratch Test Setup (Subsection 4.1.2). The measured values are tabulated in Table 7.1. The radius  $r_g$  measured through the approximation of a cylindrical grain geometry, presented in Figure 7.7 for grain 3. The real color Alicona IFM and color coded images show the position and measured radius of the single grain. The interface area  $A_b$  is calculated using Eq. 7.9. The average limit load for the grain pullout is calculated as  $\tau_p = 591 \pm 101 \text{ MPa}$ .

Table 7.1: Measurements on the pulled out grains in scratch tests.

	<b>Grain 1</b>	<b>Grain 2</b>	<b>Grain 3</b>
<b>Embedded height</b> $h_b$ [ $\mu\text{m}$ ]	20.3	7.3	8.8
<b>Protruded height</b> $h_g$ [ $\mu\text{m}$ ]	7.8	8.2	11.3
<b>Radius</b> $r_g$ [ $\mu\text{m}$ ]	11.4	10.0	14.0
<b>Interface area</b> $A_b$ [ $\mu\text{m}^2$ ]	1454.06	458.67	774.09
<b>Cutting force at the pullout point</b> $F_c$ [ $N$ ]	0.77	0.34	0.38
<b>Bonding strength</b> $\tau_p$ [ $\text{MPa}$ ]	529	743	500

A further grain pullout criterion can be established by estimating the grain retention forces, as a function of the penetrating grain height and the embedded grain height. Figure 7.8 schematically presents the configuration of a grain on the wire with its bonded (embedded) and penetrating areas. The grain section that is embedded in the nickel bond  $h_b$ , the protruding grain height  $h_g$  and the grain section active in material removal  $h_{cu}$  are shown in Figure 7.8a.

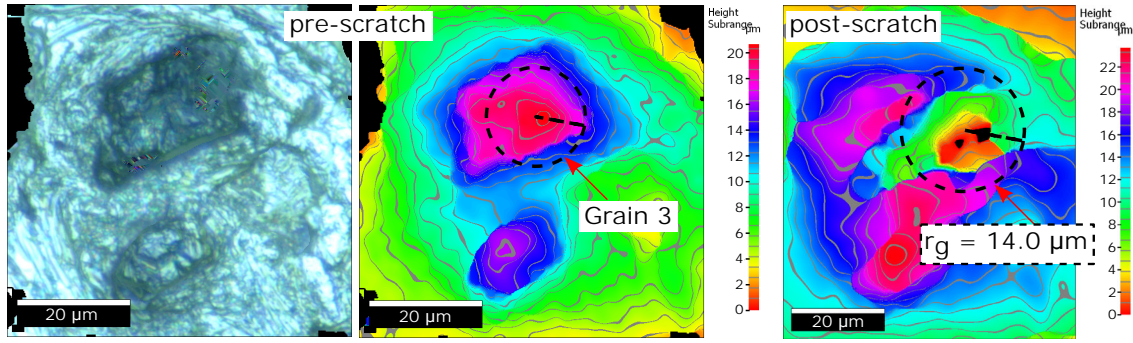


Figure 7.7: Real color Alicona IFM and color coded images of pre- and post-scratch states of Grain 3 given in Table 7.1. Measured grain radius with the approximation of a cylindrical grain geometry is shown with dashed lines.

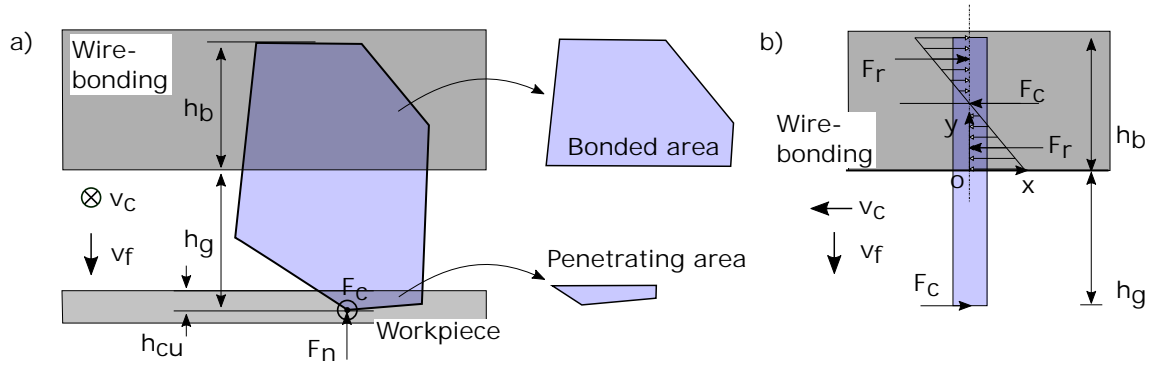


Figure 7.8: The parameters of the embedded grain height  $h_b$ , protruding grain height  $h_g$  and grain penetration depth  $h_{cu}$ .

The forces acting on the grain body are shown in Figure 7.8b. The cutting force  $F_c$  is in the direction opposite to the cutting direction and the locations of the concentrated grain retention forces  $F_r$  are shown. For the equilibrium condition in  $x$ -direction and the moment around point  $O$ , it can be written that:

$$\sum F_x = F_c - F_c + F_r - F_r = 0 \quad (7.10)$$

$$\sum M_O = -F_r \frac{5h_b}{6} + F_c \frac{h_b}{2} + F_r \frac{h_b}{6} + F_c \cdot h_g = 0$$

The force limit for grain pullout then can be defined as:

$$F_r = F_c \frac{6h_g + 3h_b}{4h_b} \quad (7.11)$$

Using the same single grains tabulated on Table 7.1, the limit retention force for grain pullout is measured as  $F_r^{lim} = 0.96 \pm 0.093$  N. The determined bonding strength  $\tau_p$  and the limit retention force  $F_r^{lim}$  with the simplification of a cylindrical

grain with an axis orthogonal to the cutting speed are used as the pullout criteria for a single grain.

However, the criterion for grain pullout further requires the definition for the wear of bonding matrix responsible with holding the abrasive elements, to be able to determine the change in grain retention forces. The definition is possible through evaluating the change of the area enveloping the bases of abrasive structures (cluster or grain). The grain is initially enveloped by the bonding material on and around the grain (Figure 5.2). The reduction of the bonding matrix holding the grain is visualized in Figure 5.14 and Figure 5.13b shows the experimental results concerning the change in the average base area as a function of cumulative material removal.

The change of the average base areas shows two distinct behaviors: at the beginning, the area experience almost-zero deviation from its initial state. With the increasing material removal volume, the filler material around the abrasives responsible with the retention is eventually exposed to the process and starts to wear rapidly, thereby reducing the base bonded area. As the filler material around the abrasive grains is being removed, the risk of occurrence of grain pullouts increase.

The relationship observed in Figure 5.13b between the grain protrusion height and the bonding matrix can be defined, so that the threshold of rapid bond wear is determined by the grain protrusion height change. Figure 7.9 presents this relationship. The x-axis shows the percentage reduction in grain protrusion, where 0 shows the initial state (100% of the grain protrusion height) and 1 shows a complete loss of grain protrusion or a pullout. The y-axis shows the state of the bonding in percentage that is responsible with grain retention, which has the initial value shown as 1 (100% of the bonding). When 80% of the grain protrusion is lost, the rapid wear of the bonding starts, hence grain pullout is more likely due to the reduction in grain retention forces.

The state of grain bonding can then be defined as:

$$h_{b,\%} = \begin{cases} 0.0571 \cdot h_{g,r,\%} + 1.0119, & h_{g,r,\%} < 0.8 \\ -5.1188 \cdot h_{g,r,\%} + 5.1462, & h_{g,r,\%} \geq 0.8 \end{cases} \quad (7.12)$$

where  $h_{b,\%}$  is the state of grain bonding and  $h_{g,r,\%}$  is the reduction of grain protrusion height, in percentages.

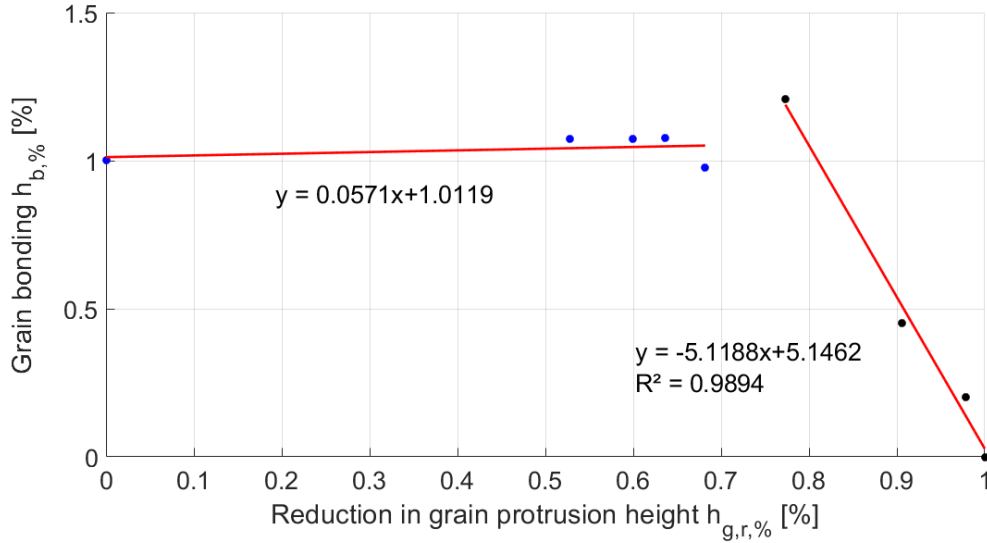


Figure 7.9: Percentage change in the bonding height as a function of the percentage change in abrasive protrusion height.

To determine the wear behavior, the time that it takes to reach the grain wear limit should be known and can be determined from the experiments presented in Section 7.1. At the feed rate of  $1.8 \text{ mm/min}$ , the average cutting time is around  $154 \text{ min}$  to wear  $4.60 \mu\text{m}$  of grain height at  $30 \text{ m/s}$  wire speed; and  $3.86 \mu\text{m}$  of grain height at  $60 \text{ m/s}$  wire speed. However, for the wear calculation based on Eq. (7.5), only the grain-workpiece contact time and not the rotation time shall be considered, which can be calculated from the wheel-workpiece contact geometry.

Considering a square grain shape, applying the experimentally determined values of the coefficients  $K, k_{c1}, m_c$ , an average value flash temperature of  $T_f = 1500 \text{ K}$  and setting  $M = 0.01$ ,  $h_0 = 4.60 \mu\text{m}$  for  $30 \text{ m/s}$  wire speed and  $h_0 = 3.85 \mu\text{m}$  for  $60 \text{ m/s}$  wire speed, the wear progress can be plotted over the process time as shown in Figures 7.10 and 7.11. The asymptotic behavior of the wear propagation is due to the preset values of  $h_{cu}$  and  $h_{lim}$ , which represents the total protrusion wear measured in the experiments.

The wear model in Eq. (7.5) represents an average wire wear condition, where only the wear progress of grains that are active at the beginning of the wire lifetime are considered. In reality, grain pullouts and activation of previously inactive grains will have an influence on the process. It should also be noted that the presented model validation considers a case where an initial grain penetration depth of  $h_0$  is set and progressing wear of the abrasive particle is simulated to a point where  $h_0 = 0$ . The best practice to simulate the real case can be achieved through conducting simulations that consider the time dependent state of individual grains with varying

geometries and step advance of the grain onto the workpiece, and is presented in Chapter 8.

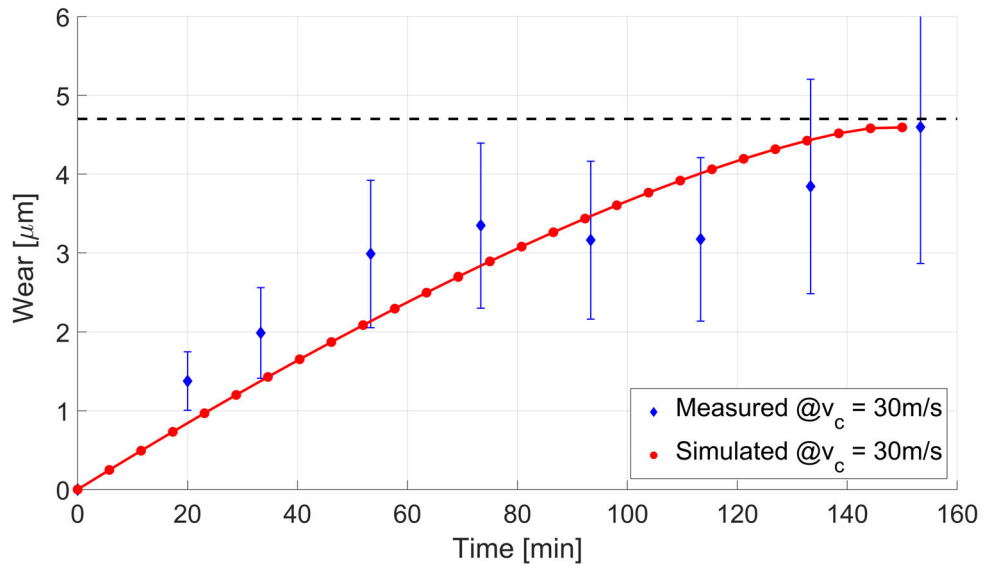


Figure 7.10: Comparison of the grain wear from the wear experiments and model at  $v_c = 30 \text{ m/s}$ ,  $v_f = 1.8 \text{ mm/min}$ .

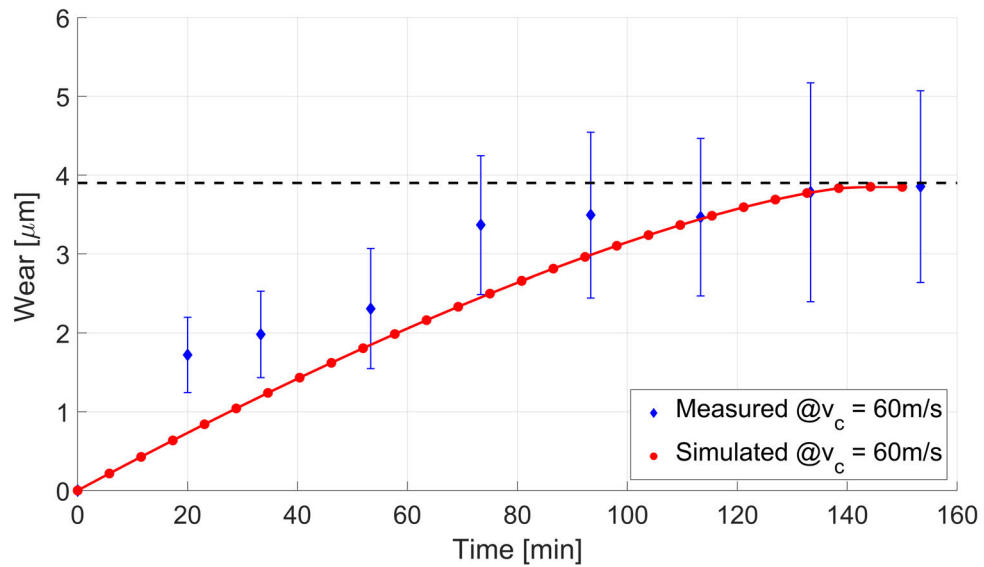


Figure 7.11: Comparison of the grain wear from the wear experiments and model at  $v_c = 60 \text{ m/s}$ ,  $v_f = 1.8 \text{ mm/min}$ .

## 7.3 Temperature Model

In mechanical removal, the highest share of the input energy is transformed to thermal energy [210]. Kennedy [108] states that 95% of the energy dissipation happens in the top of the bodies in contact and according to Kato [106], virtually all of this energy is converted to heat at the grain-workpiece interface. The energy created during the short contact time leads to high temperatures at the grain, called the flash temperatures [12]. In grinding, the time of contact of a grain on a point of the workpiece is in the range of  $1 \mu s$ , hence the interaction can be defined as near-adiabatic. However in wire sawing, the presence of long contact lengths emphasizes the influence of temperature effects. In either case, it is evident that the temperatures in the cutting zone have great influence on the abrasive grain wear and workpiece surface quality, therefore are of major importance.

For this work, flash temperatures at the grain tips are measured with single grain scratch tests using the Fire-3 two-color fiber optic pyrometer introduced in Subsection 4.2.3. Abrasive grains that are geometrically isolated on the wire surface are used for the experiments and consecutive scratches are conducted with each grain. Flash temperatures from individual scratches are measured. Figure 7.12 shows the voltage readings from the two fibers of different wavelengths where each peak corresponds to a single scratch.

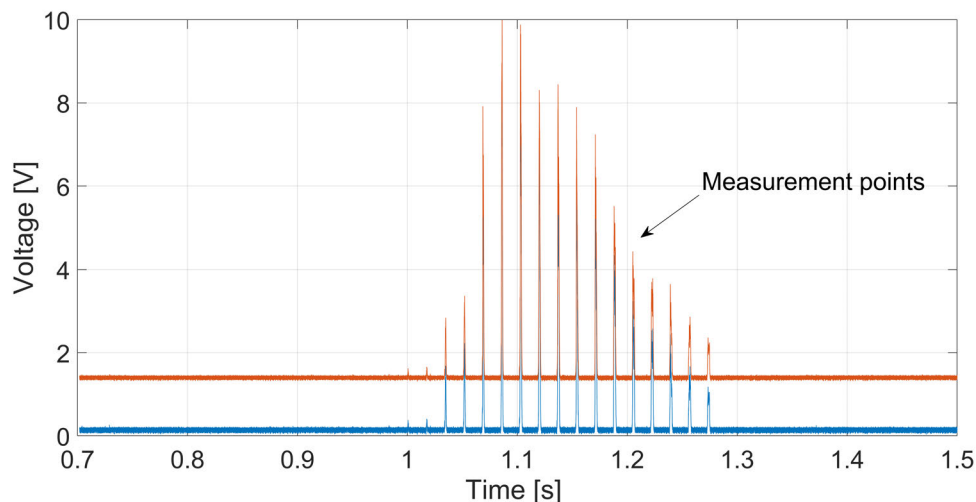


Figure 7.12: Voltage readings from the two colors of the pyrometer.

The corresponding measured temperatures are shown in Figure 7.13. The raw measurement data is presented on top, where a very high noise-to-signal ratio necessitates defining a threshold voltage value for the identification of the measured temperatures. In this case, a threshold value of  $0.1 V$  is applied.



A useful observation is presented in Figure 7.13b and Figure 7.13c, where measured temperatures of brittle and ductile scratches are presented. In both graphs, the grain starts its penetration from the left side and the contact ends at the right side of the plot. The middle part of the plot shows the state at the maximum grain penetration. In the case of brittle material removal, as the penetration depth increases, rate of fracture increases, the grain-workpiece interface area reduces and lower temperatures are measured at the grain tip. In the ductile material removal case, a higher share of energy is dissipated in the form of thermal energy, leading to a temperature increase as the grain penetration increases.

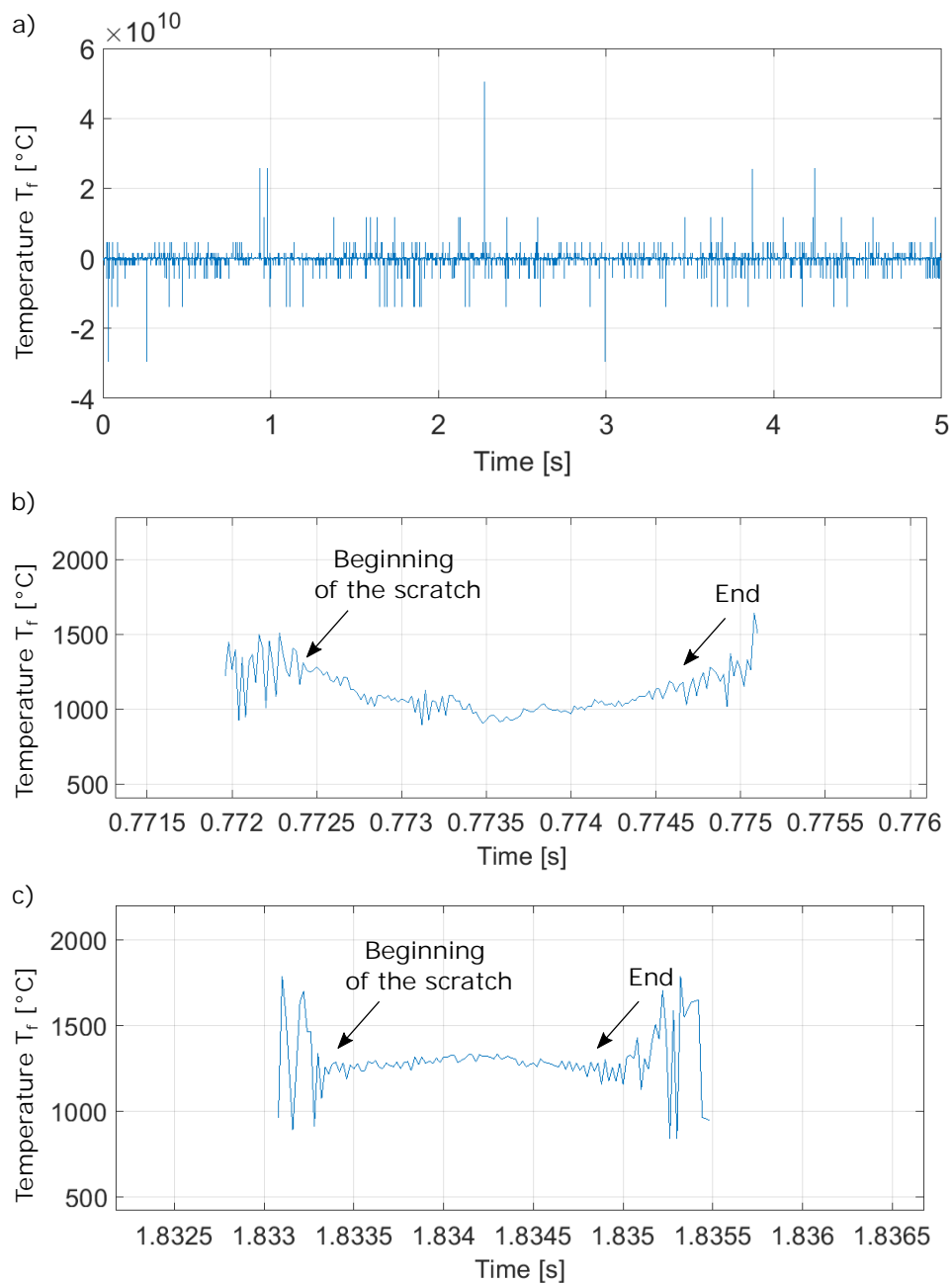


Figure 7.13: (a) Plot of the raw temperature data. (b) Measured temperatures of an individual brittle scratch. (c) Measured temperatures of an individual ductile scratch.

The problem of flash temperatures at the grain tip can be described as the distribution of the energy produced in the contact area through relative sliding of the grain and workpiece. The total heat generated  $Q_t$  is distributed as  $Q_g$  to the grain,  $Q_w$  to the workpiece,  $Q_{ch}$  to the chip, and  $Q_f$  to the coolant. However, the share of heat annihilated by the chips is limited [180] and much smaller in comparison to the heat conduction to the grain and workpiece, hence  $Q_{ch}$  can be neglected. Moreover, in the contact region, temperatures are far higher than the coolant boiling temperature, limiting the convection effects in the cutting zone [88]. The effect of the cooling fluid is hence restricted to cooling of the tool outside the contact region [178]. Further, the scratch tests are conducted without coolant and in the WWGW process, the coolant is applied outside the grinding zone (Figure 4.1). The total heat rate generated per unit area per unit time  $\dot{q}_t$  is then shared between the grain and workpiece:

$$\dot{q}_t = \dot{q}_g + \dot{q}_w \quad (7.13)$$

where  $\dot{q} = Q/A_\perp$ , and  $A_\perp$  is the orthogonal grain area in the direction normal to the workpiece surface. The total heat rate generated is:

$$\dot{q}_t = \frac{F_c \cdot v_{rel}}{A_\perp} \quad (7.14)$$

where the cutting force  $F_c$  is acting on the grain parallel to the relative sliding velocity  $v_{rel}$ .

The problem is then reduced to the determination of the share of the produced heat to the workpiece and to the diamond grain. The condition on the workpiece side can be defined as a stationary heat source on a moving body, as schematically described in Figure 7.14. The heat source (grain) is stationary with the origin of the fixed coordinate system  $(x, y, z)$  and the semi-infinite body is sliding at  $z = 0$  with a constant velocity  $v_{rel}$  with the coordinate system  $(x', y', z')$  attached to its body.

A significant simplification of the solution is to assume steady-state heat flow instead of a transient condition. The time frame until the steady-state conditions are reached were studied by Bhushan [26], to find that the flash temperature reaches its steady-state after a sliding distance of 1.25 times the length of the source. Further, for a moving circular heat source, Yevtushenko [240] stated that the temperature at the contact zone reaches 87% of its steady-state almost instantly. The transient

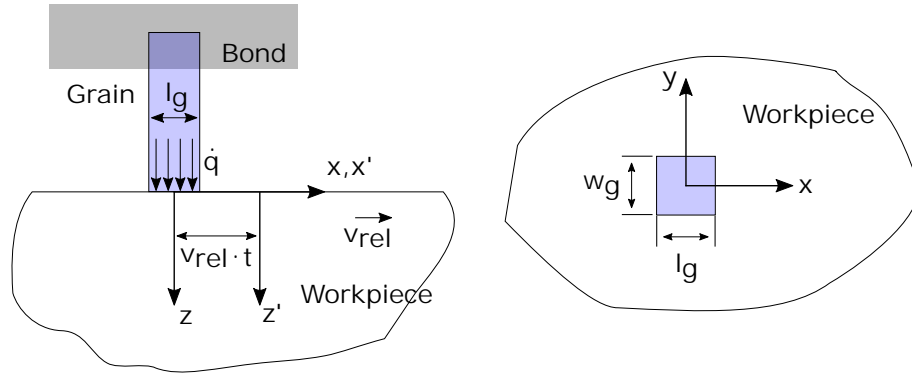


Figure 7.14: Dimensions and definitions of the grain-workpiece contact conditions.

conditions were studied by Jaeger [101] in the case of a moving square heat source over a surface to evaluate the time until steady state is reached can be described by the nondimensional Peclet number. The rate at which the temperature reaches the steady-state condition are plotted in Figure 7.15. The Peclet number for square and band sources is defined as:

$$Pe = \frac{v_{rel} \cdot (l_g/2)}{2 \cdot \kappa_w} \quad (7.15)$$

where  $l_g$  is the length of the contact surface in the sliding direction,  $l_g = w_g$  is assumed in Figure 7.14 and  $\kappa_w$  is the thermal diffusivity of silicon, defined as:

$$\kappa_w = \frac{k_w}{\rho_w \cdot C_p^w} \quad (7.16)$$

where  $k_w$  is the thermal conductivity,  $\rho_w$  is the density and  $C_p^w$  is the specific heat of silicon.

The primary assumptions of the temperature model can be listed as:

- Steady-state heat flow in the diamond
- The bonding material has constant temperature
- The penetration area between the grain and the workpiece is constant over the contact time
- Diamond and silicon have constant material properties
- There is no heat exchange between the grain and the surroundings
- No internal heat generation

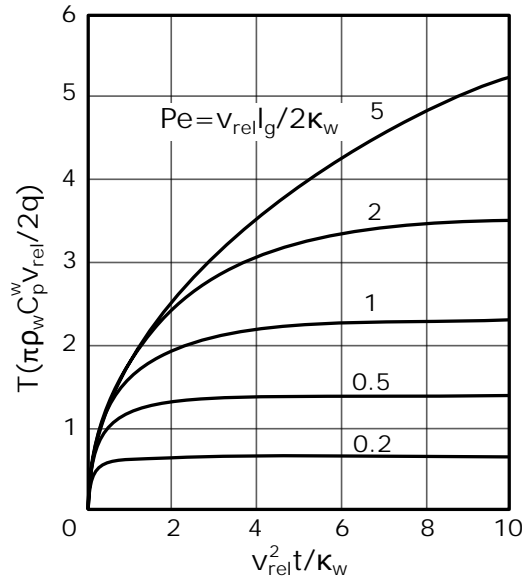


Figure 7.15: Temperatures at the surface of a square heat source sliding with a constant velocity as a function of time and Peclet number (From Bhushan [27], original source: Jaeger [101]).

The solution for a square uniform band heat supply acting on a semi-infinite solid surface is defined by Carslaw and Jaeger [47] and the results are plotted in Figure 7.16, which are highly dependent on the Peclet number.

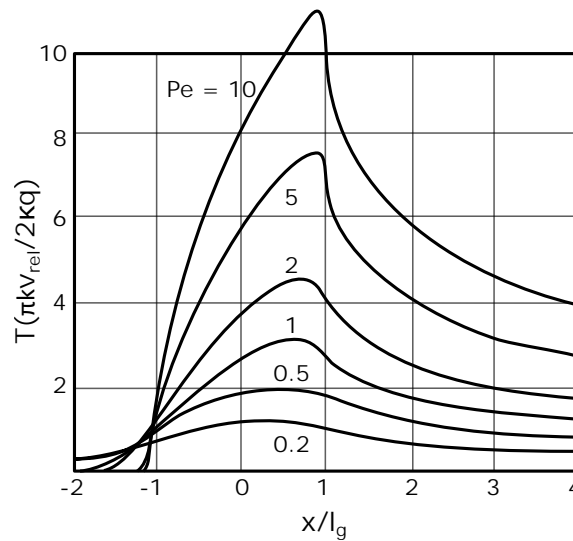


Figure 7.16: Temperature behavior on a semi-infinite solid, resultant of a sliding of a surface with width  $2b$  (From Bhushan [27], original source: Carslaw and Jaeger [47]).

For  $Pe \leq 10$  and a uniform band source heat distribution, the maximum flash temperature rise  $\Delta T_f$  is approximated by Tian [205]:

$$\Delta T_f = \frac{2 \cdot \dot{q}_w \cdot (l_g/2)}{k_w \sqrt{\pi(1 + Pe)}} \quad (7.17)$$

where  $k_w$  is the thermal conductivity of silicon,  $Pe$  is the Peclet number defined for the relative sliding speed and  $l_g$  is the grain side length orthogonal in the direction of sliding.

On the grain side, for a solid object with no internal heat generation and uniform material properties, Fourier's heat equation is written in the case of one-dimensional steady-state conduction:

$$\frac{\partial T}{\partial t} = \frac{k_g}{\rho_g \cdot C_p^g} \frac{\partial^2 T}{\partial x^2} \quad (7.18)$$

It is required to define the initial and boundary conditions to approach the problem. Based on Figure 7.17, in the case of a steady-state, linear, one-dimensional heat transfer in a column, the initial and boundary conditions can be stated as:

$$I.C. : \quad \text{at } t = 0 \quad T = T_i \quad (7.19)$$

$$B.C.^1 : \quad \text{at } x = 0 \quad \dot{q} = -k_g \frac{\partial T}{\partial x} \quad (7.20)$$

$$B.C.^2 : \quad \text{at } x = h_g \quad \dot{q} = -k_g \frac{\partial T}{\partial x} = -k_b(T_{x=h_g} - T_b) \quad (7.21)$$

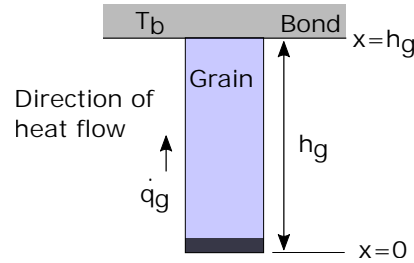


Figure 7.17: Parameters of the grain model and the direction of heat flow.

The temperature distribution as a function of distance from the grain tip is then defined as:

$$T(x) = \frac{T_b - T_f}{h_g} x + T_f \quad (7.22)$$

The rate of heat flow per unit area is then found as:

$$\dot{q}_g = k_g \frac{(T_f - T_b)}{h_g} \quad (7.23)$$

Combining Eqs. (7.14), (7.17), (7.23), (6.30) and using Eq. (7.13), the flash temperature at the grain tip can be approximated:

$$T_f = \frac{k_{c1} \cdot A_{cu}^{1-m_c} \cdot 2 \cdot (l_g/2) \cdot h_g}{k_g \cdot A_{\perp} \cdot 2 \cdot (l_g/2) + k_w \cdot A_{\perp} \cdot h_g \sqrt{\pi(1 + Pe)}} \quad (7.24)$$

where  $k_{c1}$  is the specific cutting force and  $m_c$  is the constant determined through the force model presented in Section 6.4. Properties of sc-Si and synthetic single-crystal diamond are tabulated in Table 7.2.

*Table 7.2: Thermal properties and densities of sc-Si and Type IIa single-crystal diamond at 300 K.*

	sc-Si [91]	Diamond [163]
<b>Density</b> $\rho$ [ $kgm^{-3}$ ]	2329	3520
<b>Specific heat</b> $C_p$ [ $Jkg^{-1}K^{-1}$ ]	713	502-519
<b>Thermal conductivity</b> $k$ [ $Wm^{-1}K^{-1}$ ]	156	2000-2100

Model validation experiments are conducted with 6 grains and 90 scratches in total, at the cutting speed of 10  $m/s$ . The comparison of the simulated and measured results show that the model underestimates the flash temperature  $T_f$  by a factor of  $\approx 4.5$ , and a linear proportionality coefficient is employed. The deviation is the result of the overestimated  $\dot{q}_g$  due to the assumption that the temperature of the bonding  $T_b$  is equal to the ambient temperature. This is clearly not the real case, where it is expected that the heat flow from the grain tip to the bonding material shall result in a background temperature rise on the wire, leading to a decrease in the temperature difference and reduction in the rate of heat flow. However, considering such a transient case requires a highly complicated model. It should also be noted that consecutive scratches with the same grain lead to geometrical deviations that are ignored in the model.

Through substituting the penetration area  $A_{cu}$  with  $h_{cu} \cdot b_{cu}$  in Eq. (7.24) the flash temperature can be plotted as a function of the grain penetration depth  $h_{cu}$ . The comparison of the measured and simulated flash temperatures is plotted in Figure 7.18 as a function of the grain penetration depth. The results suggest that the flash temperature values decrease with increasing penetration, showing that grains cutting in the brittle removal regime result in slightly lower temperature values.

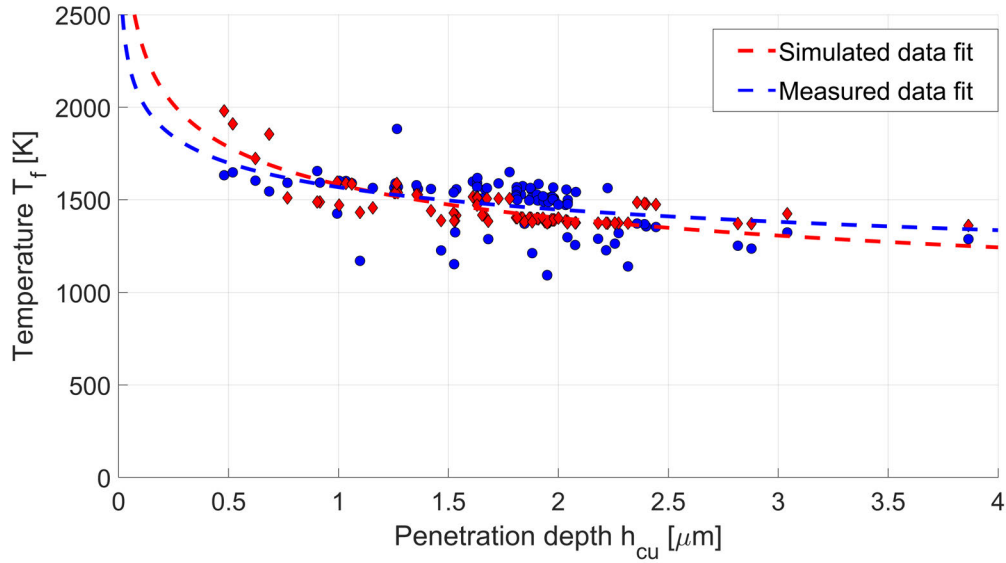


Figure 7.18: Comparison of the measured temperatures at single grain scratch test and simulation results of the flash temperature model using Eq. (7.24).

The flash temperature model and the experiments show that at lower depths of cut, with the presence of ductile material removal mode, higher temperatures are present at the grain tip. Moreover, as long as the ductile material removal is available, an increase in the depth of cut results in higher temperatures. As the depth of cut increases, material is removed in a more brittle regime, resulting in lower temperatures. The model also considers the influence of the sliding velocity through the Peclet number. With increasing velocity, the Peclet number increases (See Eq. (7.15) and the surface temperature decreases in the case of constant heat generation. Hence, at higher cutting speeds, where  $Pe \geq 10$ , lower flash temperatures may be observed.

# Chapter 8

## Process Simulation

*“Even if a scientific model, like a car, has only a few years to run before it is discarded, it serves its purpose for getting from one place to another.”*

— David L. Wingate,  
*Complex Clocks, 1983*

In the previous chapters, the physical models that are required to describe the grain geometry and diamond wire topography, WWGW kinematics, process forces, material removal mechanisms, abrasive grain wear and flash temperatures at the grain tip are developed and validated through experiments. The following chapter explains the details of the process simulation where the models will be employed to simulate the material removal, process forces and diamond wear. The simulation flow will be presented and the application of the developed models in the simulation environment will be described in further detail.

### 8.1 Details of the Simulation

The simulation flowchart is presented in Figure 8.1. The simulation inputs are the initial diamond wire topography, grain-workpiece contact characteristics through the kinematics-geometric process model, process parameters, initial workpiece geometry, material removal and diamond wear mechanisms, and material properties of the silicon workpiece and diamond grains. The outputs are the resultant workpiece surface topography, process forces, cutting temperature and grain wear. The following simplifications are considered for the simulations:



- Ideal kinematic cutting conditions, ignoring elastic and/or plastic deformations.
- The machine, workpiece and wire has infinite stiffness.
- The diamond grain wear occurs gradually.
- The process is adiabatic.
- Workpiece material and diamond grain are homogeneous.

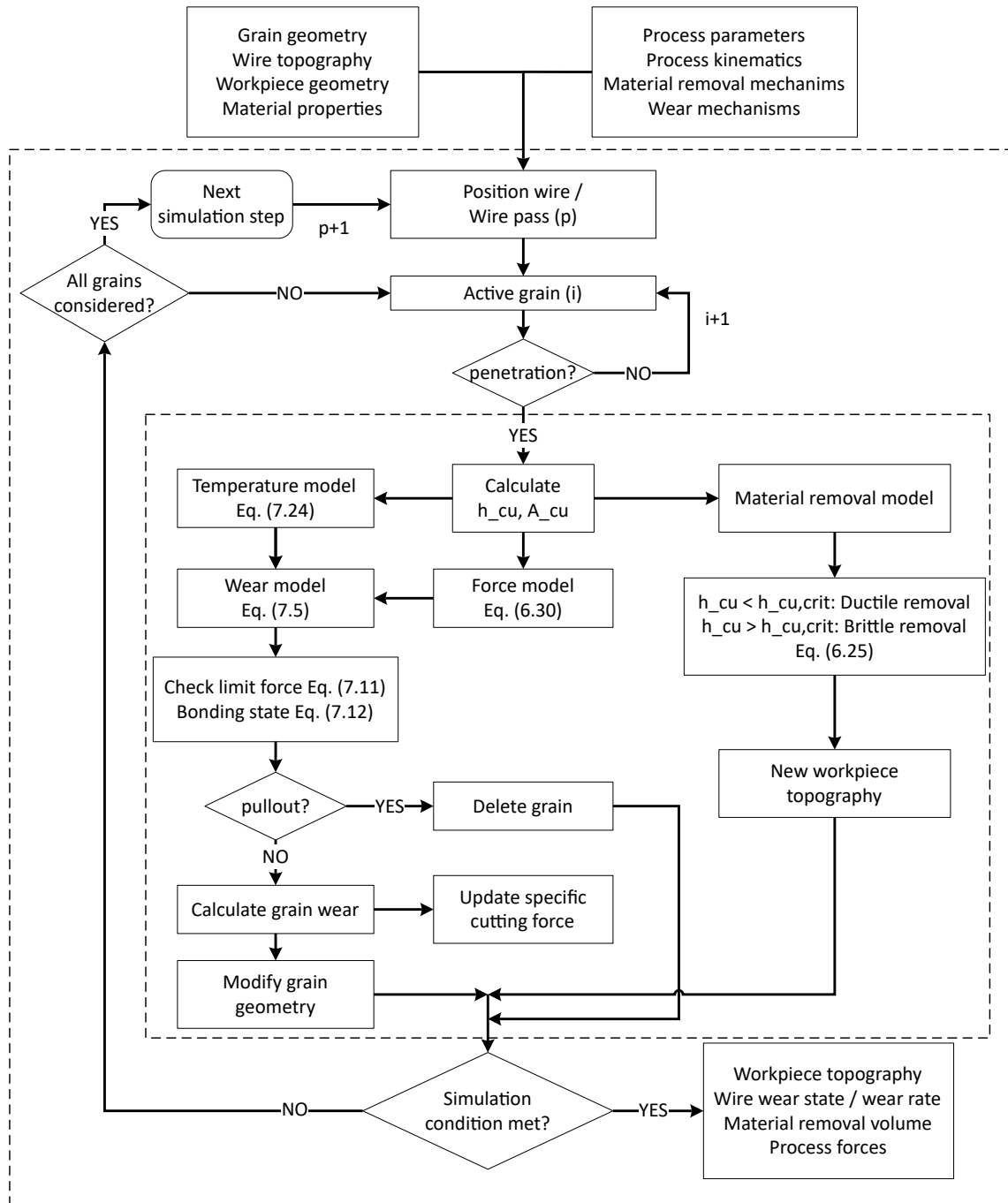


Figure 8.1: Simulation flowchart.

Initially, the wire is positioned around the wheel and over the workpiece as shown in Figure 6.17. Only the grains that are in the active wire section described in Figure 4.10 are considered in the simulations to reduce the processing time. Then for each wire pass over the the workpiece surface, the path and penetration of the individual grain starting from the first wire cross-section are calculated. In the case where the grain-workpiece contact happens, the simulation for this grain starts. When the grain is not active in the current wire pass, the next grain is considered.

The grain path is determined using the kinematic descriptions in Section 6.2. The grain penetration depth  $h_{cu}$  and the penetrating area  $A_{cu}$  are calculated based on the individual grain geometries. The grain geometry is defined by the tool model where 2D grain geometries are employed as polygons with varying number of vertices. The position of a grain on the wire circumference is defined by the angle  $\gamma$  which dictates the intersection nodes of the workpiece and grain.

The intersection between the grain polygon and workpiece nodes are calculated using the MATLAB function *inpolygon()*. The grain polygon is saved in an N-by-3 matrix where N denotes the number of grain vertices and each vertex  $V(x, y, z)$  is defined by a row array. In Figure 8.2a, a wire cross-section at the workpiece entrance position is shown and below, the final state of the workpiece surface is given. The wire moves into the paper plane and the active grain removes material from the workpiece surface.

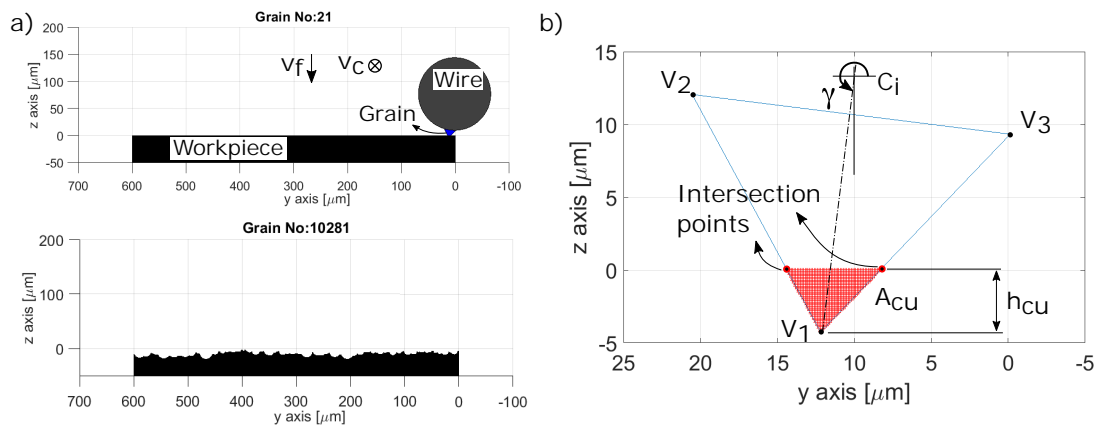


Figure 8.2: (a) The position of the wire cross-section and active grain at the beginning of cut and the cross-section of the final workpiece surface. (b) Interaction area of the grain-workpiece contact and the overlapped nodes of the grain and workpiece (red).

Details of the grain-workpiece contact area are given in Figure 8.2b, where three grain vertices  $V(1)$ ,  $V(2)$  and  $V(3)$  are indicated as well as the grain and workpiece surface intersection points. The red section at the grain tip shows the positioning of the individual nodes in the intersection area  $A_{cu}$ . The chipping thickness  $h_{cu}$  is

measured from the highest of the intersection points to each vertex on the penetrated grain section. The intersection area has a resolution of  $0.1 \mu m$  in  $y$  and  $z$  directions and the grain position angle  $\gamma$  is shown.

The grain penetration depth  $h_{cu}$  is then evaluated to determine the material removal mode. In the simulation environment, three cases of material removal are defined: ductile, brittle and ductile-brittle material removal modes present at the same time at different grain edges that are in contact with the workpiece. The schematic descriptions of brittle and ductile-brittle cases are given in Figure 8.3. For the case of grain A, only brittle material removal mechanism is active and the removal cross-section is half ellipse shaped, which has its center point at the grain tip. The dimensions  $h_{cu}$  and  $c_l$  are shown and the material is removed from the sections where the workpiece overlaps with the calculated removal area.

In the case of grain B, ductile and brittle removal mechanisms are observed at different grain edges. The brittle removal volume is again defined by the relationship between the grain penetration depth  $h_{cu}$  and the lateral crack length  $c_l$  by Eq. (6.25); and the grain tip location is the center of the brittle removal area. However, the second grain edge is in contact with the workpiece and its penetration depth is below the critical chip thickness. Hence, ductile removal is also considered and the penetrated grain geometry is mapped onto the workpiece surface.

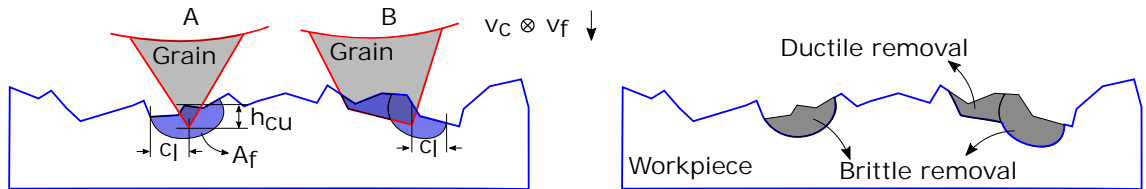


Figure 8.3: Conditions of brittle and ductile workpiece removal modes, dimensions and geometry of brittle and ductile material removal.

For the simulation of diamond wear, the grain penetration depth  $h_{cu}$  is employed in the temperature model given in Eq. (7.24) to determine the flash temperature at the grain tip. This temperature value is then used in the diamond wear model given in Eq. (7.5). Additionally, the penetrated grain area  $A_{cu}$  is used to calculate the cutting and normal forces acting on individual grains, using Eqs. (6.30) and (6.32). The cutting force value is then used in the wear model.

The wear model initially determines the height of the bonding responsible with grain retention and the bonding strength, based on the grain protrusion as described in Section 7.2 and Figure 7.9. If the load is over the pullout load limit, the grain is considered to be a pullout and excluded from the next simulation step. Following, based on the calculated grain wear, if the pullout doesn't occur, the geometry of

grain is updated as shown in Figure 8.4. The modification due to the grain wear is applied to the leading grain edge at the lowest point of the grain. If the wear propagates and another edge becomes the lowest, the wear propagation continues from that edge in the next step. With the grain wear, the specific cutting force  $k_{c1}$  is updated and used in the next simulation step.

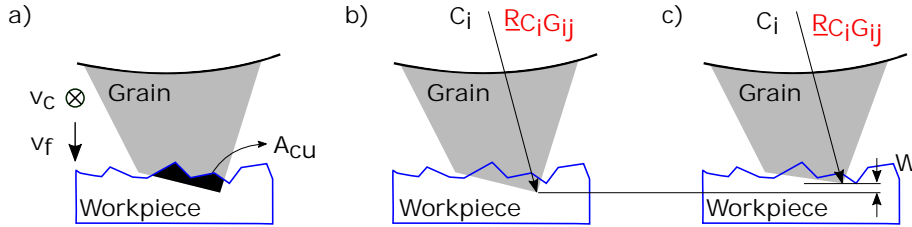


Figure 8.4: (a) Grain-workpiece cut area  $A_{cu}$ . (b) Position of the leading grain edge. (c) Change of grain protrusion height and modification of the leading grain edge.

## 8.2 Results

The simulations are conducted with the workstation available to the Institute of Machine Tools and Manufacturing (IWF) of ETH Zurich. The workstation has Intel Xenon E5-2687W v4 3GHz Dual processor and 192 GB of RAM, and runs on 64-bit Windows 10 environment. Initially, the material removal simulations that are conducted at 30 and 60  $m/s$  wire speeds and 1.8  $mm/min$  feed rate will be presented. The simulations were run twice for each parameter pair and one simulation involve 30 wire passes over the workpiece that takes around 3.5 hours of run time. For each simulation run, a new 3D diamond wire model is constructed that has a length of 452.72  $mm$ , equal to one wire wrap on the WWGW. Each wire model consist of around 60,000 diamonds which of 9,000 are on the active wire surface (Figure 4.7), while possessing 1,000 distinct grain geometry models. The diamond wire is modeled based on an Asahi 12-25 high concentration wire, with which the experiments are conducted. The 3D model is then reduced to a 2D model to save processing time.

Figure 8.5 shows sample output surfaces from the simulations and experiments at 30 and 60  $m/s$  wire speeds and 1.8  $mm/min$  feed rate with their respective profiles orthogonal to the cutting direction. Measurements of the surface roughness are conducted on two simulation surfaces at each wire speed; and for the experiment surfaces, five profile measurements are taken from ten Si workpiece sections. Workpiece surfaces from the experiments are measured with an Alicona IF Microscope. Grain wear is not considered for surface simulations and experiment surfaces are sampled at the beginning of cut, where no significant wire wear is present. As the kinematic analysis of WWGW setup (Subsection 4.1.1) explains and the developed

kinematic-geometric process model (Section 6.2) suggests, at the same feed rate, lower grain depth of cut is evident at higher wire speeds. This results in higher ductility and lower surface roughness, agreeing with the experimental results in Section 5.3, where the correlation between ductility and roughness is shown in Figure 5.10.

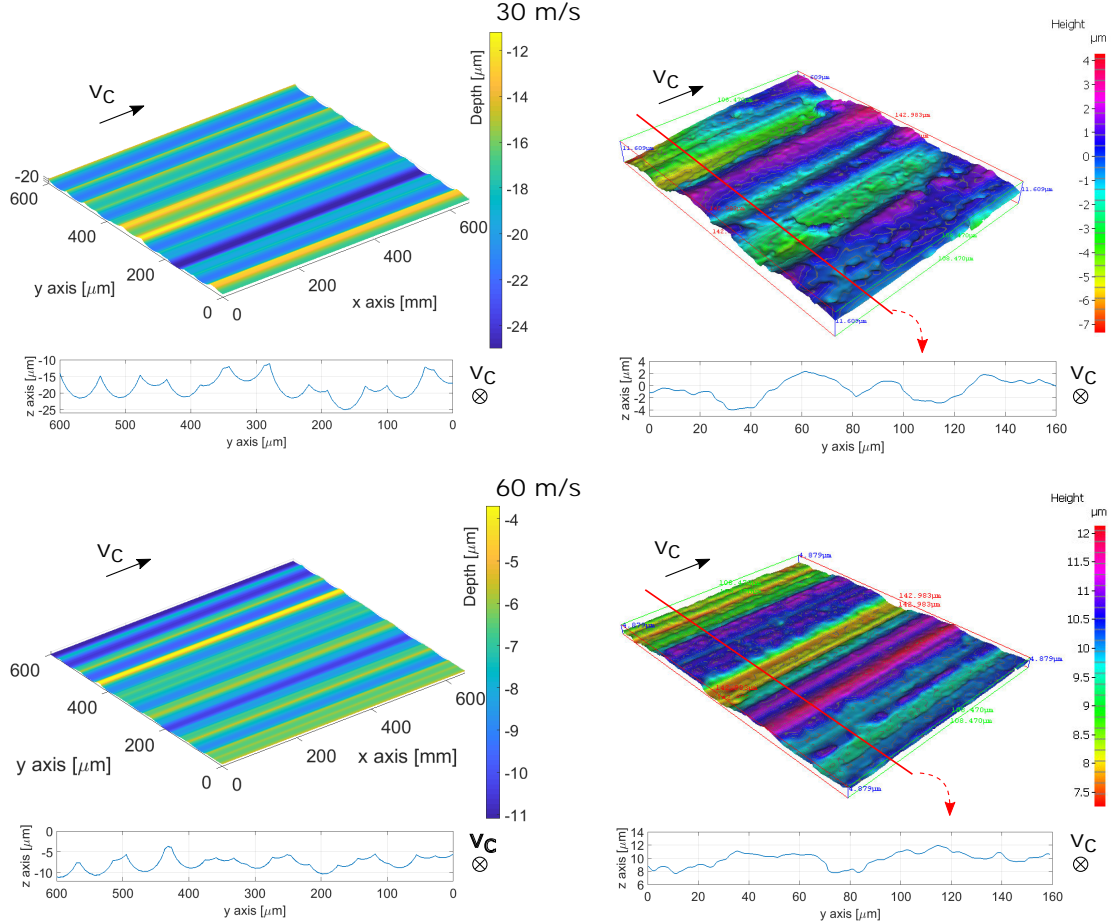


Figure 8.5: Silicon workpiece surfaces from the simulations on the left and experiments on the right at  $v_c = 30$  and  $60$  m/s and  $v_f = 1.8$  mm/min. Below each, surface profiles orthogonal to the cutting direction are given.

Calculation of the surface roughness values  $R_a$  and  $R_q$  from simulations and experiments is done by applying Eqs. (6.17) and (6.18) with five sampling distances over the measured profile lengths. The results are presented in Figure 8.6. The measurements show an expected correlation, where lower wire speed results in higher roughness values both for the simulations and experiments. Individual roughness values show that the simulations underestimate the experiment results within the range of standard deviations. This is mainly due to the fact that in simulations, components i.e. dynamic factors, material inhomogeneity are not considered.

The cutting and normal force results from the simulations are presented in Figures 8.7 and 8.8. The cutting force values are calculated based on 2D grain penetration areas at discrete time steps of the wire motion, depending on the angular velocity

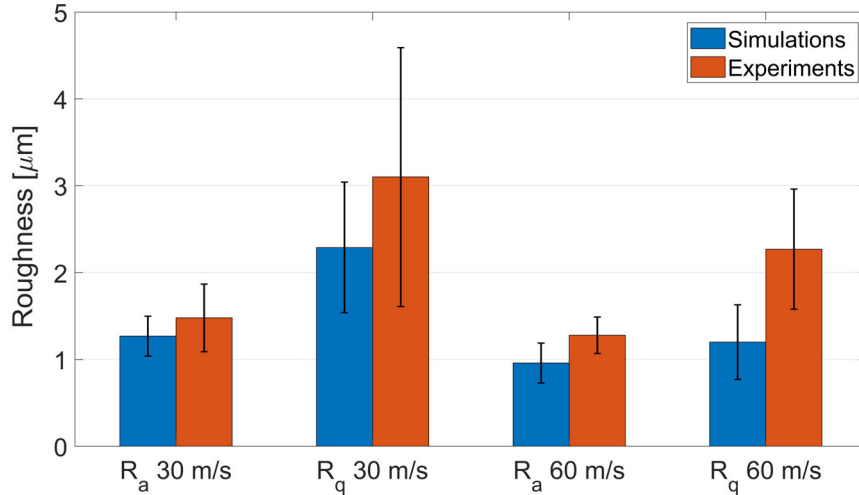


Figure 8.6: Comparison of the roughness values of  $R_a$  and  $R_q$  from the simulations and experiments at  $v_c = 30$  and  $60$  m/s.

and the distance between two wire cross-sections in the direction of cut as explained in Eq. (6.16). The normal forces are then calculated with the relationship given in Eq. (6.32). The forces are transformed to the directions of the force sensor, based on the grain position on the concave workpiece at the respective time step, as defined in Eqs. (6.33) through (6.36). At both wire speeds, the first passes show significantly higher force values. At the first wire pass, grains with higher protrusion will have higher grain penetration depths due to the initial positioning of the wire. The gradual increase in both cutting and normal forces over the cutting time can be explained as the result of the increase in grain width of sharp grains as the wire moves in the feed direction; and partly with the involvement of the new grains in the wire peripheral as the wire moves further into the workpiece and form a groove shaped cut. The forces eventually reach an equilibrium when the wires are completely engaged into the workpiece.

Measurements of cutting and normal forces from experiments at  $30$  m/s wire speed are presented in Figure 8.9. The force values represent  $60$  s of cutting time and sampled after  $5$  mm of wheel depth of cut, where no significant grain wear is present. The deviation between the measured and simulated forces is mainly due to the fact that the geometric wire model considers both the bonding material and grain as one element and simulates the grain dimensions based on these measurements; and hence the actual grain dimensions are smaller than the modeled grains. Moreover, the force model does not distinguish the difference between the bonding material and the diamond. The model parameters  $k_{c1}$  and  $m_c$  only consider the diamond-silicon contact, and hence it is expected to overestimate the process force at the beginning of the sawing, where the nickel bonding plays role in the material removal.

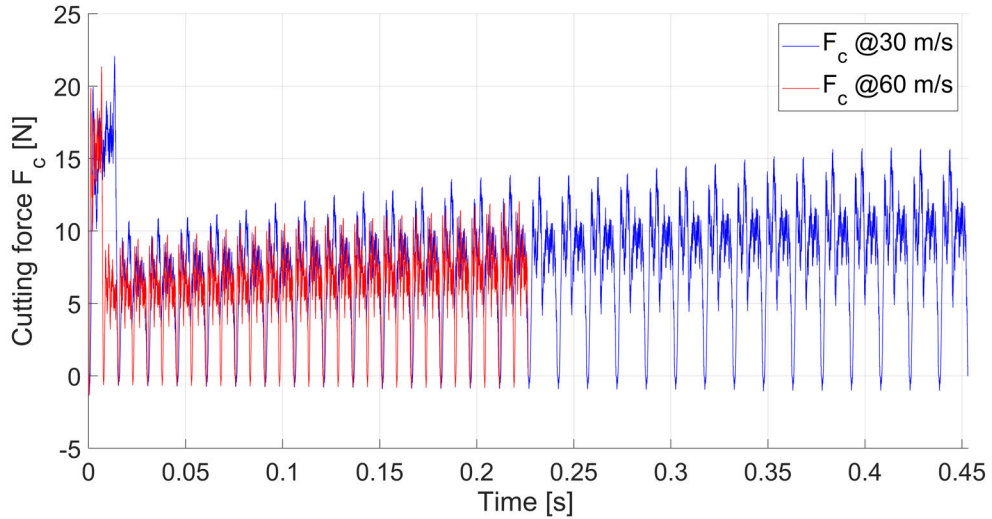


Figure 8.7: Comparison of the cutting forces at  $v_c = 30$  and  $60$  m/s over 30 wire passes.

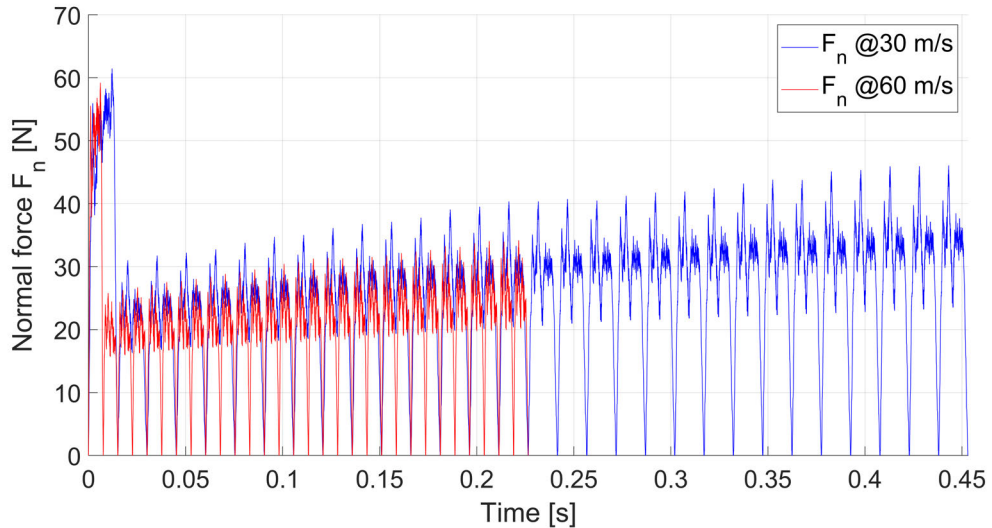


Figure 8.8: Comparison of the normal forces at  $v_c = 30$  and  $60$  m/s over 30 wire passes.

Next, the wear for individual grains is simulated where the change in grain geometries and grain pullouts are considered. Such a simulation requires very high computation time and power due to the fact that wear of around  $3\text{-}4\ \mu\text{m}$  diamond protrusion needs in the vicinity 1.2 Million wheel rotations (circa. 150 min of real cutting time), as suggested by the experimental evaluation and the respective wear model. Hence, simplifications are required for the wear simulations with single grains.

The single grain wear simulations shall be based on individual wire rotations, so that it is possible to determine the grain-workpiece contact area and the penetration depth of the grain at each wheel rotation. To realized this, instead of a complete wire wrap as done in the material removal simulations, a small section of the wire



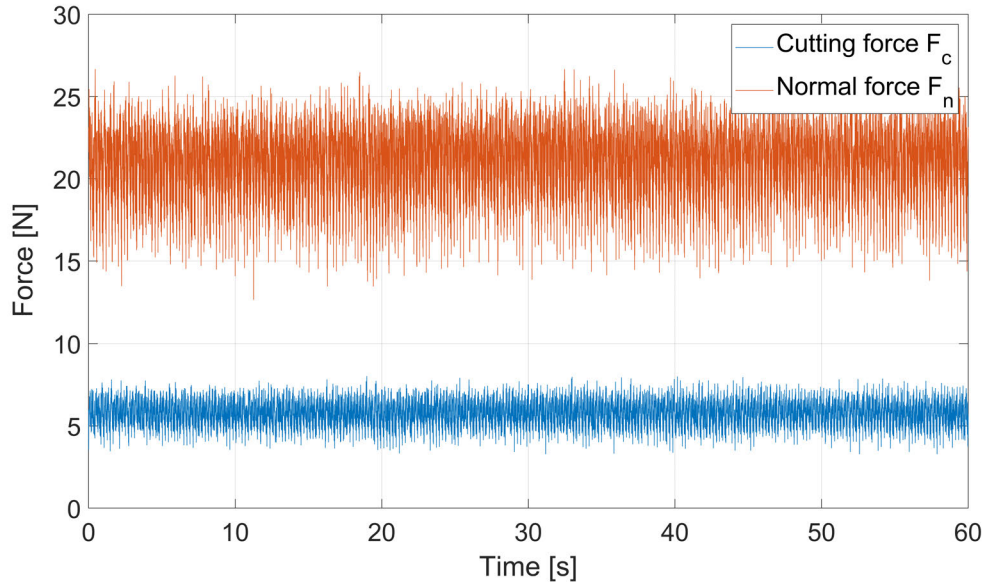


Figure 8.9: Cutting and normal forces from experiments at  $v_c = 30$  m/s,  $v_f = 1.8$  mm/min without wire wear.

with 24 grains on the active wire section are employed. Grains are fed onto the workpiece at a rate equal to 1.8 mm/min. To reduce the number of wire passes for reaching the required grain wear, no material removal of workpiece surface is considered, which means the grains are sliding on the workpiece surface that has no wear. Finally, the grain wear rate is multiplied with a coefficient of 1000 to reach the wear criterion in a shorter time frame. The coefficients  $K$  and  $M$  of the wear model and  $k_{c1}$  and  $m_c$  of the force model are given in Section 7.2. Here, the flash temperature  $T_f$  is calculated for each penetration depth at each simulation step.

The average wear rate as a function of the cutting time is plotted in Figure 8.10. The asymptotic shape of the curve shows the behavior observed in the wear experiments, where the rate of wear is decreasing with progressing wear. The slight peak at the end is possible with the involvement of previously inactive grains towards the end of the wire lifetime. These grains may be of lower protrusion and/or the grains that are at the sides of the wire active area. The latter can be observed in Figure 8.11.

In an ideal case, where an equal, gradual grain wear and constant feed rate are considered, the grain cutting area  $A_{cu}$  would be identical at each step for a rectangular grain and increase for a sharp grain. However, in reality, the grains may wear out faster due to macro-fractures, material inhomogeneity etc. and the average or total  $A_{cu}$  is decreasing with time. Figure 8.10 illustrates the case, where both grain dulling (through modification of the specific cutting force) and fracture (through modification of grain geometry) are considered.



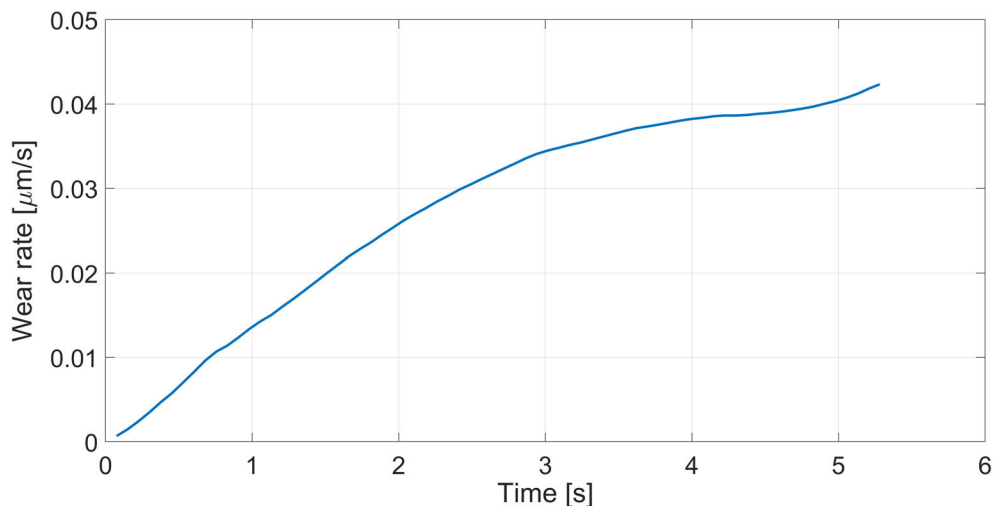


Figure 8.10: Average wear rate over wire lifetime.

Figure 8.11 shows the superposition of grains on adjacent wire cross-sections as the viewer looking in the direction of cut at  $t = 0$ ,  $t = 4.07$  s and at the end of the simulated lifetime at  $t = 5.28$  s. The grains start their contact with the workpiece according to their protrusion heights and positions around the wire surface, hence the number of active grains increase with progressing wear, or decrease as grain pullouts occur.

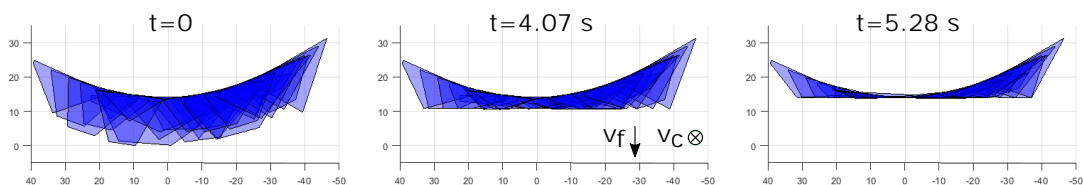


Figure 8.11: Superposed grains on the wire surface and their wear stages

The wear propagation of individual grains and modification of the grain geometries are schematically explained in Figures 8.12 and 8.13 on 2D grain models that are plotted according to their  $\gamma$  angle position on the wire circumference, such that the grain in Figure 8.12a is at the left side, the grain in Figure 8.12b is at the right side and the grains in Figure 8.13a and b are in the middle of the wire circumference. The grain positions influence the wear propagation since they dictate the grain-workpiece contact geometries. The outer contour shows the initial grain geometry and the stages of wear are plotted on top of this surface, where the inner contour indicates the final stage of grain wear.

In Figure 8.12a, the wear starts at the lowest grain edge and propagates in ‘direction 1’, as the leading edge is shifted, the wear propagation continues in ‘direction 2’ and shifts to ‘direction 1’ again, eventually resulting in a flat contact surface indicated in red color. A similar wear behavior occurs in Figure 8.12b, where the wear propagates in three different directions as the leading grain edge changes. In both cases, new cutting edges are created and worn out gradually throughout the wear process.

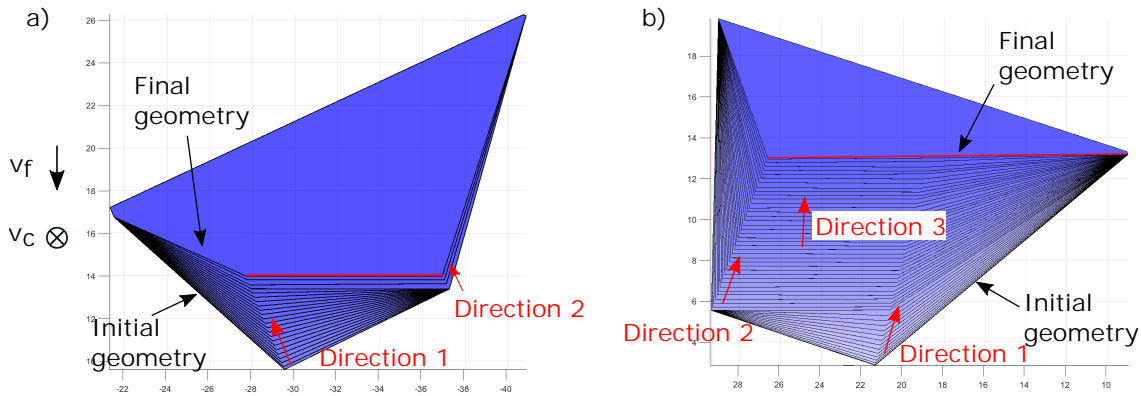


Figure 8.12: Alteration of 2D grain geometries with progressing wear.

Figure 8.13 presents the progressing wear of an initially sharp and a dull grain. In Figure 8.13a, the grain wears only in ‘direction 1’, resulting in a gradual change in the penetrating tip angle, eventually leading to a grain pullout. In Figure 8.13b, the wear starts in ‘direction 1’ at the initial stages of the wear and continues in ‘direction 2’ by alternating the leading edges.

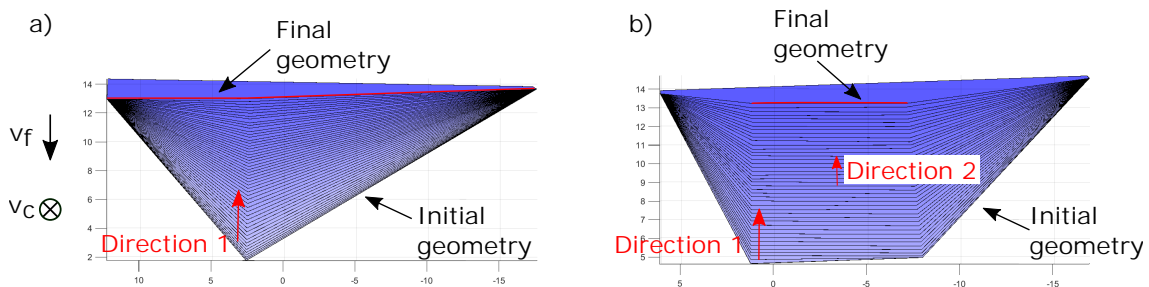
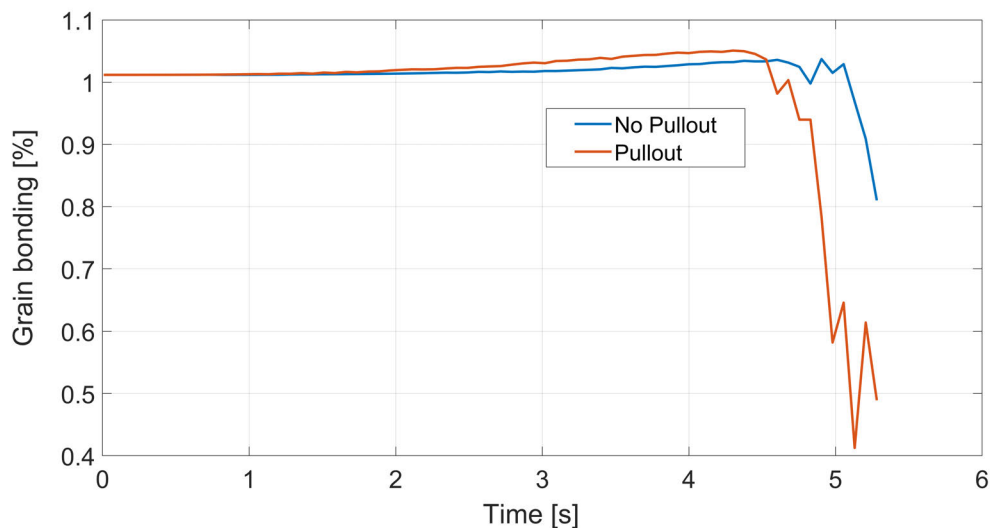


Figure 8.13: Change in geometries of sharp and dull grains with progressing wear.

The method used to define the wear of individual grain geometries is able to produce new grain edges or dull grains with progressing wear, depending on the initial grain geometry, grain position on the wire circumference and interaction geometry with the workpiece, depending on the workpiece topography and grain shape.

Out of the 24 grains that are used in the simulation, eight of them experience pullouts towards the end of cutting time, after  $t > 4.9$  s. The pullout criterion considers the change in grain retention forces, based on the wear of grain bonding, behaving as described in Figure 7.9. Figure 8.14 shows the change of the average bonding of grains that have experienced pullouts and those hold on until the end of cutting time.

Based on the bonding wear criterion, grains wearing out faster would also experience a more rapid bonding wear compared to the grains of the same initial protrusion heights. It can be observed that all the grains experience bonding wear, however pulled out grains were exposed to a faster bonding wear propagation. The bonding wear model suggests that this is the result of a more rapid grain protrusion wear. The faster wear is the result of the grain position or grain geometry which influences the contact area, hence the rate of wear. Figure 8.14 shows that even with less cutting time, the grains may experience pullouts if the conditions are satisfied.



*Figure 8.14: The change of grain bonding over cutting time for pulled out grains and grains with no pullout.*

Additionally, the evolution of average protrusion heights of the pulled out grains and grains that hold till the end of their lifetime are plotted in Figure 8.15. The red line shows the average behavior of all the grains in simulation. As suggested, pulled out grains have higher rate of wear, hence experiencing higher bonding wear and higher cutting forces in the same time frame, in comparison to the other grains.

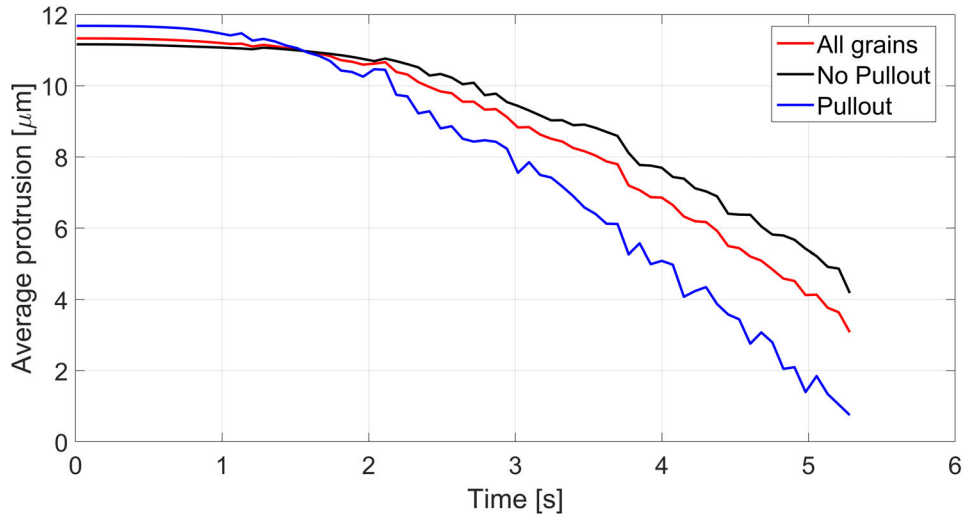


Figure 8.15: The change in average protrusion heights of all grains, grains with no pullout and grains that are pulled out at some point of the cutting time.

The progress of the cutting and normal forces acting on the grains is given in Figure 8.16 and the evolution of the specific cutting force  $k_{c1}$  is given in Figure 8.17. The change in process forces is the result of the alteration of grain geometries and the evolution of the specific cutting force with dulling.

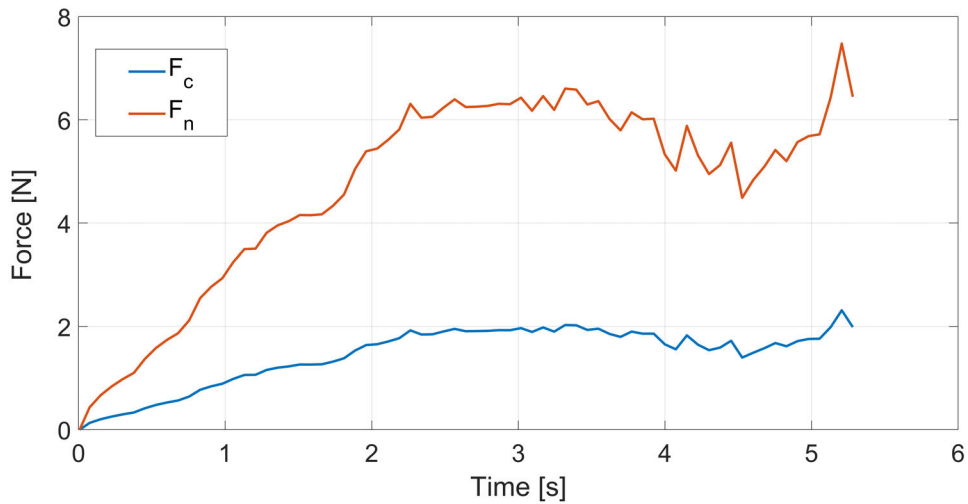


Figure 8.16: The change in total cutting and normal forces acting on the grains over the cutting time.

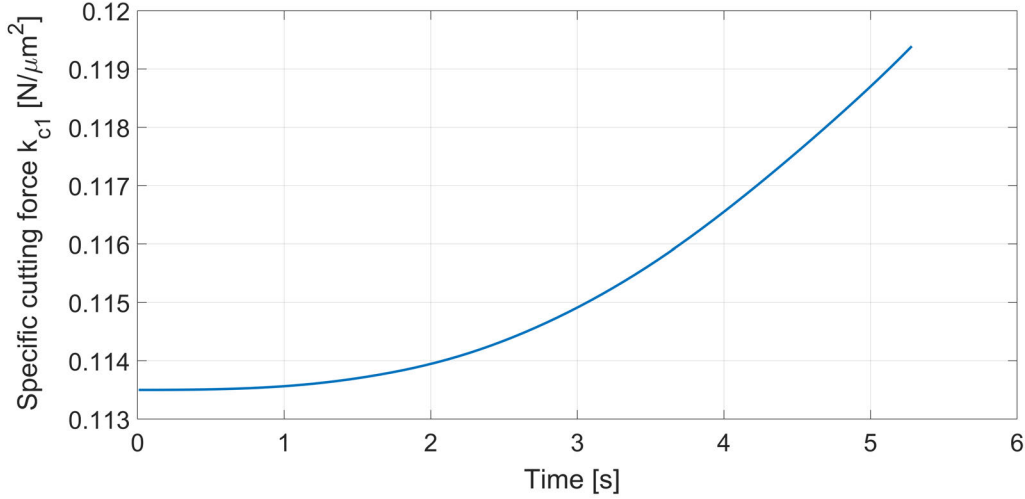


Figure 8.17: The evolution of specific cutting force  $k_{c1}$  over the cutting time.

The acting stresses measured in the single grain wear simulations are presented in Figure 8.18. The load on a grain can be defined using the Rankine theory (or the maximum principle stress theory) which estimates the maximum stress where the brittle materials fail without elastic prolongation.

The Rankine equation can be expressed as:

$$\sigma_r = \frac{(\sigma_c + \sigma_n)}{2} + \frac{\sqrt{(\sigma_c - \sigma_n)^2 + 4\tau_s^2}}{2} \quad (8.1)$$

where  $\sigma_r$  is the principal stress,  $\sigma_c$  is the cutting stress,  $\sigma_n$  is the normal stress, and  $\tau_s$  is the shear stress. The cutting stress  $\sigma_c$  in the direction of cut is defined as:

$$\sigma_c = \frac{F_c}{A_{cu}} \quad (8.2)$$

where  $F_c$  is the cutting force and  $A_{cu}$  is the penetrating grain area orthogonal to the cutting direction. The normal stress  $\sigma_n$  is defined as:

$$\sigma_n = \frac{F_n}{A_{\perp}} \quad (8.3)$$

where  $F_n$  is the normal force and  $A_{\perp}$  is the orthogonal grain area in the direction normal to the workpiece surface. For simplicity, the grain cross-sections in the direction of wire surface normal are approximated as circles.

Finally, the third stress component  $\tau_s$  is defined as:

$$\tau_s = \frac{F_c}{A_{\perp}} \quad (8.4)$$

The average cutting stress is increasing drastically towards the end of the grain lifetime, mainly due to increase of the process forces with grain dulling. The increase of the average normal and shear stresses are lower, as the orthogonal grain areas are increasing with progressing grain wear, due to the presence of sharp grain geometries. The local drops and peaks in the stress values are related to the changes in grain geometries; and the drop in the stress values at the end of the cutting time is the result of the pulled out grains that are no longer contributing to the process.

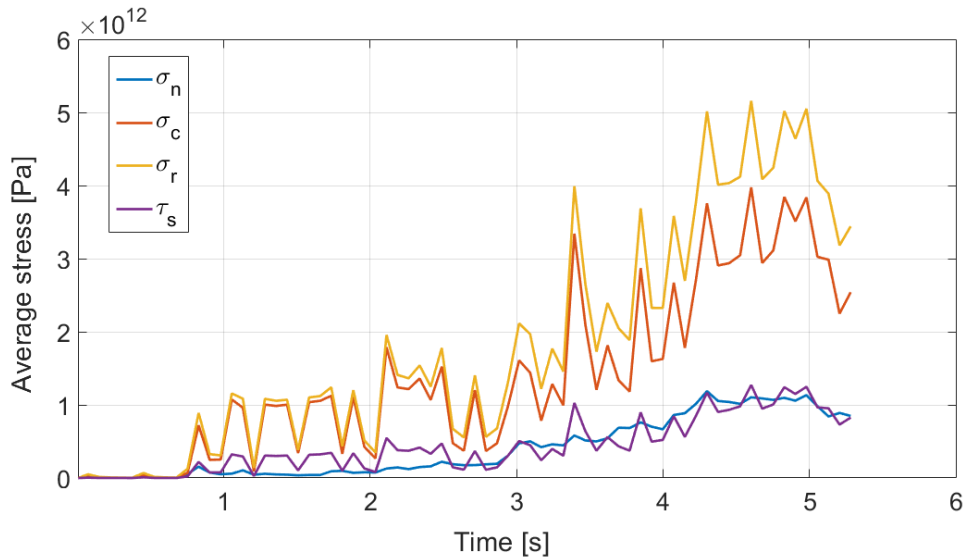


Figure 8.18: The evolution of normal, cutting, shear and resultant stresses components over lifetime.

# Chapter 9

## Conclusion and Outlook

In this thesis, the diamond wire sawing of sc-Si is investigated theoretically and experimentally, concerning the wire-workpiece interaction at single grain level and the influence of different process parameters on workpiece quality and wire wear. Two experiment setups are developed to emulate the wire sawing process at high wire speeds. The influence of the process parameters on workpiece surface and wire wear, process forces and temperature at the grain tip are investigated; parameters, software tools and analysis methods for the evaluation of electroplated diamond wires and silicon surfaces are developed. Models concerning the wire and abrasive grain, material removal, process forces and wire wear are constructed so that prediction of the process behavior and process results become possible.

The diamond wires are characterized for their topographic aspects (i.e. diamond concentration and distribution, grain geometry and size) through microscopy and by employing the Wire Analysis Software (WAS). Further, the Surface Analysis Software (SAS) is developed for the characterization of resultant silicon workpiece surfaces for their brittle and ductile material removal modes. For several process parameters, the influence of diamond wires are experimentally evaluated based on the process forces, silicon surface quality and diamond wear.

A grain geometry model is constructed considering the grain size and geometry, which is then employed in a stochastic wire model to simulate the diamond wire topography. The simulated wire model is validated through the comparison of Abbott-Firestone curves and grain geometries; and is then employed in the kinematic model to establish a kinematic-geometric process model. A material removal model which considers the brittle and ductile material removal mechanisms and a modified Kienzle force model are developed and validated through single grain scratch tests. These

models are combined to determine the process forces and resultant workpiece surface at different process conditions. A temperature model for estimating the flash temperatures at the grain tip is constructed. The wear of diamond wires at different wire speeds is experimentally investigated and used for the validation of the wear model.

The experimental investigation based on single grain material removal shows that with increasing grain penetration, brittle removal is more evident and a threshold could be defined as the penetration depth for the onset of brittle removal. However, this threshold doesn't only depend on the depth of penetration, but is highly correlated with the width to depth ratio of the penetrating grain.

Ductile and brittle material removal regimes are present at the same time. Each abrasive grain can cause brittle or ductile material removal and the material removal regime may change along the cutting path of an abrasive grain. On the other hand, at higher wire speeds, a better Si surface quality is possible through a higher ductile finish. With increasing wire speeds, normal and cutting forces decrease, resulting in the domination of ductile material removal mechanism and lead to lower surface roughness.

On the influence of wire parameters on process outputs, it is found that there is a wire speed threshold of around  $30\text{ m/s}$ , where below this limit, wires with smaller average diamond size and lower average diamond protrusion experience lower cutting and higher normal forces. The behavior reverses over this threshold and also cutting and normal forces are less affected by the change in diamond size and protrusion. Over the wire speed threshold of  $30\text{ m/s}$ , cutting and normal forces of all wires gradually decrease with a similar trend as wire speed increases. Moreover, it is evident that diamond size and protrusion have a stronger influence on process forces than diamond concentration.

The temperature values and thermal behavior at the grain tip also depend on the contact conditions and material removal regime. It is shown that higher temperature values are present in the case of ductile material removal. Moreover, in a ductile cut, the temperature increases as the grain penetration depth increases, whereas in the case of brittle material removal, temperature decreases with increasing grain penetration. This mainly shows that the energy dissipation into heat for massive plastic deformation is larger than the generation of a brittle crack, which is aligned with the observation of decreasing forces with increasing brittleness.



---

The wire wear experiments show that the reduction of grain protrusion and volume experience an exponential decrease. The wire is wearing out through grain edge fracture, dulling and pullouts that are mainly at the end of the wire lifetime. It is found that the bonding wear shows two distinctive ranges: at the beginning, the grain base areas don't deviate from their initial state. With propagating wear, the filler material accumulated around the base of the grain is eventually exposed to the process and starts to wear rapidly, thereby reducing the bonding strength and leading to a grain pullout. The developed grain wear model and bonding wear model can well explain these behaviors. In addition, a lower wire wear rate is evident at higher wire speeds.

The experimental setups, analysis and measurement methods and software, the models regarding the wire, workpiece and process presented in this thesis provide a modular, complete methodology for diamond wire characterization. They can be employed as a toolbox for the prediction of diamond wire behavior in silicon machining. In addition to the presented topics, the kinematics of the wire sawing process can be implemented to a modular modeling scheme. However, the investigated process parameter limits are currently not possible in wire sawing due to the process limitations. In today's multi-wire sawing technology, due to dynamic effects on the saw, the beneficial wire speeds cannot be reached. Nevertheless, the WWGW experiments show that improvements in terms of wear and surface quality are possible at high speeds.

The material removal model presented is based on stochastic grain geometries, which provides a highly realistic case; but also makes it impossible to characterize the grain shapes so that their influence on brittle removal mechanism can be clearly defined. It is possible to reach a higher understanding of the brittle removal mechanisms in silicon by using the Scratch Test Setup and defined diamond geometries at high speeds. The force model, which considers both brittle and ductile removal cases can be improved so that the coefficients are determined for these modes separately, and also at different cutting speeds. The temperature model on the other hand, can reach a higher accuracy with the implementation of a 3D grain model and/or including the transient case of heat flow, for a better estimation of the thermal interaction in the cutting zone.

# Bibliography

- [1] DIN 50320: Wear Terms Systematic Analysis of Wear Processes: Classification of Wear Phenomena, Technical report, Deutsches Institut für Normung E.V. (DIN).
- [2] ISO 1101-2017: Geometrical Product Specifications (GPS) - Geometrical Tolerancing: Tolerances of Form, Orientation, Location and Run-out, Technical report.
- [3] ISO 3002-5: Basic Quantities in Cutting and Grinding Part 5: Basic Terminology for Grinding Processes Using Grinding Wheels, Technical report, International Organization for Standardization (ISO).
- [4] ISO 5436-2012: Geometrical Product Specifications (GPS) - Surface Texture: Profile Method; Measurement Standards – Part 2: Software Measurement Standards, Technical report, International Organization for Standardization (ISO).
- [5] ISO/DIS 25718-606: Geometrical Product Specifications (GPS) - Surface Texture: Areal - Part 606: Nominal Characteristics of Non-contact (Focus Variation Instruments, Technical report, International Organization for Standardization (ISO).
- [6] Abbott E. J., Firestone F. A., 1933, Specifying Surface Quality - A Method Based on Accurate Measurement and Comparison, *Journal of Mechanical Engineering*, 55:569–572.
- [7] Alagumurthi N., Palaniradja K., Soundararajan V., 2006, Optimization of Grinding Process Through Design of Experiment (DOE)—A Comparative Study, *Materials and Manufacturing Processes*, 21(1):19–21, doi:10.1080/AMP-200060605.
- [8] Alicona Imaging GmbH, *Alicona IFM Manual G4 3.5 EN*, 2009.

- [9] Anspach O., Hurka B., Sunder K., 2014, Structured Wire: From Single Wire Experiments to Multi-Crystalline Silicon Wafer Mass Production, *Solar Energy Materials and Solar Cells*, 131:58–63, doi:10.1016/j.solmat.2014.06.008.
- [10] Anton R. J., Subhash G., 2000, Dynamic Vickers Indentation of Brittle Materials, *Wear*, 239(1):27–35, doi:10.1016/S0043-1648(99)00364-6.
- [11] Archard J. F., 1953, Contact and Rubbing of Flat Surfaces, *Journal of Applied Physics*, 24(8):981–988, doi:10.1063/1.1721448.
- [12] Archard J. F., 1959, The Temperature of Rubbing Surfaces, *Wear*, 2(6):438–455, doi:10.1016/0043-1648(59)90159-0.
- [13] Archard J. F., Hirst W., 1956, The Wear of Metals under Unlubricated Conditions, *Proceedings of the Royal Society of London. Series A. Mathematical and Physical Sciences*, 236(1206):397, doi:10.1098/rspa.1956.0144.
- [14] Arefin S., Li X. P., Rahman M., Liu K., 2006, The Upper Bound of Tool Edge Radius for Nanoscale Ductile Mode Cutting of Silicon Wafer, *The International Journal of Advanced Manufacturing Technology*, 31(7):655, doi:10.1007/s00170-005-0245-0.
- [15] Arif M., Xinquan Z., Rahman M., Kumar S., 2013, A Predictive Model of the Critical Undeformed Chip Thickness for Ductile–Brittle Transition in Nanomachining of Brittle Materials, *International Journal of Machine Tools and Manufacture*, 64:114–122, doi:10.1016/j.ijmactools.2012.08.005.
- [16] Attanasio A., Ceretti E., Rizzuti S., Umbrello D., Micari F., 2008, 3D Finite Element Analysis of Tool Wear in Machining, *Cirp Annals-Manufacturing Technology*, 57(1):61–64, doi:10.1016/j.cirp.2008.03.123.
- [17] Aurich J. C., Biermann D., Blum H., Brecher C., Carstensen C., Denkena B., Klocke F., Kröger M., Steinmann P., Weinert K., 2009, Modelling and Simulation of Process: Machine Interaction in Grinding, *Production Engineering*, 3(1):111–120, doi:10.1007/s11740-008-0137-x.
- [18] Aurich J. C., Braun O., Warnecke G., Cronjäger L., 2003, Development of a Superabrasive Grinding Wheel With Defined Grain Structure Using Kinematic Simulation, *CIRP Annals*, 52(1):275–280, doi:10.1016/S0007-8506(07)60583-6.
- [19] Aurich J. C., Kirsch B., 2012, Kinematic Simulation of High-performance Grinding for Analysis of Chip Parameters of Single Grains, *CIRP Journal of Manufacturing Science and Technology*, 5(3):164–174, doi:10.1016/j.cirpj.2012.07.004.

- [20] Aurich J. C., Steffes M., 2011, Single Grain Scratch Tests to Determine Elastic and Plastic Material Behavior in Grinding, *Advanced Materials Research*, 325:48–53, doi:10.4028/www.scientific.net/AMR.325.48.
- [21] Azizi A., Mohamadyari M., 2015, Modeling and Analysis of Grinding Forces Based on the Single Grit Scratch, *The International Journal of Advanced Manufacturing Technology*, 78(5-8):1223–1231, doi:10.1007/s00170-014-6729-z.
- [22] Badger J. A., Torrance A. A., 2000, A Comparison of Two Models to Predict Grinding Forces from Wheel Surface Topography, *International Journal of Machine Tools and Manufacture*, 40(8):1099–1120, doi:10.1016/s0890-6955(99)00116-9.
- [23] Barber J., 1991, Is Modeling in Tribology a Useful Activity?, *Tribological Modeling for Mechanical Designers*, pages 165–172, doi:10.1520/STP17664S.
- [24] Basore P. A., 1994, Defining Terms for Crystalline Silicon Solar Cells, *Progress in Photovoltaics: Research and Applications*, 2(2):177–179, doi:10.1002/pip.4670020213.
- [25] Bhattacharya A. K., Nix W. D., 1988, Finite Element Simulation of Indentation Experiments, *International Journal of Solids and Structures*, 24(9):881–891, doi:10.1016/0020-7683(88)90039-X.
- [26] Bhushan B., 1987, Magnetic Head-Media Interface Temperatures. Part 1-Analysis, *Trans. ASME, J. Tribol.*, 109:243, doi:10.1115/1.3261346.
- [27] Bhushan B., 2000, *Modern Tribology Handbook Volume 1*. CRC Press.
- [28] Bhushan B., 2001, Nano- to Microscale Wear and Mechanical Characterization Using Scanning Probe Microscopy, *Wear*, 251(1):1105–1123, doi:10.1016/S0043-1648(01)00804-3.
- [29] Bidiville A., Wasmer K., Meer M. Van der, Ballif C., 2015, Wire Sawing Processes: Parametrical Study and Modeling, *Solar Energy Materials and Solar Cells*, 132:392–402, doi:10.1016/j.solmat.2014.09.019.
- [30] Bifano T. G., 1989, Ductile-Regime Grinding of Brittle Materials: Experimental Results and The Development of a Model, *Proceedings of SPIE - The International Society for Optical Engineering*, 966:108–115, doi:10.1117/12.948055.
- [31] Bifano T. G., Dow T. A., Scattergood R. O., 1991, Ductile-Regime Grinding - a New Technology for Machining Brittle Materials, *Journal of Engineering for Industry-Transactions of the Asme*, 113(2):184–189, doi:10.1115/1.2899676.

- [32] Bifano T. G., Fawcett S. C., 1991, Specific Grinding Energy as an In-process Control Variable for Ductile-Regime Grinding, *Precision Engineering*, 13(4):256–262, doi:10.1016/0141-6359(91)90003-2.
- [33] Blake P. N., Scattergood R. O., 1990, Ductile-Regime Machining of Germanium and Silicon, *Journal of the American Ceramic Society*, 73(4):949–957, doi:10.1111/j.1151-2916.1990.tb05142.x.
- [34] Blunt L., Ebdon S., 1996, The Application of Three-dimensional Surface Measurement Techniques to Characterizing Grinding Wheel Topography, *International Journal of Machine Tools and Manufacture*, 36(11):1207–1226, doi:10.1016/0890-6955(96)00041-7.
- [35] Bredell L. J., Prins J. F., 1982, Microcutting of Steel Using Pyramidal Diamonds with Different Apex Angles, *Wear*, 76(2):177–187, doi:10.1016/0043-1648(82)90004-7.
- [36] Bridgman P. W., Šimon I., 1953, Effects of Very High Pressures on Glass, *Journal of Applied Physics*, 24(4):405–413, doi:10.1063/1.1721294.
- [37] Brinksmeier E., Aurich J. C., Govekar E., Heinzl C., Hoffmeister H. W., Klocke F., Peters J., Rentsch R., Stephenson D. J., Uhlmann E., Weinert K., Wittmann M., 2006, Advances in Modeling and Simulation of Grinding Processes, *CIRP Annals - Manufacturing Technology*, 55(2):667–696, doi:10.1016/j.cirp.2006.10.003.
- [38] Brinksmeier E., Werner F., 1992, Monitoring of Grinding Wheel Wear, *CIRP Annals*, 41(1):373–376, doi:10.1016/S0007-8506(07)61225-6.
- [39] Brinksmeler E., Glwierzew A., 2003, Chip Formation Mechanisms in Grinding at Low Speeds, *CIRP Annals*, 52(1):253–258, doi:10.1016/s0007-8506(07)60578-2.
- [40] Bruecher T., 1996, *Kühlschmierung beim Schleifen Keramischer Werkstoffe*, PhD dissertation, Technische Universität Berlin.
- [41] Buchwald R., Fröhlich K., Würzner S., Lehmann T., Sunder K., Möller H. J., 2013, Analysis of the Sub-surface Damage of mc- and cz-Si Wafers Sawn with Diamond-plated Wire, *Energy Procedia*, 38:901–909, doi:10.1016/j.egypro.2013.07.363.
- [42] Buhl S., 2012, *Failure Mechanisms of Heavily-loaded Brazed Diamonds*, PhD dissertation, ETH Zurich, doi:10.3929/ethz-a-007333271.

- [43] Buhl S., Leinenbach C., Spolenak R., Wegener K., 2013, Failure Mechanisms and Cutting Characteristics of Brazed Single Diamond Grains, *The International Journal of Advanced Manufacturing Technology*, 66(5):775–786, doi:10.1007/s00170-012-4365-z.
- [44] Burwell J. T., Strang C. D., 1952, On the Empirical Law of Adhesive Wear, *Journal of Applied Physics*, 23(1):18–28, doi:10.1063/1.1701970.
- [45] Cai M. B., Li X. P., Rahman M., 2007, Study of the Mechanism of Groove Wear of the Diamond Tool in Nanoscale Ductile Mode Cutting of Monocrystalline Silicon, *Journal of Manufacturing Science and Engineering*, 129(2):281, doi:10.1115/1.2673567.
- [46] Callahan D. L., Morris J. C., 1992, The Extent of Phase Transformation in Silicon Hardness Indentations, *Journal of Materials Research*, 7(7):1614–1617, doi:10.1557/JMR.1992.1614.
- [47] Carslaw H. S., Jaeger J. C., 1959, *Conduction of Heat in Solids*. Oxford University Press, London, UK, 2nd edition.
- [48] Chandra A., Anderson G., Melkote S., Gao W., Haitjema H., Wegener K., 2014, Role of Surfaces and Interfaces in Solar Cell Manufacturing, *CIRP Annals*, 63(2):797–819, doi:10.1016/j.cirp.2014.05.008.
- [49] Chao C. L., Ma K. J., Liu D. S., Bai C. Y., Shy T. L., 2002, Ductile Behaviour in Single-point Diamond-turning of Single-Crystal Silicon, *Journal of Materials Processing Technology*, 127(2):187–190, doi:10.1016/S0924-0136(02)00124-3.
- [50] Chiang S. S., Marshall D. B., Evans A. G., 1982, The Response of Solids to Elastic/Plastic Indentation. I. Stresses and Residual Stresses, *Journal of Applied Physics*, 53(1):298–311, doi:10.1063/1.329930.
- [51] Chung C., Le V.-N., 2015, Depth of Cut per Abrasive in Fixed Diamond Wire Sawing, *The International Journal of Advanced Manufacturing Technology*, 80(5-8):1337–1346, doi:10.1007/s00170-015-7089-z.
- [52] Chung C., Nhat L. V., 2014, Generation of Diamond Wire Sliced Wafer Surface Based on the Distribution of Diamond Grits, *International Journal of Precision Engineering and Manufacturing*, 15(5):789–796, doi:10.1007/s12541-014-0401-2.

- [53] Chung C., Tsay G. D., Tsai M.-H., 2014, Distribution of Diamond Grains in Fixed Abrasive Wire Sawing Process, *The International Journal of Advanced Manufacturing Technology*, 73(9):1485–1494, doi:10.1007/s00170-014-5782-y.
- [54] Chung C. H., 2012, Abrasive Distribution of the Fixed Diamond Wire in Wire Sawing Process, *Advanced Materials Research*, 579:145–152, doi:10.4028/www.scientific.net/AMR.579.145.
- [55] Clark W. I., Shih A. J., Hardin C. W., Lemaster R. L., McSpadden S. B., 2003, Fixed abrasive Diamond Wire Machining-Part I: Process Monitoring and Wire Tension Force, *International Journal of Machine Tools and Manufacture*, 43(5):523–532, doi:10.1016/s0890-6955(02)00215-8.
- [56] Clark W. I., Shih A. J., Lemaster R. L., McSpadden S. B., 2003, Fixed Abrasive Diamond Wire Machining—Part II: Experiment Design and Results, *International Journal of Machine Tools and Manufacture*, 43(5):533–542, doi:10.1016/s0890-6955(02)00216-x.
- [57] Coustier F., Penot J.-D., Lac L. Bourget-du, Sanchez G., Ly M., 2012, Diamond Wire Sawing State of the Art and Perspectives, *Photovoltaics International*, pages 40–45.
- [58] Crisp J., Sejdel J. R., Stokey W. F., 1968, Measurement of Forces during Cutting with a Single Abrasive Grai, *International Journal of Production Research*, 7(2):159–171, doi:10.1080/00207546808929806.
- [59] Crompton D., Hirst W., Howse M. G. W., 1973, The Wear of Diamond, *Proceedings of the Royal Society of London. Series A, Mathematical and Physical Sciences*, 333(1595):435–454.
- [60] Darafon A., Warkentin A., Bauer R., 2013, Characterization of Grinding Wheel Topography Using a White Chromatic Sensor, *International Journal of Machine Tools and Manufacture*, 70:22–31, doi:10.1016/j.ijmachtools.2013.03.003.
- [61] De Pellegrin D. V., Corbin N. D., Baldoni G., Torrance A. A., 2009, Diamond Particle Shape: Its Measurement and Influence in Abrasive Wear, *Tribology International*, 42(1):160–168, doi:10.1016/j.triboint.2008.04.007.
- [62] De Pellegrin D. V., Stachowiak G. W., 2002, Assessing the Role of Particle Shape and Scale in Abrasion Using ‘Sharpness Analysis’: Part I. Technique Development, *Wear*, 253(9):1016–1025, doi:10.1016/S0043-1648(02)00232-6.

- [63] Doman D. A., Warkentin A., Bauer R., 2006, A Survey of Recent Grinding Wheel Topography Models, *International Journal of Machine Tools and Manufacture*, 46(3):343–352, doi:10.1016/j.ijmachtools.2005.05.013.
- [64] Einstein A., 1905, Uber Einen die Erzeugung und Verwandlung des Lichtes betreffenden heurischen Gesichtspunkt (transl. On a Heuristic Viewpoint Concerning the Production and Transformation of Light), *Ann. Phys.*, 17:132–148.
- [65] Feng B. F., Cai G. Q., Sun X. L., 2006, Groove, Chip and Force Formation in Single Grain High-Speed Grinding, *Key Engineering Materials*, 304-305:196–200, doi:10.4028/www.scientific.net/KEM.304-305.196.
- [66] Feng Y. B., Chen B., Sun T., 2014, Research on Tension Control System of Wire Saw Slicing Machine, *Key Engineering Materials*, 621:419–424, doi:10.4028/www.scientific.net/KEM.621.419.
- [67] Field J. E., 2012, The Mechanical and Strength Properties of Diamond, *Reports on Progress in Physics*, 75(12), doi:10.1088/0034-4885/75/12/126505.
- [68] Fritts C. E., 1883, On a New Form of Selenium Cell, and Some Electrical Discoveries Made by its Use, *American Journal of Science*, s3-26(156):465–472, doi:10.2475/ajs.s3-26.156.465.
- [69] Funke C., Wolf S., Stoyan D., 2009, Modeling the Tensile Strength and Crack Length of Wire-Sawn Silicon Wafers, *Journal of Solar Energy Engineering*, 131(1):011012–1–011012–6, doi:10.1115/1.3028048.
- [70] Gahr K. H. Z., 1987, *Microstructure and Wear of Materials*. Tribology Series Volume 10. Elsevier, doi:10.1016/S0167-8922(08)70718-1.
- [71] Gao Y., Ge P., Liu T., 2016, Experiment Study on Electroplated Diamond Wire Saw Slicing Single-Crystal Silicon, *Materials Science in Semiconductor Processing*, 56:106–114, doi:10.1016/j.mssp.2016.08.003.
- [72] Ge P. Q., Zhang L., Gao W., Liu Z. C., 2004, Development of Endless Diamond Wire Saw and Sawing Experiments, *Materials Science Forum*, 471-472:481–484, doi:10.4028/www.scientific.net/MSF.471-472.481.
- [73] Goodrich A., Hacke P., Wang Q., Sopori B., Margolis R., James T. L., Woodhouse M., 2013, A Wafer-based Monocrystalline Silicon Photovoltaics Roadmap: Utilizing Known Technology Improvement Opportunities for Further Reductions in Manufacturing Costs, *Solar Energy Materials and Solar Cells*, 114:110–135, doi:10.1016/j.solmat.2013.01.030.



- [74] Gopal A. V., Rao P. V., 2004, A New Chip Thickness Model for Performance Assessment of Silicon Carbide Grinding, *International Journal of Advanced Manufacturing Technology*, 24(11-12):816–820, doi:10.1007/s00170-003-1788-6.
- [75] Graham D., Baul R. M., 1972, An Investigation into the Mode of Metal Removal in the Grinding Process, *Wear*, 19(3):301–314, doi:10.1016/0043-1648(72)90122-6.
- [76] Graham W., Voutsadopoulos C. M., 1978, Fracture Wear of Grinding Wheels, *International Journal of Machine Tool Design and Research*, 18(2):95–103, doi:10.1016/0020-7357(78)90012-4.
- [77] Green M. A., Emery K., Hishikawa Y., Warta W., 2011, Solar Cell Efficiency Tables 37, *Progress in Photovoltaics: Research and Applications*, 19(1):84–92, doi:10.1002/pip.1088.
- [78] Gu W. B., Yao Z. Q., Liang X. G., 2011, Material Removal of Optical Glass BK7 During Single and Double Scratch Tests, *Wear*, 270(3-4):241–246, doi:10.1016/j.wear.2010.10.064.
- [79] Guimarães L., Santos R., Almada-Lobo B., 2011, Scheduling Wafer Slicing by Multi-wire Saw Manufacturing in Photovoltaic Industry: A Case Study, *The International Journal of Advanced Manufacturing Technology*, 53(9):1129–1139, doi:10.1007/s00170-010-2906-x.
- [80] Hagiwara S., Obikawa T., Usui E., 1998, Edge Fracture Characteristics of Abrasive Grain, *Journal of Manufacturing Science and Engineering*, 120(4):708–714, doi:10.1115/1.2830210.
- [81] Han X. S., Wang S. X., Yu S. Y., 2003, Molecular Dynamics Simulation of Nanometric Grinding - the Effect of Crystal Anisotropy on the Quality of Machined Surface, *Key Engineering Materials*, 259-260:361–365, doi:10.4028/www.scientific.net/KEM.259-260.361.
- [82] Hardin C. W., Qu J., Shih A. J., 2004, Fixed Abrasive Diamond Wire Saw Slicing of Single-Crystal Silicon Carbide Wafers, *Materials and Manufacturing Processes*, 19(2):355–367, doi:10.1081/Amp-120029960.
- [83] Hecker R. L., Ramoneda I.M., Liang S. Y., 2003, Analysis of Wheel Topography and Grit Force for Grinding Process Modeling, *Journal of Manufacturing Processes*, 5(1):13–23, doi:10.1016/S1526-6125(03)70036-X.

- [84] Henerichs M., Egeter M., Liebrich T., Voss R., Wegener K., 2014, Evaluation of the IWF-Wunder Reproduction Method for Generating Positive Replica, *International Journal of Automation Technology*, 8(1):49–56, doi:hdl.handle.net/20.500.11850/78235.
- [85] Hill R., 1950, *The Mathematical Theory of Plasticity*, book section 5. Oxford Univ. Press.
- [86] Hirst W., Lancaster J. K., 1960, The Influence of Speed on Metallic Wear, *Proceedings of the Royal Society of London. Series A. Mathematical and Physical Sciences*, 259(1297):228, doi:10.1098/rspa.1960.0220.
- [87] Holm R., 1946, *Electrical Contacts*, Report, Almqvist and Wilselles, Stockholm.
- [88] Howes T. D., Neailey K., Harrison A. J., McKeown P. A., 1987, Fluid Film Boiling in Shallow Cut Grinding, *CIRP Annals*, 36(1):223–226, doi:10.1016/S0007-8506(07)62591-8.
- [89] Hsu C. Y., Chen C. S., Tsao C. C., 2008, Free Abrasive Wire Saw Machining of Ceramics, *The International Journal of Advanced Manufacturing Technology*, 40(5-6):503–511, doi:10.1007/s00170-007-1355-7.
- [90] Huang H., Zhang Y., Xu X., 2015, Experimental Investigation on the Machining Characteristics of Single-Crystal SiC Sawing with the Fixed Diamond Wire, *The International Journal of Advanced Manufacturing Technology*, 81(5-8):955–965, doi:10.1007/s00170-015-7250-8.
- [91] Hull R., 1999, *Properties of Crystalline Silicon*. INSPEC, The Institute of Electrical Engineers, London, UK.
- [92] Hung N. P., Fu Y. Q., 2000, Effect of Crystalline Orientation in the Ductile-Regime Machining of Silicon, *International Journal of Advanced Manufacturing Technology*, 16(12):871–876, doi:10.1007/s001700070004.
- [93] Huo F. W., Jin Z. J., Zhao F. L., Kang R. K., Guo D. M., 2007, Experimental Investigation of Brittle to Ductile Transition of Single Crystal Silicon by Single Grain Grinding, *Key Engineering Materials*, 329:433–438, doi:10.4028/www.scientific.net/KEM.329.433.
- [94] Hwang T. W., Evans C. J., Malkin S., 2000, High Speed Grinding of Silicon Nitride With Electroplated Diamond Wheels, Part 2: Wheel Topography and Grinding Mechanisms, *Journal of Manufacturing Science and Engineering*, 122(1), doi:10.1115/1.538909.

- 
- [95] Inasaki I., 1987, Grinding of Hard and Brittle Materials, *CIRP Annals - Manufacturing Technology*, 36(2):463–471, doi:10.1016/s0007-8506(07)60748-3.
- [96] Inasaki I., 1996, Grinding Process Simulation Based on the Wheel Topography Measurement, *CIRP Annals*, 45(1):347–350, doi:10.1016/S0007-8506(07)63077-7.
- [97] International Energy Agency, 2010, Technology Roadmap Solar Photovoltaic Energy, Report.
- [98] ITRPV, 2018, International Technology Roadmap for Photovoltaic, Report, ITRPV.
- [99] Jackson M. J., Davim J. P., 2011, *Machining with Abrasives*. Springer, New York, doi:10.1007/978-1-4419-7302-3.
- [100] Jacobson S., Wallen P., Hogmark S., 1988, Fundamental Aspects of Abrasive Wear Studied by a New Numerical Simulation Model, *Wear*, 123(2):207–223, doi:10.1016/0043-1648(88)90100-7.
- [101] Jaeger J. C., 1942, Moving Sources of Heat and the Temperature of Sliding Contacts, *Proceedings of the Royal Society of New South Wales*, 76:203–224.
- [102] Jaeggi C., DeMeyer C., Wiedmer F., Stierli R., Simoncic P., Assi F., Wasmer K., 24-28 September 2012, Effects of Wire Lifetime in Diamond Wire Wafering on the Wafer Roughness and Mechanical Strength, In *27th European Photovoltaic Solar Energy Conference*, 24-28 September 2012.
- [103] Jester T. L., 2002, Crystalline Silicon Manufacturing Progress, *Progress in Photovoltaics: Research and Applications*, 10(2):99–106, doi:10.1002/pip.414.
- [104] Jiang J., Arnell R. D., 1998, The Effect of Sliding Speed on Wear of Diamond-like Carbon Coatings, *Wear*, 218(2):223–231, doi:10.1016/S0043-1648(98)00202-6.
- [105] Kato K., 2002, Classification of Wear Mechanisms/Models, *Proceedings of the Institution of Mechanical Engineers, Part J: Journal of Engineering Tribology*, 216(6):349–355, doi:10.1243/135065002762355280.
- [106] Kato T., Fujii H., 1998, Temperature Measurement of Workpieces in Conventional Surface Grinding, *Journal of Manufacturing Science and Engineering*, 122(2):297–303, doi:10.1115/1.538918.
- [107] Kegg R. L., 1983, Industrial Problems in Grinding, *CIRP Annals*, 32(2):559–561, doi:10.1016/S0007-8506(07)60183-8.

- [108] Kennedy F. E., 1982, Single Pass Rub Phenomena—Analysis and Experiment, *Journal of Lubrication Technology*, 104(4):582–588, doi:10.1115/1.3253293.
- [109] Kienzle O., 1952, Die Bestimmung von Kräften und Leistungen an Spanenden Werkzeugen und Werkzeugmaschinen, *VDI-Z*, 94(11-12):299–305.
- [110] Kienzle O., Victor H., 1957, Spezifische Schnittkräfte bei der Metallbearbeitung, *Werkstattstechnik und Maschinenbau*, 47(5):224–225.
- [111] Kim D., Kim H., Lee S., Jeong H., 2015, Effect of Initial Deflection of Diamond Wire on Thickness Variation of Sapphire Wafer in Multi-wire Saw, *International Journal of Precision Engineering and Manufacturing-Green Technology*, 2(2):117–121, doi:10.1007/s40684-015-0015-x.
- [112] Kim D., Kim H., Lee S., Lee T., Jeong H., 2016, Characterization of Diamond Wire-cutting Performance for Lifetime Estimation and Process Optimization, *Journal of Mechanical Science and Technology*, 30(2):847–852, doi:10.1007/s12206-016-0139-0.
- [113] Kim H., Kim D., Kim C., Jeong H., 2013, Multi-wire Sawing of Sapphire Crystals with Reciprocating Motion of Electroplated Diamond Wires, *CIRP Annals - Manufacturing Technology*, 62(1):335–338, doi:10.1016/j.cirp.2013.03.122.
- [114] Kim H. J., Kim D. Y., Lee S. J., Jeong H. D., Choi H. J., 2014, Characterization of Cutting Ability of Electroplated Diamond Wire Used for Multi-wire Saw, *Advanced Materials Research*, 1017:549–552, doi:10.4028/www.scientific.net/AMR.1017.549.
- [115] King R. F., Tabor D., 1954, The Strength Properties and Frictional Behaviour of Brittle Solids, *Proceedings of the Royal Society of London. Series A. Mathematical and Physical Sciences*, 223(1153):225–238, doi:10.1098/rspa.1954.0111.
- [116] Kitagawa T., Maekawa K., Shirakashi T., Usui E., 1988, Analytical Prediction of Flank Wear of Carbide Tools in Turning Plain Carbon Steels. Part I: Characteristic Equation of Flank Wear, *Bulletin of the Japan Society of Precision Engineering*, 22(4):263–269.
- [117] Klocke F., 2011, *Manufacturing Processes 1: Cutting*. Springer, Berlin Heidelberg, RWTH edition, doi:10.1007/978-3-642-11979-8.
- [118] Komanduri R., Chandrasekaran N., Raff L. M., 2000, M.D. Simulation of Nanometric Cutting of Single-Crystal Aluminum—effect of Crystal Ori-

- entation and Direction of Cutting, *Wear*, 242(1):60–88, doi:10.1016/S0043-1648(00)00389-6.
- [119] Kramer B. M., Turkovich B. F. von, 1986, A Comprehensive Tool Wear Model, *CIRP Annals - Manufacturing Technology*, 35(1):67–70, doi:10.1016/s0007-8506(07)61840-x.
- [120] Kuffa M., 2017, *High Performance Dry Grinding - HPDG*, PhD dissertation, ETH Zurich, doi:10.3929/ethz-b-000268402.
- [121] Kumar A., Kovalchenko A., Pogue V., Pashchenko E., Melkote S. N., 2016, Ductile Mode Behavior of Silicon During Scribing by Spherical Abrasive Particles, *Procedia CIRP*, 45:147–150, doi:10.1016/j.procir.2016.02.341.
- [122] Kumar A., Melkote S. N., 2018, Diamond Wire Sawing of Solar Silicon Wafers: A Sustainable Manufacturing Alternative to Loose Abrasive Slurry Sawing, *Procedia Manufacturing*, 21:549–566, doi:10.1016/j.promfg.2018.02.156.
- [123] Kumar A., Melkote S. N., Kaminski S., Arcona C., 2017, Effect of Grit Shape and Crystal Structure on Damage in Diamond Wire Scribing of Silicon, *Journal of the American Ceramic Society*, 100(4):1350–1359, doi:10.1111/jace.14732.
- [124] Kurtz S., Haegel N., Sinton R., Margolis R., 2017, A New Era for Solar, *Nature Photonics*, 11:3, doi:10.1038/nphoton.2016.232.
- [125] Lane B. M., Dow T. A., Scattergood R., 2013, Thermo-chemical Wear Model and Worn Tool Shapes for Single-Crystal Diamond Tools Cutting Steel, *Wear*, 300(1):216–224, doi:10.1016/j.wear.2013.02.012.
- [126] Lawn B., 1993, *Fracture of Brittle Solids*. Cambridge Solid State Science Series. Cambridge University Press, Cambridge , UK, 2nd edition.
- [127] Lawn B. R., Evans A. G., 1977, A Model for Crack Initiation in Elastic/Plastic Indentation Fields, *Journal of Materials Science*, 12(11):2195–2199, doi:10.1007/BF00552240.
- [128] Lawn B. R., Evans A. G., Marshall D. B., 1980, Elastic/Plastic Indentation Damage in Ceramics: The Median/Radial Crack System, *Journal of the American Ceramic Society*, 63(9-10):574–581, doi:10.1111/j.1151-2916.1980.tb10768.x.
- [129] Lawn B. R., Jensen T., Arora A., 1976, Brittleness as an Indentation Size Effect, *Journal of Materials Science*, 11(3):573–575, doi:10.1007/bf00540940.

- [130] Lawn B. R., Marshall D. B., 1979, Hardness, Toughness, and Brittleness: An Indentation Analysis, *Journal of the American Ceramic Society*, 62(7-8):347–350, doi:10.1111/j.1151-2916.1979.tb19075.x.
- [131] Lawn B. R., Swain M. V., 1975, Microfracture Beneath Point Indentations in Brittle Solids, *Journal of Materials Science*, 10(1):113–122, doi:10.1007/BF00541038.
- [132] Lawn B. R., Wilshaw R., 1975, Indentation Fracture: Principles and Applications, *Journal of Materials Science*, 10(6):1049–1081, doi:10.1007/bf00823224.
- [133] Lazard, 2018, Lazard’s Levelized Cost of Energy Analysis, Report.
- [134] Lee S., Kim H., Kim D., Park C., 2015, Investigation on Diamond Wire Break-in and its Effects on Cutting Performance in Multi-wire Sawing, *The International Journal of Advanced Manufacturing Technology*, 87(1-4):1–8, doi:10.1007/s00170-015-7984-3.
- [135] Li B., Ni J., Yang J., Liang S. Y., 2014, Study on High-speed Grinding Mechanisms for Quality and Process Efficiency, *The International Journal of Advanced Manufacturing Technology*, 70(5):813–819, doi:10.1007/s00170-013-5297-y.
- [136] Li S., Du S., Tang A., Landers R. G., Zhang Y., 2015, Force Modeling and Control of SiC Monocrystal Wafer Processing, *Journal of Manufacturing Science and Engineering*, 137(6), doi:10.1115/1.4029432.
- [137] Li S., Tang A., Liu Y., Wang J., Cui D., Landers R. G., 2016, Analytical Force Modeling of Fixed Abrasive Diamond Wire Saw Machining With Application to SiC Monocrystal Wafer Processing, *Journal of Manufacturing Science and Engineering*, 139(4):041003, doi:10.1115/1.4034792.
- [138] Li X., Cai M., Rahman M., Liang S., 2010, Study of the Upper Bound of Tool Edge Radius in Nanoscale Ductile Mode Cutting of Silicon Wafer, *The International Journal of Advanced Manufacturing Technology*, 48(9):993–999, doi:10.1007/s00170-009-2347-6.
- [139] Li X., Zhi G., Wolf S., Zhu T., Rong Y., 2015, Modelling and Analysis of the Bonding Mechanism of CBN Grains for Electroplated Superabrasive Tools—Part 2: Finite Element Modelling and Experimental Verification, *The International Journal of Advanced Manufacturing Technology*, 77(1):43–49, doi:10.1007/s00170-014-6412-4.

- [140] Liang Y. N., Li S. Z., Li S., 1994, Evaluation of Abradability of Porous Seal Materials in a Single-Pendulum Scratch Device, *Wear*, 177(2):167–173, doi:10.1016/0043-1648(94)90242-9.
- [141] Linke B. S., 2015, Review on Grinding Tool Wear With Regard to Sustainability, *Journal of Manufacturing Science and Engineering*, 137(6):060801–060801–8, doi:10.1115/1.4029399.
- [142] Liu B. C., Zhang Z. P., Sun Y. H., 2004, Sawing Trajectory and Mechanism of Diamond Wire Saw, *Key Engineering Materials*, 259-260:395–400, doi:10.4028/www.scientific.net/KEM.259-260.395.
- [143] Liu K., Li X. P., Liang S. Y., 2007, The Mechanism of Ductile Chip Formation in Cutting of Brittle Materials, *The International Journal of Advanced Manufacturing Technology*, 33(9):875–884, doi:10.1007/s00170-006-0531-5.
- [144] Liu K., Li X. P., Rahman M., Neo K. S., Liu X. D., 2006, A Study of the Effect of Tool Cutting Edge Radius on Ductile Cutting of Silicon Wafers, *The International Journal of Advanced Manufacturing Technology*, 32(7):631–637, doi:10.1007/s00170-005-0364-7.
- [145] Liu T., Ge P., Gao Y., Bi W., 2016, Depth of Cut for Single Abrasive and Cutting Force in Resin Bonded Diamond Wire Sawing, *International Journal of Advanced Manufacturing Technology*, pages 1–11, doi:10.1007/s00170-016-8896-6.
- [146] Lonardo P. M., Trumpold H., De Chiffre L., 1996, Progress in 3D Surface Microtopography Characterization, *CIRP Annals*, 45(2):589–598, doi:10.1016/S0007-8506(07)60513-7.
- [147] Luque A., Hegedus S., 2011, *Handbook of Photovoltaic Science and Engineering*. Wiley and Sons, United Kingdom, 2nd edition, doi:10.1002/9780470974704.
- [148] Maekawa K., Kitagawa T., Shirakashi T., Usui E., 1989, Analytical Prediction of Flank Wear of Carbide Tools in Turning Plain Carbon Steels. Part II: Prediction of Flank Wear, *Bulletin of the Japan Society of Precision Engineering*, 23(2):126–133.
- [149] Malkin S., Cook N. H., 1971, The Wear of Grinding Wheels: Part 1—Attritious Wear, *Journal of Engineering for Industry*, 93(4), doi:10.1115/1.3428051.
- [150] Malkin S., Guo C., 2008, *Grinding Technology: Theory and Applications of Machining with Abrasives*. Industrial Press, New York, 2nd edition.

- [151] Mamalis A. G., Manolacos D. E., Markopoulos A., Kunádrk J., Gyáni K., 2003, Thermal Modelling of Surface Grinding Using Implicit Finite Element Techniques, *The International Journal of Advanced Manufacturing Technology*, 21(12):929–934, doi:10.1007/s00170-002-1410-3.
- [152] Maradia U., 2014, *Meso - Micro EDM*, PhD dissertation, ETH Zürich, doi:10.3929/ethz-a-010353008.
- [153] Marinescu I. D., Hitchiner M., Uhlmann E., Rowe B. W., Inasaki I., 2007, *Handbook of Machining with Grinding Wheels*. CRC Press, doi:10.1201/9781420017649.
- [154] Marshall D. B., Lawn B. R., 1979, Residual Stress Effects in Sharp Contact Cracking, *Journal of Materials Science*, 14(8):2001–2012, doi:10.1007/bf00551043.
- [155] Marshall D. B., Lawn B. R., Evans A. G., 1982, Elastic/Plastic Indentation Damage in Ceramics: The Lateral Crack System, *Journal of the American Ceramic Society*, 65(11):561–566, doi:10.1111/j.1151-2916.1982.tb10782.x.
- [156] Matsuo T., Okamura K., 1981, Wear Characteristic of General and Superhard Abrasive Grains against Various Hard Materials, *CIRP Annals*, 30(1):233–236, doi:10.1016/S0007-8506(07)60932-9.
- [157] Matsuo T., Toyoura S., Oshima E., Ohbuchi Y., 1989, Effect of Grain Shape on Cutting Force in Superabrasive Single-grit Tests, *CIRP Annals - Manufacturing Technology*, 38(1):323–326, doi:10.1016/s0007-8506(07)62714-0.
- [158] McKinsey & Company, January 2019, Global Energy Perspective 2019: Reference Case, Report.
- [159] Meng H. C., Ludema K. C., 1995, Wear Models and Predictive Equations: Their Form and Content, *Wear*, 181-183:443–457, doi:10.1016/0043-1648(95)90158-2.
- [160] Meng J. F., Li J. F., Ge P. Q., Gao W., 2004, Removal Mechanism in Wire-Sawing of Hard-Brittle Material, *Materials Science Forum*, 471-472:192–195, doi:10.4028/www.scientific.net/MSF.471-472.192.
- [161] Meyer Burger AG, 2018. [www.meyerburger.ch](http://www.meyerburger.ch), Accessed on 15 June 2018.
- [162] Meyers M. A., 1994, *Dynamic Behavior of Materials*. John Wiley and Sons, Inc., doi:10.1002/9780470172278.



- 
- [163] Miyoshi K., 1998, Structures and Mechanical Properties of Natural and Synthetic Diamonds, Report, NASA Lewis Research Center, Cleveland, Ohio.
- [164] Moore M. A., King F. S., 1980, Abrasive Wear of Brittle Solids, *Wear*, 60(1):123–140, doi:10.1016/0043-1648(80)90253-7.
- [165] Möller H. J., 2004, Basic Mechanisms and Models of Multi-wire Sawing, *Advanced Engineering Materials*, 6(7):501–513, doi:10.1002/adem.200400578.
- [166] Möller H. J., 2006, Wafering of Silicon Crystals, *Physica Status Solidi (A)*, 203(4):659–669, doi:10.1002/pssa.200564508.
- [167] Möller H. J., 2015, *Handbook of Crystal Growth, Chapter 18: Wafer Processing*. Elsevier, Boston, doi:10.1016/B978-0-444-63303-3.00018-3.
- [168] Ozturk S., Aydin L., Celik E., 2018, A Comprehensive Study on Slicing Processes Optimization of Silicon Ingot for Photovoltaic Applications, *Solar Energy*, 161:109–124, doi:10.1016/j.solener.2017.12.040.
- [169] Park S. S., 2003, *High Frequency Bandwidth Cutting Force Measurements in Milling Using the Spindle Integrated Force Sensor System*, PhD dissertation, University of British Columbia, doi:10.14288/1.0081000.
- [170] Perfilyev V., Lapsker I., Laikhtman A., Rapoport L., 2016, Scratching of Copper and Silicon: Acoustic Emission Analysis, *Tribology Letters*, 65(1):24, doi:10.1007/s11249-016-0799-z.
- [171] Philipps S., March 14 2019, Photovoltaics Report, Report, Fraunhofer ISE and Werner Warmuth, PSE Conferences & Consulting GmbH.
- [172] Powell D. M., Winkler M. T., Choi H. J., Simmons C. B., Needleman D. B., Buonassisi T., 2012, Crystalline Silicon Photovoltaics: A Cost Analysis Framework for Determining Technology Pathways to Reach Baseload Electricity Costs, *Energy and Environmental Science*, 5(3):5874–5883, doi:10.1039/C2EE03489A.
- [173] Priolo F., Gregorkiewicz T., Galli M., Krauss T. F., 2014, Silicon Nanostructures for Photonics and Photovoltaics, *Nature Nanotechnology*, 9:19, doi:10.1038/nnano.2013.271.
- [174] Rabinowicz E., 1981, The Wear Coefficient—Magnitude, Scatter, Uses, *Journal of Lubrication Technology*, 103(2):188–193, doi:10.1115/1.3251624.
- [175] Rabinowicz E., 1995, *Friction and Wear of Materials*. Wiley and Sons, New York, 2nd edition.

- [176] Ravikiran A., 1999, Wear Quantification, *Journal of Tribology*, 122(3):650–656, doi:10.1115/1.555416.
- [177] REN21, 2019, Renewables Global Status Report, Report.
- [178] Rowe W. B., Morgan M. N., Black S. C. E., Mills B., 1996, A Simplified Approach to Control of Thermal Damage in Grinding, *CIRP Annals*, 45(1):299–302, doi:10.1016/S0007-8506(07)63067-4.
- [179] Rowe W. B., Yan Li, Inasaki I., Malkin S., 1994, Applications of Artificial Intelligence in Grinding, *CIRP Annals*, 43(2):521–531, doi:10.1016/S0007-8506(07)60498-3.
- [180] Rowe W.B., 2009, *Principles of Modern Grinding Technology*. William Andrew, Oxford, UK, doi:10.1016/C2013-0-06952-6.
- [181] Ruoff A. L., 1979, *The Fracture and Yield Strengths of Diamond, Silicon and Germanium*, pages 1557–1580. Springer US, Boston, MA, doi:10.1007/978-1-4684-7470-1194.
- [182] Sakakura M., Inasaki I., 1992, A Neural Network Approach to the Decision Making Process for Grinding Operations, *CIRP Annals*, 41(1):353–356, doi:10.1016/S0007-8506(07)61221-9.
- [183] Sasaki T., Okamura K., 1960, The Cutting Mechanism of Abrasive Grain : (1st Report, Experimental Observations of the Stock Removal and the Swell-up Phenomena), *Bulletin of JSME*, 3(12):547–555, doi:10.1299/jsme1958.3.547.
- [184] Schwinde S., Berg M., Kunert M., 2015, New Potential for Reduction of Kerf Loss and Wire Consumption in Multi-wire Sawing, *Solar Energy Materials and Solar Cells*, 136:44–47, doi:10.1016/j.solmat.2014.12.020.
- [185] Shaw M. C., 1996, *Principles of Abrasive Processing*. Oxford Series on Advanced Manufacturing. Oxford, Clarendon.
- [186] Shaw M. C., Dirke S. O., 1956, On the Wear of Cutting Tools, *Microtechnic*, 10(4):187–193.
- [187] Shibata T., Fujii S., Makino E., Ikeda M., 1996, Ductile-Regime Turning Mechanism of Single-Crystal Silicon, *Precision Engineering-Journal of the American Society for Precision Engineering*, 18(2-3):129–137, doi:10.1016/0141-6359(95)00054-2.

- [188] Shimada S., Ikawa N., Inamura T., Takezawa N., Ohmori H., Sata T., 1995, Brittle-Ductile Transition Phenomena in Microindentation and Micromachining, *CIRP Annals - Manufacturing Technology*, 44(1):523–526, doi:10.1016/s0007-8506(07)62377-4.
- [189] Siems S., Warnecke G., Aurich J. C., 2005, *Mechanismen der Werkstoffbeanspruchungen sowie deren Beeinflussung bei der Zerspanung mit hohen Geschwindigkeiten*, pages 304–329. doi:10.1002/3527605142.ch14.
- [190] Solar Cell Central, 2011. Photovoltaic History, [www.solarcellcentral.com](http://www.solarcellcentral.com), Accessed on 16 September 2019.
- [191] Solar Power Europe, 2017, Global Market Outlook for Solar Power 2017-2021, Report.
- [192] Solar Power Europe, 2019, Global Market Outlook for Solar Power 2019-2023, Report.
- [193] Sopori B., Basnyat P., Devayajanam S., Schnepf R., Sahoo S., Gee J., Severico F., Manens A., Seigneur H., Schoenfeld W. V., 2015, Analyses of Diamond Wire Sawn Wafers: Effect of Various Cutting Parameters, In *42nd Photovoltaic Specialist Conference (PVSC)*. IEEE, 2015.
- [194] Sopori B., Devayajanam S., Basnyat P., 2016, Surface Characteristics and Damage Distributions of Diamond Wire Sawn Wafers for Silicon Solar Cells, *AIMS Materials Science*, 3(2):669–685, doi:10.3934/matserci.2016.2.669.
- [195] Stachowiak G. W., Batchelor A. W., 2005, *Engineering Tribology*. Elsevier Butterworth-Heinemann, Amsterdam, 3rd edition.
- [196] Studman C. J., Field J. E., 1977, The Indentation of Hard Metals: The Role of Residual Stresses, *Journal of Materials Science*, 12(2):215–218, doi:10.1007/bf00566260.
- [197] Sunlight Electric, 2013. [www.sunlightelectric.com/pvhistory](http://www.sunlightelectric.com/pvhistory), Accessed on 15 June 2018.
- [198] Suzuki T., Nishino Y., Yan J., 2017, Mechanisms of Material Removal and Subsurface Damage in Fixed-abrasive Diamond Wire Slicing of Single-Crystalline Silicon, *Precision Engineering*, 50:32–43, doi:10.1016/j.precisioneng.2017.04.011.
- [199] Swain M. V., 1979, Microfracture About Scratches in Brittle Solids, *Proceedings of the Royal Society of London. Series A, Mathematical and Physical Sciences*, 366(1727):575–597, doi:10.1098/rspa.1979.0070.

- [200] Swanson R. M., 2006, A Vision for Crystalline Silicon Photovoltaics, *Progress in Photovoltaics: Research and Applications*, 14(5):443–453, doi:10.1002/pip.709.
- [201] Takeyama H., Murata R., 1963, Basic Investigation of Tool Wear, *Journal of Engineering for Industry*, 85(1):33–37, doi:10.1115/1.3667575.
- [202] Tamaki J., Mahmoud T., Jiwang Y., Sato G., Iyama T., 2004, Effect of Cutting-edge Shape on Ductile Regime Grinding of Optical Glass in Single-grit Diamond Grinding, *Advances in Abrasive Technology VI*, 257-258:89–94, doi:10.4028/www.scientific.net/KEM.257-258.89.
- [203] Taylor F. W., 1906, On The Art Of Cutting Metals, Report, ASME.
- [204] Thomas T. R., 1982, *Rough Surfaces*. Imperial College Press, London, UK, 2nd edition.
- [205] Tian X., Kennedy F. E., 1994, Maximum and Average Flash Temperatures in Sliding Contacts, *Journal of Tribology*, 116(1):167–174, doi:10.1115/1.2927035.
- [206] Trachet A., Subhash G., 2016, Microscopic and Spectroscopic Investigation of Phase Evolution within Static and Dynamic Indentations in Single-Crystal Silicon, *Materials Science and Engineering: A*, 673:321–331, doi:10.1016/j.msea.2016.07.037.
- [207] Transchel R., 2014, *Cutting Mechanism of Active Brazed Single Diamond Grains*, PhD dissertation, ETH Zurich, doi:10.3929/ethz-a-010350887.
- [208] Tyagi V. V., Rahim N. A. A., Rahim N. A., Selvaraj J. A. L., 2013, Progress in Solar PV Technology: Research and Achievement, *Renewable and Sustainable Energy Reviews*, 20:443–461, doi:10.1016/j.rser.2012.09.028.
- [209] Tönshoff H. K., Friemuth T., Becker J. C., 2002, Process Monitoring in Grinding, *CIRP Annals*, 51(2):551–571, doi:10.1016/S0007-8506(07)61700-4.
- [210] Tönshoff H. K., Peters J., Inasaki I., Paul T., 1992, Modelling and Simulation of Grinding Processes, *CIRP Annals - Manufacturing Technology*, 41(2):677–688, doi:10.1016/S0007-8506(07)63254-5.
- [211] Uetz H., Föhl J., 1978, Wear as an Energy Transformation Process, *Wear*, 49(2):253–264, doi:10.1016/0043-1648(78)90091-1.
- [212] Usui E., Shirakashi T., Kitagawa T., 1978, Analytical Prediction of Three Dimensional Cutting Process—Part 3: Cutting Temperature and

- Crater Wear of Carbide Tool, *Journal of Engineering for Industry*, 100(2), doi:10.1115/1.3439415.
- [213] Usui E., Shirakashi T., Kitagawa T., 1984, Analytical Prediction of Cutting Tool Wear, *Wear*, 100(1-3):129–151, doi:10.1016/0043-1648(84)90010-3.
- [214] Vargas G. E., 2010, *Analyse und Simulation des Prozesses Honräumen von gehärteten Innenprofilen mit Diamantwerkzeugen*, PhD dissertation, ETH Zurich, doi:10.3929/ethz-a-006300284.
- [215] Verkerk J., 1977, Final Report Concerning CIRP Cooperative Work on the Characterization of Grinding Wheel Topography, *Annals of the CIRP*, 26(2).
- [216] Vingsbo O., Hogmark S., 1984, Single-pass Pendulum Grooving — A Technique for Abrasive Testing, *Wear*, 100(1):489–502, doi:10.1016/0043-1648(84)90028-0.
- [217] Wallbridge N. C., Dowson D., 1987, Distribution of Wear Rate Data and a Statistical Approach to Sliding Wear Theory, *Wear*, 119(3):295–312, doi:10.1016/0043-1648(87)90037-8.
- [218] Wang C., Chen J., Fang Q., Liu F., Liu Y., 2016, Study on Brittle Material Removal in the Grinding Process Utilizing Theoretical Analysis and Numerical Simulation, *The International Journal of Advanced Manufacturing Technology*, pages 1–12, doi:10.1007/s00170-016-8647-8.
- [219] Wang C., Fang Q., Chen J., Liu Y., Jin T., 2016, Subsurface Damage in High-speed Grinding of Brittle Materials Considering Kinematic Characteristics of the Grinding Process, *The International Journal of Advanced Manufacturing Technology*, 83(5):937–948, doi:10.1007/s00170-015-7627-8.
- [220] Wang J.-J. J., Liao Y.-Y., 2007, Critical Depth of Cut and Specific Cutting Energy of a Microscribing Process for Hard and Brittle Materials, *Journal of Engineering Materials and Technology*, 130(1):011002–011002–6, doi:10.1115/1.2806253.
- [221] Wang P., Ge P., Gao Y., Bi W., 2017, Prediction of Sawing Force for Single-Crystal Silicon Carbide with Fixed Abrasive Diamond Wire Saw, *Materials Science in Semiconductor Processing*, 63:25–32, doi:10.1016/j.mssp.2017.01.014.
- [222] Wegener K., Hoffmeister H. W., Karpuschewski B., Kuster F., Hahmann W. C., Rabiey M., 2011, Conditioning and Monitoring of Grinding Wheels, *CIRP Annals*, 60(2):757–777, doi:10.1016/j.cirp.2011.05.003.

- [223] Wegener K., Vargas G. E., Wunder S., Kuster F., Pinto F. W., May 2008, An Experimental Approach for Grain Wear for Improving Kinematic-Geometrical Simulation, In *Proceedings of the EUSPEN International Conference*, May 2008, doi:10.1007/s40430-013-0085-z.
- [224] Wu C., Jiang Z., Fan W., Chen L., 2016, Finite Element Analysis of Multi-wire Saw Silicon Rods with Consolidated Abrasive Diamonds, *The International Journal of Advanced Manufacturing Technology*, pages 1–8, doi:10.1007/s00170-016-9321-x.
- [225] Wu H., Melkote S. N., 2012, Effect of Crystallographic Orientation on Ductile Scribing of Crystalline Silicon: Role of Phase Transformation and Slip, *Materials Science and Engineering a-Structural Materials Properties Microstructure and Processing*, 549:200–205, doi:10.1016/j.msea.2012.04.034.
- [226] Wu H., Melkote S. N., 2012, Study of Ductile-to-Brittle Transition in Single Grit Diamond Scribing of Silicon: Application to Wire Sawing of Silicon Wafers, *Journal of Engineering Materials and Technology*, 134(4), doi:10.1115/1.4006177.
- [227] Wu H., Yang C., Melkote S., 2015, Modeling and Analysis of the Grit Level Interaction in Diamond Wire Sawing of Silicon, *The International Journal of Advanced Manufacturing Technology*, doi:10.1007/s00170-015-7771-1.
- [228] Wunder S., 2012, *Verschleissverhalten von Diamantabrichtrollen beim Abrichten von Korund-Schleifschnecken*, PhD dissertation, ETH Zurich, doi:10.3929/ethz-a-007587878.
- [229] Würzner S., Falke A., Buchwald R., Möller H. J., 2015, Determination of the Impact of the Wire Velocity on the Surface Damage of Diamond Wire Sawn Silicon Wafers, *Energy Procedia*, 77:881–890, doi:10.1016/j.egypro.2015.07.124.
- [230] Xie J., Wei F., Zheng J. H., Tamaki J., Kubo A., 2011, 3D Laser Investigation on Micron-scale Grain Protrusion Topography of Truncated Diamond Grinding Wheel for Precision Grinding Performance, *International Journal of Machine Tools and Manufacture*, 51(5):411–419, doi:10.1016/j.ijmactools.2011.01.010.
- [231] Xie J., Xu J., Tang Y., Tamaki J., 2008, 3D Graphical Evaluation of Micron-scale Protrusion Topography of Diamond Grinding Wheel, *International Journal of Machine Tools and Manufacture*, 48(11):1254–1260, doi:10.1016/j.ijmactools.2008.03.003.

- [232] Yan J., Asami T., Harada H., Kuriyagawa T., 2009, Fundamental Investigation of Subsurface Damage in Single-Crystalline Silicon Caused by Diamond Machining, *Precision Engineering*, 33(4):378–386, doi:10.1016/j.precisioneng.2008.10.008.
- [233] Yan J., Syoji K., Kuriyagawa T., Suzuki H., 2002, Ductile Regime Turning at Large Tool Feed, *Journal of Materials Processing Technology*, 121(2):363–372, doi:10.1016/S0924-0136(01)01218-3.
- [234] Yang C., Wu H., Melkote S., Danyluk S., 2013, Comparative Analysis of Fracture Strength of Slurry and Diamond Wire Sawn Multi-Crystalline Silicon Solar Wafers, *Advanced Engineering Materials*, 15(5):358–365, doi:10.1002/adem.201200262.
- [235] Yang J., Banerjee S., Wu J., Myung Y., Rezvanian O., Banerjee P., 2015, Phase and Stress Evolution in Diamond Microparticles During Diamond-coated Wire Sawing of Si Ingots, *The International Journal of Advanced Manufacturing Technology*, 82(9-12):1675–1682, doi:10.1007/s00170-015-7446-y.
- [236] Yang L. J., 2005, A Test Methodology for the Determination of Wear Coefficient, *Wear*, 259(7):1453–1461, doi:10.1016/j.wear.2005.01.026.
- [237] Yao C. Y., Wang M. H., Peng W., 2010, The Progress of Fixed Abrasive Wire Saws in the Last Decade, *Advanced Materials Research*, 97-101:15–18, doi:10.4028/www.scientific.net/AMR.97-101.15.
- [238] Yao P., Gong Y., Matsuda T., Zhou T., Yan J., Kuriyagawa T., 2012, Investigation of Wheel Wear Mechanisms During Grinding Optical Glasses Through Statistical Analysis of Wheel Topography, *International Journal of Abrasive Technology*, 5(1):33–47, doi:10.1504/ijat.2012.046818.
- [239] Yeh R. H., Chen H. Y., Lee C. K., Tan A. H., 2015, Study of Electroplated Nickel Layer Thickness and Saw Parameters on Cutting Performance in Diamond Wire Sawing of Sapphire Ingots, *Key Engineering Materials*, 656-657:450–455, doi:10.4028/www.scientific.net/KEM.656-657.450.
- [240] Yevtushenko A. A., Ivanyk E. G., Ukhanska O. M., 1997, Transient Temperature of Local Moving Areas of Sliding Contact, *Tribology International*, 30(3):209–214, doi:10.1016/S0301-679X(96)00044-8.
- [241] Yoshikawa H., Sata T., 1963, Study on Wear of Grinding Wheels: Part 1—Bond Fracture in Grinding Wheels, *Journal of Engineering for Industry*, 85(1):39–42, doi:10.1115/1.3667580.

- [242] Yu T., Bastawros A. F., Chandra A., 2017, Experimental and Modeling Characterization of Wear and Life Expectancy of Electroplated CBN Grinding Wheels, *International Journal of Machine Tools and Manufacture*, 121:70–80, doi:10.1016/j.ijmachtools.2017.04.013.
- [243] Yu X., Wang P., Li X., Yang D., 2012, Thin Czochralski Silicon Solar Cells Based on Diamond Wire Sawing Technology, *Solar Energy Materials and Solar Cells*, 98:337–342, doi:10.1016/j.solmat.2011.11.028.
- [244] Zhang G. X., Hu H. J., Ta D., 2004, Ultrasonic Detection of the Metallurgical Defects in the Steel and its Evaluation by Neural Network Based on the Wavelet Transform Noise Suppression, *Key Engineering Materials*, 270-273:160–167, doi:10.4028/www.scientific.net/KEM.270-273.160.
- [245] Zhang L. Y., Wang J. G., Yang Y., Wang C., 2011, Research on the Counterweight in the Process of Diamond Wire Saw Cutting Polysilicon, *Advanced Materials Research*, 418-420:1048–1055, doi:10.4028/www.scientific.net/AMR.418-420.1048.
- [246] Zhang Z., Wang B., Kang R., Zhang B., Guo D., 2015, Changes in Surface Layer of Silicon Wafers from Diamond Scratching, *CIRP Annals*, 64(1):349–352, doi:10.1016/j.cirp.2015.04.005.
- [247] Zhao Q. L., Chen J. Y., 2009, Investigation of Material Removal and Grain Wear Mechanism in Single Point Diamond Scratching Tests on SiC, *Advanced Materials Research*, 69-70:209–213, doi:10.4028/www.scientific.net/AMR.69-70.209.
- [248] Zmitrowicz A., 2006, Wear Patterns and Laws of Wear, *Journal of Theoretical and Applied Mechanics*, 44(2):219–253.
- [249] Zulehner W., 2000, Historical Overview of Silicon Crystal Pulling Development, *Materials Science and Engineering: B*, 73(1):7–15, doi:10.1016/S0921-5107(99)00427-4.



# CURRICULUM VITAE

## Uygar Pala

### Education

2012–2020	PhD. Production Technology, ETH Zurich
2010–2011	MSc. Manufacturing Engineering and Management, Uni. of Nottingham
2005–2009	BSc. Mechanical Engineering, Middle East Technical University NCC

### Professional Experience

2018–2020	Research Engineer, inspire AG, Zurich, Switzerland
2012–2018	Research Assistant, ETH Zurich, Zurich, Switzerland
2010–2011	Postgraduate Project Student, Rolls-Royce plc., Derby, UK
2009–2010	Process Engineer, Roketsan Missiles Inc., Ankara, Turkey

### Research Projects

2017–2020	CTI Project: High-feed grinding of glass edges: A holistic approach to the development of a new process (KTI 25966.2 PFIW-IW)
2015–2017	SNF Project: Experimental analysis and modelling of the process behavior of compliantly supported diamond grains and grain-surface interactions in brittle materials (SNF 200021_162611)
2012–2015	CTI Project: High-speed sawing process of silicon wafers with fixed-diamond wires (KTI 13079.1 PFIW-IW)

### Publications

Pala, U., Süssmaier, S., Wegener, K., 2020, Schnelltest für die Eignung von Diamantdraht zum Wafering, *Jahrbuch Schleifen, Honen, Läppen und Polieren: Verfahren und Maschinen*.

Pala, U., Kuster, F., Wegener, K., 2020, Characterization of Electroplated Diamond Wires and the Resulting Workpiece Quality in Silicon Sawing, *Journal of Materials Processing Technology*, 276:116390, doi: 10.1016/j.jmatprotec.2019.116390.

Pala, U., Wegener, K., 2019, A Novel Method for the Characterization of Diamond Wire Topography and Abrasive Grain Geometries. *MM Science Journal*, 4:3236-3242, doi: 10.17973/mmsj.2019\_11\_2019076.

Pala, U., Süssmaier, S., Kuster, F., Wegener, K., 2018, Experimental Investigation of Tool Wear in Electroplated Diamond Wire Sawing of Silicon, *Procedia CIRP*, 77:371-374, doi: 10.1016/j.procir.2018.09.038

